Modeling Frictional Processes in the Presence of Fluids: From Earthquakes in the Laboratory to Induced Seismicity in Geothermal Reservoirs

Thesis by
Taeho Kim

In Partial Fulfillment of the Requirements for the
Degree of
Doctor of Philosophy

CALIFORNIA INSTITUTE OF TECHNOLOGY
Pasadena, California

2025
Defended July 22nd of 2024

Taeho Kim
ORCID: 0000-0002-2560-7728

ACKNOWLEDGEMENTS

Ending what I consider to be the most formative six years of my life so far is inevitably a bittersweet feeling. I leave the experience a better researcher but more importantly a better person, thanks to the cumulative influence of the amazing people I have had the privilege of meeting during my time at school. I feel that to properly express my gratitude is the best way to dampen the bitterness of the ending of this chapter in my life.

First, I would like to thank my advisors Nadia Lapusta and Jean-Philippe Avouac. I still remember our first meetings on visit day very clearly (Nadia walked with me after our meeting at Gates-Thomas and helped me find Jean-Philippe's office at Mudd). Prior to the visit, I barely expected any general audience from the prestigious faculty members of Caltech. To receive the personal attention from Nadia and Jean-Philippe that I did and to be presented the idea of possibly working together in the future is a feeling that I will never forget. Six years and many more personal meetings later, that initial feeling of excitement has evolved into a relationship that I cherish. Nadia, thank you for sharing with me your infallible knowledge of frictional mechanics, but also your life stories, often in response to hearing mine, and the Ukranian proverbs and jokes that help me make sense of the most confusing and difficult parts of life. Jean-Philippe, thank you for leading me through what was to me originally (and I regret to say perhaps still) the foreign world of seismology and structural geology, but also my first ever geology field trips (including a very frightful moment at Ridgecrest when you counted on me to identify to industry partners the Riedel-shears branching from main trace, which I thankfully and somehow ended up doing correctly) and the largest presentations I have ever made (at SSA and GMG). I am forever indebted to the kindness you have both shown me.

I would like to thank my committee members, Professors Daniel Faulkner, Kaushik Bhattacharya and Ruby Fu for generously accepting to serve on my thesis committee. Dan, thank you for advising our collaborative work ever since my second year, including the numerous late evening meetings on Zoom to accommodate the time difference between Liverpool and LA. I believe that the continued enthusiasm I had in analyzing experiments I have never seen from halfway across the globe was largely possible thanks to the enthusiasm you always showed in working with me. I would also like to thank Professor Zhongwen Zhan, for leading us through

our collaborative work in interpreting high-frequency DAS signals of the 2021 Antelope Valley earthquake — my first ever experience with DAS. I now hope to continue working with DAS in my postdoctoral studies, and Zhongwen's brilliance and optimism are the main parts of that inspiration.

Perhaps the biggest source of motivation for me to continue in the world of research is the brilliant and inspiring group of people I have the privilege of working with everyday. I would like to especially thank Valere Lambert, who took the self-initiative to take me under his wing upon my arrival at Caltech. Thank you for the countless conversations about the life and future of a PhD student, friction and rupture dynamics but also for the late night excursions in the Benioff room for whiskey tasting and watching the Halloween and SAW series. I'd like to thank Mateo Acosta for being the unending beam of optimism and encouragement that makes me feel more valuable as a researcher. I'd like to thank Jiaxuan Li and Ettore Biondi for continuing to introduce me to the world of DAS and inspiring me to pursue it in the future. I'd also like to thank Kyungjae Im for helping me with work with Quake-DFN but also for helping me navigate the great Korean network of academia. Thank you to all those that I do not have the space to mention in more detail here such as Pond Sirorattanakul, Hojjat Kaveh, Stacy Larochelle, Kavya Sudhir, Mary Agajanian among many others from the Lapusta and Avouac research groups.

During the time of my graduate studies, I have been lucky enough to make incredible personal connections to people that I consider my dearest friends. I'd like to thank the roommates of my first two years, Alex Perzoim de Faveri and Andrei Shubin, especially for the late night runs around San Marino during the COVID lockdown. I'd like to thank the roommates of my next two years, Alex Perzoim de Faveri (again), Salvador Gomez, Neehar Kondapaneni, and Eric Ocegueda, for what was easily the best set of roommates that I have ever had in my life, not the least for the night of Tichu and our endless asking Neehar to remind us the purpose of the dog. I'd like to make a special shoutout to Iretomiwa (Tomi) Esho for helping me lead the SOPS IM soccer team, and for being a constant friend ever since visit day, and then even after he switched to a different option. I'd like to thank Shengduo Liu, for the bountiful source of joy that he is and the endless pit of knowledge about East Asian history that I love to siphon from (oh, and also for constantly referring to me as Dr. Kim in his defense presentation that was only five days after mine).

Life in research is only possible for me thanks to the support and love from my family. I'd first like to thank my parents, Sun-Mi Choi (Mom) and Joo-Sun Kim

(Dad) for their belief in me ever since I could memorize a few dinosaur names as a child. I'd like to thank my older sister, Yesse Kim, whose incredible talent and artsmanship as a pianist have always been a inspiration to me. I'd like to thank my partner's family, for accepting me into theirs so graciously, especially her parents Roguelina and Pablo Mora, for their love and understanding — and for practically adopting me into their home during the lockdown — and also her siblings, Lupe, Peter, Che (thank you Peter & Che, for helping me keep my car alive), and Mary Mora (who makes the best Birria that I've ever had) for helping me feel at home. I'd like to thank my friends from middle school, Peter Burke and Boris Burman, who I consider to be the brothers I never had, and who help me connect the disjointed past of my life to the present. Last but not least, I'd like to thank my partner Raqueline Linda Mora, for sharing with me the joy of life outside of work. The completion of this thesis has a deeper meaning because of what it means to us, as opposed to just me alone. I love you, and thank you.

ABSTRACT

Induced seismicity — earthquakes driven by injections of fluids into the subsurface — is of growing societal importance in its impact on clean energy technology. Advancements central to the world's transition to a greener economy such as geothermal energy and long-term geologic storage of CO2 are hampered by a lack of understanding and control of the associated seismic hazards. In its mechanics, frictional processes in the presence of fluids is a difficult problem to model given the challenges of studying frictionally unstable material in a controlled environment. Unstable gouge material is commonly found along faults in nature, due to pulverization of brittle rock in to granular layers called 'gouge.' This thesis approaches the challenge at two different scales: 1. at the scale of the localized shear layer along the interface between two faults where we model laboratory earthquakes in the presence of pressurized fluids, and 2. at the scale of a reservoir where we model the rate of earthquakes given the injection/extraction schedule.

In order to infer the frictional properties of unstable gouge material from laboratory experiments, we develop a probabilistic model based on a spring-slider representation of the experiment along with the rate-and-state friction law. Inversions indicate that the presence of pressurized pore fluids stabilizes the gouge — by an increase in the strength of the contacts and a lesser decrease in the grain size with slip — even under the same effective normal stress. Assuming purely slip-dependent healing of friction leads to an evolution of parameters with slip that is consistent with previously established interpretations of rate-and-state parameters. The best fitting spring-slider model still shows significant discrepancies to the experiment in the evolution of creep and in the dependence on loading rate. A quasi-static finite-element model with the same rate-and-state properties suggests that the gouge in the sample likely slides in a spatially uniform manner. Thus, the discrepancies between the spring-slider model and the experiment can likely be attributed to flaws in the rate-and-state formalism and the slip law rather than the idealization of a finite geometry to a single-degree-of-freedom system. The results prove that quantitative analysis of frictional processes of gouge in the unstable regime is possible, and that future development of constitutive relationships for friction should aim to reproduce key features of stick-slip in detail.

To model seismicity induced by a geothermal well stimulation, we develop physical and statistical models of the seismicity rate. The physical models are based

on rate-and-state friction and stress changes due to pore-pressure diffusion. The statistical model performs a convolution of a kernel function inspired by Omori law decay with the injection rate. Both models successfully reproduce the seismicity observed during the 2018 enhanced geothermal system (EGS) simulation in Otaniemi, Finland. We find that the effect of time-dependent nucleation from rate-and-state friction is crucial in reproducing the temporal and spatial patterns of the observed seismicity. We also find that the effect of finite nucleation cannot be approximated well by introducing a stress threshold in the standard Coulomb friction model, at least in the context of rapid variations of injection rates common in EGS operations.

We highlight the major assumptions of the Dieterich seismicity rate model and examine how they may bias interpretations of induced seismicity observed in real reservoirs by comparing it directly to a Discrete Fault Network (DFN) model. The spatio-temporal pattern of seismicity in the finite setting is not only dependent on fluid transport properties and its combination with nucleation characteristics but also the distribution of initial conditions of the fault network. The back-propagation front, in particular, occurs co-injection if the time to instability for the minimum slip rate is shorter than the injection duration. The relocated catalogue of the 1993 GPK1 stimulation in Soultz-Sous-Forêts shows such a back-front which can be fit qualitatively using the time to instability measure. A simple model for the rate of magnitudes that accounts for the evolution of frictional stability reproduces the apparent increase in the source radius of induced events in Soultz-Sous-Forêts. The rate of larger events is overestimated by the model, possibly due to an overestimation of maximum magnitudes by the volume of stimulation. The comparisons reveal that parameters of the Dieterich model lack clear physical meaning in the finite analogue and highlight the importance of using realistic physics, especially in models at large scales where uncertainty due to assumptions at smaller scales may be amplified.

We end the thesis with the application of rate-and-state friction to dynamic rupture modeling of seismic data from distributed acoustic sensing (DAS). The modeling of the high-frequency DAS recordings of a M_w 6.0 earthquake suggests a highly heterogeneous underlying fault with several prominent asperities and barriers that may control rupture dynamics. The model demonstrates how the high-stress patches both inhibit and promote the overall rupture, while also contributing to a significant amount of the energy release themselves. The successful interpretations of modern seismological data encourage future development efficient models that can be used for dynamic inversions.

PUBLISHED CONTENT AND CONTRIBUTIONS

Kim, Taeho and Jean-Philippe Avouac (2023). "Stress-based and convolutional forecasting of injection-induced seismicity: application to the Otaniemi geothermal reservoir stimulation." In: *Journal of Geophysical Research: Solid Earth* 128.4, e2022JB024960. DOI: 10.1029/2022JB024960.

T.K and J-P.A participated in the conception of the project and the writing of the manuscript. T.K. implemented the numerical codes.

Li, Jiaxuan et al. (2023). "The break of earthquake asperities imaged by distributed acoustic sensing." In: *Nature* 620.7975, pp. 800–806. DOI: s41586-023-06227-w.

J.L. and Z.Z. designed the work. J.L. performed the back-projection imaging. T.K. and N.L. designed the rupture modelling. T.K. performed the rupture simulations. J.L. and E.B. implemented the processing code. J.L., Z.Z., T.K. and N.L. prepared and revised the paper. E.B. collected the DAS data and determined the fibre channel locations.

TABLE OF CONTENTS

LIST OF ILLUSTRATIONS

Number *Page*

LIST OF TABLES

Chapter 1

INTRODUCTION

The 2017 M_w 5.4 Pohang earthquake was a historic event for a country with minimal history of seismic activity and an alarm for the industry of geothermal energy world-wide. The earthquake occurred approximately 3 months after a year and a half of fluid injection into the subsurface of Pohang, an industrial city on the eastern coast of South Korea, for the country's first ever stimulation of a geothermal energy reservoir. The unexpected earthquake caused nearly 300 million dollars of damages to nearby infrastructure, and litigation between the government and the city's residents for compensation continues to this day. An even greater loss may be the opportunity cost for the future of geothermal energy in Korea. In March of 2022, the Korean government demolished the geothermal power plant of Pohang. A permanent asterisk now marks all existing and future plans for the expansion of geothermal energy in the country (Figure 1.1).

The Pohang earthquake is only one notable example of an earthquake triggering the immediate termination of an industrial operation which involved injection of fluid underground (Ellsworth et al., 2019; Kim et al., 2018). A lack of clear understanding and control of the maximum magnitude event that orders immediate suspension of all operations (Häring et al., 2008; Schultz et al., 2020) hamper advancements central to the world's transition to a greener economy such as geothermal energy (Gaucher et al., 2015; Majer et al., 2007; Zang et al., 2014) and long-term geologic carbon sequestration (Vilarrasa and Carrera, 2015; White and Foxall, 2016; Zoback and Gorelick, 2012). At the same time, fluid injections offer a relatively repeatable and controllable environment to study the complex network of earthquake processes, and the collection of seismic and geodetic data accommodating fluid injections has provided invaluable knowledge regarding earthquake physics. A better understanding of injection-induced seismicity could therefore help international efforts in limiting or offsetting emissions of CO_2 (Bertani, 2012; Tester et al., 2006) and advance our understanding of devastating natural earthquakes that may pose even greater threat to civil safety.

With respect to geothermal energy, the changing landscape of the global energy sector poses further challenges. As solar and wind energy increases its capacity to

Figure 1.1: The 2017 M_w5.4 Pohang Earthquake. A M_w5.4 earthquake struck the coast of Pohang, South Korea (top left) on Nov. 15th, 2017. Nearly 300 million dollars of damages followed, mostly in the form of infrastructure damage due to the ground motion (e.g., bottom left - Gwon and Song, 2017). (Top right) Korean news channel JTBC reports on the earthquake at the time of its occurrence and (bottom right) the same news agency reports on the demolition of the geothermal plant 5 years after the earthquake in 2022. The earthquake has caused a significant dent in future expansion of geothermal energy production in the country.

support energy demand, so has the dependence of the power grid on their seasonal and daily fluctuations. The so-called 'Duck Curve' (Figure 1.2), which traces the net energy demand during the course of a day closely resembling the shape of a duck, demonstrates the ever increasing demand for energy sources complementary to solar and wind power. The long-held pride of the geothermal community as a baseline source of energy has begun to lose its place in modern society. Geothermal energy must adapt to becoming an on-demand source of power that can be flexible in terms of its injection and extraction rate of fluids. Introduction of such sudden or oscillatory changes in the stress state of the injected medium requires a commensurate understanding of the physics for safe and optimal operation.

This thesis approaches the problem of induced seismicity from the modeling perspective at two different scales: 1. at the scale of the localized shear layer along the interface between two faults where we model laboratory earthquakes in the presence

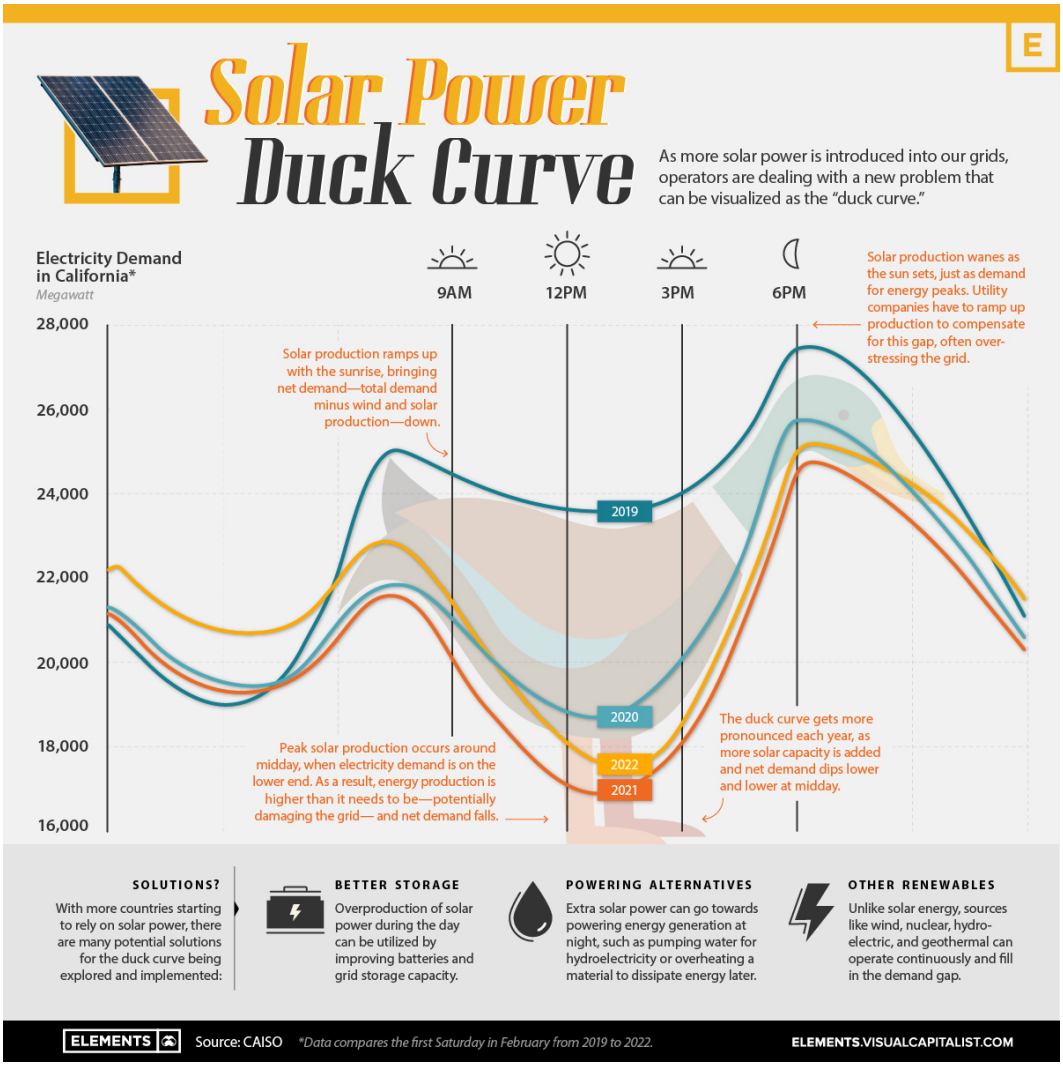

Figure 1.2: The Duck Curve (*The Solar Power Duck Curve Explained* n.d.): The colored lines plot the net demand of electricity in California from 2019 to 2022. The graph begins during nighttime, when energy demand is the lowest. Demand picks up in the morning before dropping again due to the production of solar energy during daytime. Net energy demand is the highest during the evening, as solar energy production decreases while demand stays high. The trough of the net energy demand during daytime (sometimes referred to as 'the belly of the duck' has steadily decrease with time due to an increase in the construction of solar panels. The curve marks a shift in the energy sector towards solutions for flattening the peak during the evening hours with alternative sources of energy that can be produced on-demand. With regards to geothermal energy, this requires a thorough understanding of the interplay between frictional instability and fluid injections for optimal operation that can be flexible in terms of the desired injection/extraction rates.

of pressurized fluids, and 2. at the scale of a reservoir where we model the rate of

earthquakes given the injection/extraction schedule. In this introduction, I discuss present challenges and existing theory in developing such models.

1.1 Multi-Scale Nature of Earthquakes

An earthquake is the culmination of a complex network of mechanisms that spans multiple scales in both time and space. Prior to the earthquake, a long period of creep potentially lasting decades precedes the short period of seismic slip that could last seconds. Neither transition between the two periods happen instantaneously. The transition from creep to dynamic slip occurs through what is often termed 'nucleation' whose finite duration has been observed in the lab (McLaskey, 2019) and numerical simulations (Ampuero and Rubin, 2008; Rubin and Ampuero, 2005). In fact, the finite nucleation process turns out to be a natural product of an initial resistance to sliding in response to a sudden increase in the slip rate that is observed in laboratory experiments. The transition from dynamic slip back to creep, a.k.a. the arrest process, can also occur gradually, depending on the balance between the amount of available energy lying ahead of the rupture tip and the energy dissipated by friction (Ke, McLaskey, and Kammer, 2022; Lambert, Lapusta, and Perry, 2021). Accurately resolving the two transitions is paramount to modeling the earthquake process; one determines how an earthquake begins and the other determines how it stops.

In space, earthquake ruptures on preexisting natural faults that is a plane of weakness embedded between larger bulk media whose damage structure is remarkably hierarchical (Figure 1.3). At a sufficient distance away from the fault, the bulk is largely undamaged and unaffected by slip from earthquakes. Gradually, a network of fractures begins to pervade the rock closer to the fault interface as a result of shear deformation. The interface that accommodates the majority of slip, sometimes referred to as the Principal Slip Zone (PSZ), is itself a continuum layer of granular particles . The brittle rock pulverizes under the high level of normal stress experienced at seismogenic depths to a material called 'gouge.' Field studies have confirmed the granular composition of the PSZ by the presence of incohesive rock particles with extremely small grain size (Chester and Chester, 1998; Chester et al., 2004). Other studies have also shown that the PSZ may not always be a single strand at the length scale of a fault but more likely a web of strands that branch along the direction of slip (Mitchell and Faulkner, 2009). Damaged rock fills the space between the branches of gouge, and slip is accommodated in a sharply heterogeneous manner across the zone that is referred to as the fault core.

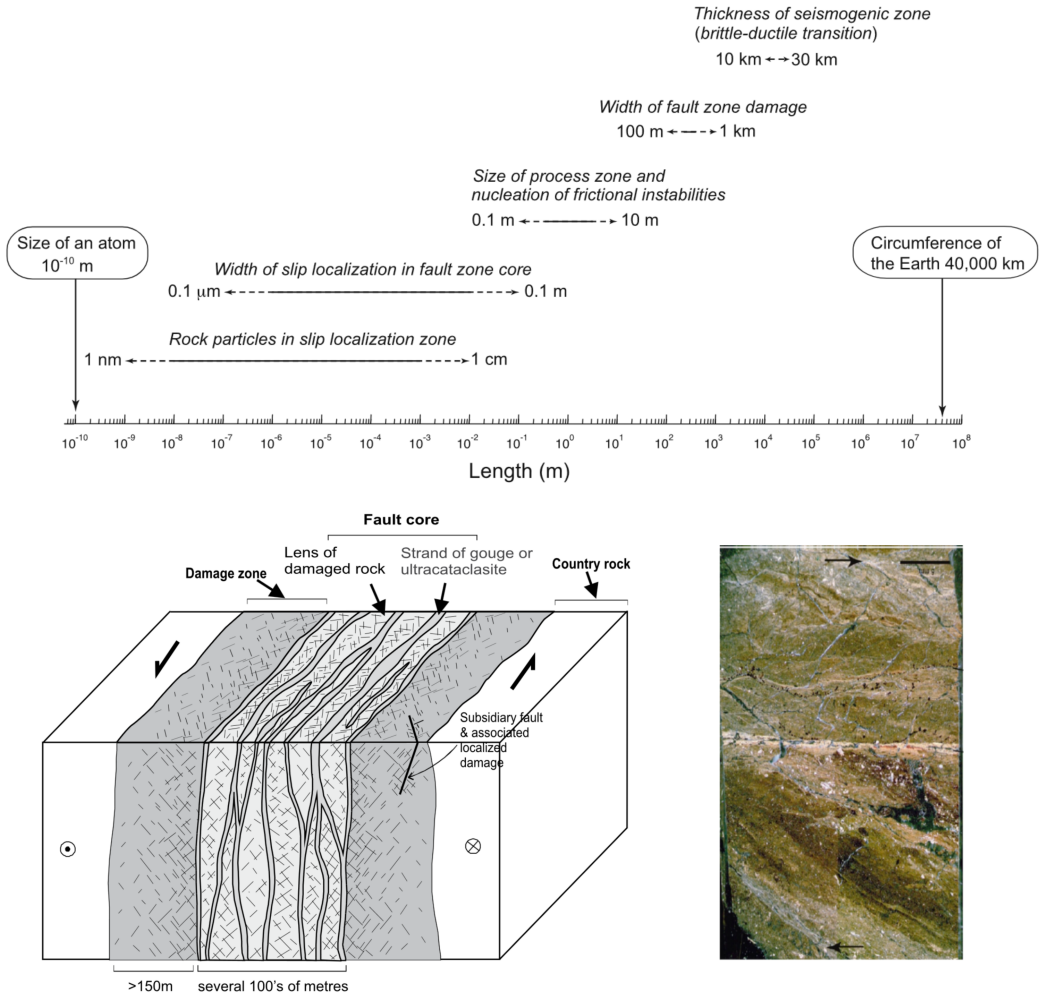

Figure 1.3: Multi-Scale Nature of Earthquakes in Space. (Top) The earthquake environment in its entirety spans a vast spectrum of length scales, bridged between the size of grains along the fault interface at the nano-scale and the thickness of the seismogenic zone at the kilometer scale (Ben-Zion, 2008). (Bottom left) More zoomed-in around the area immediately adjacent to a fault, a complex damage structure surrounds a fault core that accommodates a bulk of the shear deformation (Mitchell and Faulkner, 2009). (Bottom right) Layers of most localized deformation are more granular in nature, due to the pulverization of the rock under high compression (Chester and Goldsby, 2003). The complex network of physics that accommodates each layer of rock with varying levels of damage poses a complex problem to model and to resolve accurately in numerical simulations.

The multi-scale nature of the earthquake process poses a significant challenge for who wishes to model it. Resolving the multiple scales in time is equivalent to solving a stiff ordinary differential equation, a well-known challenge in numerical mathematics. Lapusta et al. (2000) made a breakthrough in resolving the time scale

by proposing an adaptive time stepping scheme that is dependent on the maximum slip rate along a fault. Resolving the multiple scales in space on the other hand, remains an unsolved problem. The development of hierarchical models aided by rapid computation of smaller scale processes using machine learning techniques raises hope for the feasibility of multi-scale models in the future (Karimi and Bhattacharya, 2024). Yet, the question of what physics is actually present in the fault core is still up to debate. Granular gouge may exhibit significantly different and possibly more complex mechanics compared to bare surfaces (Marone, 1998; Melosh, 1979). In anticipation of a numerical method that can resolve various length scales simultaneously, the community must first identify and understand the physics to model and the competitive or cooperative interplay between them.

1.2 Friction in the Presence of Fluids

Even without injections, fluids are already common at seismogenic depths. Water percolates through the rock pores by diffusive transport. To first order, the gravitational weight of the fluid imposes a fluid pressure to the surrounding rock medium which reduces the effective stress felt by the poroelastic continuum when subtracted from the gravitational weight of the solid rock. The decrease in normal stress generally decreases the shear stress in the media as well. Since frictional resistance is believed to be directly proportional to the normal stress, the presence of fluid also decreases shear strength.

In fact, the interplay between fluid and rock can be much more complicated (Figure 1.4). For example, dissipation of frictional energy into heat during dynamic slip can cause a rapid increase in temperature along the PSZ, which includes the pore fluids. The increase in temperature causes a rapid increase in pore pressure which dramatically decreases frictional resistance. Such dynamic weakening by the presence of pressurized pore fluids has been proposed as a possible mechanism for the propagation of slip into a previously stable fault segment during the 2011 M_w 9.0 Tohoku-Oki earthquake (Noda and Lapusta, 2013). Additionally, the transfer of heat to the pore fluids helps explain the 'heat paradox' — the question of why geological evidence of melt is so hard to find along the PSZ in nature despite the expected increase in temperature far exceeding the melting temperature of rocks (Rice, 2006). Poroelasticity can also destabilize slip. Namely, slip causes compression of the bulk rock in the propagating direction and expansion in the opposite direction (Heimisson, Dunham, and Almquist, 2019). Such gradient in pore pressure causes a transfer of fluids across the PSZ such that friction weakens ahead of the rupture tip.

Both pore pressurization and poroelastic fluid transfer are positive feedback mechanisms; slip promotes both phenomenon that in turn promote more slip, facilitating the nucleation and propagation of rupture and delaying the arrest process.

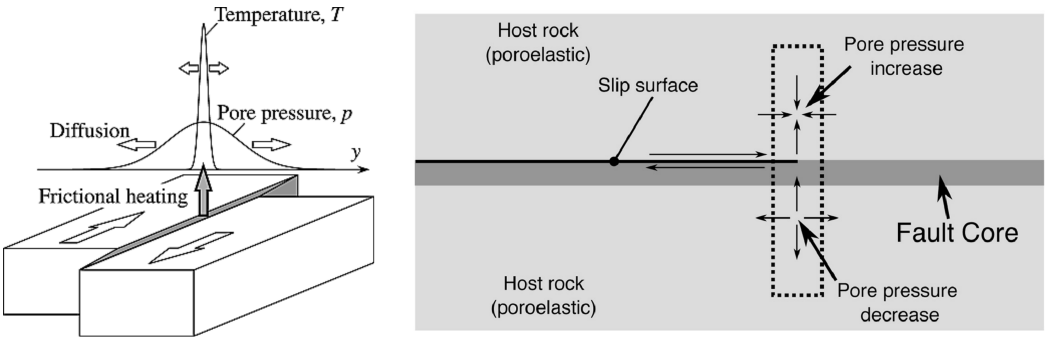

Figure 1.4: Examples of Fluid-Rock Interactions in Earthquakes. (Left) Rapid slip along a localized layer with relatively small thickness produces a significant amount of heat, enough to melt the rock. Heat transfers to the pore fluids and raises its temperature and pressure. The increase in pressure reduces the effective normal stress and friction (Noda and Lapusta, 2010). (Right) Poroelastic deformation of bulk medium during slip induces fluid transport across the layer of slip such that frictional resistance weakens ahead of the rupture tip. Both phenomenon create positive feedback loops that dynamically weakens frictional resistance and promotes rupture propagation. Such interactions between the pore fluid and the solid rock matrix highlight the non-linear relationship between the two materials that affects friction beyond the effective stress principle (Heimisson, Dunham, and Almquist, 2019).

The aforementioned examples are only two of the numerous mechanisms that comprise the fluid-rock interaction. Other studies have highlighted the role of adhesion, mineralization, lubrication, and phase transition, among others (Acosta et al., 2018; Di Toro et al., 2011; Frye and Marone, 2002; Scuderi, Collettini, and Marone, 2017). Given the ubiquitous presence of water underground, fluid is sure to play a dominant role in the earthquake process, although which of the identified mechanisms may be dominant amongst each other is yet to be fully understood.

1.3 Physical Models of Seismicity Rate and Magnitudes Based on Coulomb Friction

In its most basic form, friction defines the resistance to motion along an interface between two materials. In the context of earthquakes, the cumulative resistance to shear deformation in the finite layer of gouge along the PSZ is most often modelled as a frictional process. The finite thickness of the gouge is idealized as a mathematical

plane considering the larger damage structure that surrounds it. Thus, the relevant constitutive relationship is the friction law to govern the resistance to slip along the approximately bare surface.

The simplest friction law — which might also be the most commonly used — is the Mohr-Coulomb friction law (also referred to hereafter as Coulomb friction). In Coulomb friction, the frictional interface does not slip until the shear stress reaches the predetermined frictional strength of the material. Once slip commences, the frictional strength and stress instantaneously drop to the dynamic level of friction, which is also assumed to be a material property. The Coulomb criterion of instability can be visualized on a Mohr-Coulomb diagram as a diagonal line with the slope corresponding to the tangent of the friction coefficient (Figure 1.5). It is common to impose a vertical shift to the curve such that the x-intercept represents the cohesion between the interface at zero compression.

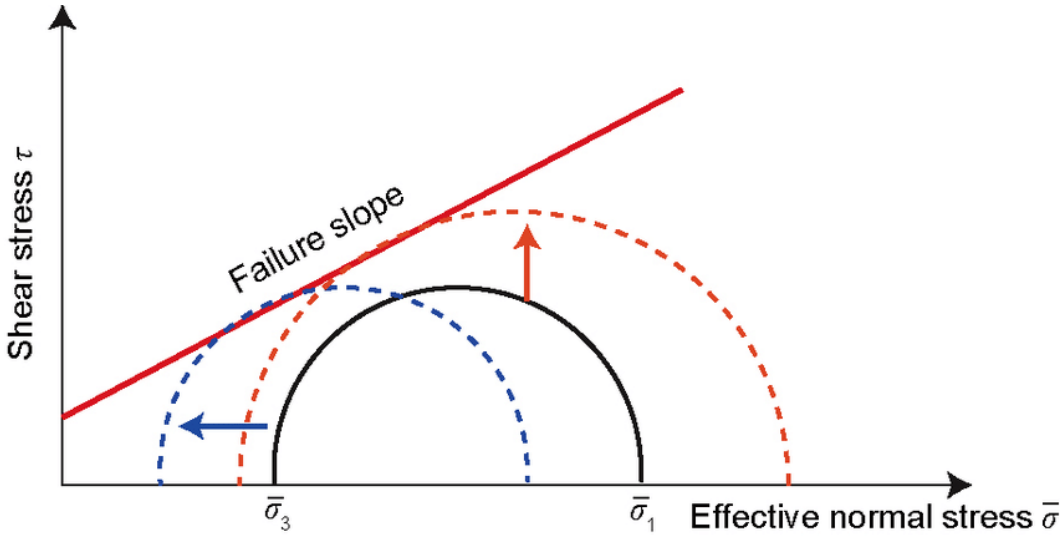

Figure 1.5: Mohr-Coulomb Criterion (Yang et al., 2017). The Mohr-Coulomb diagram plots the state of stress along a plane or arbitrary orientation in 2D. The Coulomb friction law states that slip occurs when the shear stress equals the frictional strength, which is a scalar multiple of the normal stress with the coefficient equal to a predetermined material property. The criterion can be drawn as a diagonal line whose slope is equal to the inverse tangent of the friction coefficient. Injection of fluid decreases the effective normal stress and moves the circle to the left on the plot, bringing closer the state of stress to the failure criterion (the blue transition). Alternatively, the the stress state of the solid constituent could also change (e.g., possibly due to poroelasticity) to increase shear and normal stress (the red transition).

A simple thought experiment can devise a model for the number of earthquakes per time, i.e., the seismicity rate, given the Coulomb friction law. Imagine a random population of faults such that a constant uniform stressing rate to all faults produces a constant seismicity rate. Then, given the Coulomb criterion for the onset of dynamic slip, the seismicity rate in response to an arbitrary stressing history is simply a scalar multiple of the stressing rate. In other words,

$$\frac{R}{r_b} = \frac{\dot{\tau}}{\dot{\tau}_r} \tag{1.1}$$

where R is the seismicity rate in response to stressing rate $\dot{\tau}$ for the constant seismicity rate, r_b, observed at the constant stressing rate $\dot{\tau}_r$. Note that the above is only true in the case of monotonically increasing stress history. If stress ever decreases, the Kaiser effect (Lavrov, 2003) would suppress seismicity until the previous maximum stress is reached.

The simple and linear proportionality between seismicity and stressing rate is in fact **not** observed in nature. Most notably, the fluctuations of seismicity rate observed at the Himalayan Main Thrust Fault show a distinctly non-linear dependence on the periodicity of the applied loading (Ader and Avouac, 2013). The seismicity rate in the Himalayas consist of a strong periodicity at the cycle of 1 year, in direct response to the annual monsoon cycle of the region (Figure 1.6). Stress changes with similar amplitude occur at a daily cycle due to tides. However, Himalayan seismicity shows almost no sensitivity to the diurnal oscillations. In other words, the rate-dependence of Equation1.1, or more precisely the lack of rate-dependence in the Coulomb friction leads to a false prediction of natural seismicity.

Coulomb friction also draws strong statements about the possible magnitude of earthquakes. In the context of induced seismicity, Coulomb friction states that slip can only occur in regions where the level of pore pressure has risen sufficiently from the injection such that there is a drop in the frictional strength. In other words, ruptures governed by Coulomb friction can only propagate as far as the volume of fluid stimulation from the injection (Shapiro, Krüger, and Dinske, 2013; Shapiro et al., 2011). Agnostic to the constitutive relationship of friction, McGarr (2014) considered the release of all potential energy stored within the reservoir from the injection through a population of events following typical statistical properties of naturally observed seismicity. Namely, the statistical relationship follows the Gutenberg-Richter law (Gutenberg and Richter, 1956; Ogata, 1988), an empirical

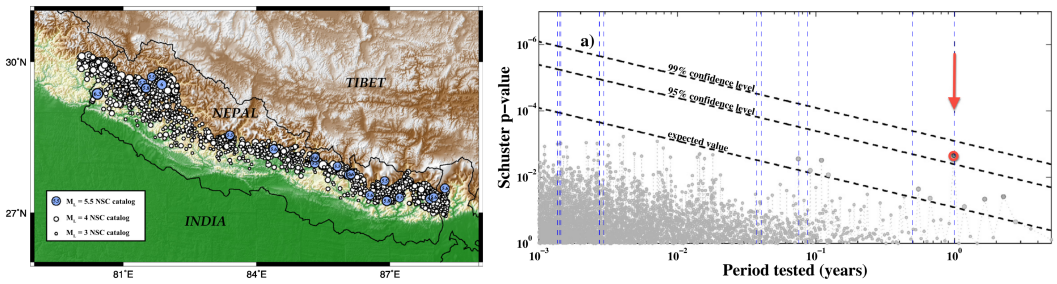

Figure 1.6: Non-linear Dependence of Seismicity on Periodicity in the Himalayas (Ader and Avouac, 2013). (Left) The Main Himalayan Thrust Fault exhibits a significant amount of natural seismicity that is sensitive to natural loading in the region. (Right) A Schuster spectrum delineates the degree of sensitivity with respect to the periodicity of the applied loading. The spectrum shows a statistically significant sensitivity to periods of a year which corresponds to the annual monsoon cycle. Conversely, there is no sensitivity with respect to tides, which occur diurnally (twice a day) and have similar amplitudes of stress change as monsoons. Thus, Himalayan seismicity shows evidence that seismicity has a non-linear dependence to the stressing rate that is not predicted by the Coulomb friction law.

power law distribution with a shape parameter b that represents the proportion of large to small events (for a fixed number of total events, lower the b-value translates to higher chances of large events). The number of events, N, larger or equal to magnitude M follows

$$N = 10^{a-bM} \tag{1.2}$$

where a is an additional parameter to match to the total number of events. This gives an estimate for the maximum magnitude of an earthquake event triggered by the injection, which then must be tapered by the consideration of the volume of stimulation if assuming Coulomb friction. The Pohang earthquake exceeds this maximum magnitude estimate by at least one order of magnitude (Figure 1.7). The occurrence of the Pohang earthquake likely points to the possibility for ruptures to self-propagate beyond the zone of stimulation. Additionally, the Gutenberg-Richter law implies that the maximum magnitude increases with the total number of events. Thus, the seismicity rate model of Equation1.1 based on Coulomb friction would also incorrectly predict the maximum magnitude observed in the Himalayas by incorrectly predicting the total number of events.

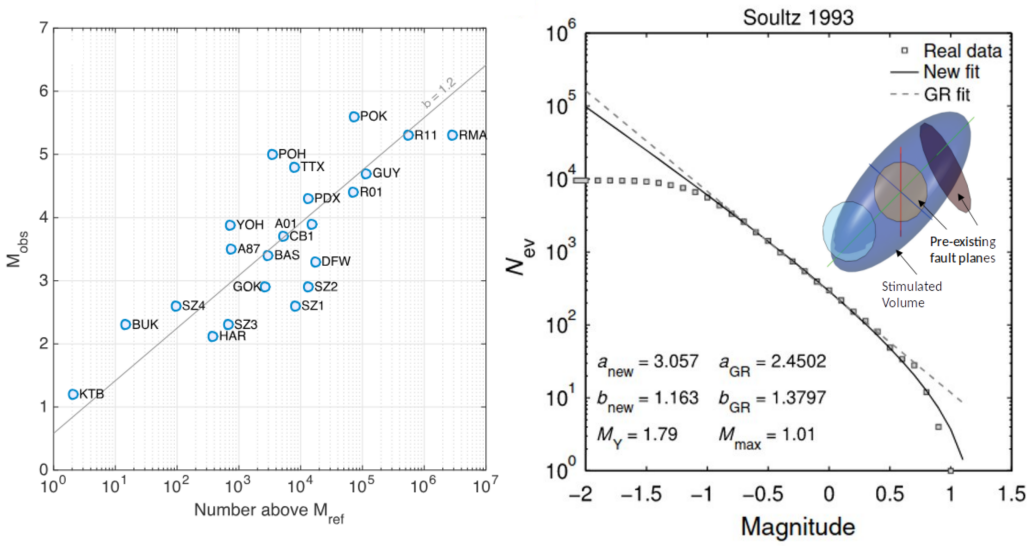

Figure 1.7: Prediction of Maximum Magnitude from Earthquake Statistics and Coulomb Friction. (Left) The blue circles plot the observed maximum magnitude against the number of total earthquakes at various fluid injection sites. The Pohang earthquake is labelled 'POK' near the top right of plot (with the highest magnitude among all sites). The expected maximum magnitude of induced earthquakes assuming the Gutenberg-Richter relationship is plotted as a grey line. A number of maximum magnitude events exceed the estimate, including Pohang (Van der Elst et al., 2016). (Right) A common assumption is that ruptures can only propagate within the zone around the injection point source stimulated by fluid diffusion (illustrated in the inset). Such ideas have tried to explain the observed tapering of the tail of the frequency-magnitude distributions (e.g., the distribution observed from the 1993 Soultz geothermal stimulation as plotted from Shapiro et al., 2011). However, such an explanation would only further under-predict the maximum magnitude observed at injection sites. Thus, ruptures likely propagate beyond the zone of fluid stimulation during injections, such that the Coulomb friction criterion cannot explain.

1.4 Overview

Accurately modeling seismic hazard from fluid injections requires a faithfulness to the complex network of physics that governs earthquakes. In this thesis, we use relatively simple models with a minimalist representation of the subjects while including the most essential set of physics in the problem. We validate and test these models against real data, and study closely the points of misfit in order to conclude the necessary additions to future models.

We start with the modelling of laboratory earthquakes in Chapter 2. We model a direct-shear sliding experiment of realistic quartz gouge with small grain size under

the presence of pressurized fluids. We use a simple, single-degree-of-freedom spring-slider representation governed by rate-and-state friction. Unlike most other experiments which only model the stable portion of the sliding history, we also model the unstable phase, utilizing Bayesian inference methods to invert for the evolution of frictional properties with accumulated slip. We also observe the differences between the experiments with and without pressurized pore fluids, in order to study the effect of fluid-rock interactions on the frictional stability of the gouge.

In Chapter 3, we develop models for the seismicity rate in a geothermal reservoir. We specifically model the 2018 geothermal well stimulation of Otaniemi, Finland which triggered approximately 60,000 events over the course of 50 days. We model the seismicity rate using both physical and statistical approaches. For the physical model, we employ the model of Dieterich (1994) based on rate-and-state friction. We compare the performance of the model to others based on Coulomb friction to investigate whether rate-and-state effects are visible in the seismicity catalogue. We also discuss the inconsistencies between the rate-and-state model and the data.

In Chapter 4 continues the final discussions of chapter 3, particularly with respect to the assumption of the infinite population of nucleation sources in the model of Dieterich (1994). We utilize a discrete fracture network model in order to investigate the effect of the assumption. We connect the bias to real observations, and demonstrate the importance of considering the finite size effects in developing physical models of the seismicity rate.

We end the thesis with Chapter 5, where we demonstrate the application of developing technology in observational seismology, namely distributed acoustic sensing (DAS), in direct conjunction with computational models to gain valuable insights into frictional processes in nature. The results of this chapter motivates promising future directions for practical applications for the models presented in this thesis, leveraged by state-of-the-art tools in remote sensing and big data.

Chapter 2

FRICTIONAL STABILITY OF REALISTIC GOUGE IN THE PRESENCE OF PRESSURIZED FLUIDS: TRACKING THE EVOLUTION OF FRICTIONAL PARAMETERS WITH SLIP BY BAYESIAN INFERENCE

2.1 Introduction

The multi-scale nature of earthquake processes is evident through the remarkably hierarchical structure of the geology that surrounds a fault (Mitchell and Faulkner, 2009). At the largest scale, most of the rock is only elastically deformed as the much of the deformation takes place in narrower zones of localized shear called the fault core. A great extent of damage characterizes the rock between the undeformed bulk and the fault core with significant alteration of rock properties such as reduced stiffness and increased permeability. At the fault core where the largest displacements are accommodated at the highest slip rates, rocks disintegrate into granular particles referred to as gouge, whose grain size distribution has a mean value of 1-10 microns and extends to sub-micron scales. Such comminution, is expected under compression given the brittle nature of rocks (Chester, Chester, and Kronenberg, 2005; Sammis and Ben-Zion, 2008). The principal shear layer that is granular in its composition has been observed at numerous sites in the field and may be ubiquitous along mature faults (Chester and Chester, 1998; Chester et al., 2004; Chester and Goldsby, 2003). Yet, realistic gouge materials with the grain size of 1-10 microns is often avoided in experimental settings due to their innate instability in frictional sliding. The results for frictional sliding of unstable materials are generally more difficult to interpret by existing methods. More commonly, experiments test gouge material with larger grain sizes of the order of 100 microns.

Another nearly ubiquitous aspect of frictional sliding along natural faults is the presence of fluids. Fluids pressurize at seismogenic depths under gravitational load and alter the effective normal stress according to Terzaghi's effective stress principle. Since shear stress is directly proportional to the effective normal stress, the level of pore pressure affects the frictional strength of the fault, to the first order. Furthermore, laboratory experiments and numerical studies have documented the role of fluids on frictional sliding beyond the effective stress principle, such as

the effect of humidity (Frye and Marone, 2002) and dynamic weakening by pore pressurization from shear heating (Noda and Lapusta, 2010; Rice, 2006).

A constitutive relationship that captures the most essential aspects of frictional sliding in the laboratory is the rate-and-state friction law (Dieterich, 1979; Marone, 1998; Ruina, 1983). In the rate-and-state formalism, friction is dependent on the slip rate, V, and an auxiliary state variable, θ, that represents the quantity or quality of contacts along the sliding surface. Namely, friction is expressed as

$$\mu(V,\theta) = \mu^* + a\log\left(\frac{V}{V^*}\right) + b\log\left(\frac{V^*\theta}{D_{RS}}\right) \tag{2.1}$$

where μ^* is the reference friction coefficient at the reference slip rate V^*, a, b, and D_{RS} are rate-and-state parameters. The evolution of the state variable has been proposed to follow various forms, the two most notable being the aging law,

$$\dot{\theta}(V,\theta) = 1 - \frac{V\theta}{D_{RS}} \tag{2.2}$$

and the slip law,

$$\dot{\theta}(V,\theta) = -\frac{V\theta}{D_{RS}}\ln\left(\frac{V\theta}{D_{RS}}\right) \tag{2.3}$$

where $\dot{\cdot} = \frac{d}{dt}$.

The two state evolution laws imply significantly different physical interpretations of the state variable and the origin of frictional healing. The aging law, due to the first term on the left-hand side of Equation 2.3, allows friction to strengthen at stationary contact ($V = 0$) with healing of the frictional surface with time. Such time-dependent healing is based upon laboratory observations of stationary surfaces whose contact area grows under constant compression (Linker and Dieterich, 1992) and slide-hold-slide experiments where the peak level of friction at reslides after holding depends on the duration of the hold (Beeler, Tullis, and Weeks, 1994). While the former experiment provides physical intuition for how friction may strengthen with time, there is no established relationship between the state variable and the size

of the contact surface. The latter experiment has been matched directly using the aging law but recent studies have questioned the basis for time-dependent healing by pointing to the finite amount of creep during holds. Bhattacharya, Rubin, and Beeler (2017) re-examined the slide-hold-slide experiments while accounting for slip in the sample during holds, and showed that the experiments can also be matched using the slip law. With the slip law, the state variable does not evolve in stationary contact, and healing can only occur with slip. Bhattacharya et al. (2022) strengthened the basis of slip dependent healing by imposing low slip rates and velocity jumps as well as holds and finding that the slip law matched different phases of the experiments with much greater consistency in rate-and-state parameters than the aging law. Slip-dependent healing mechanisms favor the view that it is the 'quality' of contact rather than the 'quantity' that determines the evolution of friction (Li et al., 2011).Note that the choice of the state evolution law also has significant impact on the nucleation and propagation of rupture when extrapolated to the scale of a finite fault (Ampuero and Rubin, 2008).

Rate-and-state friction allows for both aseismic creep and unstable stick-slip motion depending on the elastic properties of the bulk medium and frictional properties of the sliding layer. The logarithmic expression of Equation 2.2 is a direct representation of the features observed from a stably sliding material following a velocity step. In the unstable regime, there are no unique relationships between the direct effect, $a \log\left(\frac{V}{V^*}\right)$, or the evolution effect, $b \log\left(\frac{V^*\theta}{D_{RS}}\right)$, and features of stick-slip motion such as the stress drop or the recurrence time. Due to this non-linearity, the use of the unstable regime of frictional sliding has been largely limited to theoretical and numerical studies. Scaling relationships to seismologically observable quantities such as the stress drop and recurrence drop were developed based on numerical simulations of spring-sliders but mostly with respect to $a - b$ (Beeler, Hickman, and Wong, 2001; Gu and Wong, 1991; He, Wong, and Beeler, 2003). Corbi et al. (2024) used simulated annealing of quasi-dynamic rupture models to invert for rate-and-state properties of asperities along a foam interface. Due to non-uniqueness, the problem was also constrained to the inversion of $a - b$.

Here, we develop methods for inference of rate-and-state parameters (a, b, D_{RS} and μ^*) from both stable and unstable regimes of slip in laboratory experiments by Bayesian inversion with Monte-Carlo sampling. We test the methods by synthetic inversions of simulated data before applying them to experimental data of frictional sliding in unstable quartz gouge with realistic grain sizes. We also study the effect

of pore fluid pressurization by considering two experiments at the same effective normal stress but different pore pressure. The inverse framework allows us to track the changes in rate-and-state frictional properties due to comminution and the presence of pressurized pore fluids. We discuss the implications of the observed evolution in rate-and-state parameters on their micro-physical interpretations. We also compare the performance of the two state evolution laws in fitting the data.

2.2 Velocity-Stepping Frictional Sliding Experiments on Quartz Gouge Under Different Pore Pressure

We use an ultrafine granular quartz powder as simulated fault gouge in the experiments. The quartz powder is Min-U-Sil 5, a commercially available powder from US Silica, with a median grain diameter of 1.9 μm and a purity of 99.5% SiO_2. We chose quartz in this study because it is a common crustal material widely found in fault zones, and it is well studied experimentally with reproducible frictional behavior (e.g., Bedford and Faulkner (2021)).

Layers of quartz gouge are sheared in a direct-shear geometry (Figure 2.1) within a triaxial deformation apparatus (Faulkner and Armitage, 2013). The initial thickness of the gouge layer is ~1.3 mm. The layer is placed between the steel direct-shear forcing blocks, with soft silicone spacers positioned at each end to allow shear displacements to be accommodated without any additional lateral resistance. To minimize boundary shear at the edges of the gouge layer, the sliding area (50 x 20 mm) on the direct-shear forcing blocks contains grooves (200 μm deep with 400 μm spacing) cut perpendicular to the sliding direction. Once the gouge layer is constructed, the direct-shear assembly is wrapped in a low-friction polytetrafluoroethylene (PTFE) sleeve (0.25 mm thickness) to minimize friction in the vicinity of the layer; it is then placed into a soft, 3 mm thick, PVC jacket (Nalgene 180 clear tubing). The jacketed assembly is then inserted into the triaxial deformation apparatus, where normal stress is applied by the hydraulic pressure of the confining fluid. For experiments with pore fluid pressure, the pore fluid (deionized water) is introduced to the gouge layer through three porous disks embedded into each direct-shear forcing block (Figure 2.1). The porous disks are positioned to ensure an even distribution of pore fluid pressure across the gouge layer. The gouge is sheared by the axial piston of the triaxial apparatus, and the sliding velocity is stepped between a lower value of 0.3 μm/s and a higher value of 3 μm/s at intervals of 1mm of the loading point displacement after the first velocity step at 1.5mm of the load point displacement. The evolution of shear stress is monitored by an internal force gauge,

with a measurement resolution better than 0.05 kN. During shearing, the confining and pore fluid pressures (and hence effective normal stress) are held constant by servocontrol pumps, with a resolution of better than 0.01 MPa. Experimental data are logged at a frequency of 10 Hz.

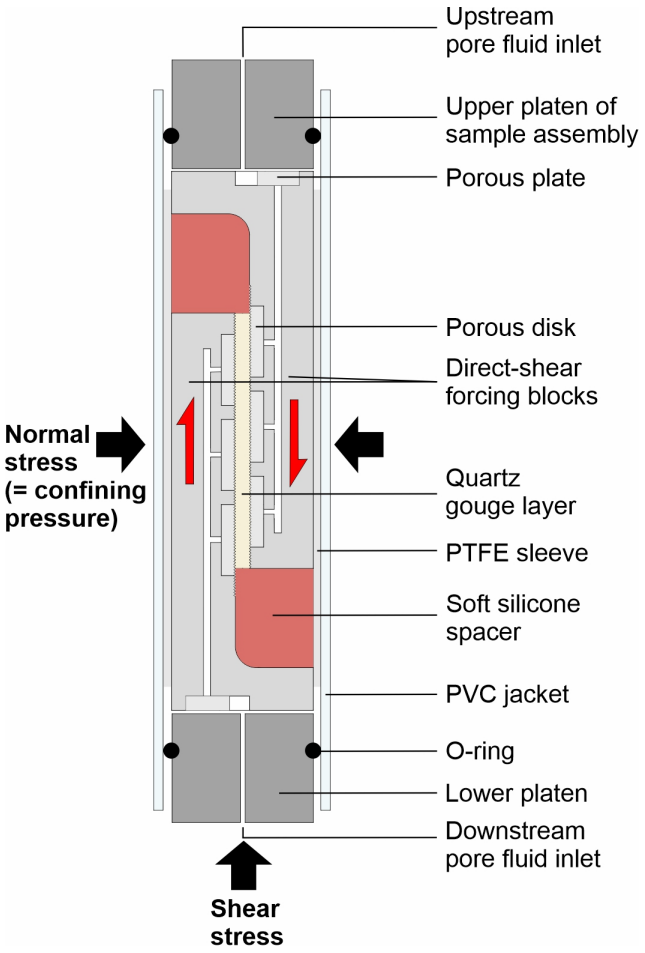

Figure 2.1: Schematic of Experimental Apparatus. Two parallel steel plates sandwich the gouge, confined by fluids that apply hydraulic pressure to a PTFE sleeve that wraps the steel cylinders. Pore pressure, if applied, enters the gouge layer through adjacent porous discs, and the pressure is regulated by a servo upstream. Silicone spacers allow horizontal confinement of the gouge between the steel sliders with negligible additional resistance. Stress is applied via the displacement of the loading column at the end of one of the cylinders, not pictured in the schematic.

We run two experiments at the same effective normal stress but different levels of pore pressure. What we hereafter refer to as the 'dry' sample slides under 40 MPa of confining stress and 0 MPa of pore pressure, while what we refer to as the 'wet' sample slides under 60 MPa of confining stress and 20 MPa of pore pressure. Thus, both experiments have the same effective normal stress of 40 MPa. We note that the

'dry' sample is at room humidity and may be wetter than what is referred to as dry in other studies. We call it 'dry' here to easily distinguish it from the experiment with pressurized fluids.

Both experiments show complex evolution of friction not often seen from frictional sliding of bare surfaces or more stable gouge material with larger particle size (Figure 2.2a). There is a clear contribution from the accumulation of slip to the development of instability not initially present in either experiment. The first velocity step at 1.5 mm of loading point displacement increases the loading rate, and the material still slides stably. After about 0.5mm of additional slip, stick-slip spontaneously develops in the wet experiment but it is then suppressed by a decrease in the loading rate at 2.5 mm of loading point displacement. Instability tends to be triggered by an increase in the loading rate and suppressed by a decrease in the loading rate, until the loading rate increase at 5.5 mm, after which stick-slip persists in both samples until the end of the experiment. The average level of friction changes gradually throughout the entire experiment, both during phases of stable sliding and unstable stick-slip motion. This is most noticeable in the dry sample past the loading point displacement of 3.5 mm, where friction initially increases for about 1 mm before decreasing throughout the rest of the experiment.

Effect of Pressurized Pore Fluids on Stick-Slip

Even while operating at the same effective normal stress, the dry and wet experiments show significant differences in the frictional behavior due to the presence of pressurized pore fluids. In part, the amplitudes and spacing of the stick-slip signals from the wet experiment are noticeably larger than those from the dry experiment at the end of the experiment (Figure 2.2b). Differences between the stick-slip events can be assessed more quantitatively by defining their characteristic features; we define four features for each event: the stress drop, $\Delta\tau$, the peak level of stress, τ_{peak}, the slope of the loading curve immediately following the last event, K_{max}, and the slope immediately prior to the event, K_{min}. If the stiffness of the system is known, K_{max} and K_{min} indicate the amount of slow slip (which we call creep in the following) in the sample during the strengthening phase at the respective times during loading. Since the amount of creep relates to the extent of healing in rate-and-state friction, K_{max} and K_{min} also contain information about the evolution of the state variable, θ. The slope is always the steepest immediately following the stress drop and flattest during the nucleation phase, hence the subscripts, max and min. We also calculate a sense of the average amount of creep in the sample during the

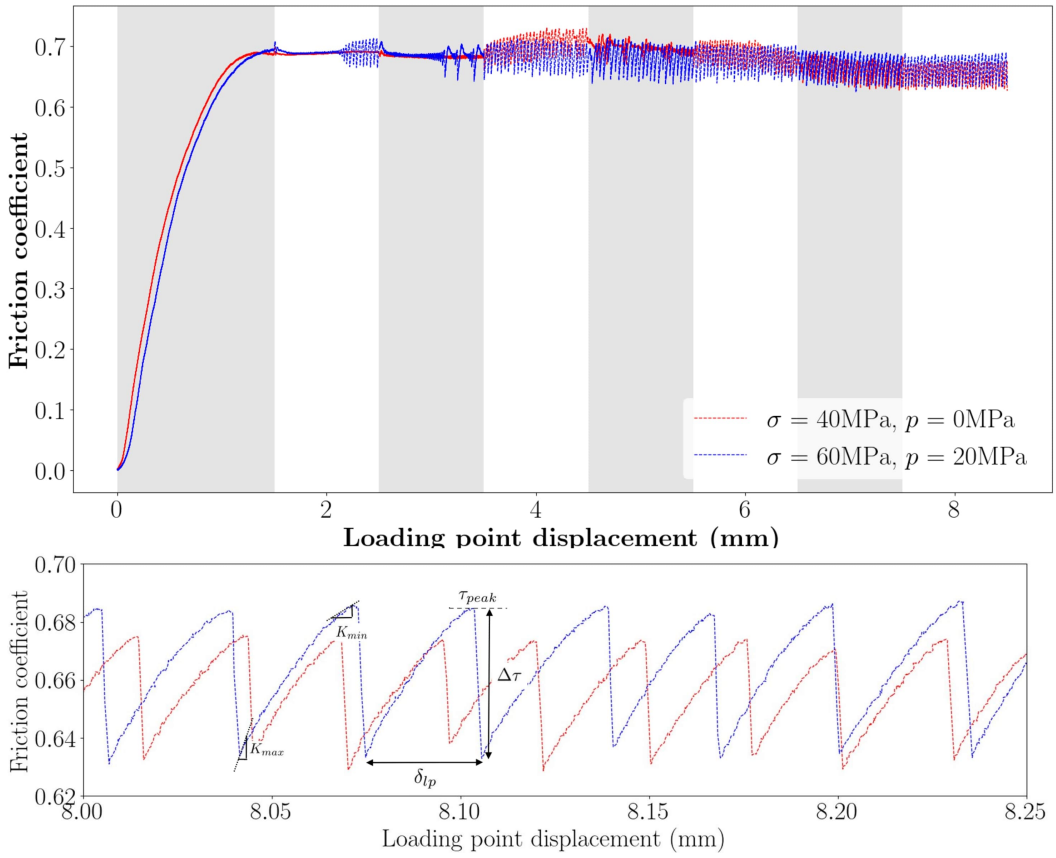

Figure 2.2: volution of Friction in Granular Quartz Gouge With and Without Pressurized Fluids: (a) Two samples with the same effective normal stress (40 MPa) but different pore pressure (0 MPa for the 'dry' sample and 20 MPa for the 'wet' sample) are loaded for 8.5 mm of total displacement. The loading rate is switched between 0.3 µm/s (grey background) and 3 µm/s (white background) at intervals of 1 mm once past the yielding point at 1.5 mm of loading point displacement. Both experiments show a development of instability with accumulation of slip and a dependence of instability on the loading rate. Characteristic features of stick-slip events highlighted in the zoom-in (b) are used for parameter inversion. Instability develops earlier for the wet experiment which also shows larger amplitudes of stick-slip than the dry experiment (b). The differences between the two experiments indicate a possible effect of pore pressure on friction beyond the effective stress principle.

loading stage by taking the difference between the measured stiffness of the system and the average linear slope of the loading curve. We call this the creep percentage,

$$\text{Creep } \% = \left(1 - \frac{(\tau_{peak} - \tau_{min})/(\delta_{lp}(\tau_{peak}) - \delta_{lp}(\tau_{min}))}{K_{mach}}\right) * 100 \tag{2.4}$$

where τ_{min} is the minimum stress at the onset of the event cycle, δ_{lp} is the loading point displacement at the time of the corresponding stress levels, and K_{mach} = 90.5MPa/mm is the stiffness of the experimental apparatus which is measured by loading the apparatus with a steel blank sample in place of the quartz gouge. We note that the creep % as defined here is analogous to the coupling coefficient used in geodesy, which is one minus the ratio of the slip rate along the fault to the plate rate during the interseismic periods.

Let us compare the stick-slip features between the dry and wet experiments (Figure 2.3) during the last millimeter of the loading point displacement, to consider as well-developed slip layer as possible. The comparisons show that the presence of pressurized pore fluids increases the stress drop to a mean value of 2.00MPa in the wet experiment compared to 1.63MPa in the dry experiment. This is contrary to what one would expect from dilatancy, which tends to stabilize frictional motion (explored in further detail in section 2.5). At the same time, the increase in stress drop is accompanied by similar levels of creep % with mean values of 24.3 and 24.4 for the wet and dry samples, respectively. Furthermore, K_{max} tends to be higher in the wet sample, corresponding to a more 'stuck' configuration following the stress drop, while K_{min} tends to be lower, suggesting more creep during event nucleation. The greater evolution in creep is noticeable in the zoom-in of the stick-slip sequence where the curvature in the friction curve of the wet experiment is noticeably larger (Figure 2.2b). The higher stress drop with nearly equal creep % translates to more creep in the absolute sense for the wet experiment. Thus, the wet sample exhibits features of both greater instability in having a larger event with a larger stress drop but also greater stability by developing more creep during the loading period. The differences highlight the effect of pressurized fluids on frictional stability that goes beyond Terzaghi's effective stress principle.

Indirect Inference of Event Slip Rate and Dependence of Nucleation on Loading Rate

Although the slip rate is not directly measured, it can be inferred indirectly from the measurement sampling rate. Figure 4 shows a zoom-in of the stick-slip sequence for a 0.2mm interval of loading point displacement surrounding the velocity step at 7.5mm. Along with connected line plots, individual points of measurement are indicated by dots, with each measurement spaced at intervals of 0.1 seconds in time (corresponding to the sampling rate of 10Hz). For both experiments, stress drops are consistently resolved by more than 2 points, indicating that the events

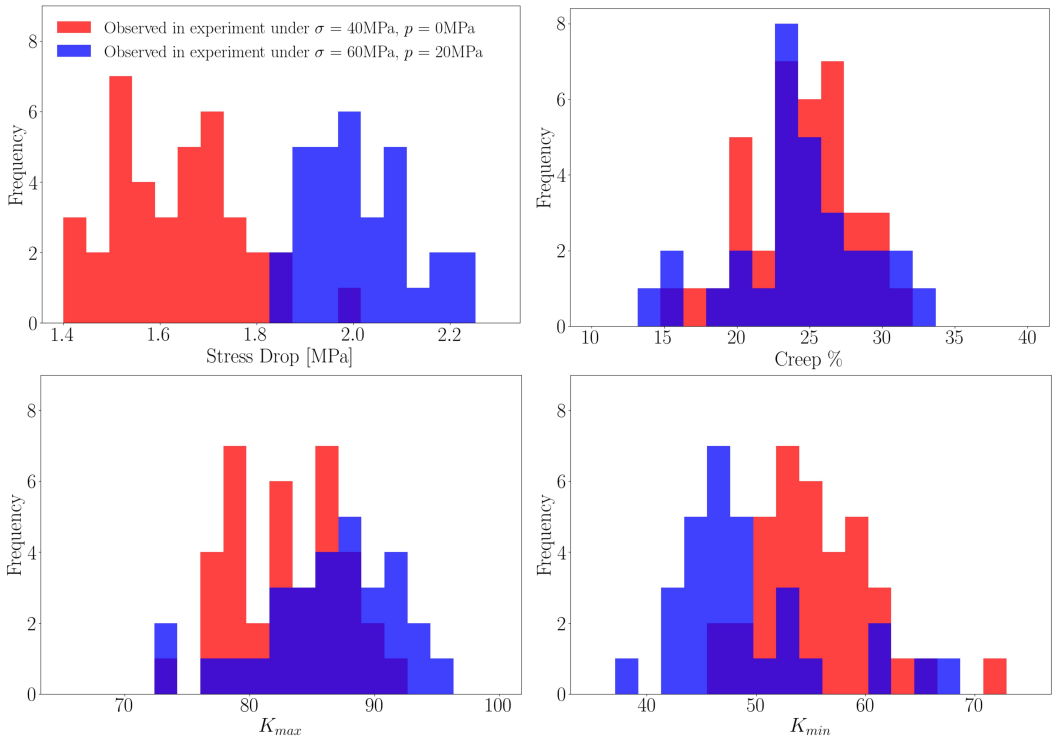

Figure 2.3: Dry and Wet Experiments Differ in Characteristics of Stick-Slip Events: Histograms of stick-slip features from the last millimeter of displacement for the dry (red) and wet (blue) experiments show differences in the distributions of stress drop and observed stiffness but similarity in the distribution of creep %. The wet experiments have generally higher stress drops indicating greater instability. At the same time, the wet experiment shows greater evolution of creep during the aseismic period, starting from higher K_{max} immediately after events leading to lower K_{min} immediately prior to the next events. This results in a greater amount of creep during the strengthening phase in the absolute sense on average and in greater curvature in the evolution of friction (Figure 2.2b). The observed differences between the two experiments indicate the effect of pore pressure on friction beyond the effective stress principle.

have durations of the order of 0.1 seconds. Assuming that the amount of slip during the event is comparable to the increment in loading point displacement leading up to it ($\sim 25\,\mu$m), such durations correspond to an average slip rate of 25 µm/0.1s = 0.25 m/s = 0.00025 m/s. Peak slip rates could be higher or much higher than this average value, the possibility of which we test by modeling later. Hence the stress drop portion of the response is accompanied by relatively rapid slip.

A closer look at the nucleation phase of the stress-drop events shows that the nucleation process is different at the lower loading rate than at the higher loading rate. At the lower loading rate of 0.3 µm/s, the initial stages of the stress drop in

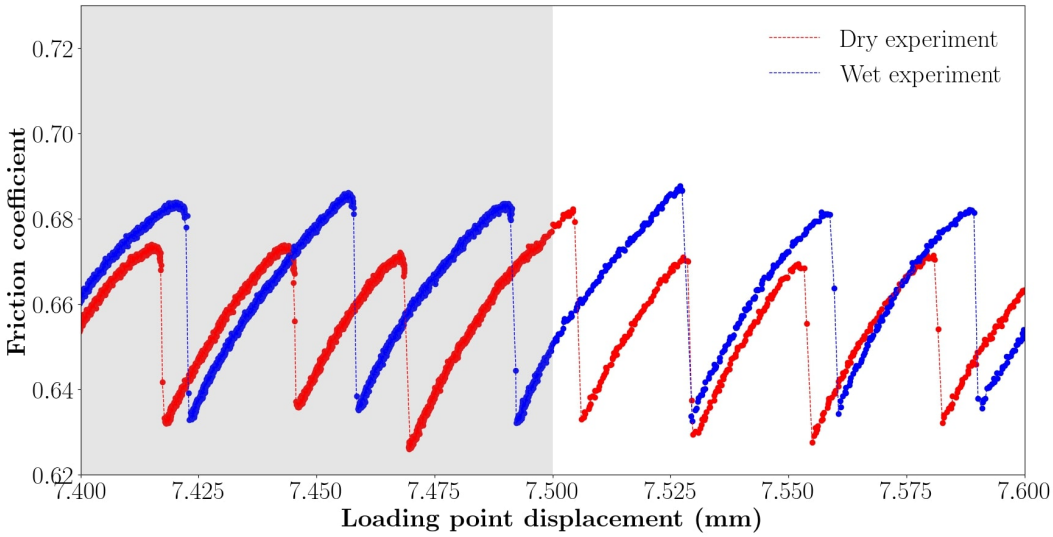

Figure 2.4: Indirect Inference of Event Slip Rate and Dependence of Nucleation on Loading Rate: A zoom-in of the stick-slip sequence for both experiments is shown around the velocity step at the loading point displacement of 7.5 mm. The periods of lower and higher loading rate at 0.3 µm/s and 3 µm/s are indicated by the grey and white background, respectively. Dots spaced by 0.1 s show the sampling rate of 10 Hz. For both experiments, the stress drop phase occasionally includes a measurement point, indicating an event duration of the order of 0.1 s. The nucleation process immediately prior to the stress drop, characterized by a roll-over of the friction curve, has longer duration at the lower loading rate for both experiments. At the lower loading rate, a significant portion of the stress drop is consistently resolved at 0.1 second intervals, while the first drop in friction is often at least half of the entire stress drop at the higher loading rate. The nucleation process shows a possible dependence on the loading rate, although the eventual stress drop is similar.

friction are resolved by many (more than 10) closely-spaced points, indicating that a significant portion of the stress drop occurs at slip rates similar to those of the loading period. At the higher loading rate of 3 µm/s, much more significant stress drop occurs in the first 0.1 s after reaching the peak, indicating that the weakening occurs much more rapidly and over smaller slip. Dependence of nucleation on the loading rate was also demonstrated in laboratory experiments of polycarbonate plates by Guérin-Marthe et al. (2019), which showed a decrease in the nucleation size due to an increase in the loading rate. The shorter and quicker nucleation period at the higher loading rate from our experiment is consistent with their results.

2.3 Spring-Slider Model of Experiment with Rate-and-State Friction, Inertia, and Dilatancy

Spring-slider models have commonly been employed to interpret experiments on the basis that the frictionally sliding sample is small compared to the portion of the experimental apparatus that applies loading. Following this approximation, the dynamics of slip are idealized as a single-degree-of-freedom system (Figure 2.5). The model consists of a spring, which represents the loading system, moving at a prescribed displacement rate at one end, with the other end attached to a slider block that represents the frictionally sliding sample. Normal stress keeps the block under compression, and friction at the base of the block resists its displacement in shear. A constitutive relationship for shear resistance closes the system, which in our case follows the rate-and-state friction law, either with the slip law or the aging law. We include inertia in the balance of momentum,

$$M\ddot{\delta}_{bl} = K_{mach}(V_{lp} - V_{bl}) - \mu(\sigma - p) \tag{2.5}$$

where M is the mass of the block in units of mass per area, δ_{bl} is the slip of the block, V_{lp} is the loading point rate, V_{bl} is the slip rate of the block, σ is the confining stress and p is the pore pressure at the base of the block. The mass is calculated by taking all moving parts of the experimental apparatus past the loading point and dividing it by the sliding area, which gives M = 7,798 kg/m^2. We also account for possible effects from pore pressure transients that may develop from dilatant expansion of the pore volume due to shear deformation. We incorporate the formulation of Segall and Rice (1995) which creates a feedback loop between pressure and slip,

$$c(p^{\infty} - p) - \dot{p} = \frac{\epsilon}{\beta}\frac{\dot{\theta}}{\theta} \tag{2.6}$$

where c is a lumped diffusivity parameter with units of inverse time, β is the storage coefficient, and ϵ is the dimensionless dilatancy coefficient which is directly proportional to the rate of pore volume expansion with slip rate. Here, we use the formulation where changes in porosity are directly connected to changes in the state variable, θ, such that changes to θ act a source term in the diffusion equation. The system of equations is solved using the Rodas4 solver of Julia's Differential Equations package which is a fourth-order implicit Runge-Kutta method for ordinary differential equations (Rackauckas and Nie, 2017).

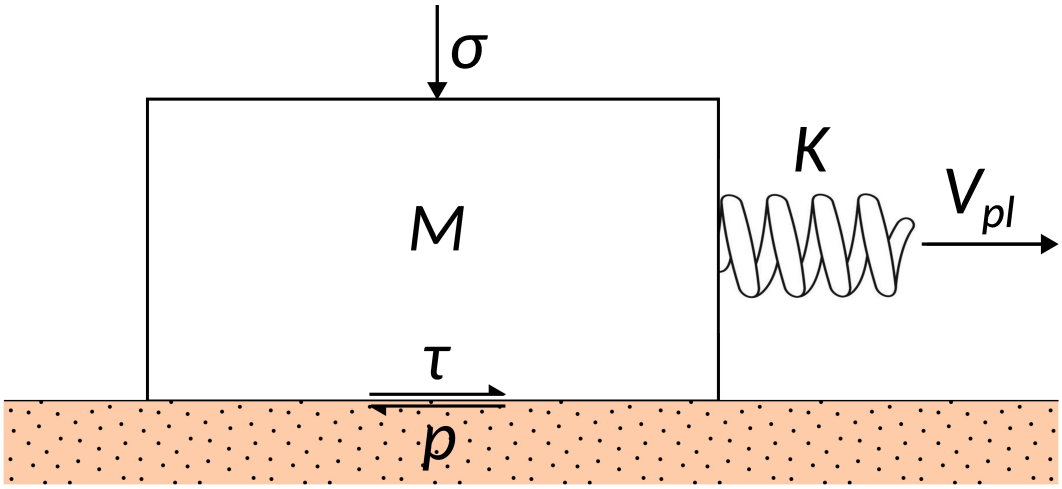

Figure 2.5: Spring-Slider Model: The simple model idealizes the experiment as a single-degree-of-freedom system. The spring, which represents the loading system, pulls the block, which represents the frictionally sliding material, at a prescribed displacement rate. A confining stress is applied to the block and rate-and-state friction governs the resistance of the block to shear displacement. Pore fluid pressure can act on the base of the block. Dilatant expansion of the pore volume can decrease pore pressure, increasing the effective stress and stabilizing the motion of the block. The simplicity of the spring-slider model, which captures the most essential physics of the experiment, allows a sampling-based inversion approach that requires many calls of the forward model.

For the spring-slider model, a linearized stability analysis of the quasi-static system in steady-state sliding gives a stability criterion dependent on the frictional parameters, the stress state, and the stiffness (Rice and Ruina, 1983; Ruina, 1983). The two state evolution laws behave similarly around steady-state and result in the same critical stiffness K_{cr} for steady-state velocity-weakening friction properties $b - a > 0$:

$$K_{cr} = \frac{(\sigma - p)(b - a)}{D_{RS}} \tag{2.7}$$

Infinitesimal perturbations to steady sliding exponentially grow for spring stiffnesses larger than K_{cr}, indicating that the sliding is unstable in this regime, and decay for stiffnesses smaller than K_{cr}, indicating stable sliding. Friction sliding with velocity-strengthening properties is unconditionally stable. Gu et al. (1984) derived the critical stability of the inertial spring-slider which multiplies equation (7) by a coefficient that is proportional to the mass and slip rate. The inclusion of dynamic effects increases the critical stiffness, making the system more unstable.

The difference in critical stiffness is only ~2.65 MPa/mm for the values of mass and loading slip rates in this study. Segall and Rice (1995) derived an analogous criterion in the presence of dilatant strengthening, which decreases the critical stiffness, stabilizing sliding. For continuum settings with faults embedded into an elastic space, the stability criterion is often formulated in terms of the nucleation size, which is the size of the slowly slipping patch that spontaneously accelerates into a dynamic rupture (Ampuero and Rubin, 2008; Dieterich, 1992; Rice, Lapusta, and Ranjith, 2001; Rice and Ruina, 1983; Rubin and Ampuero, 2005).

2.4 Probabilistic Framework for Bayesian Inversion of Rate-and-State Parameters from Stable Velocity Step by Monte-Carlo Sampling

We employ a Bayesian probabilistic framework for the inversion of rate-and-state parameters from a stable velocity step. We find from preliminary tests that dilatancy is negligible at the low slip rates induced by the stable velocity step and apply the following inversions with a zero dilatancy coefficient. To pose the inverse problem in a probabilistic setting, we add a component of stochastic uncertainty to the deterministic spring-slider model which arises from experimental noise, the distribution of which can be approximated directly from the data. The differences from a moving average of the friction curve during the initial strengthening phase (from 0 to 1.5 mm in loading point displacement) resembles a Gaussian distribution with a standard deviation of 0.0004 (shown in Appendix A.1). We define the following probabilistic model of friction observed from the experiment, μ_{prob},

$$\mu_{prob}\left(t|\Omega_{RS,stable}\right) \sim \mu_{det}\left(t|\Omega_{RS,stable}\right) + N(0, s_{exp}) \tag{2.8}$$

where $\Omega_{RS,stable}$ is a set of rate-and-state parameters, μ_{det} is the friction coefficient given by Equation 2.1 for this set, and $N(0, s_{exp})$ is the normal distribution of noise with a mean of zero and standard deviation of $s_{exp} = 0.0004$. We can then define the likelihood function of observing a certain evolution of friction, μ_{exp}, given a set of rate-and-state parameters, which is the Gaussian likelihood,

$$\mathbb{P}_{stable}(\mu_{exp}|\Omega_{RS,stable}) = (2\pi s_{exp}^2)^{-N/2} \exp\left(-\frac{1}{2s_{exp}^2}\sum_{i=1}^{N}(\mu_{exp}(t_i) - \mu_{prob}(t_i))^2\right) \tag{2.9}$$

where $\mathbb{P}_{stable}(\mu_{exp}|\Omega_{RS,stable})$ is the likelihood function and $\{t_i\}$ for $i \in \{1...N\}$ is the set of times corresponding to the set of N measurements in the fitting win-

dow. Bayes' theorem gives the likelihood of the set of rate-and-state parameters, $\Omega_{RS,stable}$, given the observed data, μ_{exp}, i.e., the posterior,

$$\mathbb{P}_{stable}(\Omega_{RS,stable}|\mu_{exp}) = \frac{\mathbb{P}_{stable}(\mu_{exp}|\Omega_{RS,stable})\mathbb{P}_{stable}(\Omega_{RS,stable})}{\mathbb{P}(\mu_{exp})} \tag{2.10}$$

where $\mathbb{P}_{stable}(\Omega_{RS,stable}|\mu_{exp})$ is the posterior distribution, $P_{stable}(\Omega_{RS,stable})$ is the unconditioned likelihood of the rate-and-state parameters (i.e., the prior), and $P_{stable}(\mu_{exp})$ is the unconditioned likelihood of the observed data. In practice, it is expensive to calculate $P_{stable}(\mu_{exp})$. Markov-Chain Monte-Carlo (MCMC) sampling methods bypass the task of computing $P_{stable}(\mu_{exp})$ by setting the target distribution as the numerator of Equation 2.10 since it is directly proportional to the posterior for a given experiment. The prior $P_{stable}(\mu_{exp})$ must often be assumed. In our case, we assume a uniform distribution for all rate-and-state parameters within a plausible region.

In order to make the sampling procedure as efficient as possible, we reduce the dimensionality of the parameter space by utilizing what we know about steady-state conditions in rate-and-state friction. Namely, we compute $a - b$ and μ^* explicitly by assuming steady-state conditions at the beginning and end of the fitting window. Given friction levels at the beginning of the window (at the lower loading rate of $V_{lp,low} = 0.3$ µm/s), μ_{begin}, and at the end of the window (at the higher loading rate of $V_{lp,high} = 3$ µm/s), μ_{end}, we can compute $a - b$ as,

$$a - b = \frac{\mu_{end} - \mu_{begin}}{\ln(V_{lp,high}/V_{lp,low})} \tag{2.11}$$

where the reference slip rate, V^*, is equal to the higher loading rate, $V_{lp,high}$, for which it follows that μ^* equals μ_{end}. Thus $\Omega_{RS,stable} \equiv \{a, D_{RS}\}$. In later sections, we account for the uncertainty associated with the determination of steady-state conditions in the experiment by testing different values of $a - b$.

One of the advantages of Monte-Carlo sampling is that the final convergence of the posterior is less sensitive to the initial starting point of the sampler than gradient-based minimization methods are to initial guesses. At the same time, this is only true for initial starting points that have non-trivial likelihood. To configure initial starting points with non-trivial likelihood for the ensemble sampler, we compute first-order estimates of a and D_{RS} analytically. Assuming that the initial peak in

friction due to the velocity step is representative of the ideal direct effect with no evolution of the state variable and an instantaneous change of the slip rate from the previous to the new loading rate, equation(2) yields for the starting point of the chains,

$$a_{sp} = \frac{\mu_{peak} - \mu_{begin}}{\ln(V_{lp,high}/V_{lp,low})} \tag{2.12}$$

where a_{sp} is the starting point for a, μ_{peak} is the peak friction level due to the direct effect, and μ_{begin} is the friction level immediately prior to the velocity jump. Assuming a constant slip rate equal to the new loading rate after friction reaches the peak value yields an exponential decay of friction,

$$\mu(\delta_{bl}) = \mu_{ss}(V_{lp,2}) + e^{-\delta_{bl}/D_{RS,sp}} \left(\mu_{ss}(V_{lp,1}) - \mu_{ss}(V_{lp,2}) + a_{sp}\ln(V_{lp,2}/V_{lp,1}))\right) \tag{2.13}$$

where $\mu_{ss}(V) = \mu^* + (a-b)\ln(V/V^*)$ is the steady-state friction coefficient at slip rate V. To summarize, Equation 2.12 can be used to find a_{sp}, which can then be plugged into Equation 2.13 to find the best fitting $D_{RS,sp}$. The set $\{a_{sp}, D_{RS,sp}\}$ defines the starting point of the MCMC sampler.

Although there is no fool-proof method for determining the convergence in MCMC sampling, a good rule of thumb is based on the ergodicity of the Markov Chain and utilizes the guaranteed convergence of the mean of the posterior. In this sense, we compute the mean of the developing Markov chain up to each iteration, and then compute the difference between the beginning and end of a moving window along the running mean with a window size of 100 iterations. In other words, we compute the following quantity,

$$\max_{i\in\{N_{chain}-100,\ldots,N_{chain}\}} \left(\frac{1}{i}\sum_{j=1}^{i} x_j - \frac{1}{i-100}\sum_{j=1}^{i-100} x_j \right) \tag{2.14}$$

and ensure that it does not exceed a threshold value at the end of N_{chain} simulations. We use the affine invariant Markov-chain Monte-Carlo (MCMC) Ensemble sampler, the details of which we refer the reader to Goodman and Weare (2010). For the stable velocity step, we find 32 walkers with chain lengths of 10,000 iterations to be sufficient to meet the convergence criterion of the quantity of Equation 2.14 to

stay below 1e-5 at the end of $N_{chain} = 320,000$ simulations. On a single CPU, the full procedure takes between $12 \sim 24$ hours. If desired, parallelization of the ensemble sampler could significantly decrease computational time, and allow longer chains for further convergence. However, we find the aforementioned criterion to be more than sufficient for accurate inference of rate-and-state parameters from both experimental and synthetic data.

A critical choice for sampling rate-and-state parameters is to sample a and D_{RS} in the logarithmic space. As discussed later along with the results, logarithmic sampling of rate-and-state parameters — especially D_{RS} — helps sample better small values of D_{RS} that have more unstable behavior.

Detrending Long-Term Evolutions of Friction

Both experiments show significant changes in the average level of friction at a time scale comparable to the experimental duration. The evolution is perhaps most visible for the dry experiment after 3.5mm of loading point displacement until the end of the experiment during which the difference in the maximum and minimum friction coefficient is close to at least 0.05. Such changes are likely attributed to the deformation of the microstructure at a length scale larger than the localized shear layer (Bedford, Faulkner, and Lapusta, 2022). A zoom-in around the first velocity step (Figure 2.6) shows that that such differences can significantly affect the inversion of the stable velocity step data. Namely, the long-term evolution affects steady-state conditions which determine $a - b$ and μ^*. Choosing the point of convergence to steady-state can be subjective. Former studies have proposed linear detrending methods to address strain-hardening and strain-weakening mechanisms. More sophisticated methods with iterative slicing of the data have addressed datasets with non-linear trends (Giacomel et al., 2024).

We detrend the long-term evolution of the friction coefficient around the stable velocity step by subtracting a moving average from the raw data (Figure 2.6). Using a constant window size of 500 points, the detrending renders the evolution of friction virtually flat aside from the oscillation following the velocity step. The friction coefficient recorded prior to the stable velocity step is added back to the detrended data to reset the zero offset from the subtraction of the moving average. We use the detrended data for the inversions that follow, and discuss in the later sections the sensitivity of the results to the associated uncertainty in $a - b$.

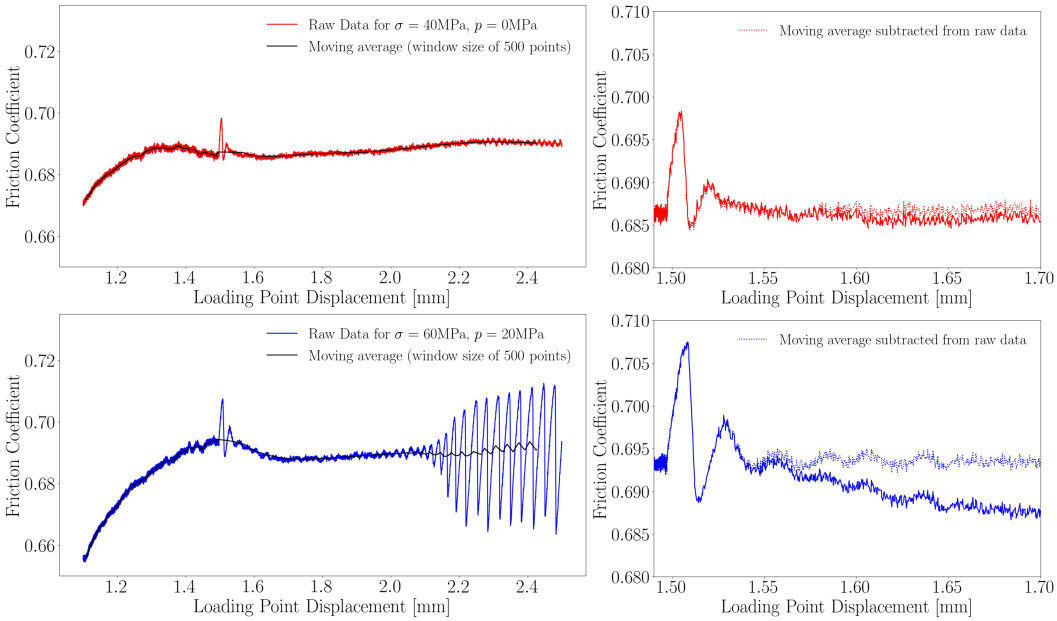

Figure 2.6: Detrending the Long-Term Evolution of the Friction Coefficient. A moving average (black curve of the panels on the left) of the raw data (solid red and blue curves) is subtracted out to give the detrended friction coefficient (dotted red and blue curves of the panels on the right). The large oscillations immediately following the velocity step (happening approximately at 1.5 mm of loading displacement in both experiments) are likely due to the velocity step and hence should be modeled as part of rate-and-state effects with constant parameters. In contrast, more gradual changes in the friction coefficient at longer time scales are likely not related to velocity steps but are rather caused by longer-term evolution of the shear layer with slip, an effect that rate-and-state formulations with constant coefficients are not intended to capture; such changes can be captured through variations in f^*. Detrending allows the inference of rate-and-state parameters to focus more sharply on the frictional properties of a localized shear surface in the gouge.

Inversion of Synthetic Data and Dependence of Uncertainty on Rate-and-State Parameters

In order to test the Bayesian inversion framework, we perform the inversions on synthetic data produced by the spring-slider model. We consider relevant ranges for rate-and-state parameters a, D_{RS}, and $a - b$, namely, 0.006 to 0.015, 1 to 100 µm, and -0.002 to 0.002) for a, D_{RS}, and $a - b$, respectively. The tested ranges of parameters also correspond to the domain of the prior, which is assumed to be a uniform distribution in the logarithmic space. Each spring-slider solution is interpolated at a sampling frequency of 10 Hz as in the experiments, and Gaussian noise with standard deviation s_{exp} = 0.004 is added to each interpolation point.

Unlike the experiments, no detrending is necessary, as the spring-slider model with constant rate-and-state parameters does not produce any long-term evolution of average friction for the same sliding rates. The fitting windows ensure that steady-state conditions have been reached. For brevity, we present in the main text the results for the slip law. The aging law yields no qualitative differences to the slip law in terms of the performance of the synthetic inversion.

Figure 2.7 shows two representative examples of synthetic data which only differ in D_{RS} and their inversion for the rate-and-state parameters. The responses using the mean of the posterior distributions for the rate-and-state parameters, a.k.a. the posterior mean estimators, provide an excellent match to the synthetic data for both cases. The mean estimators have larger errors relative to the true parameters for the lower value $D_{RS} = 1\,\mu\text{m}$. The posterior distributions are also significantly wider for the lower D_{RS}, indicating higher uncertainty. Yet, solutions corresponding to parameter sets that are a single standard deviation away from the mean estimators still match well the reference data for both D_{RS}. The larger range of uncertainty and lack of accuracy with lower D_{RS} arises due to the significant amount of slip (relative to the small D_{RS}) that occurs during the direct effect immediately after the velocity step. The state variable evolves more during the initial increase in friction with lower D_{RS}, allowing a larger range of a to fit the velocity step when accommodated by the appropriate change in D_{RS}. The posterior distributions illustrate the necessary trade-off to conserve the amplitude and period of the oscillations. Namely, an increase in a (larger direct effect) needs to be accompanied by a decrease in D_{RS} to allow greater evolution of the state variable and weakening of friction. On the other hand, the model with higher $D_{RS} = 100\,\mu\text{m}$ has relatively little evolution of the state variable during the direct effect, and the posterior distributions lie tightly around the true parameters with standard deviations smaller than 1% in relative error.

Figure 2.8 plots together the relative error and the quantiles of the posterior distribution from all tested synthetic inversions. A clear dependence of uncertainty on D_{RS} is visible throughout the whole parameter regime. On average, relative error also tends to decrease with increasing D_{RS}. The error of the posterior mean estimators rarely exceeds 10%, demonstrating that the inversion method can infer rate-and-state parameters from stable velocity step sufficiently well.

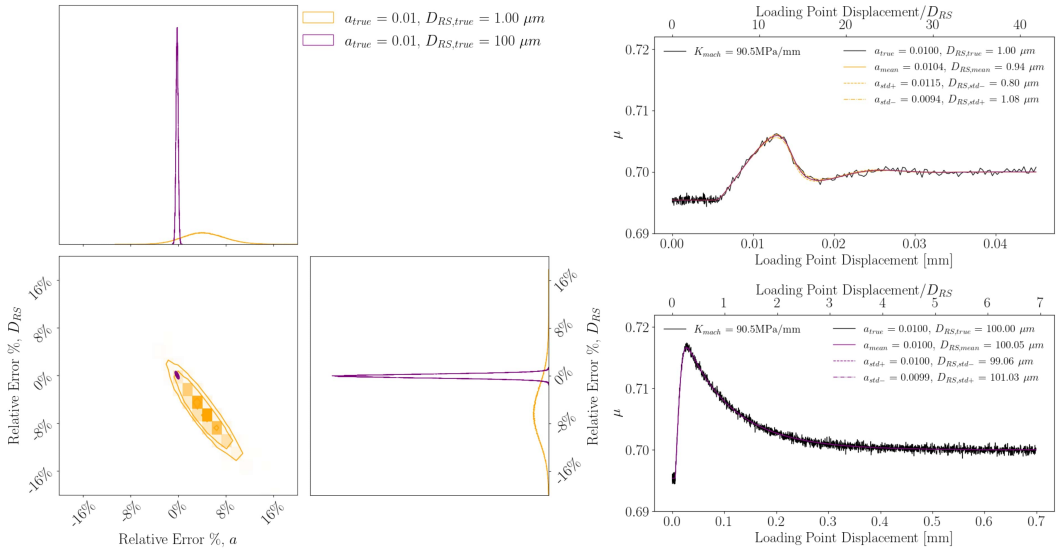

Figure 2.7: Inversions of Synthetic Stable Velocity Step using Bayesian MCMC Sampling for two representative examples differing in the true values of D_{RS} (1 µm for the yellow curves and 100 µm for the purple curves). The posterior distributions of a and D_{RS} are shown on the left in terms of their relative error to the true value. The 2D frequency density maps between the two inferred parameters are plotted as contour maps in between the histograms. The posterior mean estimators (solid colored curves) and parameter sets that are a single standard deviation away (dotted and dashed curves) produce fits that match well the reference synthetic data (black curves) for both cases (right panels). The inversion of the simulation with lower D_{RS} has higher range of relative uncertainty, largely due to the significant amount of state evolution that occurs during the initial rise in friction. At the measured spring-stiffness of 90.5 MPa/mm, the direct effect takes place over a finite amount of slip in the spring-slider model, which is several multiples of D_{RS} = 1 µm while it is only a fraction of D_{RS} = 100 µm. The ratio of slip to D_{RS} is indicated by the second x-axis at the top of the plots in the right panels. The trade-off is also visible in the 2D frequency density map of the posteriors, where an increase in a, or an increase in the direct effect, is accommodated by a decrease in D_{RS} to promote state evolution during the direct effect. In both cases, MCMC inversions of synthetic stable velocity steps successfully infer the true rate-and-state parameters with less than 10% relative error.

Inversion of Experimental Data and Uncertainty Associated with Long-Term Evolution

We apply the validated inversion method to the experimental data, using both the slip and the aging law. Assuming steady-state conditions at the beginnings and ends of the fitting windows, $a - b$ is fixed to 0.0002 and 0.0001, and μ^* is fixed to 0.694 and 0.693 at a V^* of 3 µm/s for the dry and wet experiments, respectively. The prior

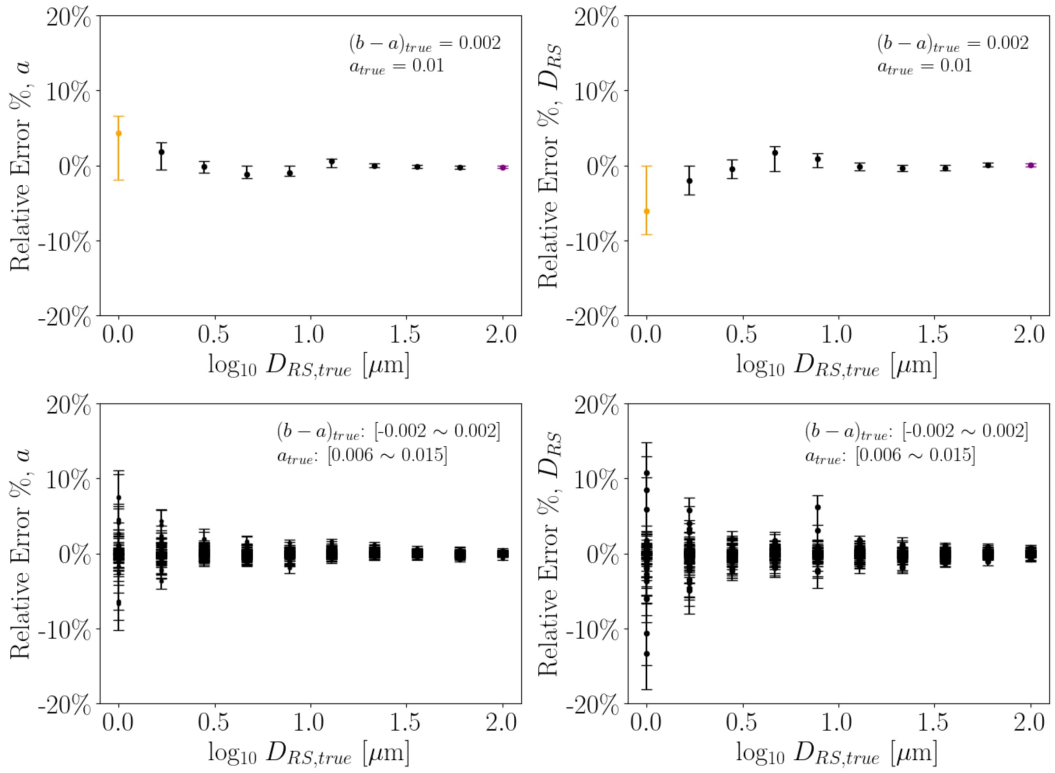

Figure 2.8: Relative Error from Inversions of Synthetic Stable Velocity Step Data by Bayesian MCMC Sampling. The relative error of the posterior mean estimators from MCMC inversions of synthetic stable velocity step data are compiled for a wide range of rate-and-state parameters (a: 0.006 ~ 0.015, D_{RS}: 1 ~ 100 µm, $b-a$: -0.002 ~ 0.002). The error bars indicate the first and third quantiles of the posterior distributions as a measure of uncertainty. The top row shows the inversions of the simulations with a and $b-a$ fixed to 0.010 and 0.002, respectively. The yellow and purple dots correspond to the simulations of Figure 2.7. The relative error in both a and D_{RS} increase with decreasing D_{RS}, due to the larger amount of state evolution during the direct effect. This trend is consistent across the full range of tested parameters (bottom row). Overall, both the relative error of the posterior mean estimators and the standard deviations of the posteriors rarely exceed 10%, showing that MCMC inversions can infer rate-and-state parameters from stable velocity step experiments sufficiently well.

is assumed to be uniform in the logarithmic space for the domain of (0.002 ~ 0.040) and (0.1 ~ 100 µm) for a and D_{RS}, respectively. Figure 2.9 shows the results for the posterior mean estimators of the rate-and-state parameters. The spring-slider models with the inferred parameters match the experimental data quite well, with no significant differences in the quality of the fit between the dry and wet experiments or between the slip and aging laws. Both state evolution laws predict an increase

in a and D_{RS} in the presence of pressurized pore fluids, from 0.0081 and 2.28 µm to 0.0113 and 3.13 µm for the slip law and from 0.0085 and 1.45 µm to 0.0118 and 2.04 µm for the aging law. The larger a and D_{RS} allow the models to fit the larger oscillation in the wet experiment. The larger oscillation may be mistakenly interpreted as a characteristic of greater instability in the wet sample, but the larger a and D_{RS} for nearly the same $a-b$ would, in fact, correspond to more stable behavior. Given that the experiment is displacement-controlled, the larger oscillation in stress corresponds to the greater amount of energy that must be supplied to displace the more stable material at the prescribed slip rate. Thus, the inversion reveals that the presence of pressurized pore fluids increased the stability of the quartz gouge at this early slip stage.

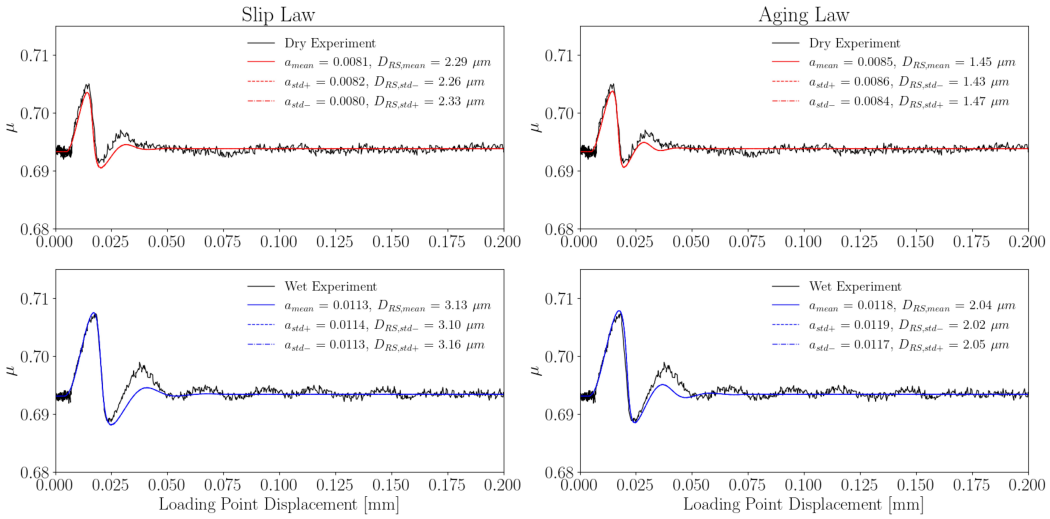

Figure 2.9: MCMC Inversion of Experimental Stable Velocity Step. The spring slider models with the rate-and-state parameters given by the posterior mean estimators produce good fits (the red and blue curves) to the experimental stable velocity step (black curve) for both state evolution laws. Assuming steady-state conditions at the beginnings and ends of the fitting windows, $a-b$ is fixed to 0.0002 and 0.0001, and μ^* is fixed to 0.694 and 0.693 at a V^* of 3 µm/s for the dry and wet experiments, respectively. The dotted lines show fits by parameters that are a single standard deviation of the posterior distributions away from the mean estimator. The two state evolution laws produce similar values of a while D_{RS} is larger for the aging law. The wet experiment requires higher values of a and D_{RS} to reproduce the larger oscillation following the velocity step, highlighting a significant effect by pressurized fluids on the frictional parameters of the gouge.

The slip law predicts significantly larger D_{RS} than the aging law, by a factor of approximately 1.6 and 1.5 for the dry and wet experiments, respectively. This is

because the slip law evolves the state variable significantly faster through slip than the aging law. To achieve a similar amount of evolution in the state variable with a similar amount of slip, the slip law requires a larger D_{RS}, or a lower ratio of slip to D_{RS}. The two state evolution laws are equally good in fitting the initial velocity step, and differ slightly in fitting the second oscillation with a longer duration of the increase in friction for the slip law. For all models, the greatest misfit is during the second oscillation, with a smaller increase in friction than observed.

Both experiments show nearly velocity-neutral behavior in the detrended data, with $a-b = 0.0002$ and 0.0001 for the dry and wet experiments, respectively. Interestingly, an inversion of the dry experiment using the slip law with $a-b$ fixed to 0.001 yields a fit that matches the oscillations significantly better than when $a-b$ is inferred from the detrended data (Figure 2.10). The new fit has higher $a = 0.0110$ and lower $D_{RS} = 1.31\,\mu m$. On the other hand, fixing $a-b$ to -0.001 yields a fit with a monotonic decay following a smaller direct effect that resembles a linear line of best fit through the oscillations, suggesting that the localized shear interface is closer to velocity-neutral or velocity-strengthening at the time of the stable velocity step. The superior fit of the oscillation with $a-b$ fixed to 0.001 has similar a and lower D_{RS} than the fit of the wet experiment. The stable velocity step of the wet experiment does not yield a significant improvement in the fit of the oscillation for different $a-b$. Thus, the uncertainty associated with $a-b$ does not affect the conclusion that the presence of pressurized pore fluids stabilizes the gouge material by increasing both a and D_{RS} for nearly the same $a-b$. We continue to take into account this uncertainty as we compare the inferred parameters of the stable phase to those of the unstable phase in later sections.

Comparison to Conventional Methods using Non-Linear Least Squares

In previous studies, inferences of rate-and-state parameters from stable velocity steps have more commonly employed non-linear minimization of least-square residuals rather than Bayesian inversion with Monte-Carlo sampling. Such methods also sample rate-and-state parameters uniformly, as opposed to the logarithmic transformation employed by our Bayesian framework. Here, we compare the effect of the two differences on the inversion of the experimental data.

We first perform the inversions of the stable velocity step data using a representative method of what is conventionally used in the field. We choose RSFit3000 of Skarbek and Savage (2019) which utilizes the implementation of the Levenberg-Marquardt

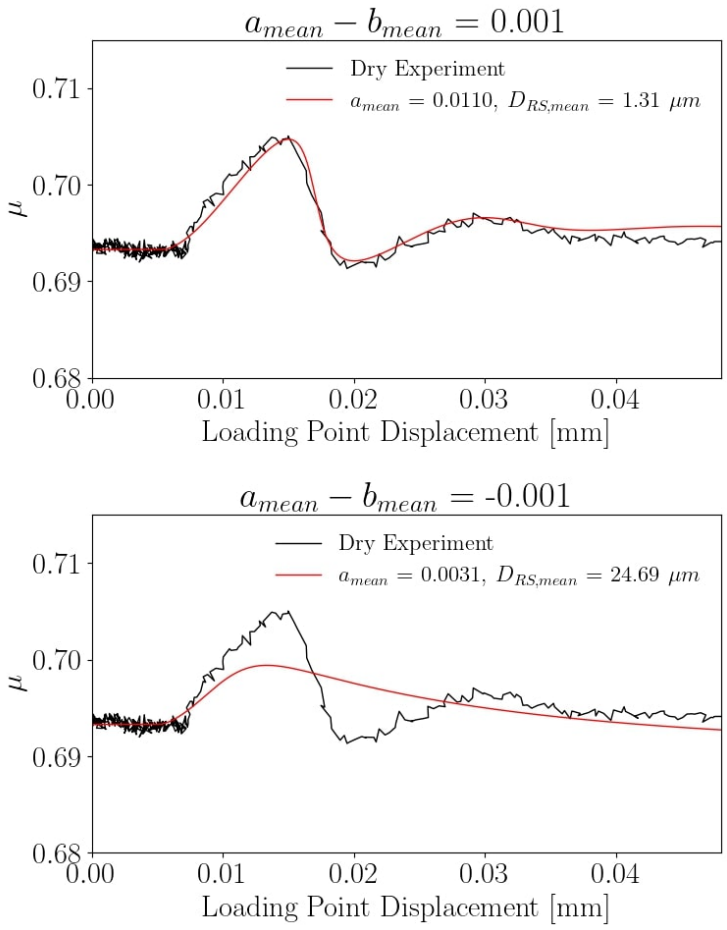

Figure 2.10: Accounting for Uncertainty in $a - b$ due to Long-Term Evolution of Friction: Fixing $a - b$ to 0.001, instead of 0.0002 as inferred from assuming steady-state conditions at the beginning and end of the original fitting window, produces a better match to the second oscillation. On the other hand, fixing $a - b$ to -0.001 produces a poorer fit with large D_{RS} such that a gradual evolution of friction fits through the oscillations by a linear line of best fit. The plots are produced for the slip law with no qualitative differences for the aging law. The fits highlight the sensitivity of the inferred parameters to detrending and the need for care in choosing the most relevant portions of the data for interpretation by rate-and-state friction in realistic gouge material with complex deformation structure.

algorithm in MATLAB for non-linear minimization of least squares. The program allows many utilities commonly employed in the inversion, such as linear detrending, inversion of the stiffness as a free parameter, and applying weights to the calculation of the residual. Figure 2.11 shows the fit by RSFit3000 using the same initial guess as that for MCMC. Although the fits are reasonable, all parameter sets determined

by RSFit3000 are more stable than those of the MCMC inversion, ultimately with a greater misfit to the real data.

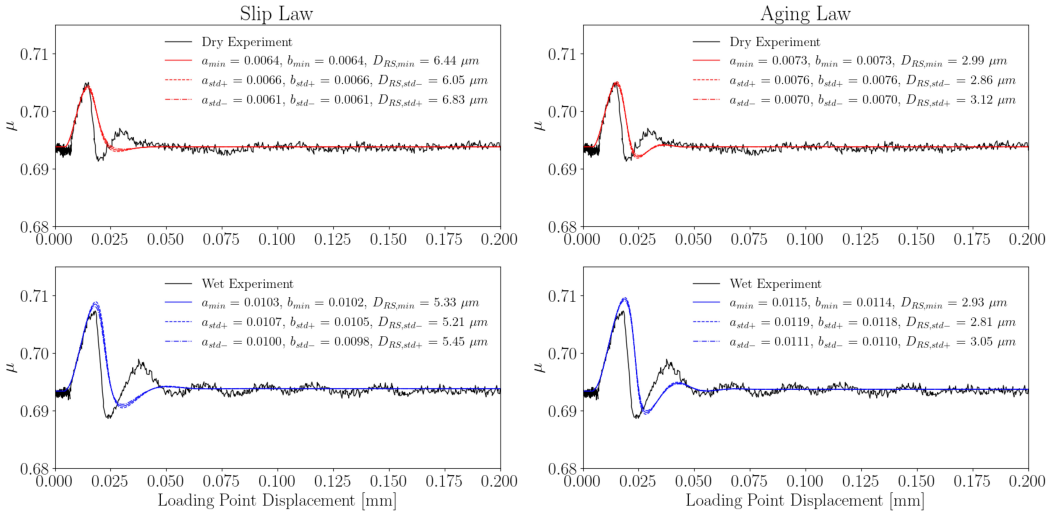

Figure 2.11: Conventional Methods using Non-linear Least Squares with Quasi-Static Spring-Slider Model Converge to Poorer Fits of Stable Velocity Step Data. All inversions result in a more stable response than experimentally observed, with broader first oscillation and poor fit to the second oscillation, which corresponds to much larger inferred values of D_{RS}. For example, D_{RS} is nearly 3 times larger for the dry experiment and slip law compared to the value found by the MCMC inversion with logarithmic sampling (Figure 2.9), and a is slightly smaller to match the peak given the smaller amount of state evolution during the friction increase due to greater D_{RS}.

One difference between the two methods is that one is a local minimizer while the other is a sampler of a global distribution. Additionally, RSFit3000 uses a quasi-static spring-slider and allows b to be a free parameter of the inversion. We find the most dominant source of the difference between the results to be that RSFit3000 samples the rate-and-state parameters uniformly while we apply logarithmic sampling in the MCMC approach. To illustrate this point, Figure 2.12 plots the best fit from the MCMC inversion of the dry experiment, along with parameter sets that are equal increments of a and D_{RS} above and below the posterior mean estimators. The solutions change significantly more for a decrease in D_{RS} which makes the material more unstable, compared to an increase in D_{RS} of the same magnitude, which makes the material more stable. Since D_{RS} of the experimental gouge is already low, slight decreases in D_{RS} result in oscillations of different period and amplitude. This causes larger changes in the normalized mean squared error (NMSE) than equal increases in D_{RS}. Changes in a cause relatively symmetric

changes to the solutions. The apparent tendency for the solutions to become more unstable for higher a is more due to the simultaneous increase in b as a consequence of conserving $b-a$. The higher sensitivity to D_{RS} is consistent with the logarithmic dependence of $1/D_{RS}$ and the linear dependence of a in rate-and-state friction.

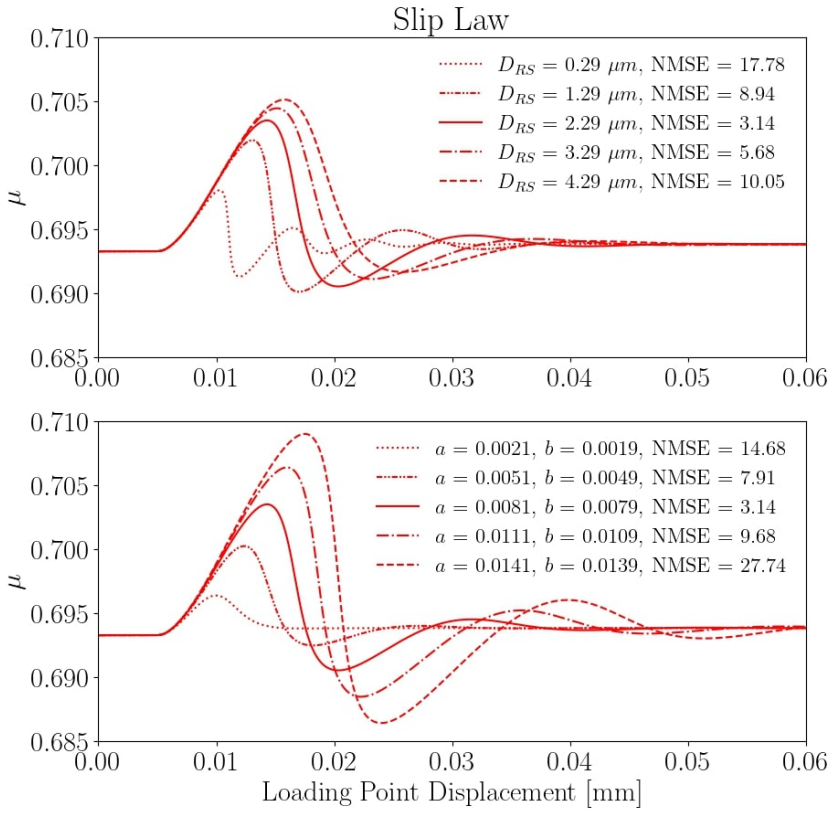

Figure 2.12: ogarithmic Sensitivity of Rate-and-State Response during Stable Velocity Step to D_{RS}: Friction response with the posterior mean estimators of the dry experiment using the slip law (solid lines) and with increments of 1 µm and 0.002 in D_{RS} (top) and a (bottom) both below and above the mean estimators (dotted and dashed lines). Changes in the response are largest for decreases in D_{RS} which produce significantly more unstable and oscillatory evolution in friction. Comparatively, increases in D_{RS} increase stability, and the qualitative change in friction evolution is relatively minimal. Higher instability due to lower D_{RS} also increases the normalized mean squared error (NMSE) more drastically, as indicated in the legend. On the other hand, changes in a produce relatively symmetric changes to the solution. The NMSE increases at a slightly higher rate for increase in a, although to a slower extent than for decrease in D_{RS}. A logarithmic transformation of D_{RS} in optimization schemes enforces asymmetry in sampling so that low values of D_{RS} where the frictional behavior is more unstable are sampled at finer resolution.

We take a closer look at the effect of the logarithmic sampling by testing convergence from different initial guesses. To isolate the effect of the sampling method, we

implement a non-linear least squares inversion framework that incorporates other features of our Bayesian framework (i.e., uses the fully dynamic spring-slider and constrains $b - a$ and μ^* from the fitting window). For the non-linear least squares algorithm, we use the trust-region reflective algorithm implemented by scipy's optimization library (Oliphant, 2007). Four different initial guesses are chosen at the corners of the parameter space defined by the range of ($0.005 \sim 0.015$) and ($1 \sim 5\,\mu$m) for a and D_{RS}, respectively. Figure 2.13 shows the comparison of paths by the minimizers and the history of the residual along each path. All initial guesses converge by logarithmic sampling to the posterior mean estimator of the MCMC inversion. Sampling uniformly converges closely for initial guesses of $a = 0.005$ although with significantly greater variance in D_{RS} along the paths, and guesses with higher values of $a = 0.015$ fail to converge to the posterior mean estimators. Furthermore, when sampling logarithmically, the minimizers reach the posterior mean estimator in a fewer number of iterations by at least an order of magnitude. The residual largely decays monotonically when sampling logarithmically while it diverges significantly from the minimizing path when sampling uniformly.

The previous results demonstrate that local minimizers can in fact achieve the accuracy of Monte-Carlo samplers with far fewer number of iterations when it also samples the logarithmic transformation of rate-and-state parameters. Now, we compare the precision of inference between gradient-based minimization and Monte-Carlo sampling (both uses logarithmic sampling). Figure 2.14 shows the posterior distributions from the MCMC inversion, along with the Gaussian distributions centered at the convergence of the non-linear least squares algorithms with standard deviations equal to the measure of uncertainty associated with the resultant covariance matrix (square root of the diagonals). While the peaks of the distributions coincide quite closely, the distributions are significantly wider for the non-linear least squares methods. Monte-Carlo approach, due to its wealth of sampling, is able to significantly reduce the range of uncertainty associated with the inversion. Although the reduction in uncertainty comes at the cost of more computations, the total duration of sampling is far from prohibitive (less than a day on a single CPU) thanks to the simplicity of the spring-slider model. Especially considering the typical amount of time required for the preparation and execution of experiments, the gain in precision outweighs the relatively minimal cost in post-processing time.

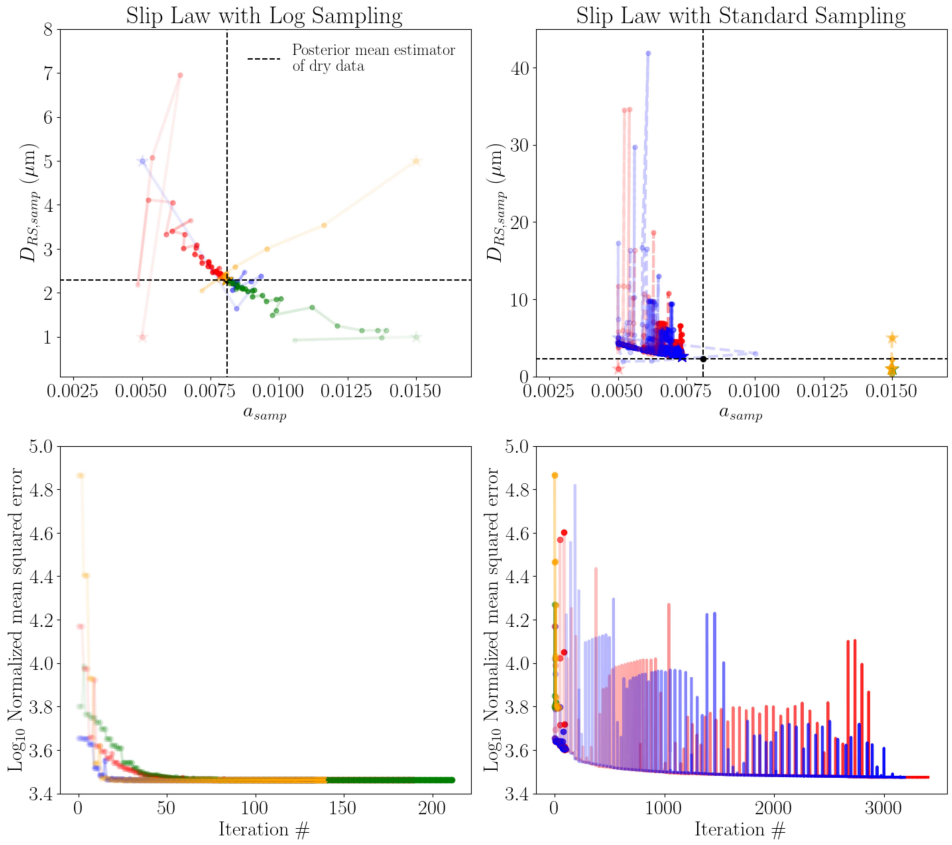

Figure 2.13: Comparison of Convergence by Non-linear Least Square Between Logarithmic and Standard Sampling: The top row compares the paths of the minimizers to convergence using logarithmic (left) and standard (right) sampling of rate-and-state parameters from four different initial guesses represented by four different colors. The paths increase in darkness with the iteration number, and star symbols mark the start and end points of the paths. With logarithmic sampling, the minimizer succeeds in converging to the posterior mean estimators of the MCMC inversion (the intersection of the dotted lines) regardless of the choice of the initial guess. The variance in rate-and-state parameters along each path is significantly greater with standard sampling, especially in D_{RS}. The bottom row compares the least square residuals along each path. Logarithmic sampling follows paths with largely monotonic decrease in the residual while standard sampling departs significantly from such paths with large peaks in the residual history, associated with sampling large values of D_{RS}. Even when paths of standard sampling converge closely to the true values (red and blue paths), they do so with an order-of-magnitude larger number of iterations and with higher final residuals. The superior convergence of logarithmic sampling, both in efficiency and accuracy, is due to the higher resolution of sampling at lower values of D_{RS} where frictional behavior is more unstable (Figure 2.12).

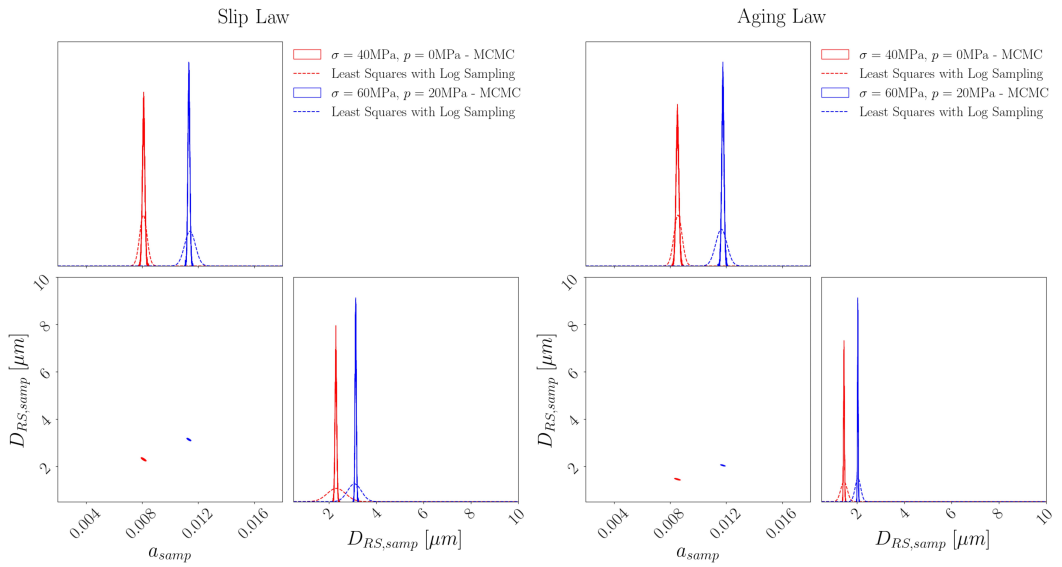

Figure 2.14: Comparison of Accuracy Between MCMC and Nonlinear Least-Squares Inversions: The solid lines plot the histograms of the posterior distributions from MCMC sampling, and the dotted lines plot Gaussian distributions centered around the non-linear least squares solution with the associated standard deviation (square roots of the diagonal entries of the covariance matrix). The 2D frequency density maps between the two inferred parameters, a and D_{RS}, are plotted as contour maps in between the histograms. Although both methods succeed in converging to the true rate-and-state parameters, the range of uncertainty is larger for the least-squares method, as evidenced by the wider shapes of the distributions.

2.5 Sensitivity of Stick-Slip Characteristics to Stability Ratio, State Evolution Laws, and Dilatancy

An example of stick-slip motion in a spring-slider model with rate-and-state friction is shown in Figure 2.15, where the friction coefficient, slip rate, and state variable are plotted vs. the loading point displacements as done in experiments. For a constant loading rate, the loading point displacement is proportional to time. The stick-slip cycle consists of two main phases: 1) the "stick" or loading phase with increasing friction coefficient and slip rate below the loading rate (the "stick" phase) and 2) the "slip" or stress drop phase where the slip rate increases drastically and the friction drops rapidly at dynamic (or near-dynamic) slip rates. In a perfect stick-slip scenario, there would be zero slip and slip rate during the "stick" phase, and the increase in loading would reflect the stiffness of the apparatus. However, in rate-and-state models, there is always a non-zero slip rate, and "stick" means slipping with slip rates lower than the loading rate, which results in a net compression of the spring (or the loading column in the experiments) and increase in shear stress

acting on the sample. Once the slip rate reaches the loading rate, the stress increase stops and the peak friction is reached. Right before that, the slip rate is increasingly closer to the loading slip rate, resulting in flattening of the loading curve. At the peak of loading, the slider is already accelerating. Hence, the period right before and after the peak corresponds to the accelerating nucleation phase. As the slider starts to slip (much) faster than the loading point, the stress rapidly drops, eventually resulting in the block slowing down below the loading rate, and the cycle repeats.

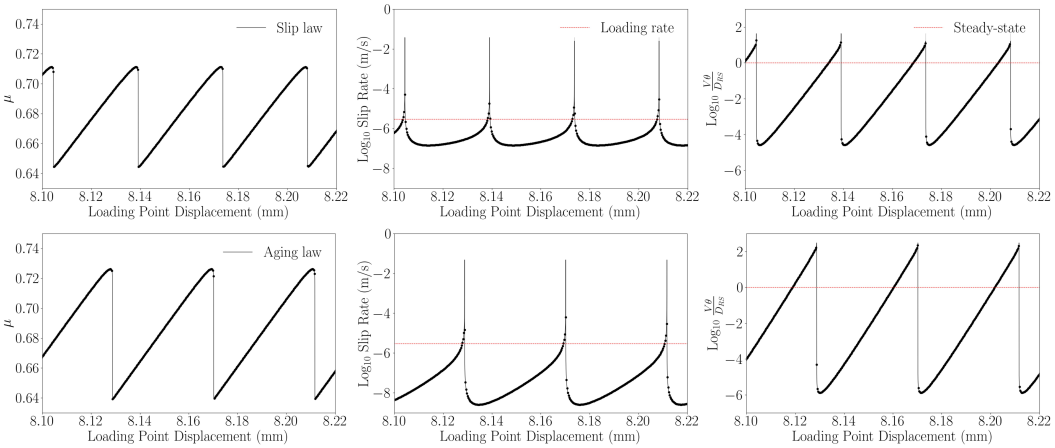

Figure 2.15: Spring-Slider Simulation of a Stick-Slip Sequence: Histories of the friction coefficient, slip rate, and normalized state variable are shown for the slip (top) and aging (bottom) laws. The loading rate and steady state are shown as red dotted lines on the plots for the slip rate and normalized state variable, respectively. Dots along the curve indicate 0.1-s intervals in time. The friction parameters are 0.010, 0.013, 1um, 0.7 and 3 µm/s for a, b, D_{RS}, μ^* and V^*, respectively. For the same frictional parameters, the aging law produces a larger stress drop. The aging law also produces a lower slip rate during the arrest phase, leading to a large evolution of the slip rate and state variable leading up to nucleation. Characteristics of stick-slip defined in Figure 2.2a can be measured from such simulations and serve as the basis for inversion for rate-and-state parameters.

Before we delve directly into the inverse problem, we run a host of stick-slip simulations to explore the sensitivity of stick-slip characteristics to rate-and-state properties. We begin with the sensitivity of the creep % (which is the amount of creep during the loading phase) shown in Figure 2.16. For both state evolution laws, the creep % decreases for increasing ratios of K_{cr}/K_{mach}. Larger K_{cr} represents higher instability in the system, leading to more dynamic events and less creep during the strengthening phase. Interestingly, the slip law consistently produces higher creep % for the same frictional parameters than the aging law. The difference occurs due to the different healing in the two laws. Since the state variable can only increase

("heal") with slip, the slider must slip to increase friction during the loading phase. With the aging law, healing can occur under stationary conditions, requiring less slip. This results in a higher state variable at the time of the event, and events tend to be larger and more dynamic for the aging law.

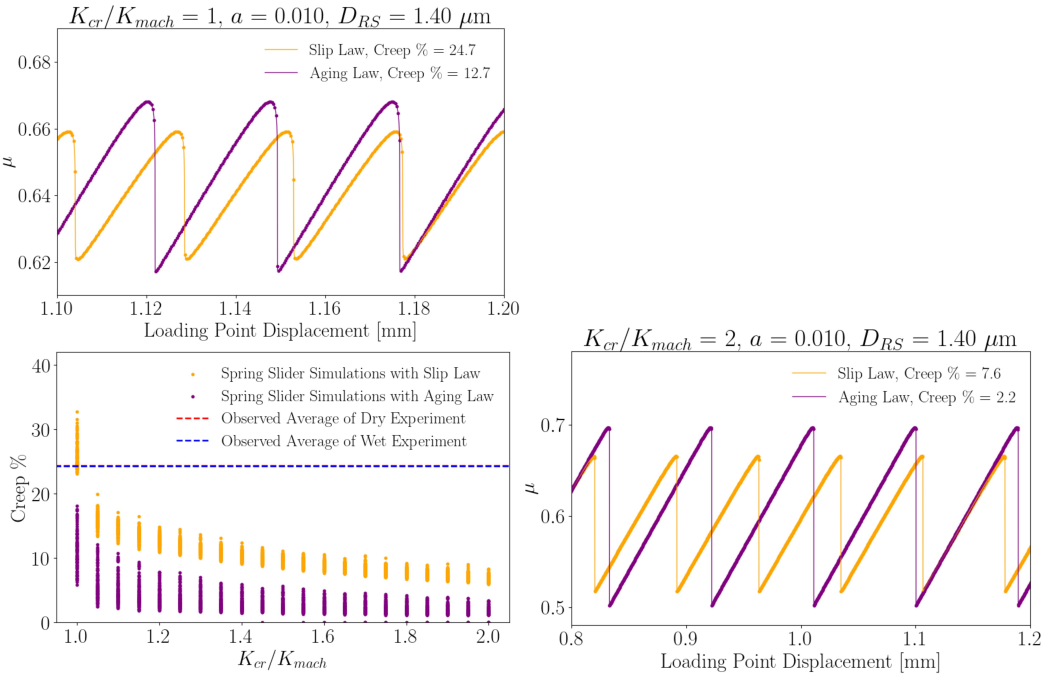

Figure 2.16: Slip Law has Higher Creep % than Aging Law. (Bottom left) The creep % for a range of rate-and-state parameters (a: 0.005 ~ 0.015, D_{RS}: 0.5 ~ 5 µm, K_{cr}/K_{mach}: 1 ~ 3 & K_{mach} = 90.5MPa/mm) is plotted for the slip (yellow dots) and the aging (purple dots) laws; the values inferred from the dry and wet experiments are shown by red and blue dashed lines. As expected, creep % is lower for more unstable regimes with greater ratios of K_{cr}/K_{mach} for both laws. For the same frictional parameters, the slip law produces higher creep % than the aging law. (Top left and bottom right) Representative simulations with the lowest and highest ratios of K_{cr}/K_{mach}, respectively. Dots along the curve indicate 0.1-s intervals in time. In both cases, the aging law produces stick-slip events with characteristics of greater instability, such as larger stress drops and lower creep %. The difference in creep is especially visible for the simulations at critical stability (top left panel), where the slip law exhibits greater curvature in the evolution of friction during the loading phase. The set of simulations also indicates that the spring-slider model would only be able to reproduce a creep % as high as that observed in the experiments near critical stability.

The experimentally observed value of the creep % is relatively high compared to the simulations (Figure 2.16); among the tested range of parameters, it can only be reproduced at critical stability using the slip law. The time history during the

simulated events using the slip law at critical stability also indicates that such events have similar average slip rate to the experiments. Figure 2.17 plots the creep % and the stress drop along a narrower region surrounding critical stability (0.99 ~ 1.01 of K_{cr}/K_{mach}). Again, plotting the experimentally observed stick-slip features shows that the experimental events can only be reproduced by a narrow range of parameters around critical stability for both state evolution laws. The narrow range of plausible sets of rate-and-state parameters is consistent with theoretical studies which have identified the stability transition as an abrupt, Hopf bifurcation point in the spring-slider model (Rice and Ruina, 1983). Leeman, Marone, and Saffer (2018) observed slow slip in sliding experiments of quartz gouge and found that stability ratios close to $K_{cr}/K_{mach} = 1$ were necessary to reproduce the experimental events. Other studies have proposed additional dependencies of rate-and-state parameters on the slip rate which widens the range of parameters that produces slow slip (Ikari and Saffer, 2011; Ikari, Saffer, and Marone, 2009; Im et al., 2020). On the other hand, simulations of finite faults have shown that relatively wider ranges of the nucleation to fault size can reproduce slow slip (Cattania and Segall, 2021).

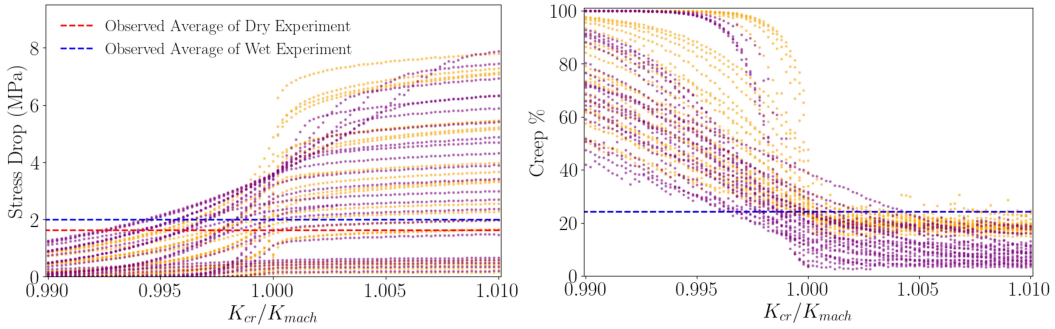

Figure 2.17: Experimentally Produced Stress Drops and Creep % Can Only Be Reproduced by Spring-Slider Model Near Critical Stability: The creep % and stress drop are plotted for a range of rate-and-state parameters (a: 0.005 ~ 0.015, D_{RS}: 0.5 ~ 5 µm) within a narrow band of the stability ratio around critical stability (K_{cr}/K_{mach}: 0.99~1.01 & K_{mach} = 90.5MPa/mm) for the slip (yellow dots) and the aging (purple dots) laws. The experimentally observed values of the stress drop and creep % (dashed horizontal lines for the dry (red) and wet (blue) experiments) can only be matched for a narrow band of the stiffness ratio near critical stability.

Dilatancy is another possible mechanism for slow slip, especially given the presence of fluids (Segall et al., 2010). Figure 2.18 shows the change in creep % and stress drop due to dilatancy-induced pore pressure variations at various ratios of stability. For all parameters, decreasing the hydraulic diffusivity — which increases the rate of dilatant strengthening due to pore pressure decrease — both decreases the stress

drop and increases creep %. In other words, dilatancy tends to stabilize all aspects of stick-slip motion. This is inconsistent with the difference that is observed between the dry and wet experiments where the presence of pressurized pore fluids increases the stress drop while maintaining similar levels of creep %. Thus, dilatant strengthening is unlikely to have affected the stability of the gouge, which is consistent with the sufficiently high diffusivity of the gouge to disallow this effect (Faulkner et al., 2018). Hence we conclude that the frictional properties of the gouge indeed need to be close to critical stability in order to reproduce the relatively high creep % during the strengthening phase.

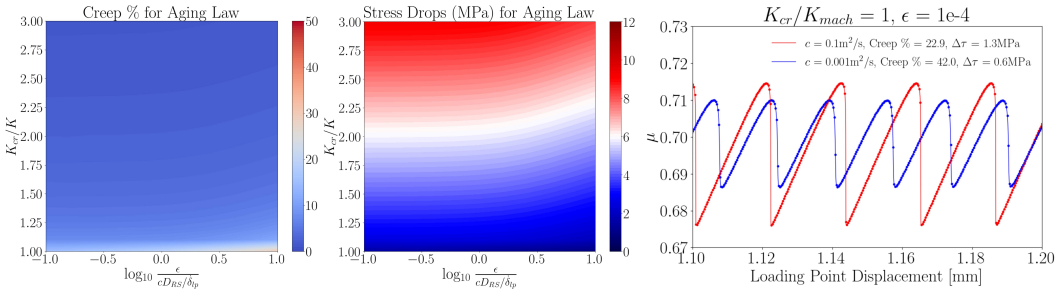

Figure 2.18: Shear Induced Dilatancy Decreases Stress Drop and Increases Creep %: (Left and middle) Stress drop and creep % are plotted as contour maps for a range of stability and dilatancy ratios (c: 0.001 $\sim$ 0.1 m^2/s & K_{cr}/K_{mach}: 1 $\sim$ 3) with a, D_{RS} and ϵ fixed at 0.01, 1 µm and 1e-4, respectively, using the aging law. For all stability ratios, dilatancy stabilizes all aspects of the stick-slip cycle. Namely, decreasing the hydraulic diffusivity, which traps the fluid more and increases the strength of dilatant stabilization, results in higher creep % as well as lower stress drops. (Right) A representative comparison between two simulations that only differ in the diffusivity. The model with lower diffusivity (blue curve) shows greater stability, with smaller stress drop and higher creep %. Hence, dilatancy effect cannot explain experimental observations in which the wet experiment results in higher stress drops while maintaining similar creep %.

We take a closer look at the sensitivity of creep % to rate-and-state parameters at and near critical stability by plotting its dependence on a and D_{RS} for ratios of K_{cr}/K_{mach} close to 1. Figure 2.19 shows the plots for the slip law at $K_{cr}/K_{mach} = 1$ and 1.001 which show nearly opposite sensitivity of creep % to D_{RS}. Example simulations with relatively high D_{RS} show that the regime of slip can change dramatically between the two stiffness ratios. The simulation at critical stability produces events with peak slip rates close to 0.1 mm/s = 0.001 m/s. In this regime, the spring-slider produces high creep % even in the presence of substantial weakening ($b - a = 0.004525$). With a small increase in b that results in $K_{cr}/K_{mach} = 1.001$, the spring-slider

produces events with peak slip rates close to 0.1 m/s and rapid nucleation and arrest phases. Thus, the opposite sensitivity of creep % to a happens across a transition in the regime of stick-slip, which happens quite abruptly in the spring-slider model. A similar transition occurs for the aging law as well, although at lower values of the stability ratio (Figure 2.20). For the aging law, parameter sets at critical stability already produce fully seismic events.

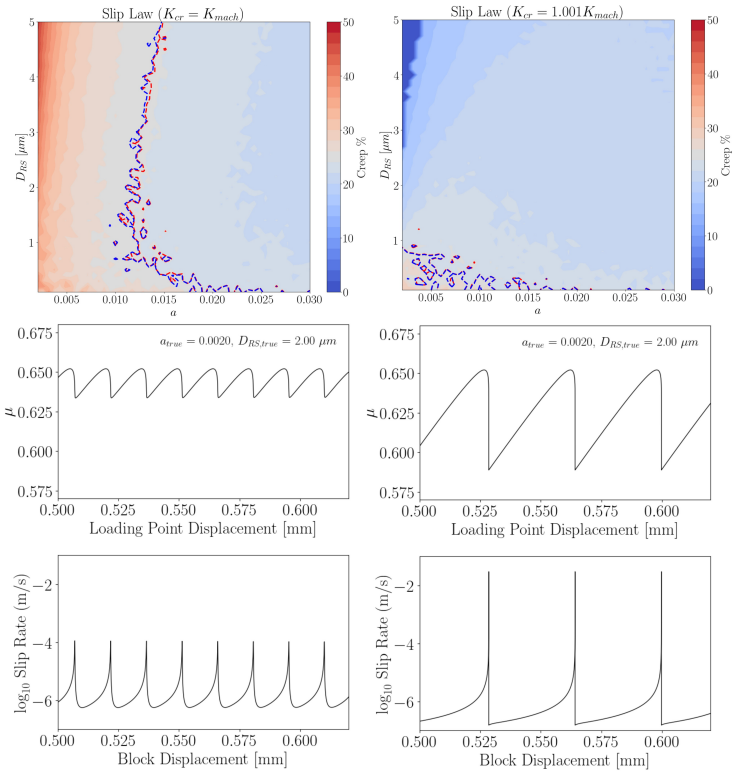

Figure 2.19: Sensitivity of Creep % to Rate-and-State Parameters Near Critical Stability for Slip Law: The contour maps plot the creep % for a range of a, D_{RS}, and b that satisfy (left) $K_{cr} = K_{mach}$ and (right) $K_{cr} = 1.001K_{mach}$. The red and blue dotted lines indicate the observed creep % from the dry and wet experiments, respectively. At critical stability (left column), creep % tends to increase with decreasing a (and decreasing b) and increasing D_{RS} (and increasing $b - a$). A small change in the stability ratio such that $K_{cr} = 1.001K_{mach}$ (right column) flips the sensitivity in terms of D_{RS} (and $b - a$). The upper left corner of the plot for $K_{cr} = 1.001K_{mach}$ marks a region where the numerical procedure fails to resolve events with strong dynamic overshoot, correlated to high ratios of $\frac{b-a}{a}$. Example simulations with a relatively low value of $a = 0.002$ and high value of $D_{RS} = 2\,\mu$m show how the regime of slip can change drastically with a slight change in b ($\Delta b <$ 1e-5).

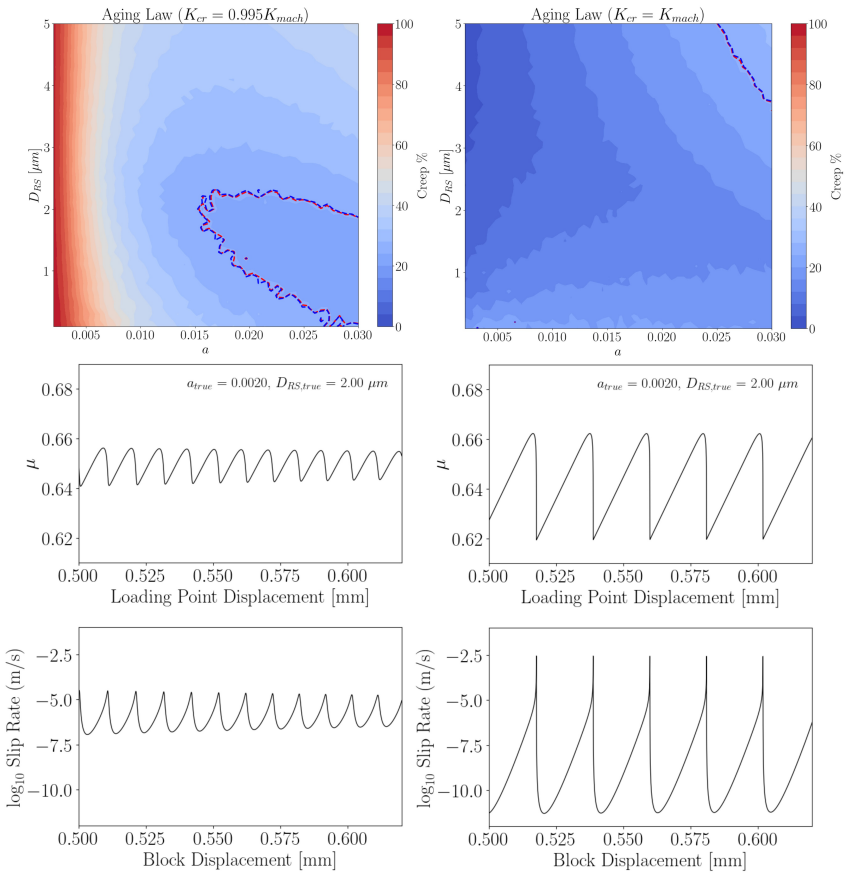

Figure 2.20: Sensitivity of Creep % to Rate-and-State Parameters Near Critical Stability for Aging Law: The contour maps plot the creep % for a range of a and D_{RS} at the stability ratios indicated at the top of the respective columns. The red and blue dotted lines indicate regions along the contours that equal the observed creep % from the dry and wet experiments, respectively. At slightly below critical stability where K_{cr} = 0.995 K_{mach} (left column), creep % tends to increase with decreasing a (and decreasing b). Exactly at critical stability (right column), the sensitivity flips in terms of a (and b). Similarly to the slip law, example simulations with a relatively low value of a = 0.002 and high value of D_{RS} = 2 µm show that the regime of slip changes drastically with slight increase in b (Δb < 3e-5), from slow slip/low-frequency events to fully seismic events. The transition occurs at lower values of the stability ratio compared to the slip law (Figure 2.19). Additionally, parameter sets with high a and high D_{RS} also produce relatively high creep % unlike the slip law. The differences to the slip law in the sensitivity of creep % imply significant differences in the plausible set of rate-and-state parameters that match the experimental creep % using the two state evolution laws.

2.6 Inversion of Rate-and-State Parameters from Stick-Slip Data

Similarly to the development of the inversion framework for the stable velocity step data, we start by formulating a probabilistic forward model for the observed

characteristics of stick-slip. Unlike the stable velocity step, we do not match the friction curves directly, which have variable stick-slip features from one event to the next. Instead, we treat the observed distribution of stick-slip features (Figure 3) as a manifestation of stochasticity in the system, centered around the prediction by the periodic spring-slider model. The observed variability between stick-slip events within the same experiment could come from a number of factors, such as sensitivity of the system to the servo control feedback in the presence of experimental noise, small variations in the average friction properties of the system, or heterogeneity of rupture along the finite slipping surface. We represent the epistemic noise of the system as a Gaussian distribution with the standard deviation equal to that observed from the experiment. All together, we arrive at the following probabilistic model of stick-slip features, SS_{prob},

$$SS_{prob}(\Omega_{RS,dynamic}) \sim SS_{det}(\Omega_{RS,dynamic}) + \eta \tag{2.15}$$

where $\Omega_{RS,dynamic} \equiv \{a, b, D_{RS}, \mu^*\}$, SS_{det} is the set of stick-slip features predicted by the deterministic spring-slider model, and η is a multivariate Gaussian with a diagonal covaraince matrix whose diagonal entries equal the standard deviations of the distributions observed in experiment for the stick-slip features of interest. The likelihood function and the posterior are then defined as:

$$\mathbb{P}_{stick-slip}(SS_{exp}|\Omega_{RS,dynamic}) = \prod_{j=1}^{M=4} (2\pi s_j^2)^{-N/2} \exp\left(-\frac{1}{2s_j^2}\sum_{i=1}^{N}(SS_{exp}^j(i) - SS_{det}^j)^2\right)$$

$$\mathbb{P}_{stick-slip}(\Omega_{RS,dynamic}|SS_{exp}) = \frac{\mathbb{P}_{stick-slip}(SS_{exp}|\Omega_{RS,dynamic})\mathbb{P}_{stick-slip}(\Omega_{RS,dynamic})}{\mathbb{P}(\Omega_{RS,dynamic})} \tag{2.16}$$

where SS_{exp} is the set of observed stick-slip features from the experiment, N is the number of stick-slip events, j spanning 1 to 4 corresponds to the index of an individual feature (out of $\Delta\tau$, τ_{peak}, K_{max} and K_{min}), and s_j is the standard deviation of the distribution of the corresponding feature. Similarly to the stable velocity step, we assume the prior to be uniform and use the affine invariant Markov-chain Monte-Carlo (MCMC) Ensemble sampler of Goodman and Weare (2010). In order to find a starting point for the sampler with non-trivial likelihood, we run the inverse problem under a gradient-descent based minimization method from a grid of initial

guesses. The grid of initial guesses is defined as a 5 x 5 x 5 uniform grid within the domain of the prior for a, D_{RS} and μ^*. Then, we choose for the starting point the parameter set with the highest likelihood among all converged solutions. Given the greater extent of non-uniqueness in the unstable regime, we significantly increase the chain length (in comparison to the inversion of the stable velocity step) to 100,000 simulations among 32 walkers. This ensures the convergence measure of equation (14) to decrease below 1e-4.

Synthetic Inversions for All Rate-and-State Parameters

We first perform inversions of synthetic data with all rate-and-state parameters (a, b, D_{RS}, μ^*) as free variables. We produce synthetic data for a wide range of parameters, namely, (0.007 $\sim$ 0.015) with spacing of 0.002, (0.5 $\sim$ 1.0 µm) with spacing of 0.1 µm, and (1 $\sim$ 3) with spacing of 0.5 for a, D_{RS}, and K_{cr}/K_{mach}, respectively, with μ^* fixed at 0.7. We intentionally avoid parameter sets with high ratios of $\frac{b-a}{a}$ which are difficult to resolve numerically (Figure 2.19). The initial conditions of the simulations are steady-state at the lower loading rate, inspired by the observation that instability is often triggered by a velocity step up. To the set of stick-slip features from each simulation, we add as noise Gaussian distributions with standard deviations equal to those observed in the dry experiment. We then perform an inversion for each friction vs. loading point displacement stick-slip sequence produced.

Unlike for the stable velocity step, we find that that the peak of the posterior distribution, a.k.a. the maximum a posteriori (MAP) estimator is consistently closer to the true parameters than the posterior mean estimator. Even so, the relative error of the MAP estimator is significant, ranging between 0 to around 60% (Figure 2.21) for a, b, and D_{RS}. Only μ^* has negligible error from the inversion. The error and the range of uncertainty also increases with K_{cr}/K_{mach}, indicative of a greater degree of non-uniqueness for regimes of greater instability. A representative example of the fit by the MAP estimator shows that the relative error in the characteristics of the stick-slip event is smaller than the relative error in the inverted parameters. Between the MAP estimator and parameter sets that are a single standard deviation away, the resultant stick-slip sequence is nearly identical, despite as great as a 50% relative difference in rate-and-state parameters. In order to regularize the non-uniqueness of the inversion of our experimental data, we utilize in the following sections the observation that stick-slip events with the relatively high creep % of the experiments

can only be reproduced near critical stability in the spring-slider model, as was discussed in Section 2.5.

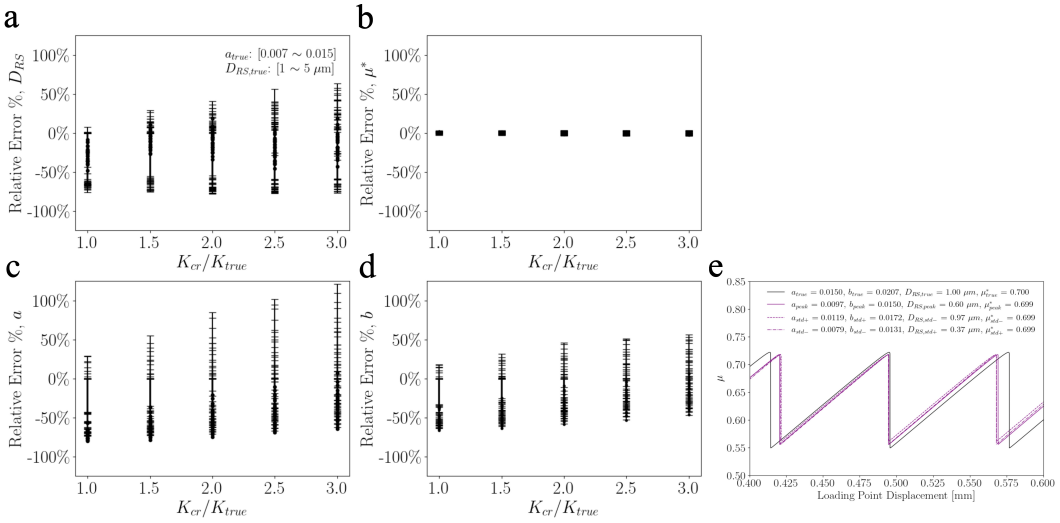

Figure 2.21: Non-unique Sets of a, b, and D_{RS} Can Produce Similar Stress Drop, Peak Stress, and Creep Evolution. (a-d) The relative error of MAP estimators from MCMC inversions, with all frictional parameters (a, b, D_{RS}, and μ^*) treated as free variables, of synthetic simulations for a range of rate-and-state parameters (a: 0.007 ~ 0.015, D_{RS}: 0.5 ~ 1 μm, μ^* = 0.7 & K_{cr}/K_{mach}: 1 ~ 3). Aside from μ^*, MCMC consistently fails to accurately infer the true parameters. Yet, models with the inverted values generally produce stick-slip events closely matching the synthetic data as shown by the representative example in the rightmost panel. Furthermore, parameter sets that are 0.5 standard deviations away from the MAP estimators produce virtually equal stick-slip cycles even though the rate-and-state parameters vary by 10% to 50% of the true value. The relatively large variability in frictional parameters that produce similar events demonstrates the non-uniqueness of the inverse problem and highlights the need for stronger constraints from observations for unique inversions. For the inversion of experiments presented in this study, we utilize the constraint that the set of frictional parameters must be close to critical stability.

Synthetic Inversions while Assuming Critical Stability

We impose a constraint to the original inverse problem of Equations 2.15 and 2.16 by enforcing the condition that the rate-and-state parameters must form a combination such that $K_{cr} = K_{mach}$. This in effect reduces the dimensionality of the parameter space by 1, since a, b, and D_{RS} are related to each other by Equation 2.7. For the simple reason to maintain similarity to the parameter space of the stable velocity step data for easier comparison, we choose to eliminate b from the inverse

problem. In other words, we replace $\Omega_{RS,dynamic}$ of equations 2.15 and 2.16 with $\Omega_{RS,critical} \equiv \left\{a, b = \frac{K_{mach} D_{RS} + a}{\sigma}, D_{RS}, \mu^*\right\}$.

Initial conditions of the models are chosen carefully in order to avoid first events with large stress drop and dynamic overshoot that are difficult to resolve numerically. Such initial conditions were identified for the slip law at critical stability by Gu et al. (1984) for the quasi-static spring-slider. The slip rates with such initial conditions go to infinity in the quasi-static solution; when resolved with inertia, these cases lead to a large event with large dynamic overshoot. Enough dynamic overshoot can severely challenge the numerical procedure during rapid arrest, when the slip rate must decrease dramatically from dynamic to near-zero values. Ranjith and Rice (1999) showed that such initial conditions do not exist at critical stability for the aging law, whose trajectories, regardless of the initial condition, all remain in the quasi-static regime. A representative set of trajectories as published in the studies are re-plotted here for reference in Figure 2.22.

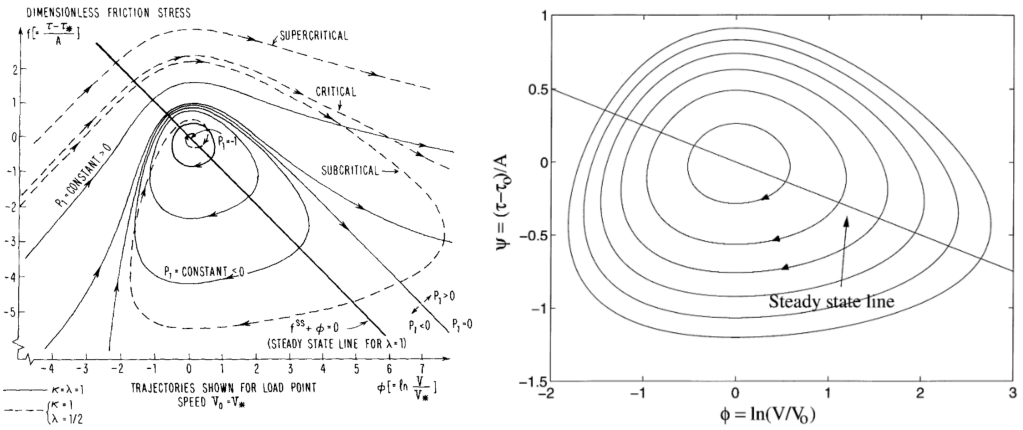

Figure 2.22: Quasi-Static Spring-Slider Predicts Singular Slip Rate for Slip Law at Critical Stability. Solutions in the phase plane of slip rate (x-axis, normalized in terms of the reference slip rate) and stress (y-axis, deviations from the reference value normalized by a times the effective normal stress) of the quasi-static spring-slider system at critical stability are re-plotted here for reference from previous studies, by Gu et al. (1984) for the slip law (left) and by Ranjith and Rice (1999) for the aging law (right). For the slip law, certain initial conditions or perturbations can lead to singular slip rates in the quasi-static system (labeled 'supercritical'). For the aging law, all trajectories are contained within the quasi-static system. Based on the quasi-static spring-slider studies, events of dynamic slip rate at critical stability (or below it) are only possible with the slip law.

The phase plane solutions derived by Gu et al. (1984) and Ranjith and Rice (1999) can be used directly in order to find initial conditions that lead to a first event

closely resembling the events of long-term convergence. We rewrite the phase plane solutions here for reference in terms of the terminology used here. For the slip and aging laws, respectively, the phases plane solutions are,

$$U_{slip} = e^{\psi} \left(\psi + (\beta - 1)(\phi + V^* e^{-\phi} - 1) - 1 \right) \tag{2.17}$$

and

$$U_{aging} = (\beta - 1)\beta \left(\frac{V_{lp}}{V^*} + \frac{e^{\phi}}{\beta - 1} \right) e^{\frac{\psi - \phi}{\beta}} - \psi\beta \tag{2.18}$$

where $\psi = \frac{\mu_{ini} - \mu^*}{a}$ with μ_{ini} being the initial value of friction, $\phi = \ln \frac{V_{ini}}{V^*}$ with V_{ini} being the initial slip rate, $\beta = \frac{b}{a}$, and U is the constant that defines a single solution in the phase plane with the subscripts corresponding to the names of the state evolution laws.

Example simulations are plotted for the slip law with $U_{slip} = 0$ and 1 in Figure 2.23. While the simulation with $U_{slip} = 1$ leads to a large first event with dynamic overshoot, once the event is fully resolved with inertia, the solution converges exactly to the initial condition with $U_{slip} = 0$. Thus, the stability result of Gu et al. (1984) only applies to the event immediately following the exponential increase in the slip rate. After the first event, solutions converge back to a steady-state sequence with a dramatically lower peak slip rate. The long-term convergence to transitional modes of slip between stable and unstable regimes in the dynamic spring-slider was also noted by Gu and Wong (1991). For the aging law, Figure 20 shows that all trajectories at critical stability have already turned dynamic. This is in fact the behavior that would be expected if considering the minute increase in critical stability due to inertia. Interestingly, the slip law allows slow slip/low-frequency events for K_{mach} smaller than the dynamic critical stiffness. For the following inversions, we set U_{slip} and $U_{aging} = 0$ as we find it to produce first events that are easily resolvable near critical stability.

Figure 2.24 shows two inversion examples of the synthetic cases that only differ in the value of D_{RS}. In both cases, the relative error of the MAP estimator is close to 0%, and the inversion accurately infers the true parameters. Similarly to the inversions of stable velocity step, the range of uncertainty is larger for lower D_{RS}. Figure 2.25 compiles the relative error and quantiles of the posterior distribution for all tested sets of parameters. The relative error is close to 0% regardless of

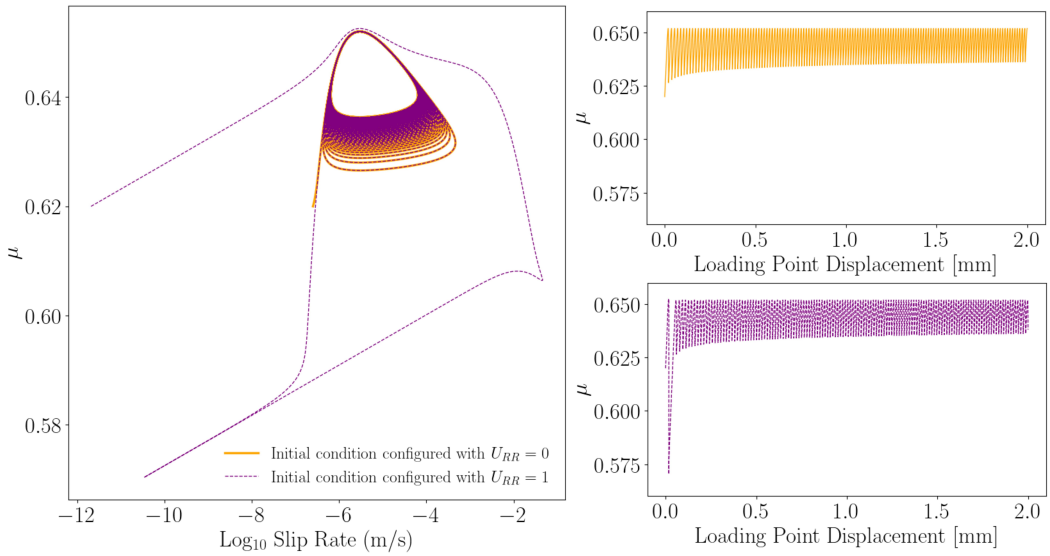

Figure 2.23: Long-term Behavior of Stick-Slip Sequences in Dynamic Spring-Slider: Two spring-slider simulations with the slip law, the same rate-and-state parameters, and the same initial stress but different initial slip rates are plotted. The simulation with higher initial slip rate (orange curve) produces a first event that is similar to the long-term behavior of the simulated sequence. The simulation with significantly lower initial slip rate (purple curve) produces a first event with a dramatically higher peak slip rate and a larger stress drop. Thereafter, both models converge to the same sequence of events. Given that different initial conditions tend to converge to the same long-term sequence, we choose ones that avoid large first events that are more difficult to resolve numerically.

the variations in a or D_{RS}. The range of uncertainty increases with decreasing D_{RS} up to approximately 75%. Despite such range in uncertainty, the inversion is still able to infer the true parameters by the MAP estimator. The success of the inversion indicates that fixing the stiffness ratio to the critical value provided enough regularization of the non-uniqueness in the original formulation.

Inversion of Experimental Stick-Slip Data

To gain a sense of what rate-and-state parameter sets may fit the experimental stick-slip data, we draw the maps of likelihood of a and D_{RS} considering the resultant stress drop and creep % (Figure 2.26) for the slip and aging laws at stability ratios of 1 and 0.995, respectively. The intersections of the narrowest contours for the stress drop and creep % indicate regions of the highest joint likelihood. The intersecting region for the slip law has a slightly lower value of a around 0.012 compared to around 0.016 for the aging law. D_{RS} is similar for both laws, at around 1.5 µm. Both

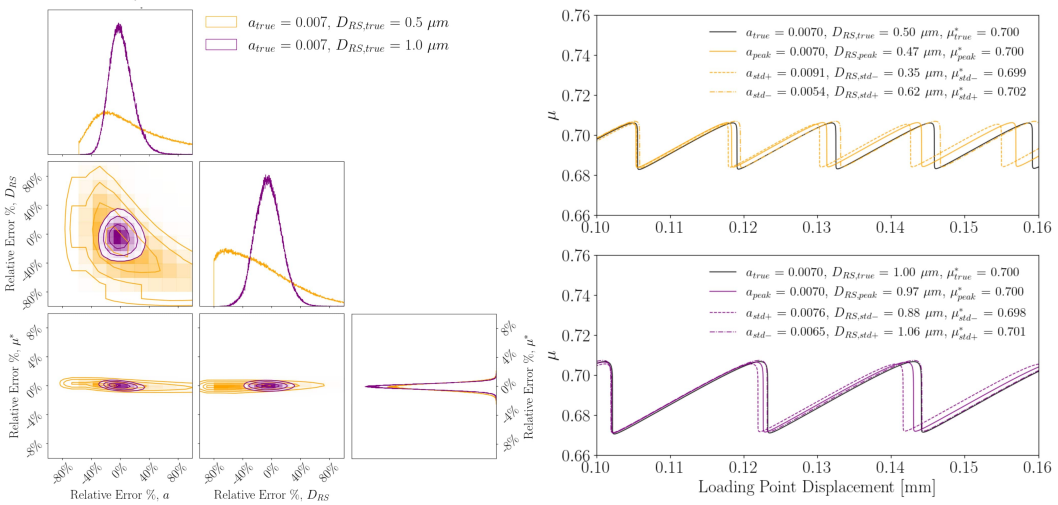

Figure 2.24: Inversions of Synthetic Stick-Slip at Critical Stability by Bayesian MCMC Sampling: Two representative examples of MCMC inversions are shown for stick-slip simulations of the spring-slider model at critical stability, differing in the true values of D_{RS} (and b). The posterior distributions of a, D_{RS} and μ^* are shown on the left in terms of their relative error to the true value. The 2D frequency density maps between the inferred parameters are plotted as contour maps in between the histograms. The maximum a posteriori (MAP) estimators (solid colored curves) and parameter sets that are a single standard deviation away (dotted and dashed curves) produce fits that match well the reference synthetic data (black curves) for both D_{RS}. The inversion of the simulation with lower D_{RS} (and lower $b - a$) has higher range of relative uncertainty in a and D_{RS}. A trade-off is noticeable in the 2D frequency density map of the posteriors of a and D_{RS}, such that an increase in a is accompanied by a decrease in D_{RS}. In both cases, MCMC inversions successfully infer the true parameters using the MAP estimators, although with a significant range of uncertainty represented by the width of the posteriors due to the non-uniqueness of inverse problem.

laws show separated contours indicating a degree of non-uniqueness. The narrowest contour for creep % is compact within the intersecting region but the contours for the stress drop are separated. The formal inversion also considers K_{max} and K_{min}, which makes the region of highest joint likelihood more compact. However, additional considerations of the evolution of creep with further dependencies of the peak stress on μ^*, quickly becomes difficult to visualize in a concise manner. We look for the MCMC inversion to sample the posterior, which corresponds to the joint density of the likelihood for all inverted parameters.

Given the indications that the experimental stick-slip is close to critical stability (due to its high creep %) and that well-behaved inversions are possible in that regime,

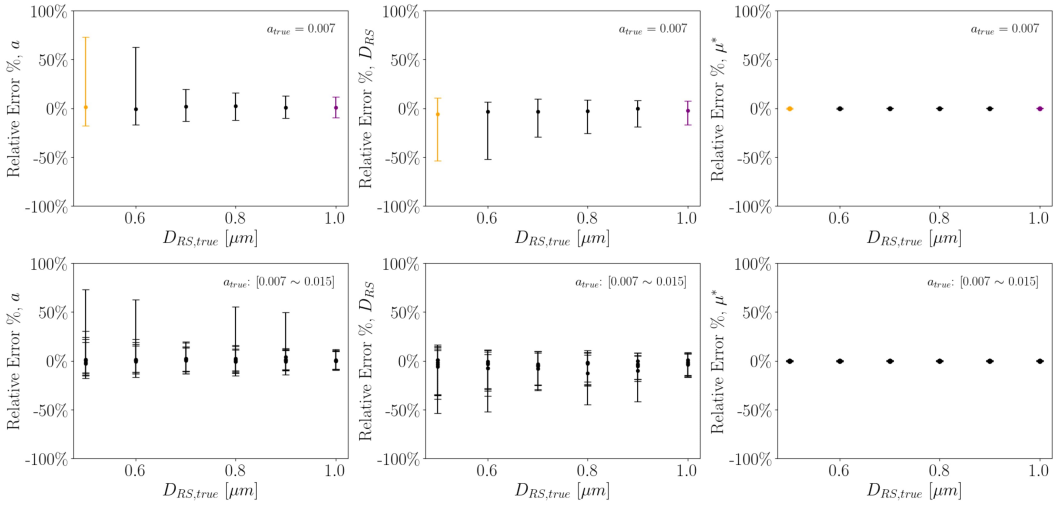

Figure 2.25: Relative Error from Inversions of Synthetic Stick-Slip Simulations at Critical Stability by Bayesian MCMC Sampling: The relative error of the MAP estimators from MCMC inversions of stick-slip simulations at critical stability are compiled for a wide range of rate-and-state parameters (a: 0.006 ~ 0.015, D_{RS}: 1 ~ 100 µm). The error bars indicate the first and third quantiles of the posterior distributions as a measure of uncertainty. The top row shows the inversions of the simulations with a fixed to 0.007. The yellow and purple lines/dots correspond to the simulations of Figure 2.24. Similarly to the inversion of the stable velocity step data, the relative error in both a and D_{RS} increase with decreasing D_{RS}. This trend is consistent across the full range of tested parameters (bottom row). Overall, the MAP estimators successfully infer the true values with less than 5% error across the range of tested parameters. At the same time, the posteriors are relatively broad in their range of uncertainty as quantile values regularly exceed 50% in relative error due to the non-uniqueness of the inverse problem.

we restrict the prior distributions to be non-zero only within the narrow band where $0.99 < K_{cr}/K_{mach} < 1.01$. The prior is further assumed to be uniform within the range of (0.002 ~ 0.030), (0.1 ~ 10 µm), and (0.65 ~ 0.75) for a, D_{RS} , and μ^*, respectively. Figure 2.27 plots the resultant posterior for the slip law along with the fit by the MAP estimators. We also indicate on the same plot the posterior mean estimators from the stable velocity step for comparison. The estimators from the stable and unstable portions of the experiment coincide well in terms of a for both experiments. On the other hand, the posteriors indicate significant changes to parameters of the evolution effect, b and D_{RS}. Namely, b increases, making the material more velocity-weakening with higher $b - a$, and D_{RS} decreases, which is consistent with the shift from the stable velocity step to more unstable stick-slip behavior.

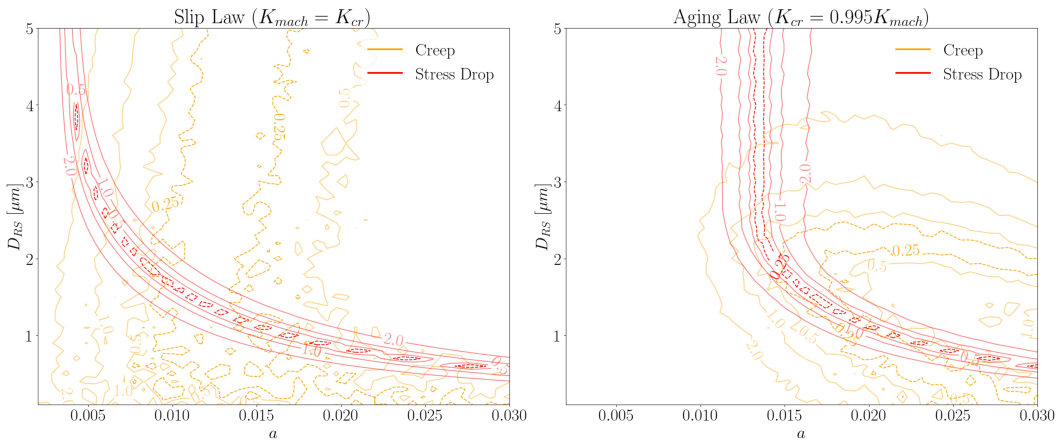

Figure 2.26: Likelihood Maps at Plausible Stability Ratios For Slip and Aging Laws: The in-line legend along the contours indicate the number of standard deviations away from the mean of the experimentally observed stress drop (red curves) and creep % (orange curves) for spring-slider simulations using the slip law (left) and the aging law (right). The intersecting regions of the closest to mean contours indicate the plausible sets of rate-and-state parameters that reproduce most closely the experimentally observed stress drop and creep %. Different ratios of stability are chosen for the two state evolution laws such that the intersecting regions are of substantial size relative to the tested range of rate-and-state parameters. Stability ratios generally need to be lower for the aging law in order to match the higher creep % from the slip law (Figure 2.16). a of the intersecting region is slightly higher for the aging law while D_{RS} is similar for both laws. We look for the inversion method to successfully infer the intersecting regions of the likelihood contours, also taking into account τ_{peak}, K_{max} and K_{min} among additional variability in μ^* and b.

The inversions also reveal the effect of pore fluid on rate-and-state parameters. a, b, and D_{RS} are all larger in the wet sample, similarly to the stable velocity step conclusions. μ^* decreases for both cases, but more for the dry sample. While the larger stress drop in the wet sample may make it appear as if the presence of pressurized pore fluids destabilized the quartz gouge, the increase in a and D_{RS} with relatively little change in $b - a$ may in fact be interpreted as greater stability. This is similar to the observation at the stable velocity step, where the larger oscillation in stress from the wet sample is indicative of the larger amount of energy needed to apply a rapid change of the slip rate in the more stable material.

The simulated stick-slip sequence by the MAP estimators and single standard deviations away from them match well the stress drop, average amount of creep, and peak stress. Sampled measurements along the friction history shows that the average slip rate of the event is also similar. Simulated slip rates reach peak values close

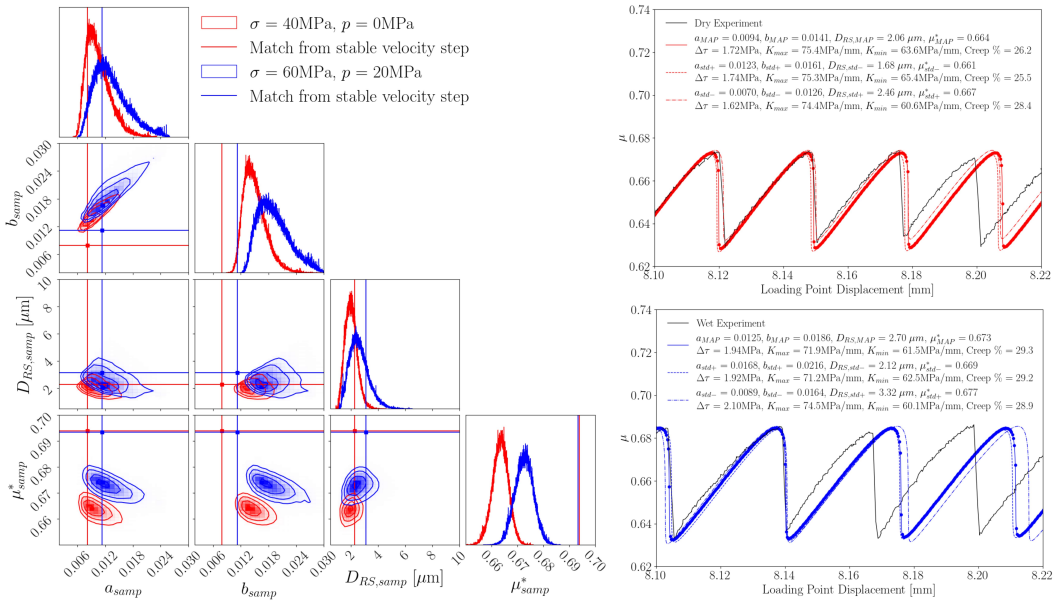

Figure 2.27: Matching Simulations of the Experimental Stick-Slip Events using the Slip Law: The posterior distributions of the MCMC inversion are shown as histograms on the left for the dry (red) and wet (blue) experiments using the slip law and assuming a range of rate-and-state properties close to the critical stability. The mean estimators from MCMC inversions of the stable velocity step data are shown in the same panels as vertical lines. For both the dry and the wet experiments, the peak of the posterior distributions of a coincide closely to the mean estimators of the stable velocity step. The distributions of the rest of the frictional parameters indicate a high chance of an increase in b, a decrease in D_{RS}, and a decrease in μ^*. The best matching solutions using the MAP estimators are shown on the right along with parameter sets that are a single standard deviation of the posterior distributions away. Although the experiments have greater variability between each event than the simulations, the models match well select events of the experimental sequence that are closer to the average event. Dots are plotted along the curves each 0.1 s, mimicking the measurement frequency of 10 Hz in the experiment. Like in the experiments, stress drops are often resolved by more than 2 points. At the same time, the nucleation process of the simulated events lasts significantly longer both in time and slip. In the simulations, a visible portion of the stress drop occurs at slip rates close to the loading rate, while in the experiments, the first 0.1-s drop in friction always marks a significant increase in the slip rate. Still, MCMC successfully infers a plausible range of rate-and-state parameters from the unstable phase of the experiment and reveals quantifiable changes in the rate-and-state properties of the quartz gouge with slip. The increase in the evolution parameter, b, and decrease in the characteristic slip distance D_{RS} between the stable step and stick-slip response is likely due to localization of shear deformation and the comminution of grains along the principal slip surface.

to a 1 mm/s. Such slip rates are not high enough to trigger dynamic weakening mechanisms such as flash heating or shear-induced pore pressurization and justifies the use of the canonical rate-and-state friction law. A visible difference between the model and the experiment is that the nucleation process appears to be significantly longer in slip and time in the simulation. In the experiment, the first drop in friction consistently marks the beginning of the stick-slip event and a significant increase in the slip rate. In the simulated events, a considerable amount of the friction drop happens at slip rates close to the loading rate. Thus, the models show a significant qualitative discrepancy to the experiments in that the simulated stress drop has a significant initial slow phase not observed in the experiments.

The results of the inversion for the aging law show several qualitative differences to those for the slip law (Figure 2.28). First, the posterior distributions of a and D_{RS} indicate their increase since the stable velocity step. b increases and μ^* decreases since the stable velocity like the slip law, but to greater extent. Similarly to the slip law, the simulated stick-slip events match well the stress drop, amount of creep and the peak stress. Unlike the slip law, the models do not reproduce similar slip rates of the event. The models predict significantly slower slip rates. In order to match the creep % of the experiment during the loading phase, the stability ratio of the best-matching fit by the aging law is lower than that of the slip law, and that results in lower slip rates during the stress-drop phase that no longer match the experiments.

For both state evolution laws, the sequence of simulated stick-slip events only matches the experimental sequence in parts, as there is variability between individual events in the experiments that does not exist in the periodic sequence of the spring-slider model. To better evaluate the quality of the match, let us compare the Gaussian distribution predicted by the probabilistic model (Equation 2.15 with the experimentally observed distributions (Figure 2.29). For both state evolution laws, the models fit well the stress drop, peak stress and the average amount of creep. The models do not match well the distributions of K_{max} and K_{min}, which are higher and lower in the experiment, respectively. In other words, the experimental stick-slip events 'stick' more following the stress-dropping events and slip more right before the friction peak (during nucleation).

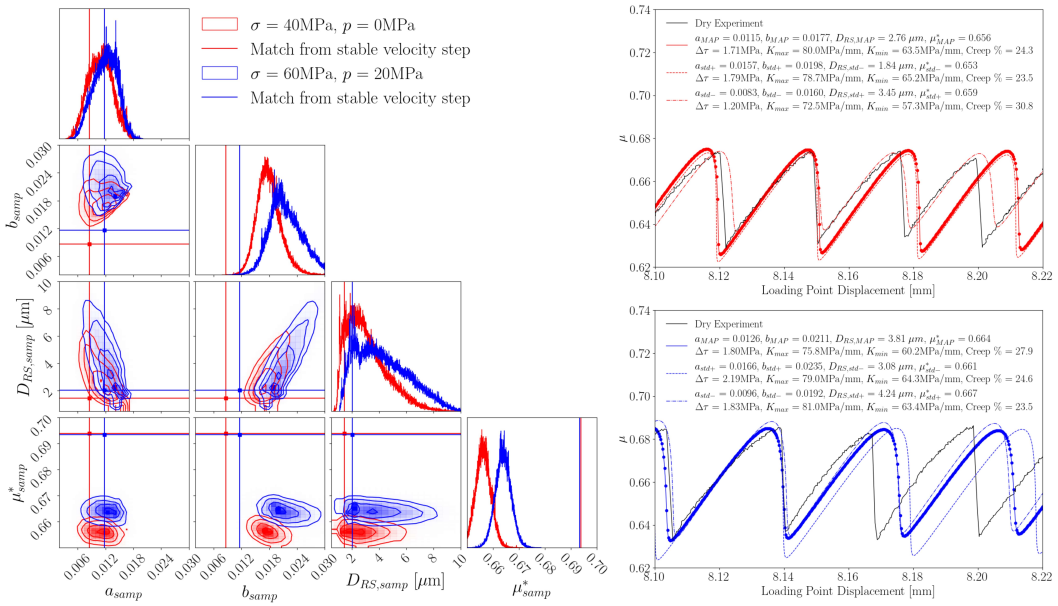

Figure 2.28: Matching Simulations of the Experimental Stick Slip Events using the Aging Law: The posterior distributions of the MCMC inversion are shown as histograms on the left for the dry (red) and wet (blue) experiments using the aging law and assuming a range of rate-and-state properties close to the critical stability. The mean estimators from MCMC inversions of the stable velocity step data are shown in the same panels as vertical lines. Unlike the slip law, the peak of the posterior distributions of a increase slightly with respect to the mean estimators of the stable velocity step. Additionally, the posterior of D_{RS} indicates an increase since the stable velocity step. b and μ^* increase and decrease, respectively, since the stable velocity step like the slip law, although to a greater extent. The best matching solutions using the MAP estimators are shown on the right along with parameter sets that are a single standard deviation of the posterior distributions away. Dots are plotted along the curves each 0.1 s, mimicking the measurement frequency of 10 Hz in the experiment. The aging law also matches the experimental stress drop and creep % well like the slip law. However, stress drops are consistently resolved by more points than in the experiment, indicating significantly lower slip rates during the events. The nucleation process of the spring-slider models last significantly longer both in time and slip than in the experiments, although this is also the case with the slip law. The fit of the aging law ultimately features more discrepancies from the experiment than the fit of the slip law.

2.7 Micro-physical Interpretations of Changes in Rate-and-State Parameters with Slip and Pore Pressure

When using the slip law, there is minimal difference between the values of a that match the stable velocity step and the stick-slip events. At the same time, b increases and D_{RS} decreases during the transition period. Similar evolution of rate-

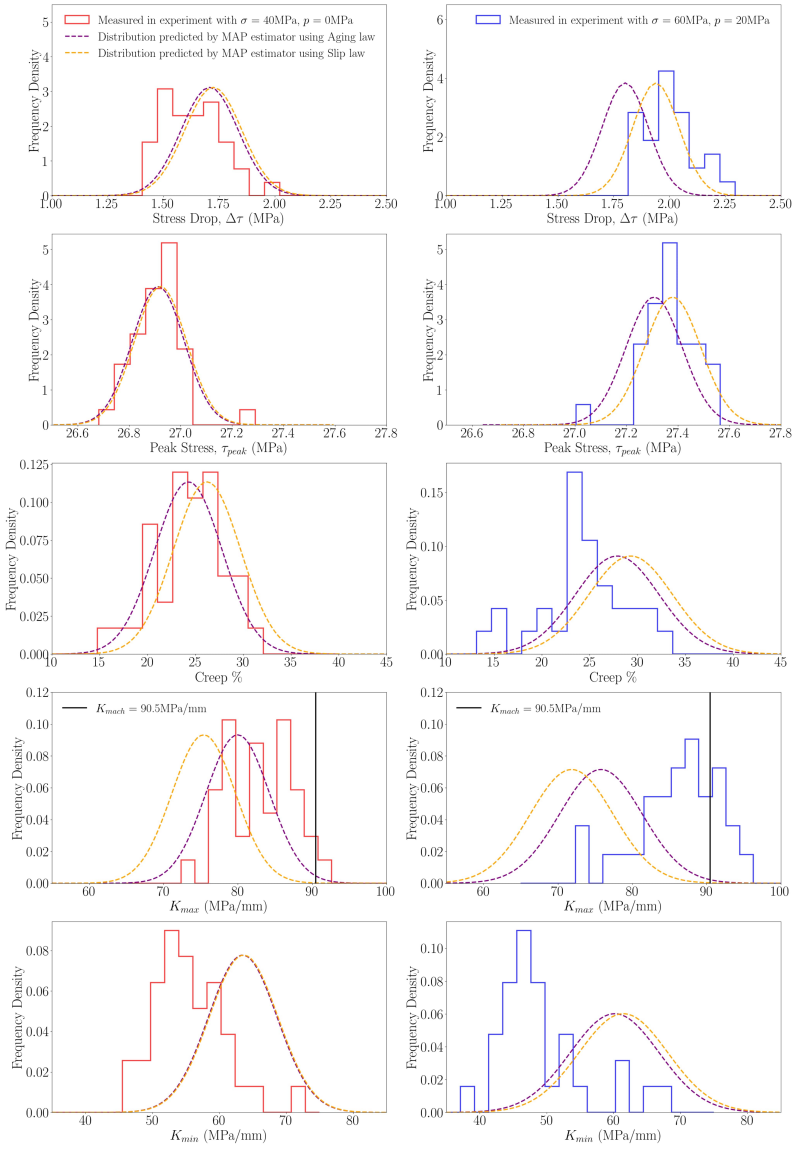

Figure 2.29: Spring-Slider Simulations Can Match Stress Drop, Creep % and Peak Stress of Experiments but Cannot Match K_{max} and K_{min}: Histograms of the stick-slip characteristics observed from the dry (red cures of left column) and wet (blue curves of right column) experiments are plotted along with Gaussian distributions predicted by the MAP estimators for the slip (yellow) and aging (purple) laws. The simulated distributions match well the observed distributions of the stress drop, creep % and peak stress. The simulated distribution for K_{max} and K_{min} are lower and higher than those of the experiment, respectively, for both state evolution laws. In other words, the experimental stick-slip consistently shows more creep during the nucleation phase right before the stress peak and a higher tendency to 'stick' right after the event.

and-state parameters with slip was observed in other experiments of quartz gouge (Noël et al., 2023, 2024) although their inference of frictional parameters did not extend into the unstable regime of stick-slip. Here, we verify that the evolution continues into the stick-slip regime. The relatively small change in a with slip is consistent with existing interpretations of its physical origin that it represents the strength of the contact asperities. In this sense, the strength of the asperities, whose length scale is comparable to the size of the smallest grains with minimal defects, should not change significantly due to comminution or shear localization. D_{RS} has been compared directly to the size of granular particles in gouge material (Rathbun and Marone, 2013), consistent with the notion that the evolution of the state variable should happen over distances of slip comparable to the grain size. The decrease in D_{RS} with comminution and localization due to slip is consistent with this logic. It is also possible that D_{RS} is rather proportional to the 'quality' of contact rather than the grain size which might directly translate to the 'quantity' of contact. Notably, clay has small particle size ($\sim < 2\,\mu m$) but also tends to slide stably with larger D_{RS}. Clay has stronger inter-particle surface charge than quartz that leads to agglomeration and possibly a larger 'effective' particle size. Whether such changes in surface properties could also affect the 'quality' of frictional contact is not yet clearly understood. Physical interpretations of b are not as clear as they are for a and D_{RS}. It has been proposed that b may be representative of the rate of change in contact area due to shear-induced dilatation and compaction (Hulikal, Lapusta, and Bhattacharya, 2018). One may expect the rate of dilatation to be dependent on the grain size distribution at the localized layer, which could explain the change in b with comminution. Other studies have also related b to the rate of healing from slide-hold-slide experiments (Noël et al., 2024).

When using the aging law, the evolution of rate-and-state effects with slip is not consistent with the physical interpretations of the parameters just discussed. First, the increase in a reflects a change in the contact strength of the asperities through shear localization and comminution. For a significant change in a to be physical, a likely requires a different physical interpretation, possibly linked to an initial resistance to motion by locking of grains to sudden perturbations. Secondly, D_{RS} increases since the velocity step, which is inconsistent with the notion that it is directly proportional to the grain size which reduces with slip. Notably, the constancy of a and decrease in D_{RS} with slip that was also observed by Noël et al. (2024) were inferred by matching the stable velocity using the aging law. However, the stable velocity step is close to steady-state conditions with smaller differences between the two state evolution

laws, and applying the slip law to the data of Noël et al. (2024) most likely would not result in any qualitative changes to the conclusions.

Regardless of the choice of the state evolution law, the presence of pressurized pore fluids tends to increase a, b, and D_{RS} in both the stable and unstable phases. The results imply higher contact strength, higher rate of healing and state evolution, and larger grain size or higher quality contact in the wet sample. How the contact strength of the asperities would increase by the presence of pressurized pore fluids is unclear. However, an increase in the contact strength would be consistent with the larger grain size or higher quality contact, such that the grains would comminute less or experience smaller decrease in contact quality under the same wear process. Previous studies have noted the role of humidity in assisting adsorption along contact surfaces which increases the rate of healing in slide-hold-slide experiments, correlated to an increase in b (Frye and Marone, 2002). However, the water content is significantly greater in our experiment where the pore fluid is pressurized to 20 MPa. The 'dry' sample of our experiment corresponds more closely to 'wet' samples in studies of the effect of humidity as our 'dry' sample is at room conditions. Given the relatively large difference in pore pressure, it may be that the origin of difference between the 'dry' and the 'wet' gouge in our experiment is more mechanical than chemical.

2.8 Discrepancy Between Model and Experiment in the Dependence of Nucleation on the Loading Rate

The simulations with both the slip and aging laws have nucleation processes that are longer in time and slip than the experiments. We further test the extent of this discrepancy by running the simulations at different loading rates. The simulations using the slip law with the lower loading rate of $V_{pl} = 0.3$ µm/s and a higher loading rate of $V_{pl} = 30$ µm/s are shown along with the original fit at $V_{pl} = 3$ µm/s in Figure 2.30. Interestingly, the nucleation process lengthens even further with a decrease in the loading rate like in the experiments. However, this is accompanied by a significant increase in the stress drop and peak stress and a decrease in the creep ‰. As seen in Figure 2.4 and more broadly in Figure 2.2, the amplitudes of the stick-slip signals nor their peaks do not change significantly at the different loading rates in the experiment. Applying the hypothetical loading rate of $V_{pl} = 30$ µm/s further decreases the stress drop and peak stress and shortens the nucleation process. The duration of the nucleation process is more like the experiments at $V_{pl} = 30$ µm/s, but with a significantly higher creep ‰. The inverse proportionality between the

loading rate and stress drop in the dynamic spring-slider with rate-and-state friction was also observed by Gu and Wong (1991).

Noël et al. (2024) noticed a dependence of stress drop on the loading rate - namely, an increase in the stress drop with a decrease in the loading rate - which was attributed to localization and de-localization by a sudden 'kick' in the loading rate. Such phenomenon would extend beyond the mechanisms of shear resistance along a localized sliding surface as captured by rate-and-state friction. Thus, the fact that the dynamic spring-slider with rate-and-state friction produces a stress drop dependence consistent to what was observed by Noël et al. (2024) does not necessarily mean that the physical mechanisms are represented accurately. Our experimental observations are opposite to those of Noël et al. (2024) in that instability is often triggered and suppressed by a step increase and decrease in the loading rate, respectively. We also do not observe a significant dependence of the stress drop on the loading rate once instability has fully developed.

The more rapid nucleation process in the experiments is interesting when considering that K_{min} of the experiment is already smaller than in the model. In other words, the quartz gouge slips more during the nucleation phase prior to the stress-drop event, implying more stable properties, but has a more abrupt transition to the event phase, implying more unstable properties. The abrupt increase in the slip rate is followed by an abrupt decrease during the arrest phase, resulting in higher experimental K_{max} than that in simulations. This is an apparent combination of both more stable and unstable behavior that is difficult to recreate with the spring-slider model and rate-and-state friction using either the slip or aging laws. In the following section, we explore whether this discrepancy could arise due to the approximation of the finite experiment with a single-degree-of-freedom system.

2.9 Quasi-Static Finite-Element Model of Experiment

We develop an approximate Finite-Element Model (FEM) of the experiment, which is still idealized but captures the finite extent of the sliding surface and the experimental apparatus (Figure 2.31). Our main goal is to see whether the experimental deviations from the spring-slider response could be caused by non-uniform slip along the experimental surface. The model is 2D and plane strain, with the finite dimension resolved in the direction of loading. The entire experimental apparatus is approximated as a single column of constant thickness (20 mm), asides from the location of the rubber spacers which are left vacant with a width of 10 mm due to

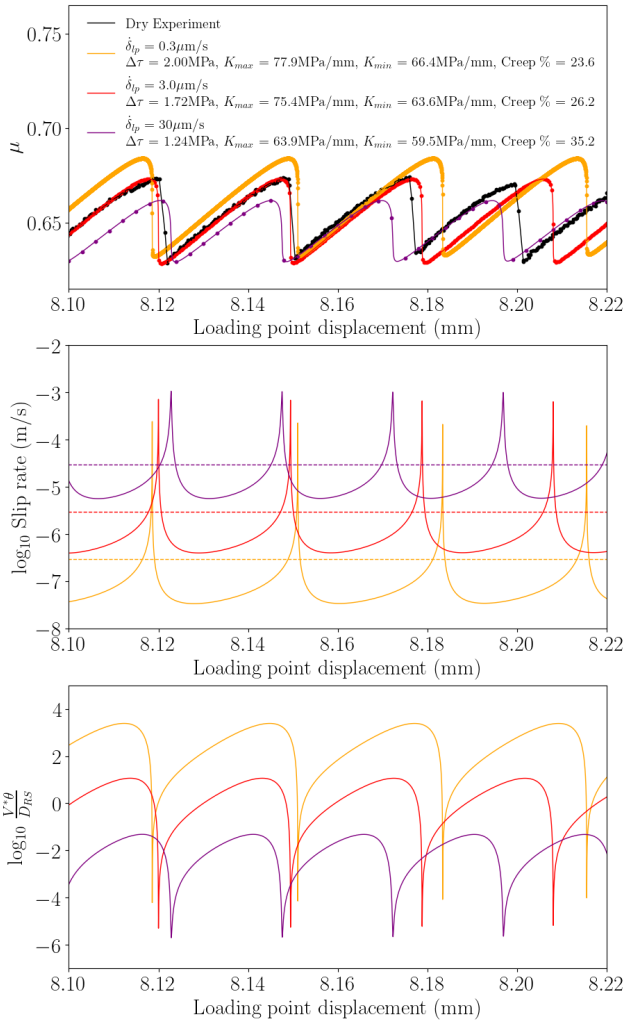

Figure 2.30: Influence of Loading Rate on Stick-Slip in the Spring-Slider: The rate-and-state parameters of the best-matching model of the stick-slip events in the dry experiment using the slip law (red) is used to conduct spring-slider simulations at different loading rates. Dots are plotted every 0.1 s, similar to the measurement sampling at 10 Hz in the experiments. The dotted lines in the second row demarcate the loading rate using the same color of the corresponding simulation. The loading rate has significant effect on both the stress drop of the event and the evolution of creep during the strengthening phase. Namely, a decrease in the loading rate lengthens the nucleation phase while decreasing the creep % and increasing the stress drop and peak stress. The longer nucleation process with a decrease in the loading rate is similar to the experiment (Figure 2.4) but the increase in stress drop and peak stress is not observed in the experiments. Thus, the spring-slider model with rate-and-state friction produces extra sensitivity of stick-slip features to the loading rate not observed in the experiments.

their negligible strength compared to the steel surrounding. The elastic properties of the apparatus are those of 17-4 stainless steel, heat treated to the H900 condition with shear modulus, density and Poisson's ratio of 76 GPa, 7800 kg/m3 and 0.262, respectively. The length of the loading column, L_{col} = 790 mm, is adjusted to match the stiffness of the loading system measured from the experiment (90.5 MPa/mm). Thus, the total length of the model is L_{total} = L_{col} + 2*10mm + 50 mm = 860 mm. Although the experimental boundary condition in the direction perpendicular to loading is technically a constant confining stress, strictly Neumann boundary conditions lead to a singular stiffness matrix in the finite element method. As a similar scenario, we apply a constant normal stress only to the top surface and enforce a zero displacement boundary condition on the bottom surface. A 50 mm interface between the two steel sliders is designated as the frictional interface with rate-and-state friction. The loading end of the column is pushed at a desired displacement rate while the other end is fixed.

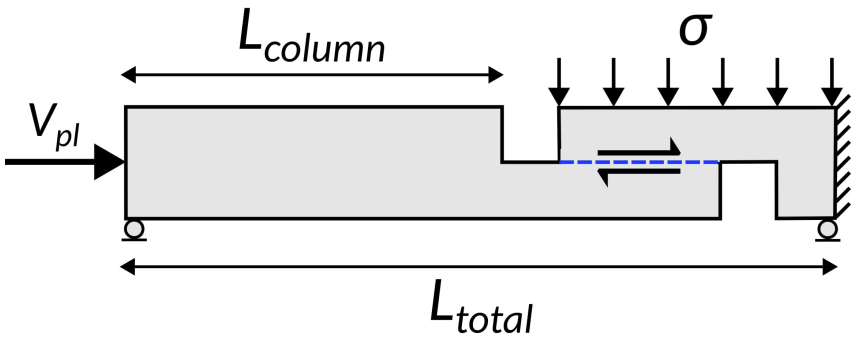

Figure 2.31: Quasi-Static Finite-Element Model: The experimental apparatus is approximated as a single column of constant thickness besides the location of rubber spacers adjacent to the gouge layer (Figure 1) which is left vacant, considering the negligible strain energy of rubber compared to the steel surroundings. A constant displacement rate is applied at the loading end of the column while the other end is held fixed. A constant normal stress is applied from along the top surface of the apparatus above the gouge layer while the displacement in the vertical direction is fixed along the bottom surface. Plane-strain conditions are applied and inertia is neglected. The simple 2D finite-element model simulates a more accurate analogue of the experiment in terms of the apparatus geometry, accounting for the effect of a finite loading system and the finite length of the sliding surface.

We first simulate the response of the finite-element model to the stable velocity step. For brevity, we present the results using the slip law, the conclusions remain qualitatively the same using the aging law. The frictional parameters are the posterior mean estimators from the inversion of the dry experiment using the spring-slider

model. Figure 2.32 shows the comparison of the spring-slider fit along with the finite-element model simulation. The two solutions are quite similar. The finite-element model exhibits a slightly larger oscillation, with a higher peak in friction and a lower trough afterwards. Overall, the finite model also matches the experimental data quite well, and suggests that a spring-slider model can serve as an accurate representation in the case of largely quasi-static slip where departure from steady-state sliding is relatively brief. Interestingly, the measurement of the friction coefficient in the finite-element model, which divides the cumulative force at the loading end by the area of the sliding layer and the normal stress, is offset from the experimental data by around 0.0645. The difference likely occurs from geometric effects of the loading column and the sharp geometry at the ends of the sliding layer.

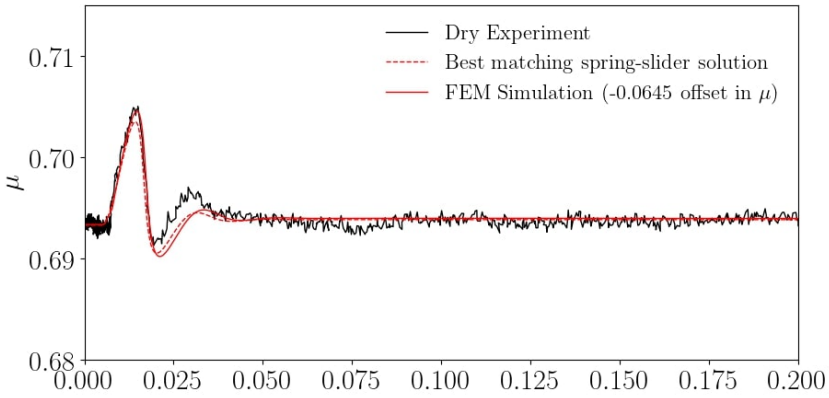

Figure 2.32: Finite-Element Model Behaves Similarly to Spring-Slider for Stable Velocity Step: The evolution of friction in the finite-element model with the rate-and-state parameters inferred from the spring-slider inversion using the slip law is plotted (solid red curve) along with the results from the spring-slider model (dotted red curve) and the dry experiment (black curve) for the stable velocity step. The finite-element model behaves similarly to the spring-slider model and matches the experiment well. The comparison shows that the spring-slider model may serve as an accurate and efficient representation of the finite experiment for the stable velocity step.

Next, we simulate a quasi-static solution with friction parameters given by the MAP estimators derived for the dry experimental stick-slip data. Again, we use the slip law. We enforce a constant step size of 0.01 s, which allows a stick-slip sequence to be resolved. The solution is not necessarily correct, as it neglects inertia and dynamic slip during the event. However, the quasi-static finite-element model provides valuable insight into the evolution of slip in the finite setting for the inferred frictional parameters, especially for the nucleation phase which is quasi-static.

We divide the plots of the evolution of slip and stress between the loading phase and the stress-drop event phase. The nucleation phase and the arrest phase slightly overlap between the two figures. Figure 2.33 shows the slip and stress history during the loading phase. Slip evolves in a mostly uniform manner, with slightly higher accelerations at the end of the sample further away from the loading column. The stress profile is non-uniform in space, where the sharp geometry at the end of the frictional layer creates stress concentrations. Due to the earlier onset of slip at the edges of the sample prior to the plotted duration, accumulated slip is higher towards the edges than in the center. Through time, the non-uniformity of the stress profile changes minimally given the nearly uniform profile of slip, although the shear stress does increase by about 1.5 MPa during the loading phase. Figure 2.34 shows the subsequent event phase. Even in the event phase, slip is also uniform in space. The event is significantly slower than the experiments, due to the absence of inertial effects. The largely uniform profile of slip is not surprising given that the experimental surface is close to the critical stability as established in our spring-slider modeling.

This modeling supports the notion that the main discrepancies between the spring-slider model and the experiment are due to differences in the constitutive behavior and not due to finite-fault effects. However, the possibility remains that the slip in experiments is non-uniform in space, e.g., due to some heterogeneity of friction properties along the sliding surface. We will investigate the continuum representations of the experiments more fully in future work.

2.10 Conclusions

In this chapter, we track the evolution of rate-and-state friction parameters in granular quartz gouge with slip, starting from the stable phase using stable velocity steps to the unstable phase using characteristic features of stick-slip events. We also analyze the effect of pore pressure, by comparing two experiments with different pore pressure but the same effective normal stress. The fine granular gouge considered in this work exhibits a deformation history that is quite complex, including the development of instability with slip, a dependence of stability and nucleation on the loading rate, and long-term changes in the average friction coefficient. At the stable velocity step, the wet sample shows slightly larger oscillations than the dry sample. In stick-slip, the wet sample has both larger stress drops and larger changes in creep during the aseismic period, transitioning from a more ‘stuck’ configuration during arrest to one

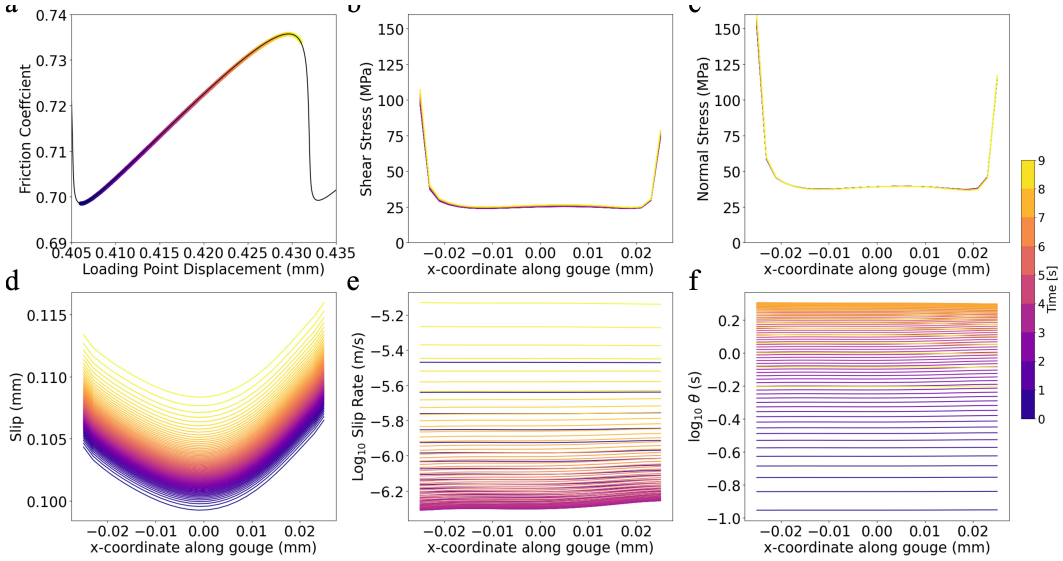

Figure 2.33: Evolution of Slip and Stress in the Finite-Element Model During the Loading phase: (a) A single stick-slip event from the event sequence of the finite-element model is plotted along with the evolution of stress (b, c) and slip, slip rate and state variable (d, e, f) during the strengthening phase. The colors on each plot correspond to the same time scale shown on the far right. Dots along the curves in (a) are spaced at 0.1-s intervals. The shapes of shear (b) and normal (c) stress profiles change little during the loading period, due to uniform slip. The shapes are non-uniform in space due to stress concentrations at the ends of the frictional layer. During the plotted duration, evolution of slip, slip-rate and the state variable are largely uniform in space aside from a slightly higher acceleration at the end further away from the loading column. This model suggests that differences between the experiments and spring-slider models during nucleation phase are not obviously due to finite-fault effects.

that creeps more during nucleation. The differences show an effect of pressurized fluids on friction beyond what can be explained by the effective stress principle.

We develop a Bayesian probabilistic framework with MCMC sampling to infer rate-and-state parameters from both stable velocity step and stick-slip data. Synthetic inversions show that the method can accurately and precisely infer rate-and-state parameters from stable velocity step data with uncertainty range smaller than those achieved by local minimization of nonlinear least-squares residuals. An important observation with regards to the inversion method is that it is better to do the sampling of rate-and-state parameters logarithmically, due to the logarithmic dependence of friction on rate-and-state parameters such as D_{RS}. The inversions of experimental data indicate that the presence of pressurized pore fluids simultaneously stabilizes

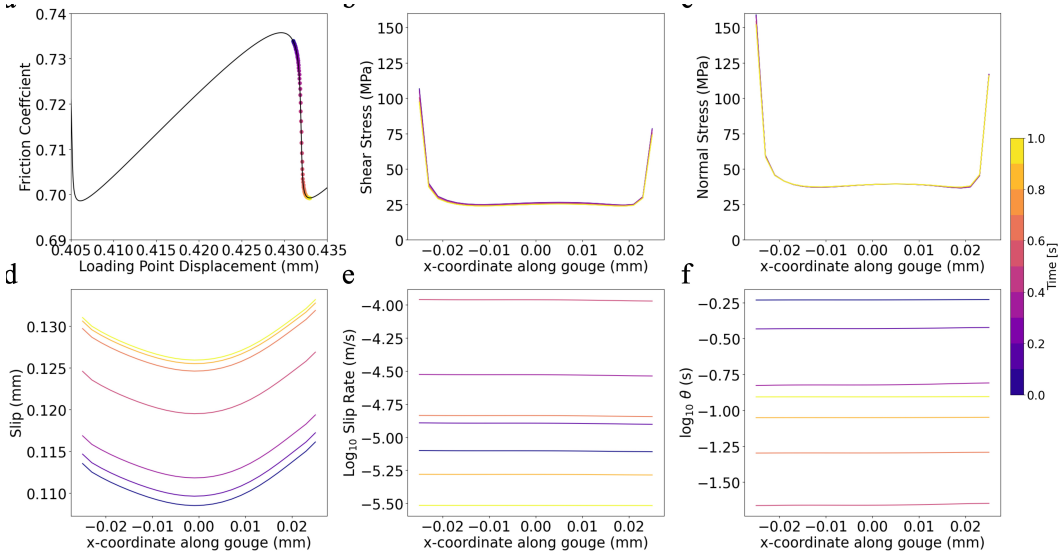

Figure 2.34: Evolution of Slip and Stress in FEM Model During the Stress-Drop Event: (a) A single stick-slip event of the finite-element model is plotted along with the evolution of stress and slip during the dynamic phase (b, c, d, e, f). The colors on each plot correspond to the same time scale shown on the far right. Dots along the curves in (a) are spaced at 0.1-s intervals. Although slightly higher acceleration of slip is visible at the edges, the evolution of slip, slip rate and the state variable are largely uniform across the length of the slipping surface. The spatially uniform evolution of slip suggests that the discrepancy between the experiments and spring-slider models are not obviously due to finite-fault effects.

and destabilizes the gouge, as the wet sample has higher a and D_{RS} that corresponds to more stability as well as higher b that corresponds to more unstable behavior.

Forward simulations of the spring-slider model in the unstable regime show that the slip law generally produces more creep than the aging law. The aging law is able to heal and evolve the state variable more at lower slip rates which leads to higher state variable values during loading and more dynamic events. The different dependence of creep to rate-and-state properties near critical stability leads to qualitatively different inversion results for the two state evolution laws. Although dilatancy increases creep %, it also decreases the stress drop, making it an unlikely explanation for the observed changes between the dry and wet experiments during the unstable phase. Thus, both the development of instability with slip and the differences between the dry and wet experiments are likely due to changes in rate-and-state friction parameters.

Synthetic inversions of rate-and-state parameters reveal a large degree of non-uniqueness when all frictional parameters are treated as free variables. Assuming

critical stability regularizes the non-uniqueness, allowing accurate inference of rate-and-state parameters from slow-slip events. Inversions of experimental data while assuming the responses are close to critical stability allow us to track the evolution of frictional parameters with slip since the stable velocity step. For the slip law, both experiments show minimal change in a along with an increase in b, decrease in D_{RS}, and decrease in μ^*. The constancy of a and decrease in D_{RS} are consistent with previously established interpretations related to the strength of the asperity contacts and the comminution of grains at the localized plane of shear, respectively. The reduction in D_{RS} could also represent a reduction in the 'quality' of contact. Distinguishing between the possibilities is difficult without detailed examination of the grain structure and surface chemistry. The aging law shows an increase in a, along with an increase in b and increase in D_{RS}. The changes to a and D_{RS} are not consistent with the micro-physical interpretations of rate-and-state effects for the aging law. Furthermore, the best fitting model with the aging law has slip rates of the event phase that are significantly lower than those of the experiment. Overall, the slip law produces a closer fit to the experimental events while also demonstrating greater consistency in the evolution of rate-and-state parameters with respect to established interpretations of their micro-physical origin.

The best fitting spring-slider model with the slip law still shows significant discrepancies to the experiments in the evolution of creep during the strengthening phase and in the dependence of stick-slip dynamics on the loading rate. The spring-slider model has lower K_{max} and higher K_{min} than the experiment, indicating that the experiments both stick more after an event and creep more prior to an event. Additionally, the nucleation process is significantly more abrupt in the experiment. The spring-slider model also cannot reproduce the (lack of) dependence of stress drop on the loading rate that is observed in the experiment. A quasi-static finite-element model with the same rate-and-state properties suggests that the gouge in the sample likely slides in a spatially uniform matter. The same model also successfully reproduces the fit of the stable velocity step by the spring-slider model. Thus, the discrepancies between the spring-slider model and the experiment can likely be attributed to flaws in the rate-and-state formalism rather than the idealization of a finite geometry to a single-degree-of-freedom system.

Although the inversion of stick-slip observed in the experiments using spring-slider models is relatively successful, it is only possible assuming regimes close to critical stability in the spring-slider model, as substantiated by the significant creep percent-

age observed during the loading phase. Inversions of more dynamic events using the proposed approach would run into difficulties with non-uniqueness. Furthermore, more dynamic events may involve dynamic weakening mechanisms such as flash heating and pore pressurization, which may make inversions even more non-unique. Thus, an interesting question to ask is what observations and data could further constrain the inverse problem. In the experimental setting, one could submit the sample to different regimes of sliding by slide-hold-slide tests during the stick-slip events. Such tests may better constrain the effect of healing which in conjunction with stick-slip characteristics could make the inverse problem more unique. The task might be more difficult in the field setting where one rarely has control on the type of loading. A case where control may be possible is in the context of induced seismicity, where one can inject or extract at desired rates. Additionally, developing technologies in observational seismology such as Distributed Acoustic Sensing (DAS) could provide stronger constraints on the spatial profile of dynamic properties (Li et al., 2023).

Chapter 3

PHYSICAL AND STATISTICAL MODEL OF SEISMICITY RATE OBSERVED DURING GEOTHERMAL WELL STIMULATION IN OTANIEMI, FINLAND

This chapter has been adapted from

Kim, Taeho and Jean-Philippe Avouac (2023). "Stress-based and convolutional forecasting of injection-induced seismicity: application to the Otaniemi geothermal reservoir stimulation." In: *Journal of Geophysical Research: Solid Earth* 128.4, e2022JB024960.

3.1 Introduction

Induced seismicity is of particular relevance to geothermal energy production. Controlled hydraulic stimulation could unlock the vast geothermal resources that could be drawn from deep crustal reservoirs with no natural hydrothermal activity. Hydraulic stimulation is used to enhance the heat exchange between the circulating fluids and the reservoir by creating or reactivating fractures which are hydraulically conductive. Induced seismicity is an undesirable by-product of this process, and a number of such Enhanced Geothermal Systems (EGS) has been stopped due to earthquakes felt by local residents. (Häring et al., 2008; Kwiatek et al., 2019; Schultz et al., 2020). The development of Enhanced Geothermal Systems (EGS) would therefore benefit from better methods to forecast injection-induced seismicity.

It has long been known that injection of fluids in the subsurface can induce seismicity (e.g., Healy et al., 1968; Raleigh, Healy, and Bredehoeft, 1976). Injection-induced seismicity can result from either a stress or strength change on a fracture or fault. The effect of injection is generally assessed by considering pore pressure diffusion in the medium and the consequent decrease in the effective normal stress as according to Terzaghi's principle (Skempton, 1984). This first-order description of the stress state has been effective in explaining various aspects of induced seismicity, including the $\sqrt{t}$ evolution of the seismicity front (Shapiro et al., 2006; Shapiro, Huenges, and Borm, 1997) and general spatio-temporal patterns of induced seismicity (Elmar and Shapiro, 2002; Shapiro et al., 2002; Shapiro and Müller, 1999) as early as the pioneering study at the Rangely oil field (Raleigh, Healy, and Bredehoeft, 1976). An additional step in the description of stress changes due to a fluid injection

is the theory of poroelasticity which describes the coupling between fluid flow and deformation of the solid skeleton. Poroelasticity has been shown to play a role in triggering earthquakes in addition to pore pressure evolution (Segall, 1989; Segall, Grasso, and Mossop, 1994; Segall and Lu, 2015), particularly outside the characteristic pore pressure diffusion length (Goebel and Brodsky, 2018; Zbinden et al., 2020). Although the magnitude of stress changes from poroelasticity is estimated to account for typically only about a tenth of that from pore pressure diffusion (Zhai and Shirzaei, 2018), its consideration is often required for complete explanations of the observed seismicity in space and time.

A fluid injection can result in 'hydrofractures' (Mode-I opening fractures) or shear fractures (Mode-II or Mode-III). Induced earthquakes generally result from shear failure. While linear elastic fracture mechanics is commonly employed in modeling the growth of cracks in Mode-I and the consequent stress changes, modeling shear failure requires an appropriate friction law. One kind of models is based on the Mohr-Coulomb failure criterion in which slip occurs once the ratio of the shear stress to the normal stress on a fault reaches a pre-defined threshold, the static friction coefficient, and drops to the dynamic friction coefficient either at the immediate onset of slip or gradually with fault slip. However, there is ample evidence from laboratory studies and natural observations that the initiation of slip involves in fact a gradual decrease of friction associated with asesimic slip, often referred to as the nucleation process. Such an evolution of friction is commonly described using the rate-and-state friction law derived from frictional sliding experiments in the laboratory (Ampuero and Rubin, 2008; Dieterich, 1994; Marone, 1998; Ruina, 1983).

The non-instantaneous nucleation process implied by rate-and-state friction can explain a number of phenomenological observations such as the Omori decay of seismicity rate during aftershocks (Dieterich, 1994) or the low sensitivity of seismicity to solid-earth tides (e.g., Beeler and Lockner, 2003). The rate-and-state formalism has also shown success in explaining the relationship between stress and seismicity rate due to diking (e.g., Toda, Stein, and Sagiya, 2002) and aseismic slip (e.g., Segall et al., 2006). In the context of induced seismicity, rate-and-state friction has been applied to explain certain non-linear features such as the time lag between induced seismicity and stress perturbations (e.g., Candela et al., 2019; Dempsey and Riffault, 2019; Norbeck and Rubinstein, 2018; Richter et al., 2020). It is important to note that, in principle, the activation of a fault by a pore pressure

increase doesn't necessarily imply seismic slip (e.g., Guglielmi et al., 2015). In fact, there is observational evidence that injection-induced fault slip is mostly conditionally stable (Bourouis and Bernard, 2007; Calò et al., 2011; Goodfellow et al., 2015; Scotti and Cornet, 1994), as is expected from the nucleation model based on rate-and-state friction and that seismicity is in fact occurring outside the zones of high pore pressure (Cappa et al., 2019; De Barros et al., 2018; Wei et al., 2015).

More specifically with regards to hydraulic stimulation of geothermal wells, important questions arise regarding the differences between the Mohr-Coulomb and rate-and-state friction-based models considering the rapid stressing rate that is common in such operations. Mohr-Coulomb models coupled with linear slip weakening can result in realistic simulations of seismic ruptures while accounting for the nucleation process (Olsen, Madariaga, and Archuleta, 1997). This is not the case for single-degree-of-freedom spring-slider systems often employed for modelling induced seismicity. The commonly used model of Dieterich (1994) based on rate-and-state friction can converge to models based on the Mohr-Coulomb criterion at the rapid equilibrium limit. It is also possible that rate-and-state effects on nucleation may be significant at the relatively short timescale of intense injection cycles during stimulation.

A hysteresis effect, often referred to as the Kaiser effect, is also commonly observed in induced seismicity. The Kaiser effect refers to the observation when a material submitted to a series of loading cycles of increasing amplitude fails gradually, further failure generally occurs at a stress level exceeding the maximum stress reached in previous cycles. This effect explains the observation that acoustic emissions during rock failure stop if the stress decreases and do not resume until the medium is loaded to its previous maximum (Lavrov, 2003). How a nucleation source "remembers" its loading history has proven to be essential in reproducing various observations in induced seismicity, such as time delays of the seismicity rate in response to perturbations of the injection rate and regions of seismic quiescence behind triggering fronts (Baisch et al., 2006, 2010; Dempsey and Riffault, 2019).

Numerous physical models have been developed to incorporate stress changes, pore-pressure changes and failure mechanisms in a single framework (Gaucher et al., 2015; Grigoli et al., 2018). A notable example of physical models that accounts for rate-and-state friction in particular, is presented by Segall and Lu (2015), where changes in stresses by fluid injections into an infinite poro-elastic medium were used as input to the model of Dieterich (1994), relating seismicity and stress rates among

a population of nucleation sources. Although the framework was originally used to investigate poroelastic effects during shut-in and to address the common observation that maximum magnitude events often occur after injections cease (Grigoli et al., 2018; Häring et al., 2008), it can be used more generally to study induced seismicity in response to various injection scenarios (e.g., Zhai and Shirzaei, 2018). Finite-fault and fracture network models accounting for rate-and-state friction have also been developed (Almakari et al., 2019; Dublanchet, 2018; Larochelle et al., 2021; McClure and Horne, 2011) to examine rupture properties and the effect of heterogeneous fault properties on the seismicity rate. Numerous factors make it difficult, however, to resort to such models in practice, such as the high computational cost of solvers and poor resolution of pre-existing heterogeneities in the sub-surface - in particular, the distribution of stress and strength - with a level of detail that cannot be constrained with observation. Some representations of heterogeneities are essential in reproducing well-established statistical properties of earthquakes (Dempsey, Suckale, and Huang, 2016; Zöller, Holschneider, and Ben-Zion, 2005) such as the Gutenberg-Richter law which describes the magnitude-frequency distribution of earthquakes (Gutenberg and Richter, 1956; Ogata, 1988).

Due to the complexity of stress-based models along with the difficulty to calibrate the model parameters, a number of studies have alternatively explored data-driven statistical modeling. Such models often hinge on the Gutenberg-Richter law and the assumption that earthquakes follow a Poisson process. Additionally, they often model earthquake triggering as a cascading process based on the Omori law (Utsu, 2002) which fits commonly observed patterns of the decay of seismicity rate during aftershock sequences. A popular example is the epidemic type aftershock model (ETAS) (e.g., Ogata, 1988), which represents the total seismicity as a linear superposition of homogeneous Poisson processes, to represent mainshock and aftershock sequences (e.g., Bachmann et al., 2011; Lei et al., 2008; Mena, Wiemer, and Bachmann, 2013). Such models have the advantage of resulting in very realistic synthetic catalogs since they incorporate statistical properties directly derived from observations. However, statistical approaches are in principle less transportable from one reservoir to another as they lack explicit connections to the mechanical and hydro-geological properties of the medium. The development of hybrid models that account for the complex network of physical mechanisms while being generalizable and applicable to various injection sites and scenarios is therefore an active area of research (Gaucher et al., 2015).

In this chapter, we develop and test physical and statistical models of induced seismicity against a seismological dataset acquired by the Finnish company St1 Deep Heat Ltd. during an EGS operation at the Aalto University's Otaniemi campus near Helsinki (Hillers et al., 2020; Kwiatek et al., 2019; Leonhardt et al., 2020). A large catalogue produced with Machine Learning techniques (Ross, Meier, and Hauksson, 2018; Ross et al., 2018) revealed that the time evolution of seismicity can be predicted well based on a simple convolution model (Avouac et al., 2020). An enhanced catalogue was also recently produced by Leonhardt et al. (2020). Building on this previous work, we present and assess physical and statistical models to forecast the spatio-temporal evolution of seismicity induced by the Otaniemi EGS stimulation.

3.2 Data Presentation And Analysis

The seismic catalogue comes from a geothermal well stimulation project operated by St1 Deep Heat Ltd. near the campus of Aalto University in Otaniemi, Finland and is compiled by Leonhardt et al. (2020). The injection well (OTN-3 in Figure 3.1) was drilled to a depth of 6.1 km into Precambrian crystalline (gneiss and granite) rocks. Approximately 18,000m^3 of water was injected over the course of 49 days from June 4th to July 22nd in 2018. The injection history was divided into five successive stages moving upward from the bottom of the well (Figure 3.1). Pumping parameters of the injection such as the injection rate and well-head pressure were tuned as part of a Traffic Light System (TLS), the details of which are presented in Ader et al. (2020) and Kwiatek et al. (2019). The stimulation consisted of numerous cycles of injections and pauses of varying duration. The injection history also included periods of bleed-off's where injection was stopped and backflow out of the well was allowed.

The stimulations were monitored with surface and borehole seismometers providing excellent detection and location of the induced earthquake (Hillers et al., 2020; Kwiatek et al., 2019). Namely, the monitoring network consisted of a seismometer array at 2.20-2.65km depth in a separate well (OTN-2), located around 400 m from OTN-3, in addition to a 12-station network installed in 0.3-1.15 km deep wells (Figure 3.1). The catalogue consists of 61,150 events in total (Figure 3.2) and 1986 relocated events with spatial uncertainty of ±52m (Figure 3.3). The magnitude of completeness is estimated to be M_c = -1.1.

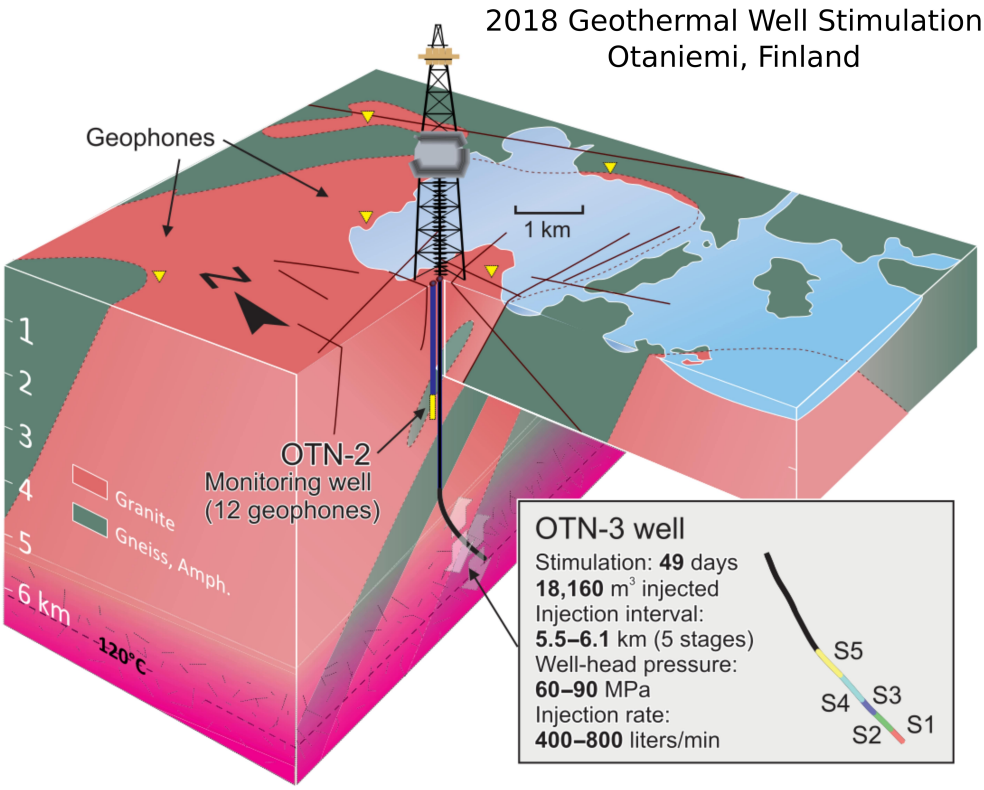

Figure 3.1: Well-Stimulation Operation in Otaniemi, Finland (Kwiatek et al., 2019). The observation well (OTN-2) and stimulation well (OTN-3) are indicated by lines extending into depth at the center of the schematic. Locations of various geophones within the area are indicated by the yellow triangles. Locations of stimulation stages S1 to S5 vary along the length of OTN-3. Basic stimulation parameters are shown in the inset.

A few salient features of the observed seismicity guide our modeling. First, the seismicity rate has a positive correlation to the injection rate in time, accompanied by finite periods over which it increases and decreases in response to injections and shut-ins, respectively. We indeed note that the seismicity rate reaches a similar magnitude for injections far apart in time but equal in the flow rate. Second, the decay pattern in the seismicity rate, R, during injection pauses is well-matched by the Omori law

$$R(t) = \frac{R_0}{1 + t/t_r}, \tag{3.1}$$

where t is time, t_r is the time it takes for the seismicity rate to halve, and R_0 is the seismicity rate at the onset of decay. A fit to one of the injection pause periods is shown in Figure 3.4. Note that the more general 'modified Omori law' (Utsu, 2002)

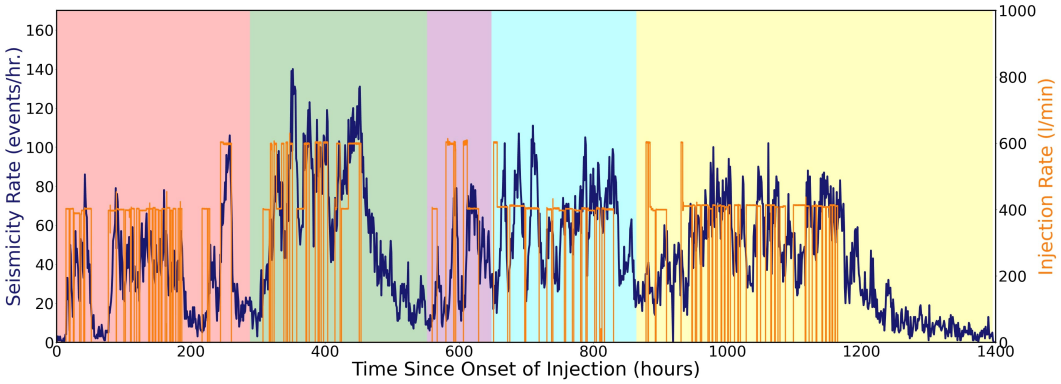

Figure 3.2: Earthquake Catalogue in Otaniemi. The complete catalogue of Leonhardt et al. (2020) is plotted in dark blue as a histogram. The injection rate history is plotted in orange. The background colors represent the timing of the individual injection stages. The seismicity rate shows a strong direct and roughly linear correlation to the injection rate, contrary to the non-linearity expected from rate-and-state friction.

allows a $1/t^p$ decay of seismicity rate; here the p-value is close to 1. The close match to the Omori law is consistent with observations of the decay rate in induced seismicity following shut-ins reported in a number of previous studies (Almakari et al., 2019; Bachmann et al., 2011, 2012; Langenbruch and Shapiro, 2010). Lastly, the relocated catalogue (Figure 3.3) shows a rather diffuse distribution of seismicity, suggesting that the injection stimulated fractures were distributed within a relatively large volume ($\sim$ 1km^3) around the open sections of the well by diffusion of pore pressure.

The exact origin of Omori law decay remains poorly understood; it could be due to the finite nucleation process governed by rate-and-state friction (Dieterich, 1994) or by instantaneous nucleation and postseismic creep that predict a p-value of approximately 1 (Perfettini and Avouac, 2004). This process was suggested to have occurred during a 10 MPa stimulation of a geothermal well at $\sim$ 3km depth at Soultz-sous-Forêt (Bourouis and Bernard, 2007). Similarly, stress relaxation by pore pressure diffusion (Nur and Booker, 1972) predicts a seismicity decay also closely resembling the Omori law with a p-value typically between 1 and 2 (Langenbruch and Shapiro, 2010; Miller, 2020). Studying the properties of the Omori-like decay provides a valuable opportunity to re-examine its mechanical origins and the physical mechanisms that drive induced seismicity.

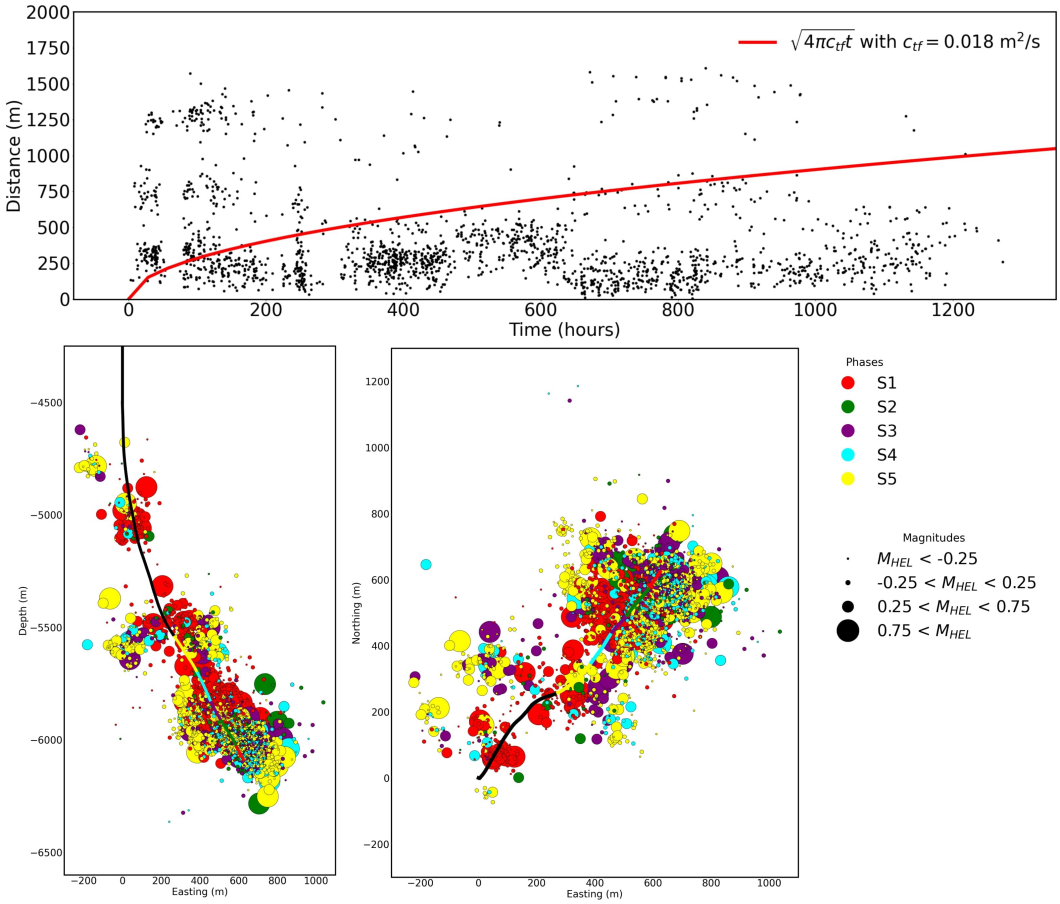

Figure 3.3: Relocated Catalogue of Leonhardt et al. (2020). 1986 relocated events are indicated as black dots according to their distances from the injection source and time of occurrence (top). The red curve outlines the theoretical triggering front of Shapiro, Huenges, and Borm (1997), $\sqrt{4\pi c_{tf} t}$, with $c_{tf} = c_{horner} = 0.018$ m^2/s. It is difficult to assess a level of agreement between the triggering front and the relocated catalogue given the limited sample size. Clusters of events far beyond the curve are likely due to leaks in the casing, as evidenced by their locations close to the well path shown in the vertical section view (bottom-left). In the map (bottom-right) and and vertical section views, the well is drawn in black with stimulated sections of the well and occurrence time of events color-coded correspondingly. M_{HEL} refers to the local Helsinki magnitude scale. The color-coding reveals little correlation in space between events and stimulation stages. Overall, the $\sqrt{t}$ evolution of the triggering front and the diffusive structure of the seismicity cluster suggests pore pressure transport as the main triggering mechanism.

3.3 The Statistical Model: Convolution of a Linear Transfer Function Inferred from Data

The direct relationship between the injection and observed seismicity rate suggests that it may be represented by a linear transfer function of the injection history

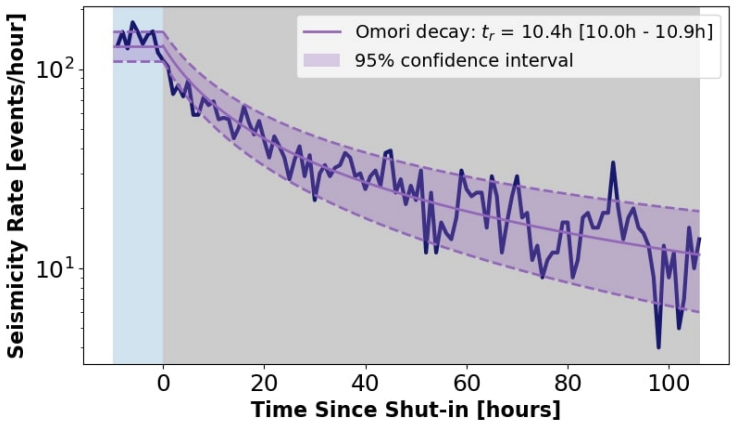

Figure 3.4: Omori Law (p=1) Decay During Shut-in. The recorded catalogue in time is zoomed-in on an interval during which injection has largely stopped (around 450-hour mark in Figure 2). A Short period prior to shut-in is shown with a sky blue background. The shut-in period is indicated with a grey background. The decay pattern in seismicity rate during the shut-in is matched well with an Omori decay function (modified Omori-Utsu law with p=1), plotted in light purple. The dotted lines and shaded areas in-between indicate the 95% confidence interval of the fit. The fitted value of t_r and the bounds of the confidence interval of the fit are indicated in the legend. Omori decay may occur due to numerous mechanisms such as the finite nucleation process, stress relaxation by pore pressure diffusion, or viscoelastic creep during the posteseismic phase. The nature of induced seismicity from fluid injections makes a mechanism related to pressure diffusion a likely candidate for Otaniemi.

(Avouac et al., 2020). To quantify this relationship, we use the algorithm of Marsan and Lengline (2008) which was originally designed to determine the kernels characterizing how earthquakes trigger other earthquakes. The algorithm estimates weights as a function of distance and time which, after normalization, represent the probability that any earthquake was triggered by any previous earthquake. We adapted the algorithm here to determine the weight relating earthquakes to injections as the source of trigger. As justified later on, secondary triggering is ignored (i.e., aftershocks of triggered events are ignored). We assume that the observed seismicity rate density, $\lambda(x,t)$, or the number of earthquakes in unit time can be modelled by a linear superposition of the influence from all previous injections such that

$$\lambda(t) = \lambda_0 + \sum_{t_i<t} \lambda_i(t), \tag{3.2}$$

where λ_0 is the uniform background rate density, and $\lambda_i(t)$ represents the rate density at time t incurred by injection i. A non-linear behaviour may in reality arise from the possible coupling between fluid pressure and permeability, and from the seismicity model. Rate-and-state friction and the Kaiser effect are indeed sources of non-linearity, as we discuss in greater detail below.

The kernel $\lambda(\Delta t)$ (referred to as the bare rates) that defines $\lambda_i(t)$ is found through an iterative process: First, we begin with an initial guess for $\lambda(\Delta t)$ and compute the triggering weights between injection i and event j, $w_{i,j} = \alpha_j \lambda(t_j - t_i)$ and the background weight $w_{0,j} = \alpha_j \lambda_0$ where α_j is a normalization coefficient to satisfy that $\sum_{i=0}^{j-1} w_{i.j} = 1$. Here, $w_{i,j} = 0$ if $t_i > t_j$ (earthquakes cannot be triggered by future injections). Secondly, $\lambda(\Delta t)$ is updated as follows

$$\lambda(\Delta t) = \frac{1}{N \cdot \delta t} \sum_{i,j \in A} w_{i,j}, \tag{3.3}$$

where A is the set of pairs such that $|t_j - t_i| \leq \delta t$, and N is the number of total earthquakes. Thus, δt becomes the discretization parameter of the algorithm. The two main assumptions of the model are linearity of the rate density that allows superposition of λ_i and the existence of a mean-field response to injections that is independent of event magnitude or injection volume. Demonstration of the algorithm on a simple synthetic catalogue and its sensitivity to discretization parameters are illustrated in Appendix B.1.

Injections are divided into individual cycles by binning them into regular 10-minute intervals. The result reveals a time decay proportional to $1/t$ (Figure 3.5). This is consistent with the observed Omori law decay following shut-ins and also with the period of build-up in seismicity at the beginning of injections. It is also possible to use this approach to estimate spatial kernels. The results are not presented here as we found the size of the dataset and the quality of the locations to be insufficient to get well constrained kernels.

The observation that the response to step-like decrease of injection rate leads to a $1/t$ Omori law decay can be used to estimate a Green's function, $g(t)$ (Avouac et al., 2020). Since the derivative of a step function is a Dirac delta function, $g(t)$ can be found by simply differentiating the Omori law in time

$$g(t) = -\frac{d}{dt}\left(\frac{R_0}{1 + t/t_r}\right) = \frac{R_0/t_r}{(1 + t/t_r)^2}. \tag{3.4}$$

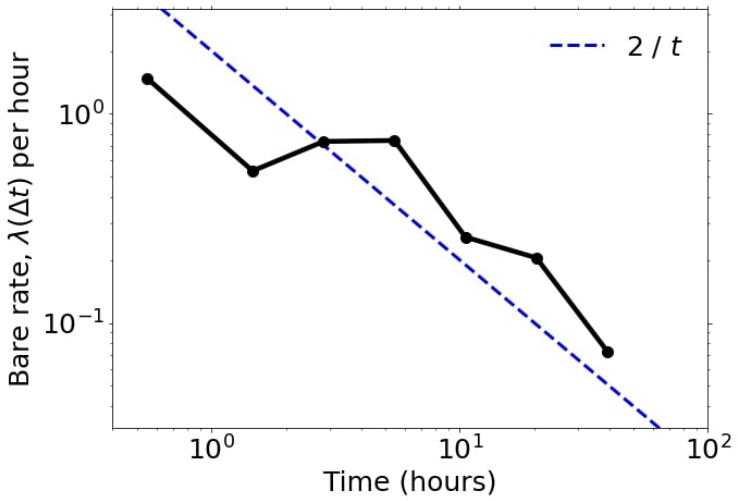

Figure 3.5: Marsan and Lengline (2008) Rate Densities. Rate densities measuring the weight of influence from individual injections onto induced events are computed through an adaptation of the cascading algorithm from Marsan and Lengline, 2008. The densities follow a $1/t$ type of decay in time, consistent with the Omori-law decay observed during shut-ins (Figure 3.4) and suggestive of the possibility for a convolution kernel relating injections to induced seismicity.

The predicted seismicity rate can then obtained from a simple convolution

$$R(t) = u(t) * g(t) = \int_{-\infty}^{\infty} u(\tau) g(t-\tau)\, d\tau, \tag{3.5}$$

where R and u are the seismicity and injection rate, respectively. Bleed-off's are implemented as negative injection rates. To construct the kernel for the specific case of Otaniemi, t_r is chosen by fitting the Omori law to the last of the injection pauses of durations significantly longer than the average injection cycle (about 20 hours). Then, R_0 is determined so as to yield a total number of events equal to the number of earthquakes in the catalog. t_r and R_0 are found to be 24.1 hours and 208.9 events per hour, respectively. Although (Avouac et al., 2020) reported that the data suggests a systematic increase of t_r during the stimulation likely due to the increasing volume of the domain of increased pore pressure, we use a constant value of t_r as the resulting difference to the fit is minor.

The model result is displayed with the observed catalogue in Figure 3.6a. It follows remarkably well the observed seismicity rate variations; bulk of the observed seismicity is included within the 95% confidence interval, calculated by assuming events are governed by an non-homogeneous Poisson process following the mod-

elled seismicity rate. The model also closely matches the decay rate during injection pauses and the build-up rate at the onset of injection cycles.

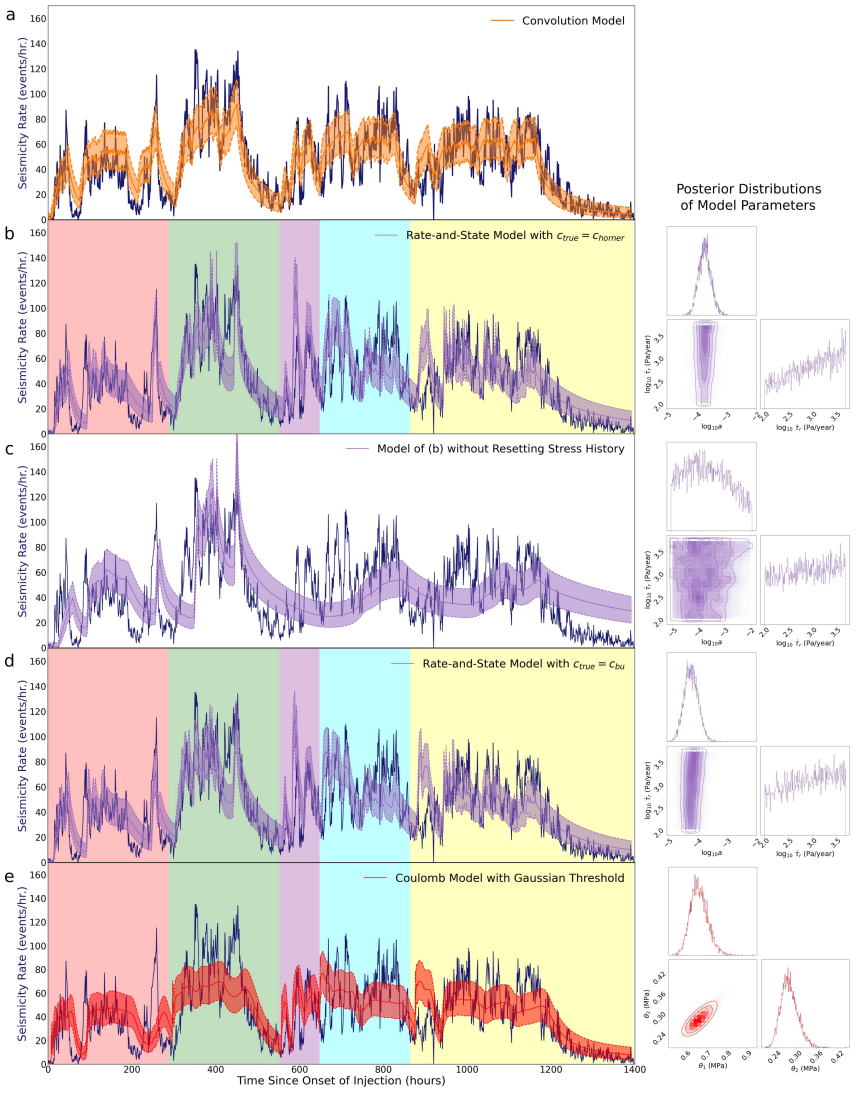

Figure 3.6: Model Predictions in Time. Model predictions are plotted in different colored shading over the observed catalogue in dark blue. The dotted-lines and shaded areas in-between indicate the 95% confidence interval of the prediction. Posterior distributions of fitted parameters are shown on the right for applicable models. Rest of the parameters are as listed in Table 3.1. While the global fit to the observations are comparable to other models, it lacks rapid variations of the seismicity rate in-between injection cycles compared to the rate-and-state models — evident of qualitative differences in modelling the stress state relative to failure and delayed nucleation mechanisms. All models (besides (c)) consistently capture temporal trends of the seismicity rate, such as the Omori-law decay during shut-ins and build-up periods at the onset of injections, with the linear convolution model requiring the fewest parameters and lowest computational cost. Model parameters and goodness-of-fit metrics are summarized in Table 3.2.

To quantify the goodness of fit, we use both the Kolmogorov-Smirnov test (Massey Jr, 1951) and the Poisson log-likelihood (Dempsey and Suckale, 2017). The Kolmogorov-Smirnov test returns the KS-statistic, which is the maximum difference between the cumulative distribution functions given by the prediction and the observation. The Poisson log-likelihood is the appropriate metric if earthquakes are assumed to result from a Poisson process, even if inhomogeneous in the case the rate varies in time and space. So the metric is valid as long as secondary aftershocks can be ignored. This assumption is tested by analyzing the distribution of interevent distances in space and time using the method of Zaliapin and Ben-Zion (2013). The result is shown in Appendix B.3, which displays a uni-modal distribution instead of the bi-modal distribution that would be expected in case of clustering due to aftershock sequences. This is consistent with the analysis by Kwiatek et al. (2019) which shows that aftershocks account for no more than 10% of the events in their seismicity catalogue and the observation that aftershock sequences are rarely observed in seismicity induced by hydraulic stimulations (e.g., Baisch and Harjes, 2003). One advantage of the Poisson log-likelihood and the Kolmogorov-Smirnov test is also that the metrics do not require binning of the point process (Dempsey and Suckale, 2017). Binning is used in the figures only for convenience to represent the data. The log-likelihood function is given by

$$\mathbb{P}(\theta|\{t_j\}) = \sum_{j=1}^{n} \log R(\theta; t_j) - \int_0^{t_n} R(\theta; t')dt', \tag{3.6}$$

where θ is the set of model parameters and t_j is the occurrence time of event $j = \{1, 2, ..., n\}$. We report the KS-statistic here, preferred to the log-likelihood which is sensitive to the choice of units for R, but we see good qualitative agreement between the two measures as summarized in Table 3.2. The KS-statistic for the convolution model returns 0.036. The quality of the fit is impressive considering the simplicity of the model – which involves only two parameters. It also contradicts the premise that various non-linear mechanisms driving induced seismicity, such as the non-linearity of rate-and-state friction, the Kaiser effect, and changes in permeability due to high pore pressure and the development of hydraulic fractures, should result in a nonlinear response overall. It may be that non-linear effects in Otaniemi are in fact small despite the relatively large stress variations induced by hydraulic stimulation, the possibility of which we explore with our physical models later on and in the appendix.

3.4 The Physical Model: Rate-and-State Friction and Finite Nucleation

We now present a physical model based on stress evolution from pore pressure diffusion and poroelasticity along with shear failure criterion following rate-and-state friction. The medium is treated to be infinite, homogeneous and isotropic. Neglecting the effect of the free surface is justified by the relatively large depth of the injections compared to the dimensions of the seismicity cloud (Figure 3.3). The induced stresses can then be calculated using the analytical solutions for a point source from Rudnicki (1986)

$$p(r,t) = \frac{q}{4\pi\rho_0 r}\frac{\eta}{k_{true}}\,\mathrm{erfc}\left(\frac{1}{2}\xi\right), \tag{3.7}$$

$$\sigma_{ij}(r,t) = -\frac{q(\lambda_u-\lambda)\mu}{4\pi\rho_0 c_{true} r\alpha(\lambda_u+2\mu)} \left\{\delta_{ij}\left[\mathrm{erfc}\left(\tfrac{1}{2}\xi\right) - 2\xi^{-2}f(\xi)\right] + \tfrac{x_i x_j}{r^2}\left[\mathrm{erfc}\left(\tfrac{1}{2}\xi\right) + 6\xi^{-2}f(\xi)\right]\right\}, \tag{3.8}$$

$$f(\xi) \quad = \mathrm{erf}(\tfrac{1}{2}\xi) - \tfrac{\xi}{\sqrt{\pi}}\exp(-\tfrac{1}{4}\xi^2),$$

$$\xi = \frac{r}{\sqrt{c_{true}t}},$$

$$c_{true} = \frac{k_{true}}{\eta}\frac{(\lambda_u-\lambda)(\lambda+2\mu)}{\alpha^2(\lambda_u+2\mu)},$$

where p and σ_{ij} are the pore pressure and stress tensor, and r and t the distance from injection source and time, respectively; $\lambda_u = 2\mu\nu_u/(1-2\nu_u)$ is the undrained Lamé parameter and the drained Lamé parameter without the subscript u; c is the hydraulic diffusivity which depends on permeability, k and viscosity, η. Here we add the subscript "true" to k and c to distinguish between the true and apparent values of the diffusivity, the notions of which are explored in greater detail by our following analysis. We assume the point source is a good approximation of the injections in Otaniemi given the length of the stimulated wells relative to the size

of the total stimulated volume. The model is nearly identical to that introduced by Segall and Lu (2015). Poroelastic properties which lack constraints from the field, along with a fixed fault-orientation are chosen as those in Segall and Lu (2015) to represent a general case. Ambient normal stress of 155 MPa is approximated using the average depth of the injection. All fixed parameters and their dimensions are listed in Table 3.1.

Stress changes become the input to the ODE formulation of Dieterich (1994), to solve for seismicity rate in space and time. The alternative integral formulation of Heimisson and Segall (2018) is used here as it is more tractable numerically for injection scenarios such as in Otaniemi that consist of abrupt onsets and shut-ins of injections

$$\frac{R}{r_b} = \frac{K(t)}{1 + \frac{1}{t_a}\int_0^t K(t')\,dt'}, \tag{3.9}$$

$$K(t) = \exp\left(\frac{\tau(t)}{a\overline{\sigma}(t)} - \frac{\tau_0}{\overline{\sigma}_0}\right),$$

$$t_a = \frac{a\overline{\sigma}_0}{\dot{\tau}_r},$$

$$\overline{\sigma} = \sigma - p,$$

where r_b is the background seismicity rate, $\dot{\tau}_r$ the background stressing rate, a the rate-and-state friction parameter, σ the normal stress, $\overline{\sigma}_0$ and τ_0 the initial effective normal and shear stress, and $\overline{\sigma}$ and τ the applied effective normal and shear stress, respectively. Synthetic catalogues are produced by sampling events from a non-homogeneous Poisson process using the acceptance-rejection method.

The Kaiser effect is inherent in the formulation of Dieterich (1994) and Heimisson and Segall (2018). This results from the fact that the nucleation process is delayed if the stress decreases and resumes once the stress gets back to its previous peak level. The Kaiser effect is clearly demonstrated if we use the model to compute the response of the seismicity rate to a sinusoidal stressing history (Appendix B.4). The different injection locations must stimulate new volumes of rock and lead to new hydraulic

pathways. So we might expect the Kaiser effect to be significant within a single stage but to be less relevant from one stage to the other. The impact of the Kaiser effect may be more appropriately represented by resetting the stressing history at the onset of each stage. To this effect, we start a new simulation with the same initial conditions and compound the results for the final catalogue. This model is hereafter referred to as the rate-and-state model. Note that the validity of resetting the stress history could be questioned given that the seismicity clouds during the different stages largely overlap (Figure 3.3) suggesting overlapping stimulated volumes.

We use the measured flow rates and pressure to estimate hydraulic diffusivity. An estimate of the diffusivity that fits the rate of pressure decay during injection pauses is made by the Horner analysis. Since the analytical solutions of the present model are derived for spherical flow in a 3-D medium, the conventional Horner analysis originally derived for 2-D flow into a vertically confined aquifer (Horne, 1995; Zimmerman, 2018) is adapted to be consistent with equations 4.7 and 4.8 . Details on the adaptation and fitting process are presented in Appendix B.2. The analysis gives a diffusivity of c_{horner} = 0.018 m^2/s, and a global fit to the entire pressure history using a Gaussian likelihood function gives an effective well radius and ambient pore pressure of 44m and 43.5MPa, respectively. The model fits the measured pressure history well during the entire stimulation, especially during the injection pauses (Figure 3.7a). A fit to the pressure history with diffusivity as a free parameter, however, gives a higher value of c_{bu} = 0.044 m^2/s (subscript 'bu' standing for "build-up") that better matches the rate of pressure build-up at the onset of injection cycles with an effective radius and ambient pore pressure of 31m and 54.9MPa, respectively (Figure 3.7b). c_{bu} also over predicts the rate of pressure decay during injection pauses. While constraints on the effective radius - a measure of the damage zone surrounding the well that causes pressure drops - are difficult to quantify, ambient pore pressure in either cases are close to its bounds considering the temperature-dependence of fluid density at injection depth. When comparing the theoretical triggering front derived by Shapiro, Huenges, and Borm (1997), i.e., $r = \sqrt{4\pi c_{tf} t}$ where c_{tf} is the diffusivity chosen to draw the triggering front, c_{horner} appears to fit the spatial extent of near-field events better (Figure 3.3). We therefore use $c_{horner} = c_{true}$ as a starting point for the models and refer to its theoretical triggering front as the 'reference triggering front.' We revise this assumption later and note that the diffusivity derived from the Horner analysis fits the pressure drop at shut-ins, as should be the case by design, but does not match the pressure build-up when injections start again.

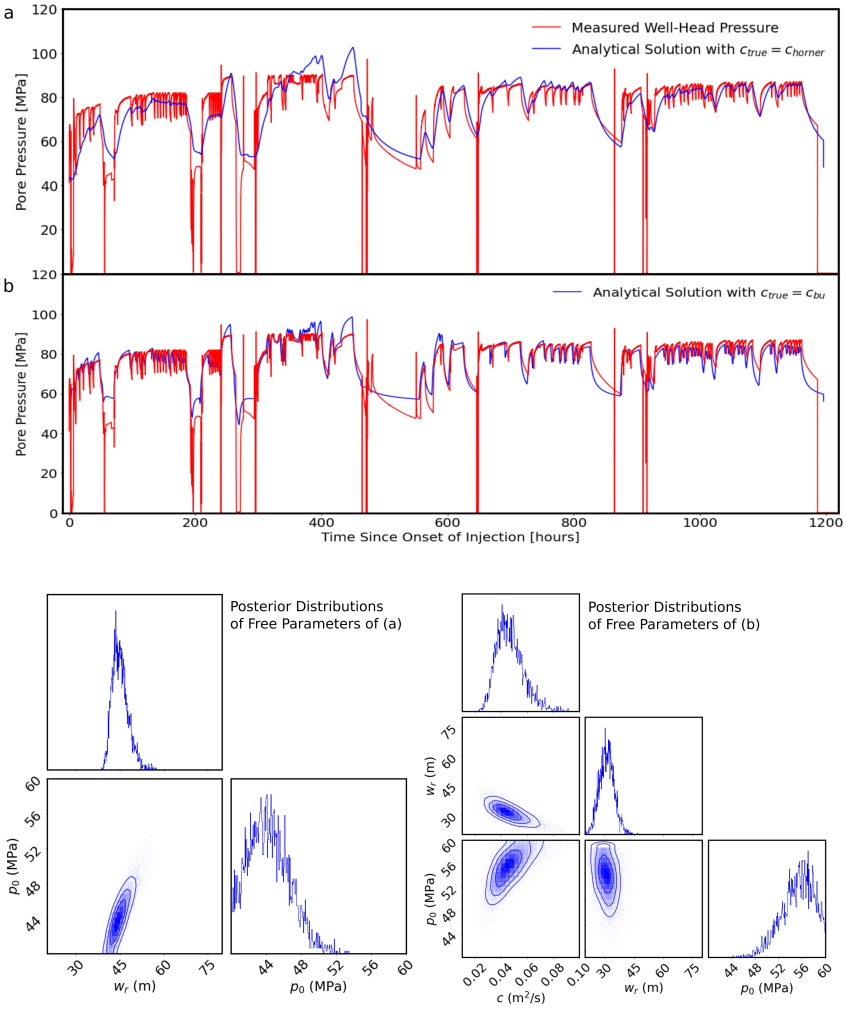

Figure 3.7: Well-Pressure Measurements and Modelled Fit. Observed well-pressure and the modelled fits are plotted in red and blue, respectively. The top fit corresponds to $c_{true} = c_{horner} = 0.018$ m^2/s, effective well radius, w_r, of 44m and ambient pore pressure, p_0, of 43.5 MPa while the bottom fit corresponds to $c_{true} = c_{bu} = 0.044$ m^2/s, $w_r = 31$m and $p_0 = 54.9$ MPa. The posterior distributions of w_r and p_0 for $c_{true} = c_{horner}$ are shown on the bottom-left and those for c_{bu}, w_r and p_0 are shown on the bottom-right. While both models provide a good global fit to the data, c_{horner} and c_{bu} tend to fit better either the drawdown of pressure during shut-ins or the build-up of pressure at injection onsets, respectively. The difference between the fits likely indicates the changing diffusivity of the injected medium with the injection pressure. Diffusivity increases at higher pressure due to the creation of fractures and hydraulic pathways and decreases at lower pressure due to fracture closure and healing.

The posterior distribution on the set of parameters associated to the seismicity model a, $\dot{\tau}_r$, and r_b is found using the affine invariant Markov chain Monte Carlo (MCMC)

Ensemble sampler of Goodman and Weare (2010) maximizing the log-likelihood given by Equation 3.6. In order to simplify the sampling process, the sampler computes the posterior of a and $\dot{\tau}_r$ given that r_b - which is a simple multiplicative factor to the normalized seismicity rate - is adjusted for each pair of a and $\dot{\tau}_r$ to match the total number of observed events (61,150 events). The sampler conducts $2000 \sim 5000$ iterations of 32 walkers with the chain length made to be longer 50 times the auto-correlation length in order to ensure full exploration of the posterior distribution. The prior is assumed to be uniform for both variables between the range of $10^{-5} \sim 10^{-2}$ and 0.1 kPa/yr. $\sim$ 5 kPa/yr. for a and $\dot{\tau}_r$, respectively, although the shape of the prior is seen to have little effect on the posterior given the large sample size.

$a, \dot{\tau}_r$, and r_b of maximum likelihood is found to be 0.0002, 3.05 kPa/yr. and 12.1 events/days, respectively, and the resulting model is shown in Figure 3.6b. The model follows the observations quite well in time, with a KS-statistic of 0.029, slightly lower than the value of 0.036 obtained with the convolution model. The model succeeds in reproducing the main temporal features of the observed catalogue: 1. direct correlation between the injection and seismicity rate and 2. Omori-law decay during shut-ins. In space, the fit is much less compelling (Figure 3.8b). The triggering front lags significantly behind the reference triggering front with a much smaller mean of the distribution. Yet in both time and space, resetting of the stress history at each injection stage turns out to be essential in reproducing important features of the observation. The best fit using the model without resetting of the stress history (a = 0.0001, $\dot{\tau}_r$ = 4.89 kPa/year, and r_b = 25.9 events/day) as shown in Figure 3.6c has relatively minimal seismicity rate during the second half of the injection history due to the Kaiser effect. In space, it is completely devoid of any seismicity close to the injection well during this period (Figure 3.8c). Far-field seismicity much beyond the reference triggering front is largely attributed to background stressing as poroelastic stress perturbations are small relative to pore pressure changes.

3.5 Inference of Diffusivity from Spatio-temporal Distribution of Seismicity Accounting for Finite Nucleation

Given that the rate-and-state model fails to match the observations in space assuming the diffusivity inferred from Horner analysis, we now examine the possible under-estimation of the diffusivity by the Horner analysis. Following the seminal study of Shapiro, Huenges, and Borm (1997), it has become common practice to infer the

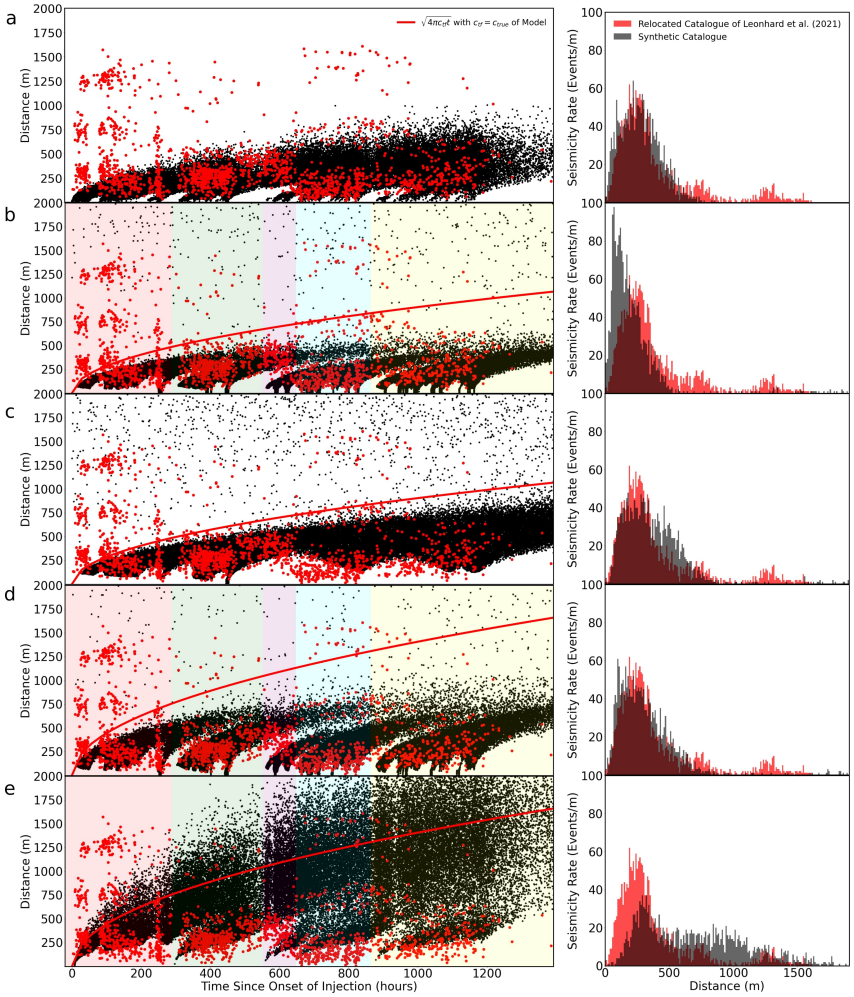

Figure 3.8: Model Predictions in Space. The synthetic catalogue is plotted as black dots in space and time with the relocated catalogue of Leonhardt et al. (2020) superposed as red dots. The red curve outlines $\sqrt{4\pi c_{tf} t}$ with $c_{tf} = c_{true}$ for each model. Histograms of the observed event distribution in space is plotted in red along with randomly sampled distributions of the synthetic catalogues in black. (a) The extension of the convolution model to space gives a good fit. (b) The rate-and-state model with $c_{true} = c_{horner}$ underpredicts the mean distance substantially. (c) Rate-and-state model without resetting of stress history shows manifestations of the Kaiser effect from large regions of seismic quiescence in stress shadows near the injection source. (d) The fit to space in the rate-and-state model is significantly improved with $c_{true} = c_{bu}$. (e) The Threshold Coulomb model with $c_{true} = c_{bu}$ significantly overpredicts the distribution of seismicity in space as does the theoretical triggering front for $c_{tf} = c_{bu}$, suggesting that the role of delayed nucleation on seismicity migration is essential in reproducing the observed spatio-temporal evolution of seismicity in Otaniemi given the likely diffusivities. Model parameters and goodness-of-fit metrics are summarized in Table 3.2.

diffusivity from fitting $r = \sqrt{4\pi c_{tf} t}$ to the propagation of the seismicity front, or the triggering front - defined by the outline of the outermost events of the seismicity cloud extending from the well. However, we note that c_{tf} of the rate-and-state model shows a significant mismatch by a factor of ~3 from $c_{true} = c_{horner}$ prescribed in the model (Figure 8b). This discrepancy is due to the role of delayed nucleation represented by $a\sigma$. As shown by Wenzel (2017), the parameter $a\sigma$ of the rate-and-state model acts as a threshold triggering stress that restricts the extent of the triggering front. The sensitivity of the triggering front to $a\sigma$ is clearly visible in Figure 3.9 which compares two synthetic catalogues that only differ in the prescribed values of a. In the scope of the rate-and-state model or stress thresholds as commonly used in Mohr-Coulomb models, inference of the diffusivity from the apparent migration of seismicity requires considerations of both c and a. Additionally, the method of inferring the diffusivity from the triggering front may depend on the earthquake detection thresholds. A higher detection threshold may give a more poorly resolved catalogue in space that could lead to a different estimation of the triggering front. Furthermore, the position of the triggering front can be obscured even more by background seismicity and far-field events triggered by poroelastic effects. Fitting the seismicity front represented by the envelope of the seismicity cloud, places a lot of weight on potentially biased and not particularly well-defined features.

In consideration of such complications, one would wish for a definition of the seismicity front that is independent of the number of events in the catalogue and robust to factors of discrepancy between observations and model predictions. We therefore propose an approach to infer c_{true} from the spatial distribution of the seismicity as opposed to the triggering front. A simple way is to fit the distribution as a function of distance and time from the point of injection with a known analytical expression. We recall that the half-norm distribution is the solution to the diffusion equation in response to a Dirac point source in a 3-D medium where the standard deviation of the distribution, $\Lambda(t)$, is a function of time such that

$$f_Y(y; \Lambda(t)) = \frac{\sqrt{2}}{\Lambda(t)\sqrt{\pi}} \exp\left(- \frac{y^2}{2\Lambda(t)^2} \right) \quad , \quad y \geq 0. \tag{3.10}$$

This inspires our approach to fit Equation 3.10 to the rate-and-state model in response to a constant injection scenario. The half-norm distribution indeed turns out to provide a relatively good fit (Figure 3.10); it matches well the bulk of the distribution but tends to slightly overestimate seismicity rate at larger distances. Indeed, we do not make the claim that the half-norm distribution is the best possible fit and

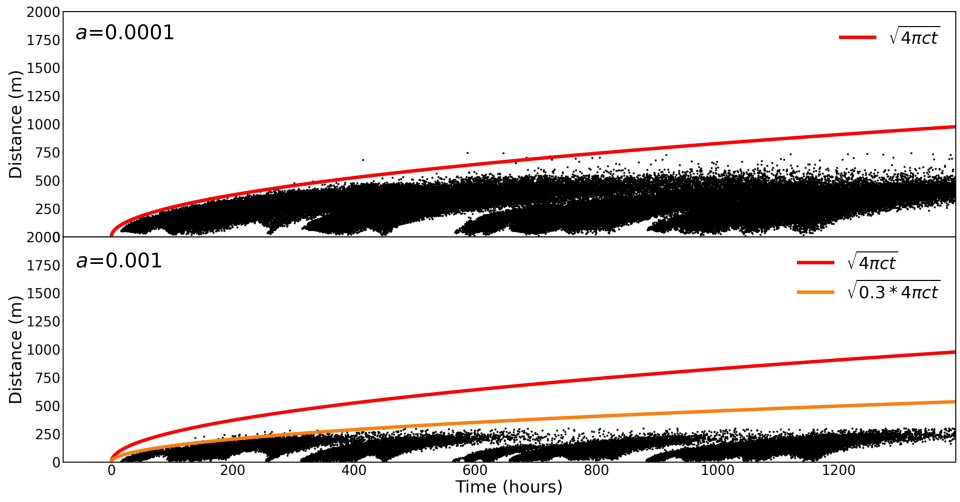

Figure 3.9: Sensitivity of Triggering Front to Delayed Nucleation. Synthetic catalogues for two parameter sets only differing in a (0.0001 and 0.001 in top and bottom, respectively) are shown. Lower a, which translates to lower $a\sigma$, results in a further extent of the triggering front, due to the role of delayed nucleation that acts proportionally to a threshold stress for the triggering of events as explained in detail by Wenzel (2017). Along with the reference triggering front in red, an additional $\sqrt{4\pi c_{tf} t}$ curve is drawn in orange for $a = 0.001$, with c_{tf} modified by a factor of 0.3 that better matches the apparent triggering front. The effect of the finite nucleation process on the spatial pattern of seismicity implies that neglecting rate-and-state effects can significantly bias the inference of diffusivity from the triggering front.

acknowledge there may be other distributions that could better match the rate-and-state model although they are not explored further here. Furthermore, plotting the evolution of Λ versus time reveals that it follows closely $\sqrt{c_{true} t}$. We make the assumption that the remaining discrepancy can be modelled as a multiplicative factor such that

$$\Lambda(t) = \sqrt{c_{hg} t} = \sqrt{\gamma(\{l\}) c_{true} t}, \tag{3.11}$$

where $\{l\}$ is a set of non-dimensional parameters. Thus, c_{hg} is a measure of the radial spreading of the seismicity relative to the point of injection ('hg' standing for half-Gaussian distribution). In order to apply this method to Otaniemi, we attempt to estimate c_{hg} from the relocated catalogue. One disadvantage of the method is that it requires a set of relocated events large enough to constrain the evolution of c_{hg} with confidence. As detailed in appendix B.5, we can indirectly estimate from the cumulative relocated catalogue giving $c_{hg} = 0.011$ m^2/s.

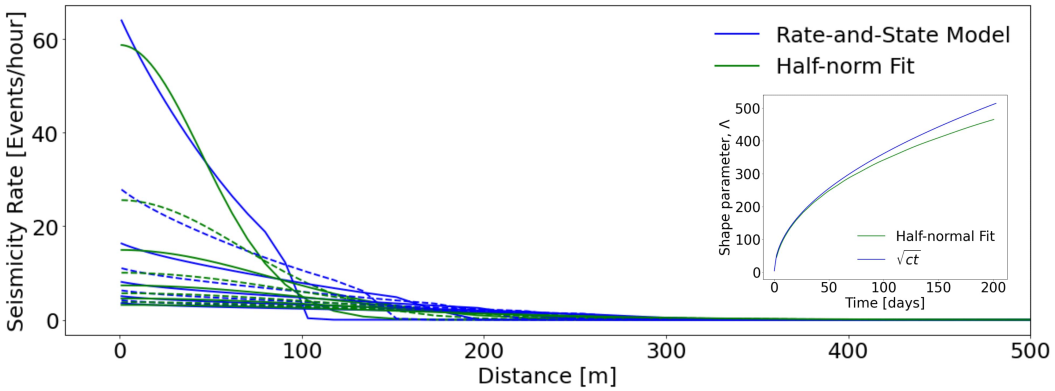

Figure 3.10: Evolution of Spatial Distribution of Seismicity for Rate-and-State Model. Spatial profiles of the seismicity rate are plotted in blue at various times for the rate-and-state model in response to a single boxcar injection. Half-norm distributions, in green, are used to fit the model-generated distribution. The line style alternates between solid and dashed between each time step for clarity. The half-norm distributions evolve with a time-dependent shape parameter, $\Lambda(t)$, which closely follows $\sqrt{c_{true}t}$ as shown in the inset of the top figure. The half-norm approximation of the spatial evolution of seismicity in the physical model can serve as the spatial component to the convolution model.

We find the relationship $\gamma_h(l)$ empirically by observing the systematic dependence of γ_h on l as reproduced by the rate-and-state model. We assume l depends not only on pore fluid transport properties but also rate-and-state properties such as a. We find to be relevant the ratio $l = a\sigma/p_q$, where $p_q = \frac{q\eta}{4\pi\rho_0 kL}$ is the characteristic pore pressure for given injection rate q, and L is the size of the computational domain. Higher values of $a\sigma$ would produce a stronger threshold effect and suppress seismicity migration, the extent of which would depend on its strength relative to the induced pressure, p_q. A series of single boxcar injections are simulated for a range of c and a. We find a rational function of $a\sigma/p_q$ that fits γ_h as shown in Figure 3.11. Although the reason for the exact functional form of the relationship is not obvious, the quality of the fit is compelling. The observed trend is also consistent with the known role of $a\sigma$: higher values of a suppresses seismicity at further distances, decreasing c_{hg} and consequentially γ_h. The functional fit allows new uncertainty estimates of the diffusivity in Otaniemi. Figure 3.11 shows the difference between the predicted and true values of diffusivity for a range of c_{true} and a, given the estimated value of $c_{hg} = 0.011$ m^2/s and an injection rate, $q =$ 10L/min. Although this is a much lower injection rate than the average in Otaniemi there are also significant differences between the idealized boxcar injections used to

produce Figure 11 and the much more complex schedule in Otaniemi. One can see that accounting for the role of delayed nucleation significantly widens the possible range of diffusivity in Otaniemi. Namely, the functional fit considers equally likely much higher values of c_{true} than would be predicted by the triggering front observed in Otaniemi given sufficient rate-and-state effects.

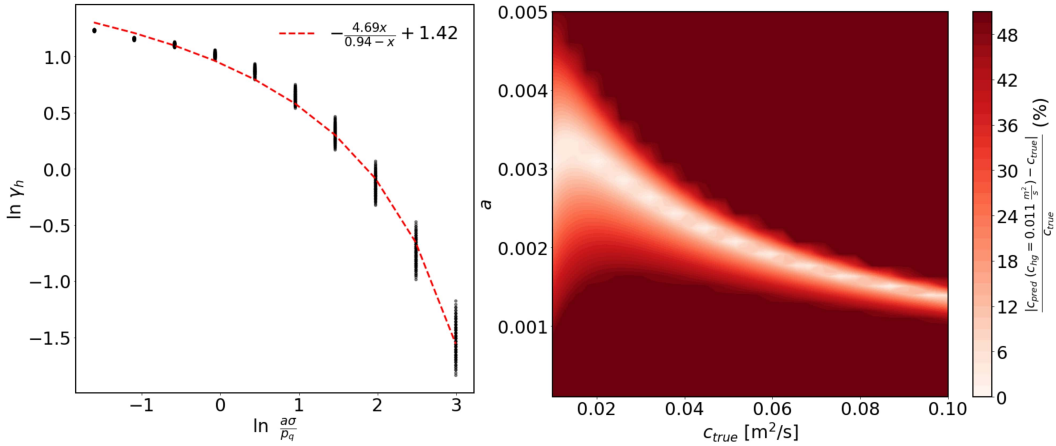

Figure 3.11: Inference of Diffusivity Accounting for Role of Delayed Nucleation on Seismicity Migration. An empirical relationship for the multiplicative factor, γ_h, of $\Lambda(t) = \sqrt{\gamma_h c_{true} t}$ is found in terms of the non-dimensional ratio $a\sigma/p_q$ (left). The fit can be used to infer new uncertainty estimates on the diffusivity of the medium given apparent spreading of the radial distribution of the seismicity in Otaniemi, i.e., $c_{hg} = 0.011$ m^2/s. Contour plot on the right shows the percent difference between the true diffusivity and the predicted diffusivity from the functional fit $\gamma_h(a\sigma/p_q)$ for a range of a and c_{true}. Considerations of the role of delayed nucleation on seismicity migration makes higher diffusivities more likely than previously considering solely the theoretical triggering front of Shapiro, Huenges, and Borm (1997).

In light of this finding, we test the possibility that $c_{bu} = 0.044$ m^2/s is in fact closer to c_{true} in Otaniemi than c_{horner} as the inconsistency between the triggering front using $c_{bu} = c_{tf}$ and the relocated catalogue are borne due to rate-and-state effects. We test this hypothesis by finding the best fit of the rate-and-state model using $c_{bu} = c_{true}$. The effective radius and ambient pore pressure are adjusted to 31.1m and 54.9MPa, respectively, to best fit the well pressure measurements. The resulting fit for the seismicity rate in time is shown in Figure 3.6d, and the corresponding synthetic catalogue in space is shown in Figure 3.8d. a, $\dot{\tau}_r$, and r_b are found to be 0.00006, 1.29 kPa/yr and 4.7 events/day, respectively. The fit in time bears no significant improvement from the fit using $c_{horner} = c_{true}$, although the KS-statistic is slightly lower at 0.025. The fit in space is much improved with a higher mean of the

distribution and cluster of events that encompasses greater portions of the relocated catalogue. One region the model performs rather poorly on is capturing the the back-propagation front starting around the 500-hour mark. It's possible that the back-propagation fronts, whose occurrence in time would correspond to the drawdown periods used for the Horner analysis, is still governed by the lower diffusivity c_{horner}. It could be that the back-propagation consists of two separate migration patterns, based on the observation that the initial portions of the back-propagation front are predicted quite well by the model (starting at around the 450-hour mark). This could be due to a propagation of the seismicity governed by different mechanisms than pore pressure diffusion, such as stress transfer by aseismic slip (Dublanchet and De Barros, 2021), although it is difficult to constrain the exact mechanism of seismicity migration given their possibly similar characteristics ($r \sim \sqrt{t}$).

The differences between c_{bu} and c_{horner} may be indications of distinct hydraulic processes that govern the well-head pressure and the spatial distribution of seismicity. One could imagine that the well-head pressure is more representative of the diffusivity of the medium immediately surrounding the well. On the other hand, the spatial distribution of seismicity may be more dependent on the path of highest hydraulic conductivity within the entire stimulated volume. The abrupt cessation of seismic activity close to the injection well following shut-in could be associated to a decrease in the diffusivity due to fracture healing, leading to the lower estimate of c_{horner}. It is also important to note that the two diffusivities require different values of a, $\dot{\tau}_r$, and r_b, such that their independent measurements would provide stricter constraints on c_{true}. We see that the higher estimate c_{bu} inferred from this analysis yields synthetic catalogues in better agreement with the observed seismicity in time and space. We conclude using the triggering front to infer the diffusivity may yield a significantly biased estimate if the effect of earthquake nucleation is ignored.

3.6 Incorporation of a Spatial Component to the Convolution Kernel

We now use the physical model as a basis to extend the temporal convolution model to space. We look for a new kernel with spatial dependence such that the convolution is as follows

$$R(t,x) = u(t) * g(t,x) = \int_{-\infty}^{\infty} u(\tau) g(t-\tau, x)\, d\tau. \tag{3.12}$$

The spatial component of the kernel is constructed by using the half-norm distribution, as identified in Section 3.6, with a shape parameter increasing as $\sqrt{c_{hg} t}$.

Combining with the Omori law as the temporal component as previously gives the integral of the kernel

$$\int_{-\infty}^{t} g(r,t')\ dt' = \frac{\sqrt{2}}{\sqrt{\pi c_{hg} t}} \exp\Big(-\frac{r^2}{2c_{hg}t}\Big) \cdot \Big(\frac{R_0}{1+t/t_r}\Big), \tag{3.13}$$

which is differentiated in time to obtain the response to Dirac forcing

$$g(r,t) = \frac{\sqrt{2}}{2\sqrt{\pi}t(c_{hg}t)^{3/2}} \exp\Big(-\frac{r^2}{2c_{hg}t}\Big) \cdot \frac{(-2c_{hg}t^2 - c_{hg}t(t+t_r) + r^2(t+t_r))R_0}{t_r(1+\frac{t}{t_r})^2}. \tag{3.14}$$

The three parameters of the model are c_{hg} = 0.011 m^2/s, R_0 = 213.5 events/hr., and t_r = 28.5 hours, as estimated from the data. The fit to the temporal evolution of seismicity is, by design, identical to the fit obtained with the kernel in time introduced earlier (Figure 3.6a). The model provides now in addition a good match to the observations in space, especially with regards to the triggering and back-propagation fronts (Figure 3.8a). Overall, the convolution method approximates the physical model and fit the observations quite well, albeit with a drastically shorter computing time — by at least an order of magnitude — thanks to the use of the fast Fourier transform (the convolution is transformed into a simple product in the Fourier domain).

3.7 Comparison of Physical Models Based on Finite and Instantaneous Nucleation

Both rate-and-state and Mohr-Coulomb models are widely used in modelling induced seismicity. The standard Coulomb model assumes a population of faults with a uniform distribution of initial stress up to the maximum shear stress allowed by static friction (e.g., Ader et al., 2014). We show in appendix B.6 that this simplest version of the Coulomb model does not fit the observations neither in time nor in space. A number of studies which have tested the applicability of the Coulomb model to induced seismicity found it necessary to introduce a stress threshold that needs to be exceeded for earthquake triggering (e.g., Bourne, Oates, and Van Elk, 2018; Dempsey and Riffault, 2019; Dempsey and Suckale, 2017; Langenbruch and Shapiro, 2010). The physical justification for the inclusion of the threshold, hereafter referred to as C_{cpt}, is to account for the population of faults activated during the stimulation that were initially in a relaxed state of stress, not close to failure. In this

case, triggering would be delayed due to their initial strength excess rather than due to the nucleation process. The explanation is probably relevant in stable tectonic areas (e.g., Bourne, Oates, and Van Elk, 2018; Dempsey and Riffault, 2019; Dempsey and Suckale, 2017; Langenbruch and Shapiro, 2010). Wenzel, 2017 demonstrates the response of the Dieterich, 1994 rate-and-state model, which assumes a population of faults above steady-state (initially already on their way to failure), can be approximated with such a threshold Coulomb model due to the tendency of $a\sigma$ to act as a stress threshold. On the other end, the application of the rate-and-state model to a population of faults below the steady-state regime also results in introducing a threshold in the rate-and-state model as well (Heimisson et al., 2022), accounting for the population of earthquake sources that are initially far from instability which is assumed negligible by Dieterich (1994). In this case, the question remains whether C_{cpt} is indeed solely representing the initial stress state, or rather acting as a proxy variable that also encompasses effects of time-dependent nucleation.

To address these questions, we consider a Coulomb model with a stress threshold representing the initial strength excess on the triggered faults. The Coulomb model is formulated as follows

$$R(t) = \frac{1}{\alpha_c} \int_V f_c\Big(p(r,t)\Big) \cdot \frac{\partial p}{\partial t}(r,t)\, dV, \tag{3.15}$$

$$\frac{\partial p}{\partial t}(r,t) = \frac{q(\lambda_u - \lambda)(\lambda + 2\mu)}{8\pi^{\frac{3}{2}}\rho_0 r^3 \alpha^2 (\lambda_u + 2\mu)} \xi^3 \exp\left(-\frac{1}{4}\xi^2\right), \tag{3.16}$$

where V is the representative volume over which seismicity is recorded, α_c is a scaling factor defined as the change in pore pressure per slip event per unit volume (Nur and Booker, 1972), and f_c is the probability density function representing the distribution of threshold triggering pressure needed for the Coulomb stress change to exceed the initial strength excess. Following the observation that poroelastic stress changes are minimal compared to pore pressure changes, they are ignored hereafter for simplicity. The derivation of Equation 3.16, which is the time derivative of Equation 3.7, is given in Appendix A of Segall and Lu (2015). The integral is restricted to where stress changes are positive, and to account for the Kaiser effect, the integral is further limited to where the past maximum pore pressure has been exceeded. Following Bourne, Oates, and Van Elk (2018) and Smith et al. (2020), we next assume a population of faults with randomly distributed strength excess using a formulation that has been found to provide a good model of seismicity induced by gas

extraction from the Groningen gas field. Seismicity starts once the Coulomb stress change exceeds the lowest value of the initial strength distribution. According to the extreme value theory, the tail of the distribution can be represented by a Generalized Pareto distribution, leading to an exponential increase of seismicity for a constant loading rate (Bourne, Oates, and Van Elk, 2018). This general formulation is valid to simulate the onset of seismicity but it does not allow the transition to a steady state regime where seismicity rate would be proportional to the loading rate. We therefore assume a Gaussian distribution of initial strength to allow for the transition to steady-state (Smith et al., 2020), and express it in term of the distribution of threshold pressure

$$f_c(p) = \frac{1}{\phi_2\sqrt{2\pi}} \exp\left(-\frac{1}{2}\left(\frac{p-\phi_1}{\phi_2}\right)^2 \right), \tag{3.17}$$

where ϕ_1 and ϕ_2 are the mean and standard deviation of the distribution, respectively. The best fitting model is found with respect to ϕ_1 and ϕ_2 within the range of 0.01 $\sim$ 5 MPa for both parameters. α_c is adjusted to match the total number of events, much like r_b of the rate-and-state model. This model is hereafter referred to as the Threshold Coulomb model.

The model fit in time and space are shown in Figure 3.6e and 3.8e, respectively, with ϕ_1 = 0.66 MPa, ϕ_2 = 0.28 MPa, and α_c = 14.3 kPa/event $\cdot$ m^3. The model fits the observations well in time, with a KS-statistic of 0.029 but significantly overestimates the extent of seismicity in space, which was also a main issue with the standard Coulomb failure mode (Appendix B.6). The model is also less sensitive to rapid variations of the injection rate compared to the rate-and-state models, with relatively muted changes in the seismicity rate in-between injection cycles. Such sensitivity is seen to grow with the time scale of stressing rates; Figure 3.12 shows the response of the both the Coulomb and rate-and-state models with the duration of injections and pauses multiplied by factors of 0.1 and 10 (parameters are fixed to those that produced figures 6d&e). While both models show more rapid variations of the seismicity rate relative to the injection rate for longer injection duration, the tendency is significantly greater in the Threshold Coulomb model. For longer injection duration, the models show rather good agreement between each other although the Threshold Coulomb model predicts lower t_r with increasing time. Similar sensitivities may be observed with respect to the choice of ϕ_1. While both the Coulomb and rate-and-state models may provide sufficient hindcasting tools

for the same observation, the calibrated models produce very different forecasts for injection scenarios with duration of injection different from those used for calibration. In addition, they may produce different predictions in space for similar predictions in time. The comparisons suggest that the stress state with respect to failure and nucleation effects must be modelled separately, as done for example in the threshold rate-and-state model of Heimisson et al. (2022), especially for fast injection cycles commonly employed in EGS operations where the effect of delayed nucleation may not be appropriately represented by the inclusion of a stress threshold in Coulomb models.

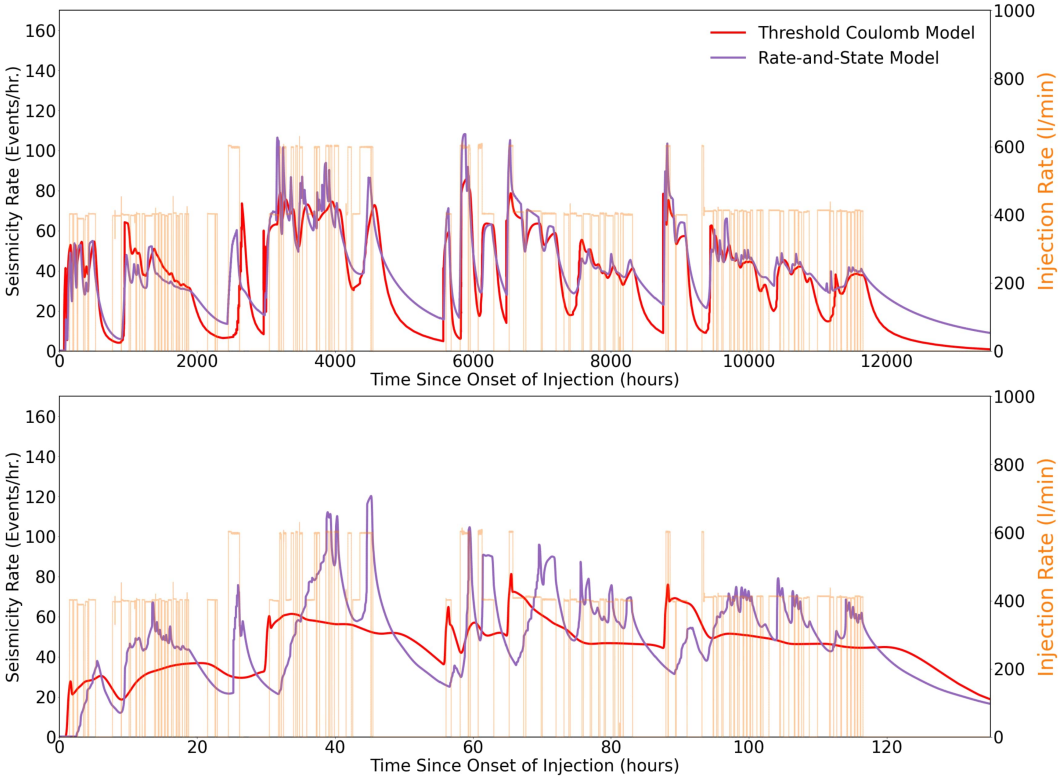

Figure 3.12: Comparison of Rate-and-State and Threshold Coulomb Model For Varying Time Scale of Injections. The rate-and-state and coulomb models that produced best fitting predictions of Figure 3.6d&e, respectively, are compared in their response to the injection scenario of Otaniemi with injection durations lengthened (top) and shortened (bottom) by 10 times. The injection rate is shown in light orange. The Threshold Coulomb model shows significant disagreement with the rate-and-state model for shorter injections, illustrating the differences in modelling the stress state with respect to failure and delayed nucleation at shorter time scales.

We remark that our modeling allows estimation of the best fitting values of a to between 0.00006 and 0.0002, which is significantly lower than the values inferred

from laboratory measurements, generally ranging between 0.01 and 0.001 (Marone, 1998). Yet, the importance of rate-and-state effects in matching the observations in both space and time suggest that even such low values do not yield, for the injection schedule studied here, the rate-independent behavior that could be matched with a Threshold Coulomb model. The reconciliation of field-inferred values of $a\sigma$ and laboratory measurements is still paramount for eventual application of such models towards seismicity forecasting. One possible explanation is that spatial heterogeneities lead to elastic interactions that produce globally inferred values lower than that in a homogeneous equivalent (Dublanchet, Bernard, and Favreau, 2013). It is also important to note that the model of Dieterich (1994) is a rather limited representation of the full complexity of rate-and-state friction. For example, the model simulates a population of spring-slider nucleation sources, whose qualitative differences in their behavior to more realistic finite fault models have been displayed for numerous aspects of rupture characteristics. Additionally, the model neglects the effect of variable effective normal stress on nucleation size, as the number of active nucleation sources remains constant throughout (Alghannam and Juanes, 2020). Further development of the model with a more holistic representation of rate-and-state friction would prove valuable for induced seismicity forecasting.

3.8 Mechanical Origin of Omori-Law Decay Following Shut-Ins

The rate-and-state model reveals that the post shut-in Omori-law decay at Otaniemi depends strongly on the stress relaxation process by pore-fluid diffusion and cannot be explained solely by nucleation effects. The dependence on both nucleation and stress relaxation can be demonstrated by a sensitivity analysis of the relaxation timescale of the Omori law, t_r, to parameters a, the rate-and-state friction parameter and k, the permeability. We find the most direct relationship to be that between the ratios of t_r and the characteristic diffusion time, $t_c = \frac{L^2}{c}$, to t_a as shown in Figure 3.13 where t_r is measured by fitting the Omori law to shut-ins following single boxcar injections under the rate-and-state model. Thus, t_r is more strongly dependent on t_c. The positive relationship t_r and t_c follows the intuitive reasoning that higher diffusivity would result in more rapid relaxation of induced pressure and consequently a faster decay of the seismicity rate. Our observations are consistent with the suggestion that the empirical Omori-law would be a result of stress relaxation by pore pressure diffusion (Almakari et al., 2019; Langenbruch and Shapiro, 2010; Miller, 2013). This explanation seems certainly reasonable in the context of EGS stimulations where pore pressure variations are particularly large.

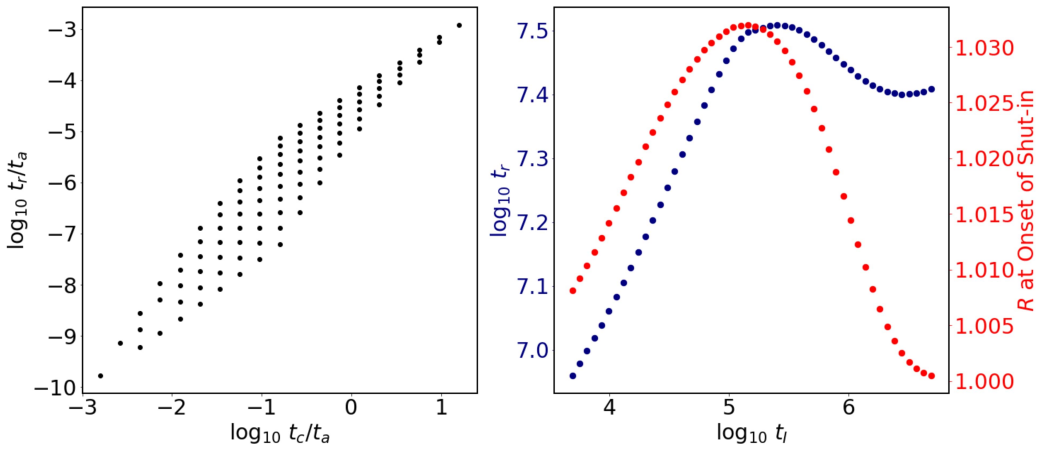

Figure 3.13: Dependence of Omori Law Decay on Fluid Transport Properties. t_r of Omori Law Decay in response to single boxcar injections under the rate-and-state model are plotted in terms of t_c and t_a (left). t_r, shows a stronger dependence on t_c, or the diffusivity, than on t_a. Namely, longer diffusion times result in longer relaxation times of the seismicity rate. t_r also shows strong dependence on injection duration, t_I (right). t_r first increases with increasing seismicity rate at time of shut-in, before decreasing as steady-state stress conditions are reached when the seismicity rate decreases as well due to the Kaiser effect. The strong dependence of the Omori decay in the physical model to transport properties suggests that the observed decay pattern in Otaneimi can be sufficiently explained by the diffusion of pressure, with negligible effects from finite nucleation.

The dependence on stress relaxation implies that t_r also depends on injection duration (Figure 13). where the sensitivity analysis is performed with a and k fixed at 0.001 and 10^{-16} m^2, respectively, while the injection duration varies between factors of 0.1 to 100 of t_c. The plot shows a non-linear relationship between t_r and the injection duration, t_I, with an initial increase followed by a decrease. The trend exhibits a strong correlation with the seismicity rate at the time of shut-in. For shorter injections, the seismicity rate continuously increases prior to shut-in, increasing the time to relax to background levels. This is until the seismicity rate begins to decrease for continued injection, as pore pressure reaches steady-state conditions, and further nucleation is suppressed by the Kaiser effect. Consequently, t_r decreases as well, as it takes less time to relax the lower seismicity rate. A similar effect arises due to the finiteness of the computational domain — the further distances where the seismicity rate would continue to increase at later times are cut-off. The sensitivity of t_r to the total injected volume is consistent with the observation that the Omori law relaxation time at shut-in increases with time during the EGS stimulation at Otaniemi (Avouac et al., 2020).

3.9 Presence of the Kaiser Effect in Otaniemi

We have seen that the fit to the temporal evolution of seismicity is improved when the Kaiser effect is reset at each new stimulation stage. Although the clouds of seismicity generated during each stimulation stage overlap largely (Figure 3.3), this reset is justified as each new stage implied the stimulation of a new volume near the wellbore. Without such an adaptation, the seismicity rate is predicted to significantly lower during the second half of the injection history (Figure 3.6c) along with large regions of seismic quiescence near the injection well (Figure 3.8c). This also implies that the efficacy of the convolution model — which does not account for the Kaiser effect at all — depends strongly on the apparent absence of the Kaiser effect in Otaniemi.

The physical mechanism behind the activation of new volumes is unclear given the diffuse and rather random structure of the relocated catalogue (Figure 3.6). If this argument is dismissed based on relocation uncertainties, one could pose that a low diffusivity stimulated non-overlapping volumes from one stage to the other. However, such a low diffusivity should manifest in inconsistencies with the observed catalogue in time, for instance a longer apparent relaxation time during shut-ins. Rather, the need to reset the stressing history for the models to reproduce the observations in Otaniemi more likely implies the creation of new hydraulic pathways due to the fracturing nature of the stimulation that activated new nucleation sources (Cladouhos et al., 2016). Such phenomenon would depend on both the physical properties of the injected medium such as its fluid transport properties and fracture toughness, and the injection scenario, especially any spatial variation of the injection location.

3.10 Demonstration of Forecasting Capability of the Models through Pseudo-Forecasting

The models so far have only been applied in a hindcasting sense such that the data has been used in its entirety in order to tune the model parameters. We test the ability of the models to truly forecast induced seismicity in Otaniemi by limiting the range of the data used for training the models. Forecasts from the best fitting physical model (rate-and-state model with $c_{true} = c_{bu}$ - Figure 3.6d & 3.8d) and the spatio-temporal convolution model are shown in Figure 3.14 & 3.15, respectively. The rate-and-state model is able to produce a forecast comparable to the hindcast using just the first injection stage as the training period with a similar value of $a = 0.00005$ although with significantly lower $\dot{\tau}_r = 0.1$kPa/year and $r_b = 0.39$ events/day.

With the same training period, the convolution model performs rather poorly, largely due to the estimation of t_r at the end of first injection stage substantially lower (2.9 hours) than the average value throughout the entire injection schedule. The forecast is significantly improved by including the second injection stage within the training period, which now consists of the Omori decay observed during the injection pause at around the 450-hour mark that significantly increases the estimated value of t_r to 10.4 hours.

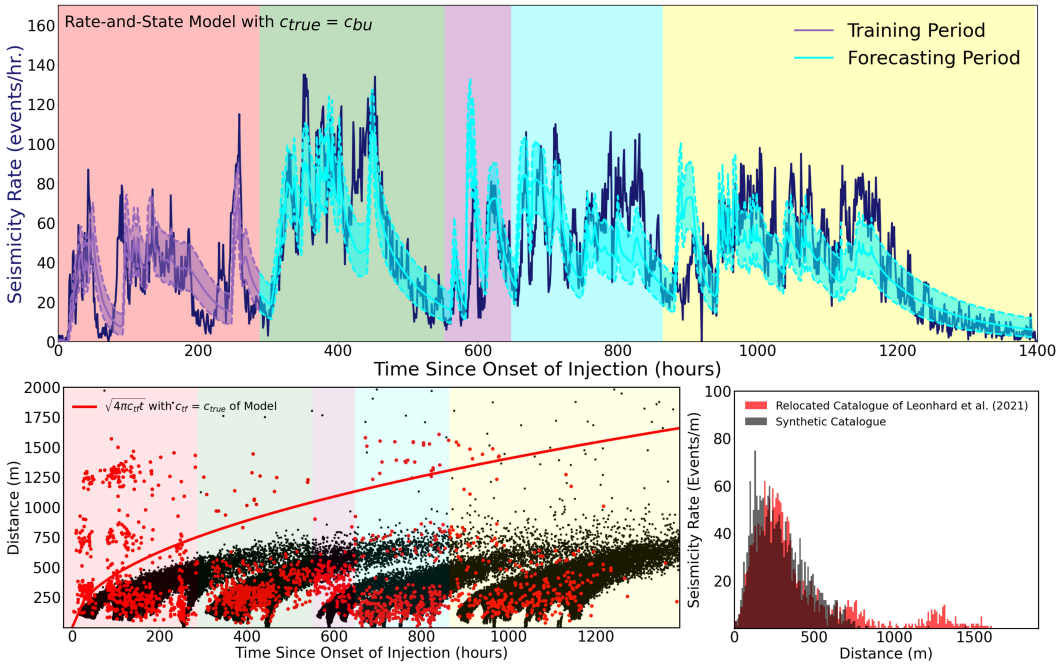

Figure 3.14: Partial Forecasting of Induced Seismicity by Physical Model. Ability of the physical model to forecast induced seismicity is tested by limiting the portion of the data used for model tuning. The rate-and-state model with $c_{true} = c_{bu} = 0.044$ m^2/s is trained using only the first injection stage. The training results in a, $\dot{\tau}_r$, and r_b of 0.00005, 0.1kPa/year, and 0.39 events/day. The pseudo-forecast is comparable to the hindcast of Figure 6d & 8d, with only a marginally higher KS-statistic of 0.040 and lower log-likelihood of 169,076, demonstrating the capability of the physical model to truly forecast seismicity.

It is likely that the rate-and-state model is more robust to the length of the training period than the convolution model due the fact that c_{true} is fixed at c_{bu} which matches the pressure history of Otaniemi in its entirety (Figure 3.7b). As discussed in Section 3.8, diffusivity plays a significantly stronger role in governing the rate of Omori decay than the tuning parameters of the rate-and-state model, namely a and $\dot{\tau}_r$. Thus, the rate-and-state model seems suited to perform well in forecasting applications given an accurate estimation of the diffusivity. Forecasts from the

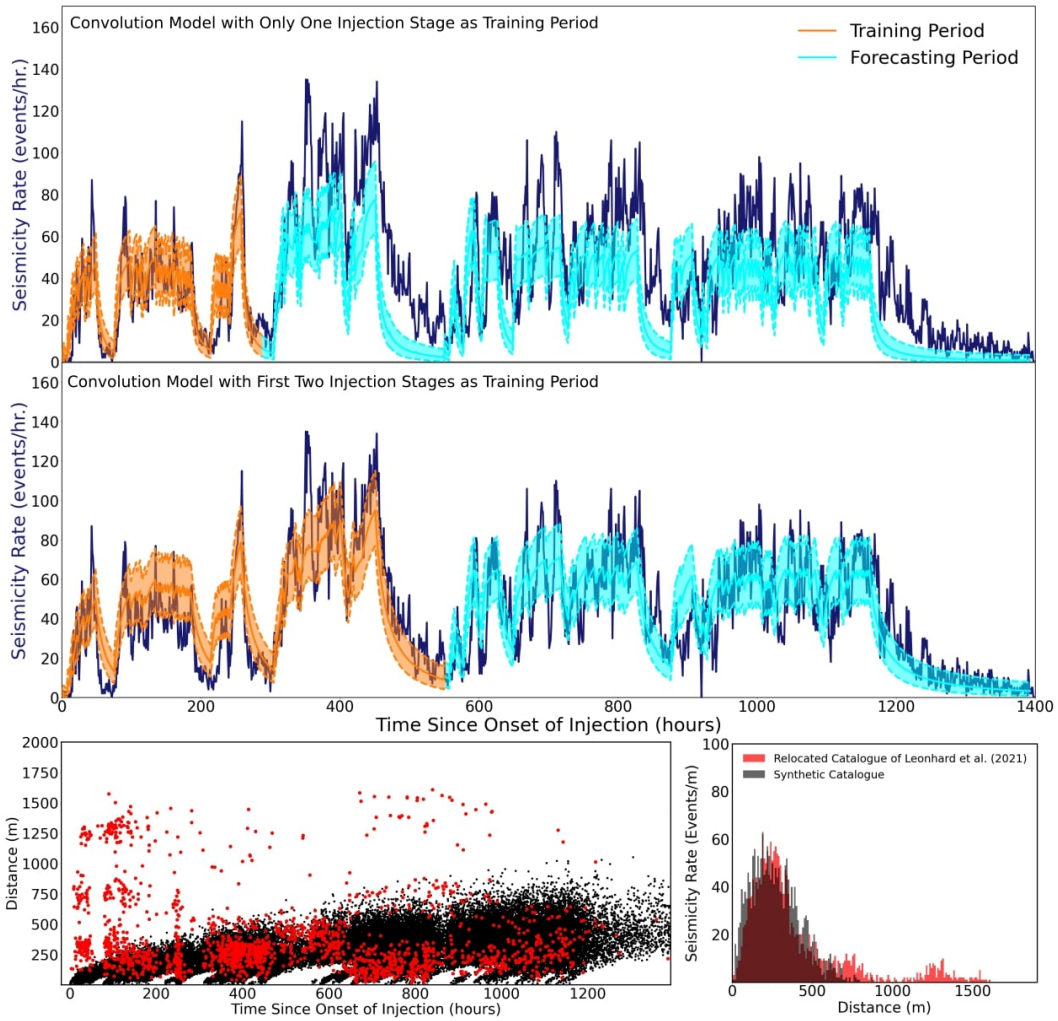

Figure 3.15: Partial Forecasting of Induced Seismicity by Convolution Model. Ability of the convolution model to forecast induced seismicity is tested by limiting the portion of the data used for model tuning. The top two rows compare forecasts using the first one and two injection stages as training periods where t_r is estimated to be 2.9 and 10.4 hours, respectively. The forecast using solely the first injection stage as the training period significantly underestimates t_r and underpredicts the seismicity rate for the rest of the injection history. The forecast using the first two injection stages as the training period is comparable to the hindcast of Figure 3.6a & 3.8a, with only a marginally higher KS-statistic of 0.047 and lower log-likelihood of 175,430.

convolution model could also be improved by accounting for the increase in t_r with cumulative injected volume as observed in Otaniemi (Avouac et al., 2020).

3.11 Conclusion

Physical models based on rate-and-state friction and stress changes due to pore-pressure diffusion and poroelasticity can successfully reproduce the seismicity observed during the EGS simulation which were carried out on the Otaniemi campus near Helsinki, Finland. While pore pressure measurements at the well indicate two possible diffusivities that fit either the build-up of pressure or its drawdown, the physical model suggests that the diffusivity of the medium is likely closer to the higher diffusivity fitting the build-up. We find that the effect of time-dependent nucleation is crucial in reconciling the higher diffusivity with the spatio-temporal distribution of triggered seismicity. Namely, the tendency of the parameter $a\sigma$ to act proportionally to a triggering threshold significantly affects the apparent diffusivity inferred from the triggering front in Otaniemi. However, the effect of finite nucleation cannot be approximated well by introducing a stress threshold in the standard Coulomb friction model, at least in the context of rapid variations of injection rates common in EGS operations. We remark that there are significant portions of the relocated catalogue that the models do not fully capture in space, such as the back-propagation front or far-field seismicity, although a significant portion of the observed far-field seismicity may have been due to leaks in the well casing. The Omori law decay observed in Otaniemi is seen to depend strongly on fluid transport properties in the physical model. Lastly, the physical model indicates that the Kaiser effect is present in Otaniemi, weakened by the successive variation of injection locations between different stages.

We show that a statistical model whereby the seismicity rate is predicted in time and space by convolution of a kernel function inspired by Omori law decay with the injection rate can provide a good match to the seismicity observed in Otaniemi. The existence of such linear convolution kernels is consistent with the identification of systematic decay patterns in the rate densities calculated by adaptation of the cascading algorithm of Marsan and Lengline (2008) to induced seismicity. The statistical model is extended to space by incorporation of a half-norm distribution component to the kernel mimicking the behavior of the physical model. We find that the validity of the method, which assumes a linear relationship between the injection history and the induced seismicity rate, depends strongly on the presence of the Kaiser effect. The convolution model would be applicable towards injection schedules that minimize the impact of the Kaiser effect by decreasing injection durations relative to the local diffusion time or by variation of injection locations in space.

The physical model makes a number of assumptions. One assumption is that it is appropriate to use Darcy's Law, which was established for a homogeneous porous medium, to model the flow in the fractured crystalline bedrock. Although the assumptions largely stem from the lack of data on local heterogeneities or anisotropy, neglecting presence of vertical or horizontal geological layers may be appropriate for Otaniemi where the objective is to fracture a largely crystalline medium. The model also ignores the effect of pore-pressure change on permeability. This is clearly an oversimplification as, in the case of fractured flow, the permeability increases substantially with pore pressure (Acosta and Violay, 2020; Cappa et al., 2006; Cornet and Jianmin, 1995; Evans et al., 2005). Common values of in-tact granite under comparable pressure are documented to be closer to 10^{-21} m^2 (Brace, Walsh, and Frangos, 1968), several orders of magnitude lower than that of the best fitting model (10^{-16} m^2). Indeed, there are indications of changes in the diffusivity from the evolution of the injectivity index, or the ratio of injection rate to the well-head pressure (Appendix B.9). Periods of heightened injectivity are well-correlated with periods of high seismicity rates, likely due to seismicity-induced increase in permeability. Reconciling the full scope of pressure variations at the well and the spatio-temporal patterns of observed seismicity would probably require an explicit account for the role of fractures and seismicity on permeability. Lastly, stress perturbations due to thermoelasticity can also be significant for EGS operations where temperature gradients between the injected fluid and surrounding medium are large (e.g., Gens et al., 2011; Im et al., 2017; Rutqvist and Oldenburg, 2008).

The modeling methods presented here could be useful in designing EGS operations or to interpret induced seismicity observations in terms of transport properties within the stimulated volume. They could additionally serve as a basis for a probabilistic traffic light system (TLS) or be incorporated in a control and optimization framework such as the one presented by Stefanou (2019). At the moment, TLS are deterministic and based entirely on the observed maximum magnitude (Ader et al., 2020; Bommer et al., 2006; Kwiatek et al., 2019; Majer et al., 2007). As such, a red light event can be triggered by the occurrence of a rare event, with improbably large magnitude, that might not necessarily reflect an increased hazard level. In addition, such TLS do not provide a way to anticipate the response to possible mitigation strategies. This is important as many operations have been terminated as the original TLS design proved to be insufficient in preventing "red-light" incurring events (Grigoli et al., 2017; Majer et al., 2007). To alleviate that issue, our forecasting methods could for example be incorporated in "Adaptive Traffic Light Systems"

(ATLS) (Hirschberg, Wiemer, and Burgherr, 2014), which are based in a real-time assessment of probabilistic hazard.

Parameter	Variable	Value and Unit
Poroelastic Properties		
Shear modulus	μ	20 GPa
Drained Poisson's ratio	ν	0.25
Undrained Poisson's ratio	ν_u	0.3
Skempton's coefficient	B	0.75
Biot's coefficient	α	0.31
Transport Properties		
Fluid viscosity	η	0.4 x 10^{-3} Pa· s
Reference fluid density	ρ_0	10^3 kg/m^3
Fault Orientation & Stress State		
Fault normal	$\hat{n}$	[-0.866, 0, 0.5]
Fault slip	$\hat{s}$	[-0.5, 0, -0.866]
Normal stress	σ	155 MPa

Table 3.1: Constant Parameters.

Figure #	Model Parameters				Goodness of Fit		
					KS-statistic		LLK
					Time	Space	Time
Convolution Model							
	c_{hg} (m^2/s)		t_r (hours)	R_0 (events/hour)			
Rate-and-State Model							
Figures 3.6a and 3.8a	0.011		24.1	208.9	0.040	0.122	177,558
	c_{true} (m^2/s)	a	$\dot{\tau}_r$ (kPa/year)	r_b (events/day)			
Figures 3.6b and 3.8b	0.018	0.0002	3.05	12.1	0.029	0.335	173,375
Figures 3.6c and 3.8c	0.018	0.0001	4.89	25.9	0.090	0.136	165,532
Figures 3.6d and 3.8d	0.044	0.00006	1.29	4.7	0.025	0.110	173,429
Coulomb Model							
	c_{true} (m^2/s)	ϕ_1 (MPa)	ϕ_2 (MPa)	α_c (kPa/event· m^3)			
Figures 3.6e and 3.8e	0.044	0.66	0.28	14.3	0.029	0.392	173,035

Table 3.2: Variable Parameters for Each Model.

Chapter 4

DIETERICH 1994 REVISITED: EFFECTS OF FINITE SIZE ON INDUCED SEISMICITY

4.1 Introduction

Although to forecast the rate of earthquakes is a difficult task, the seismicity rate model of Dieterich (1994) — hereafter referred to as the Dieterich model — has provided a relatively simple method for simulating the response of a population of nucleation sources with realistic frictional behavior in both natural and anthropogenic settings. An immediate advantage of the Dieterich model in comparison to most other physics-based models of seismicity rate is that it considers the rate- and state- dependence of friction (Linker and Dieterich, 1992; Marone, 1998; Ruina, 1983) that gives rise to a nucleation process of finite duration in shear failure (Rubin and Ampuero, 2005). Under the rate-and-state formalism, the friction coefficient f, is a function of the slip rate, V, and the state variable, θ, which is associated with the quality and/or quantity of the contact points. A commonly used logarithmic formulation (Marone, 1998) along with the aging law to govern the evolution of the state variable is,

$$\begin{aligned} f(V,\theta) &= f^* + a\log\left(\frac{V}{V^*}\right) + b\log\left(\frac{V^*\theta}{D_{RS}}\right) \\ \dot{\theta}(V,\theta) &= 1 - \frac{V\theta}{D_{RS}} \end{aligned} \tag{4.1}$$

where f^* is the reference friction coefficient at the reference slip rate V^*, a, b, and D_{RS} are material parameters, and $\dot{\cdot} = \frac{d}{dt}$. In particular, a is attached to the logarithmic dependence on slip rate and is directly proportional to what is called the 'direct effect,' a nearly instantaneous increase in frictional resistance to a sudden increase in the slip rate. The direct effect, along with others, induces the nucleation process of finite duration in a fault governed by rate-and-state friction (Heimisson and Segall, 2018). The Dieterich model translates the nucleation period to a time to instability, t_{inst}, which can be used to calculate the seismicity rate among a population of faults represented as single-degree-of-freedom spring-sliders. Perhaps most notably, the Dieterich model reproduces the Omori decay of aftershocks following a sudden

change in stress induced by a large earthquake as a result of the relaxation time scale of the seismicity rate that is proportional to the time to instability.

One of the most prominent applications of the model outside the naturally tectonic setting in recent years has been induced seismicity. Assuming one-way coupling from stress change to seismicity rate allows flexibility in the physical mechanisms one can consider to be responsible for the stress state. The distribution of stress perturbations in time and space due to an injection — presumably solved for in a separate, independent framework that may regard complex physics with heterogeneities — becomes input to an ODE to be solved for at each point in space (Segall and Lu, 2015). Such framework has proven to be successful in reproducing the observed rate of induced seismicity at various injection settings (Acosta et al., 2023; Heimisson et al., 2022; Kim and Avouac, 2023; Zhai and Shirzaei, 2018). The studies have highlighted the importance of considering the finite duration of nucleation, as it may affect characteristic features of induced seismicity such as its spatial extent of the triggering front (Kim and Avouac, 2023) and its periodicity in response to seasonal loading (Acosta et al., 2023).

The impressive level of success by the Dieterich model in explaining and reproducing both natural and induced seismicity warrant a closer look at the significance — or possibly the lack thereof — of the number of assumptions made in the model derivation. Three main assumptions are highlighted here:

1. All nucleation sources are already close to instability, distributed at even intervals away from the timing of the dynamic event such that a constant seismicity rate would result from a constant stressing rate.
2. Stress interactions between sources are negligible.
3. Frictional stability of sources do not change with respect to the stress state.

Assumption 1 is a question of initial conditions. Heimisson et al. (2022) accounted for nucleation sources far from instability through a stress threshold that must be passed prior to observing seismicity. The threshold formulation still assumes the existence of a steady seismicity rate under steady stressing rate which in fact requires a rather particular distribution of initial slip rates due to the nonlinearity of rate-and-state friction. Additionally, an important and implicit statement of assumption 1 is that the population of nucleation sources is infinite, which results from the lack of a

length scale in the point-wise consideration of the region containing the population. Assumption 2 is perhaps the most widely cited assumption of the model although incorporation of source interactions into the model by Heimisson (2019) showed that it may only manifest itself as a difference in the total number of events. Assumption 3 is unphysical considering the known inverse relationship between frictional stability and normal stress. Namely, a linear stability analysis of a spring-slider system under steady-state conditions gives the critical stiffness (Ruina, 1983),

$$\kappa_{cr} = \frac{(b-a)\bar{\sigma}}{D_{RS}} \qquad \bar{\sigma} = \sigma - p \tag{4.2}$$

where $\bar{\sigma}$ and σ are the effective and ambient normal stress, respectively, and p is the pore pressure experienced by the slider. For springs of stiffness higher than κ_{cr}, the slider is unconditionally stable to all perturbations for a constant loading rate (Ranjith and Rice, 1999). In a finite fault, the stability condition is determined by the nucleation size - the minimum size that a slipping patch must reach to grow dynamic - which is inversely proportional to the normal stress (Ampuero and Rubin, 2008; Rubin and Ampuero, 2005). A decrease in the effective normal stress due to an injection therefore increases the stability of a fault which may increase its time to instability, possibly to infinity in the case of an unconditionally stable fault. Furthermore, both experiments (Guérin-Marthe et al., 2019) and theoretical studies (Alghannam and Juanes, 2020) have shown that the stressing rate can also affect stability characteristics. In the context of fluid injections, the effect of increased stability from an increase in pore pressure on the seismicity distribution has not yet been explored.

An immediate advantage of the Dieterich model in comparison to most other physics-based models of seismicity rate is that it considers the rate- and state- dependence of friction (Linker and Dieterich, 1992; Marone, 1998; Ruina, 1983) that gives rise to a nucleation process of finite duration in shear failure (Rubin and Ampuero, 2005). In particular, a of rate-and-state friction is attached to the logarithmic dependence on slip rate and is directly proportional to what is called the 'direct effect', a nearly instantaneous increase in frictional resistance to a sudden increase in the slip rate. The direct effect, along with others, induces the nucleation process of finite duration

in a fault governed by rate-and-state friction (Heimisson and Segall, 2018). The Dieterich model translates the nucleation period to a time to instability, t_{inst}, which can be used to calculate the seismicity rate among a population of faults represented as single-degree-of-freedom spring-sliders. Perhaps most notably, the Dieterich model reproduces the Omori decay of aftershocks following a sudden change in stress induced by a large earthquake as a result of the relaxation time scale of the seismicity rate that is proportional to the time to instability. Yet, a number of studies have cited inconsistencies between inferred parameters of the Dieterich model and what one would expect based on geological considerations and laboratory experiments. Relatively low values of $a\bar{\sigma}$ have required either values of a that are orders of magnitude lower than those measured in the laboratory or near-lithostatic pore pressure such that $\bar{\sigma}$ would be low (Bettinelli et al., 2008; Gross and Bürgmann, 1998; Gross and Kisslinger, 1997; Toda et al., 1998, 2012). Matching the Dieterich model to induced seismicity catalogues from different geothermal stimulation sites showed that r_b can be orders of magnitude apart, beyond the differences in levels of natural seismicity (Kim and Avouac, 2023).

Addressing the assumptions of the model is a non-trivial task given that the most straightforward approach is to deal with the system of equations in their full, original formulation without the simplifications allowed by the assumptions that make the Dieterich model a much more computationally tractable problem. Initial conditions close to nucleation (assumption 1) corresponds to what is called the no-healing limit, at which the ODE for state evolution admits an analytical solution (due to $\frac{V\theta}{D_{RS}}$ being large enough to ignore the 1 term in the aging law). For the general case with arbitrary initial conditions, a closed form for the seismicity rate is not possible. Similarly, solving the friction law in its entirety addresses assumption 3, where the change in stability would naturally arise from the friction evolution. Assumption 2 requires solving for the stress transfer between each fault. Addressing source interactions rigorously significantly departs from the formulation of the Dieterich model which does not explicitly specify the spatial distribution and orientation of the population of nucleation sources. Including dynamic stress changes and wave propagation in an arbitrary network of faults is not yet computationally feasible at the time scale meaningful to most fluid injection settings.

Here, we address the assumptions and investigate their effect on the seismicity rate through a Discrete Fault Network (DFN) model (Im & Avouac, 2024). The DFN model addresses assumptions 1 and 3 in their full, by solving the friction law in

the non-simplified form. The model addresses assumption 2 in the quasi-dynamic sense, by accounting for the quasi-static stress transfer between individual faults and the dynamic radiation of stress away from each fault into the bulk medium. We use the DFN model to consider various initial conditions among a finite number of faults as in a realistic injection medium for direct comparison to the Dieterich model as an objective test for the significance of the aforementioned assumptions.

4.2 The Dieterich Model and the Finite Discrete Fault Network Model

The Dieterich model simulates the seismicity rate among a (infinite) population of nucleation sources by computing their times to instability. The analytical treatment of this problem is possible thanks to the simplification of the state evolution law in rate-and-state friction under the assumption that the nucleation sources are accelerating towards instability. In the context of Equation 4.1, this corresponds to large values of $\frac{V\theta}{D_{RS}}$ such that the 1 term of the aging can be ignored. This leads to the equation for the time to instability, t_{inst}, given an arbitrary stressing history,

$$\int_0^{t_{inst}} K(r,t')\,dt' = \frac{a}{HV_{ini}}$$

$$K(r,t) = \exp\left(\frac{\tau(r,t)}{a\bar{\sigma}(r,t)} - \frac{\tau_{ini}(r)}{a\bar{\sigma}_{ini}(r)}\right) \tag{4.3}$$

$$H = \frac{b}{D_{RS}} - \frac{\kappa_{fault}}{\bar{\sigma}_{ini}}$$

where r and t are the radial distance and time, V_{ini} is the initial slip rate of the nucleation source, τ and $\bar{\sigma}$ are the applied shear and effective normal stress, τ_{ini} and $\bar{\sigma}_{ini}$ are the initial shear and effective normal stress, and κ_{fault} is the spring stiffness of the fault represented by a spring-slider. Next, the initial conditions of the nucleation sources are solved for by assuming the existence of a steady seismicity rate r_b under a steady stressing rate $\dot{\tau}_r$. Rearranging equation (14) of Heimisson & Segall (2018) gives the distribution of initial slip rate,

$$V_{ini}^n = \frac{\dot{\tau}_r}{H\bar{\sigma}_{ini}\left(\exp\left(\frac{n}{r_b}\frac{\dot{\tau}_r}{a\bar{\sigma}_{ini}}\right) - 1\right)},\ n \in \mathbb{N} \tag{4.4}$$

for the nth nucleation source. Note that n ranges from 1 to infinity in the Dieterich model, allowing infinitesimal values of V_{ini} such that t_{inst} is infinitely large. For the seismicity rate, $R_{Dieterich}$, we opt to use the integral formulation of Heimisson and Segall (2018) in place of the original ODE formulation,

$$\hat{R}_{Dieterich}(r,t) = \frac{R_{Dieterich}(r,t)}{r_b} = \frac{K(r,t)}{1 + \frac{1}{t_a}\int_0^t K(r,t')\,dt'}, \qquad t_a = \frac{a\overline{\sigma}_{ini}}{\dot{\tau}_r} \tag{4.5}$$

where $\hat{R}_{Dieterich}(r,t)$ is the normalized seismicity rate with respect to the background seismicity rate. The integral formulation explicitly accounts for changes in normal stress without resorting to the often used Coulomb stress approximation. Computing the fraction of exponentials in Equation 4.5 can be difficult for large changes in stress such that a large argument of the exponential in Equation 4.3 for $K(r,t)$ causes overflow. To avoid computing the exponential explicitly, we derive a numerical algorithm for computing the log of the seismicity rate in increments such that the overflow can always be avoided for small enough time steps (Appendix C.1).

The Discrete Fault Network (DFN) model solves for the frictional motion and stress transfer by connecting a number of boundary integral solutions for slip along discrete and planar, embedded fractures in an infinite, homogeneous and elastic medium (Im & Avouac, 2024). Thus, the number of faults in the model is inherently finite, unlike the Dieterich model. Quasi-static stress transfer between the faults is resolved by the Okada solutions for slip along dislocations (Okada, 1985). Along the direction of slip, inertia is only accounted for in the form of radiation damping. While dynamic stress tress transfer between faults and wave propagation along slip are neglected, a lumped mass per area term is attached to acceleration. Such a parameter has been shown to be necessary to reproduce simulations closely matching community benchmark problems for quasi-dynamic rupture of a single fault (Im & Avouac, 2024). Combined all together, the system of equations comprise of a number of PDE's equal to the number of 2D cells that discretize the embedded fractures,

$$M\ddot{\delta}_n = \sum_m K^{\tau}_{nm}(\delta_m(t=0) - \delta_m(t)) \\ - f_i\left(V_n(t), \theta_n(t)\right) \cdot \left(\bar{\sigma}_n(t=0) + \sum_m K^{\sigma}_{nm}\delta_m(t)\right) - \frac{G}{2c_s}\dot{\delta}_n(t) \quad (4.6)$$

$$n \in 1, ..., N_{fault}$$

where M is the lumped mass per area, δ_n is the slip along the nth cell, K^{τ} and K^{σ} are the shear and normal stiffness matrices that results from the Okada solutions for stress transfer between discrete dislocations, G is the shear modulus of the medium, and c_s is the shear wave speed. f, the coefficient of friction is given by the rate-and-state friction law of Equation 4.1 as a function of the slip rate and the state variable. In the models presented here, we discretize all faults by a single cell such that N_{fault} is equal to the number of cells in the simulation for computational efficiency. In other words, we also approximate the faults as single-degree-of-freedom systems, and we do not consider here the effects of finite nucleation sources with rupture dynamics. The finite quality of the model enters through the effect of the fault size on the effective stiffness of each fault (the diagonal elements of the shear stiffness matrix, K^{τ}), the effect of fault size on stress transfer to the surroundings, and the finite number of faults in the model. At the same time, we emphasize that to discretize the faults with multiple cells and to resolve rupture dynamics on individual faults is fully possible in the DFN model.

To apply stress perturbations from injections, analytical solutions for the pressure due to a point source injection in a poroelastic medium (Rudnicki, 1986) are pre-computed,

$$p(r,t) = \frac{q}{4\pi\rho_0 r}\frac{\eta}{k_{perm}}\,\mathrm{erfc}\left(\frac{1}{2}\xi\right)$$

$$\xi = \frac{r}{\sqrt{c_{diff}t}} \quad (4.7)$$

$$c_{diff} = \frac{k_{perm}}{\eta}\frac{(\lambda_u - \lambda)(\lambda + 2G)}{\alpha^2(\lambda_u + 2G)}$$

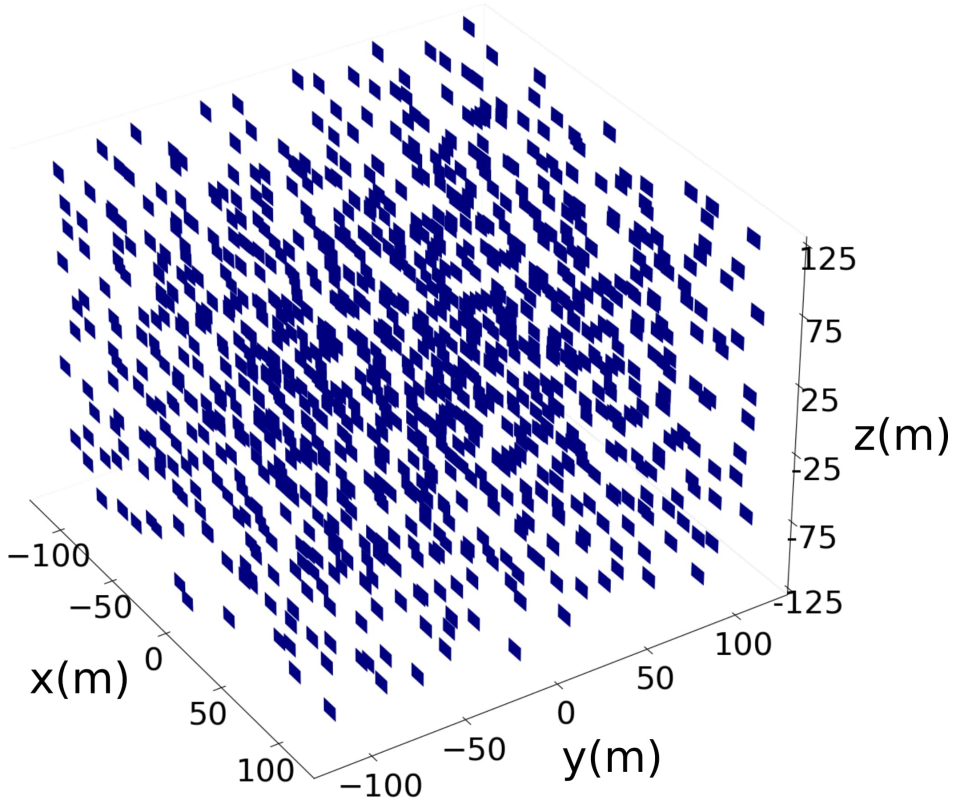

Figure 4.1: The Network of Embedded Fractures in the DFN Model. Discrete fractures are embedded in an infinite medium along a 10x10x10 grid with an average spacing of 25m. The fractures share the same size (10m x 10m) and the same orientation. Boundary element solution for each fault is coupled to the rest by solutions for quasi-static stress transfer between dislocations (Okada, 1985). Shear resistance on each fault is governed by rate-and-state friction, radiation damping, and inertial forces along the direction of slip. Unlike the Dieterich model, the DFN model accounts for the finite size of the seismogenic reservoir, the full evolution of friction from any initial conditions, and stress interactions between each fault.

where $\lambda_u = 2G\nu_u/(1-2\nu_u)$ is the undrained Lamé parameter and the drained Lamé parameter without the subscript u for shear modulus, G, and the drained and undrained Poisson's ratio ν and ν_u, $\alpha = \frac{3(\nu_u-\nu)}{B(1+\nu_u)(1-2\nu)}$ is the Biot coefficient for Skempton's coefficient B, c_{diff} is the hydraulic diffusivity which depends on permeability, k_{perm} and viscosity, η, q is the mass injection rate and ρ_0 is the reference fluid density. Interpolations of the pre-computed analytical solutions are superposed to the current stress state at each time step. In general, the model allows any arbitrary stress conditions to be provided as input, regardless of how they have been computed, similarly to the Dieterich model.

The initial conditions emulate the assumptions of the Dieterich model as closely as possible by following the derivation for the initial slip rate distribution that is at even intervals of the time to instability at constant loading. To ensure that all faults are accelerating towards instability and are at the no-healing limit, we choose initial states such that $\frac{V_{ini}\theta_{ini}}{D_{RS}}$ is greater than 100. The exact values of θ_i are computed using the phase-plane solutions of quasi-static spring-sliders driven by constant loading as derived in Ranjith and Rice (1999),

$$
\begin{aligned}
U_{RR} &= (\beta - 1)\beta \left(\frac{V_{lp}}{V^*} + \frac{e^{\phi}}{\beta - 1} \right) e^{\frac{\psi - \phi}{\beta}} - \psi\beta \\
\psi &= \frac{f_{ini} - f^*}{a} \\
\phi &= \ln \frac{V_{ini}}{V^*} \\
\beta &= \frac{b}{a}
\end{aligned}
\tag{4.8}
$$

where $V_{lp} = \frac{\dot{\tau}_r}{\kappa_{fault}}$ is the constant velocity of the loading point and U_{RR} is the constant that defines a single solution in the phase plane. We note that Equation 4.8 is derived for the special case that $\kappa_{fault} = \kappa_{cr}$ (analytical solutions for the more general case are not possible) and that we use it to solve approximately for θ_{ini} that arises naturally from long-term loading. In summary, we use Equation 4.4 to compute V_{ini}, then use Equation 4.8 to compute θ_{ini} with U_{RR} large enough to ensure that $\frac{V_{ini}\theta_{ini}}{D_{RS}}$ is greater than 100 for all faults. Equation 4.1 then uniquely defines the initial friction, f_{ini}, for the given initial slip rate and state variable. This procedure generates a network of faults with initial conditions that approximately draw from points along the same seismic trajectory that would naturally arise from long-term steady loading.

The DFN models presented here all share the same geometry in terms of the fault size and their spacing, unless explicitly stated to be otherwise. 10m x 10m faults are spaced in a 10 x 10 x 10 interval with 25m spacing in-between (Figure 1). The initial conditions for the slip rate, stress and the state variable are distributed randomly among the faults with no consideration of their relative location along the grid. Rate-and-state properties are fixed at constant values for all faults. Initial

normal stress is distributed uniformly at 100MPa,and a constant stressing rate of 1kPa/year is applied to all faults.. The physical and computational parameters of the model are summarized in Table 4.1. The initial distribution for the parameters of Table 4.1 with r_b = 1 event/year and U_{RR} = 10,000 is shown in Figure 4.2. The distribution traces out a path along the portion of a typical seismic trajectory of a spring-slider under rate-and-state friction that satisfies the no-healing assumption.

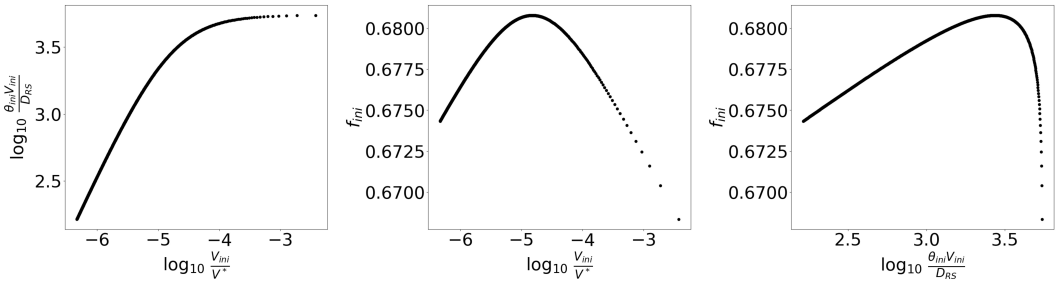

Figure 4.2: Distribution of Initial Conditions for Individual Faults in the DFN Model. Initial conditions of all faults are plotted in their phase-plane for the slip rate, $\frac{V_{ini}}{V^*}$, the normalized state variable, $\frac{\theta_{ini}V_{ini}}{D_{RS}}$, and friction, f_{ini}. To satisfy the no-healing assumption used by Dieterich (1994), the normalized state variable is ensured to be above 100. By using analytical solutions for the quasi-static spring-slider, the initial distribution traces the aseismic period of the lifecycle of a spring-slider under constant loading.

4.3 Spatio-Temporal Pattern of Induced Seismicity in a Reservoir with Finite Number of Faults

To illustrate how the assumption of the infinite population of nucleation sources in the Dieterich model may manifest itself in the finite analogue, we run two simulations of the DFN model for the same injection scenario with different values of r_b used to configure the initial conditions — one higher at r_b = 1 event/hour and one lower at r_b = 1 event/year. We emphasize that the Dieterich model would not predict any differences in the spatio-temporal pattern of the seismicity rate for different values of r_b. Since r_b is a simple scalar multiplier to the normalized seismicity rate, the only difference between the two catalogues would be the total number of events by the ratio of one hour to one year. The injection rate is fixed at 30kg/s for both simulations.

Figure 4.3 shows the resulting catalogues on top of a contour plot of the log seismicity rate predicted by the Dieterich model ($R_{Dieterich}$). Configuring the initial conditions with higher r_b results in both steeper triggering and back-propagation fronts as the

initial slip rates are generally higher and the times to instability are shorter. Events of the simulation with lower r_b are spread out noticeably further in time. The shapes of the seismicity fronts can in fact be predicted by considering the time to instability as a function of distance,

$$\int_0^{t_{inst}(r|V_{front})} K(r,t')\,dt' = \frac{a}{HV_{front}} \tag{4.9}$$

where V_{front} is the characteristic slip rate of the initial distribution that traces the seismicity front of interest. For the general stress history, closed form solutions of the integral on the left hand side of Equation 4.9 are not possible. We solve numerically for $t_{inst}(r)$ given the simulated injection scenario and find that the average slip rate of the distribution, V_{mean}, and the minimum slip rate of the distribution, V_{min}, as V_{front} trace excellently the triggering and back-propagation fronts, respectively. In previous studies, the triggering front has been associated with a pressure diffusion process (Shapiro, Huenges, and Borm, 1997) or its combination with the delay to nucleation from rate-and-state characteristics of friction (Kim and Avouac, 2023). Most commonly, the diffusivity of the injected medium is inferred by matching the curve $r_{tf}(t) = \sqrt{4\pi c_{tf} t}$ where $r_{tf}(t)$ is the triggering front and c_{tf} is the inferred diffusivity of the injected medium (Shapiro, Huenges, and Borm, 1997). It is important to distinguish that c_{tf} does not necessarily equal the true diffusivity of the medium. In the DFN catalogues, c_{tf} can be expressed as,

$$c_{tf} = \frac{r_{tf}^2}{4\pi t_{inst}(r_{tf}|V_{front} = V_{mean})}. \tag{4.10}$$

In summary, the shape of the seismicity front in the DFN model is a function of three main factors: 1. the transport characteristics of pressure diffusion (c_{diff}); 2. the delay to nucleation in rate-and-state friction (or the magnitude of the direct-effect, a); and 3. the initial distribution of the time to instability (V_{mean} and V_{min}).

Interestingly, the back-propagation that appears midst injection in the DFN catalogue is qualitatively different from those more commonly discussed in observations of field data which only appear after shut-in. Such phenomenon has been associated with the back front of pressure diffusion that propagates negative stressing rates from the injection point once an injection stops (Langenbruch and Shapiro, 2010).

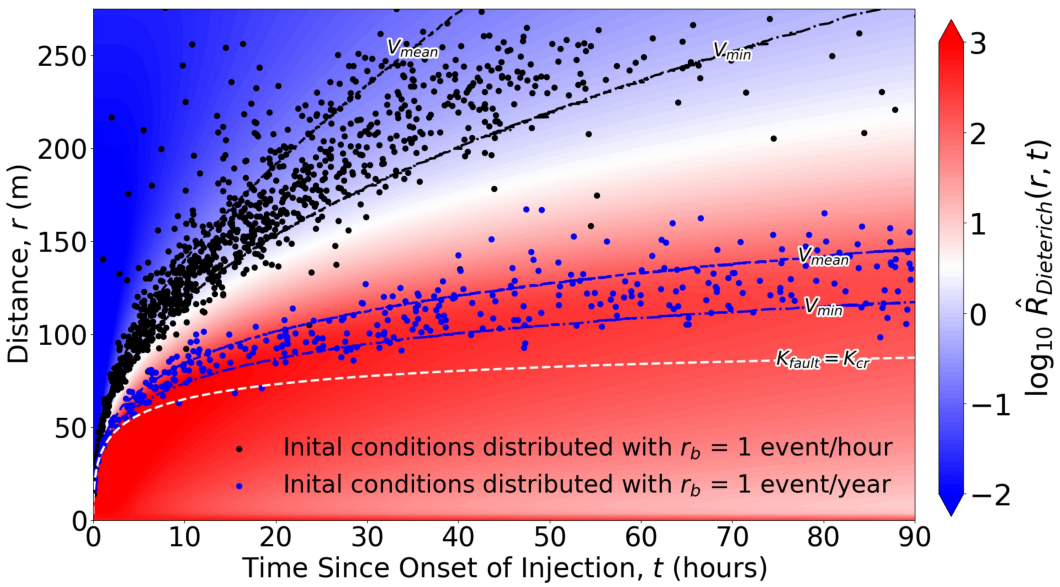

Figure 4.3: DFN Catalogues with Different r_b and the Dieterich Model Prediction. The Dieterich model (contour plot of the background) and two DFN Models (black and blue scatter plots) are simulated for the same injection scenario at a constant injection rate of 30 kg/s. The initial conditions of the DFN model are configured with different values of r_b (1 event/hour for the black catalogue and 1 event/year for the blue catalogue). The catalogue with higher r_b has steeper triggering and back-propagation fronts due to shorter times to instability. For different values of r_b, the normalized seismicity rate of the Dieterich model does not change. The back-propagation front during the injection only appears for the DFN catalogue due to the exhaustion of a finite number of sources. Although the Dieterich model does not predict different densities of seismicity rate for different r_b, the DFN catalogues differ significantly due to the difference in the range of initial distribution of times to instability.

A similar back-propagation front is predicted by the Dieterich model, additionally considering delayed nucleation. There is no back-propagation front for a continuous injection in the Dieterich model, as the infinite pool of nucleation sources accommodates sources with infinitely small initial slip rates and infinitely large times to instability (equivalent to plugging in $V_{front} = V_{min} = -\infty$ in Equation 4.9). In the DFN catalogue, the back-propagation front for a continuous injection occurs by the sequential exhaustion of available nucleation sources at further distances.

4.4 Long-Term Source-to-Source Interactions and Normal Stress Dependent Frictional Stability

We highlight two additional differences between the Dieterich and DFN model regarding source-to-source interactions and the dependence of frictional stability on normal stress through a long-term simulation driven by both tectonics and fluid injections. An injection rate of 30kg/s is applied for ~ 68,500 years (25e6 days) before a shut-in of equal duration. The initial conditions of the faults are distributed using r_b of 1 event/hour. The resulting catalogue in space and time, superposed on top of the Dieterich model prediction is shown in Figure 4.4.

The injection first produces the seismicity rate profile of Figure 4.3, although the particular characteristics at the time scale of pressure diffusion discussed in the previous section are not distinguishable at the time scale of the long-term simulation (the earliest set of events of the DFN catalogue shows as a nearly vertical line at t = 0). Thereafter, the DFN catalogue exhibits long periods of quiescence separating compact periods of steady seismicity with rates much lower than the prescribed rate of r_b = 1 event/hour. With increasing time (or more precisely slip), the average interevent duration between events within a compact seismic period increases while maintaining the natural return period of each fault. As a result, more and more seismic events begin to fill the quiescent gaps. By the end of the simulation, events further away from the injection point, whose stress histories are dominated by constant shear loading, appear to converge to a steady state with roughly constant interevent duration. The steady seismicity at the end of the simulation is around 66 events/millenium, accommodating both the number of faults in the reservoir and their natural return period. The convergence reveals a self-organizing nature of source-to-source interactions that leads to a steady seismicity rate at a constant stressing rate. To affirm that the gradual convergence to steady seismicity rate is due to source interactions, we run the same simulation with the distance between each fault increased to 500m. Decreasing the stress transfer between each fault maintains the alternating sequence between quiescence and steady seismicity for the entire simulation. Additionally, the interevent duration remains equal to the intervals of time to instability initially prescribed (1 hour). The Dieterich model maintains a constant seismicity rate for constant injection rate without such quiescent gaps, as it continues to draw from the infinite population of nucleation sources. Apart from the relatively short periods at the onset of injection and shut-in, the total seismicity rate is exactly r_b = 1 event/hour as prescribed.

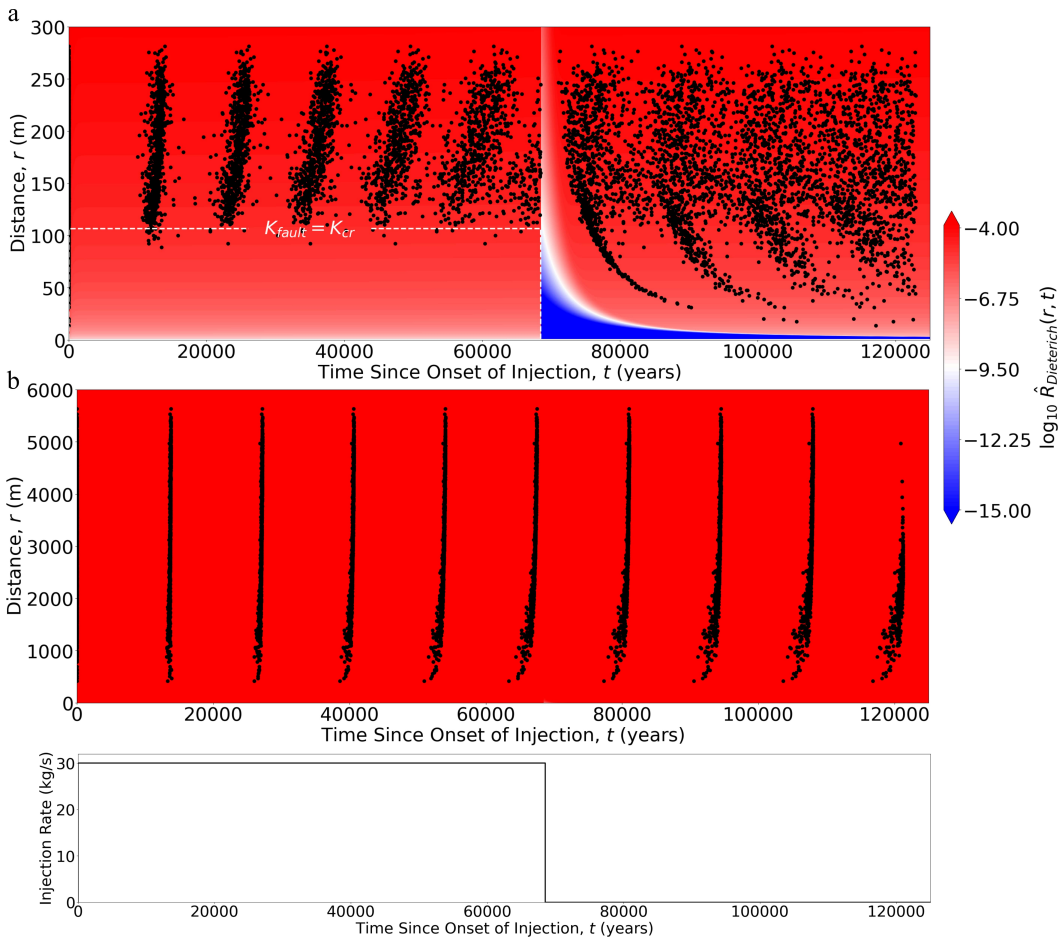

Figure 4.4: Long-Term Simulations with Different Fault Spacing: (a) The Dieterich model and the DFN model with r_b = 1 event/hour of Figure 3 is extended in time along with a shut-in of the injection at the half point of the simulation duration. The DFN catalogue exhibits a long-term convergence to steady seismicity rates due to source interactions at constant loading. The increased frictional stability due to increase in pressure also creates an aseismic region in the DFN model (the region is traced at its upper boundary by the white dotted line). The shut-in delays the time to instability for faults close to the injection source for both the Dieterich and DFN model. Otherwise, the Dieterich model predicts a constant seismicity rate for the simulation period. (b) Fault spacing is increased from 25m to 500m to decrease the extent of source interactions with slip, which fully eliminates the convergence of the fault network to a steady seismicity rate. The long-term simulation reveals the the effect of source interactions in the redistribution of the stress state across the fault network that is not accounted for in the Dieterich model.

Prior to shut-in, the DFN catalogue exhibits a strictly aseismic region $\sim$ 100m in radial distance from the injection point. The long-term absence of seismicity close to the injection point is due to the increased frictional stability as a result of a decrease

in the effective normal stress. As long as the injection continues, the rise in pore pressure is maintained until shut-in, and the consequent decrease in effective normal stress decreases the critical stiffness of the faults, κ_{cr}. The contour line along the transition points in time and space at which the stiffness of the fault, κ_{fault}, equals the critical stiffness, κ_{cr}, traces excellently the distance until which the faults are aseismic. Faults under the stable condition such that $\kappa_{fault} > \kappa_{cr}$ steadily creep in the DFN model. The Dieterich model continues to predict stick-slip motion of all nucleation sources as according to assumption 3, resulting in an unaltered, steady seismicity rate near the injection point.

The Dieterich and DFN model coincide well qualitatively in the predictions of the delay in time to instability caused by the shut-in. The shut-in induces an abrupt and negative stressing rate, which 'sets back' the faults in time with respect to their current position in their respective seismic life cycles. This delay in time to instability is largest for faults closest to the injection source which experience the largest negative stressing rates, causing the curved shape of the first seismicity front observed after the shut-in. The qualitative match between the Dieterich and DFN model is not obviously intuitive given that the nucleation sources in the two cases have different initial conditions. Unlike the beginning of the simulation where the initial states of the faults in the DFN model were also configured to be at the no-healing limit, the majority of the faults of the DFN model are far from this condition by the time of the shut-in. The faults that were creeping in the previously linearly stable region are at steady-state ($\dot{\theta} = 0$), whereas the majority, if not all of the rest of the faults are below healing ($\frac{V\theta}{D_{RS}} < 1$) as the interseismic loading period dominates (in time) the life cycle of a seismic fault. In an absolute sense, the times to instability following the shut-in differ significantly between the two models, to the order of a 1000 years. Thus, the matching shape of the seismicity front following shut-in does not necessarily suggest the applicability of the Dieterich model to more general initial conditions not constrained to assumption 1, but moreso that both models correctly predict a delay in time to instability in response to a negative stress change. Once the effective normal stress of the medium has equilibriated to initial levels prior to injection, the previously aseismic faults resume stick-slip motion and converge to a steady seismicity rate along with the rest of the faults due to source interactions.

4.5 Inference of Dieterich Model Parameters from DFN Catalogues

Given the qualitative differences between the Dieterich model and a model of a finite number of faults such as in a real reservoir, it is interesting to consider the implications to the meaning of the Dieterich model parameters that have been inferred from real data. In fact, a number of studies have cited inconsistencies between inferred parameters of the Dieterich model and what one would expect based on geological considerations and laboratory experiments. Relatively low values of $a\bar{\sigma}$ have required either values of a that are orders of magnitude lower than those measured in the laboratory or near-lithostatic pore pressure such that $\bar{\sigma}$ would be low (Acosta et al., 2023; Bettinelli et al., 2008; Gross and Bürgmann, 1998; Gross and Kisslinger, 1997; Toda et al., 1998, 2012). Matching the Dieterich model to induced seismicity catalogues from different geothermal stimulation sites showed that r_b can be orders of magnitude apart, beyond the differences in levels of natural seismicity Kim and Avouac, 2023.

We examine the possible origin of these inconsistencies and the meaning of the Dieterich model parameters in a finite setting by inferring them directly from catalogues produced by the DFN model. The injection rate is varied between 0, 1, 2, 3, 4, 5, 10, 15, and 30 kg/s for an otherwise equal configuration with the same initial conditions, physical parameters and geometry. The Dieterich model is adjusted to fit the resulting DFN catalogues in two different ways to better isolate the effect of parameters r_b and a. At this point, we differentiate between the parameters used to configure the DFN model ($r_{b,DFN}$ & a_{DFN}) and those inferred by matching the Dieterich model ($r_{b,Dieterich}$ & $a_{Dieterich}$). In the first approach, $a_{Dieterich}$ is fixed to a_{DFN} and only $r_{b,Dieterich}$ is adjusted to match the total number of events of the DFN catlaogue. In the second approach, the best matching value of $a_{Dieterich}$ is inferred by minimizing the mismatch between the seismicity rates. Namely, the Poisson likelihood of the DFN catalogue for the given prediction from the Dieterich model is maximized (Dempsey and Suckale, 2017), i.e., the best matching value of $a_{Dieterich}$ is defined as

$$\underset{a_{Dieterich}}{\arg\max} \sum_{j=1}^{N_{events}} \log R_{Dieterich}(a_{Dieterich}; t_j) - \int_0^{t_{N_{events}}} R_{Dieterich}(a_{Dieterich}; t')dt', \tag{4.11}$$

where t_j for $j \in 1, ..., N_{events}$ is the timing of the jth event of the DFN catalogue. Then, $r_{b,Dieterich}$ is scaled to fit N_{events}.

Figure 4.5 shows select examples of the comparisons between the DFN catalogue and the prediction of the Dieterich model where only r_b is inferred as a free parameter. For all injection rates, $r_{b,Dieterich}$ underpredicts $r_{b,DFN}$, and the underprediction is greater at higher injection rates (Figure 4.6). $r_{b,Dieterich}$ most closely matches $r_{b,DFN}$ for the zero injection case, where the DFN model produces close to the prescribed constant seismicity rate in the beginning before all faults have triggered their first event. Afterwards, the total seismicity is close to zero as the faults must be loaded for their natural return period in order to nucleate again. For the fitting period that is longer than $t_{N_{events}}$, $r_{b,Dieterich}$ must be lower than $r_{b,DFN}$ to match N_{events}. At higher injection rates, more events from the infinite pool of nucleation sources are triggered in the Dieterich model by the higher stressing rates. In the DFN catalogues, N_{events} meanders closely to N_{fault} for all injection rates. This exhaustion of nucleation sources in a finite reservoir can only be matched with the Dieterich model by further decreasing $r_{b,Dieterich}$ at higher injection rates.

When $a_{Dieterich} = a_{DFN}$, the predictions of the seismicity rate in time and space differ significantly between the two models. In space, the Dieterich catalogue generally samples a seismicity cloud significantly closer to the injection point than the DFN catalogue which has steeper triggering and back-propagation fronts. The seismicity cloud closer to the injection point in the Dieterich model results from sampling a continuous distribution of the seismicity rate that rapidly decays with distance. The higher seismicity rate closer to the injection point is accommodated in the DFN model through a finite, uniformly distributed grid of faults. Rather, the shape of the seismicity cloud in the DFN catalogue are determined by the average and maximum time to instability of the available population of nucleation sources (Section 4.3). The triggering fronts of the DFN catalogues do not necessarily follow the $\sqrt{t}$ curve assuming instantaneous nucleation and pressure diffusion (Shapiro, Huenges, and Borm, 1997), or the logarithmic curve accounting for delayed nucleation (Kim and Avouac, 2023). For low injection rates where the background stressing rate dominates, the triggering and back fronts can become nearly vertical (Figure 4.5b), converging more closely to the zero injection case where the time to instability is no longer a function of distance. With higher injection rates, the seismicity cloud assumes more closely the $\sqrt{t}$ shape dominated by pressure diffusion (Figure 4.5d). At intermediary injection rates, a noticeable transition in the shape of the triggering front can occur, from the $\sqrt{t}$ shape close to the injection source to a more linear curve at greater distances (Figure 4.5c). In this case, Equation 4.10 is in fact not applicable and c_{tf} cannot be meaningfully inferred from the full catalogue. The

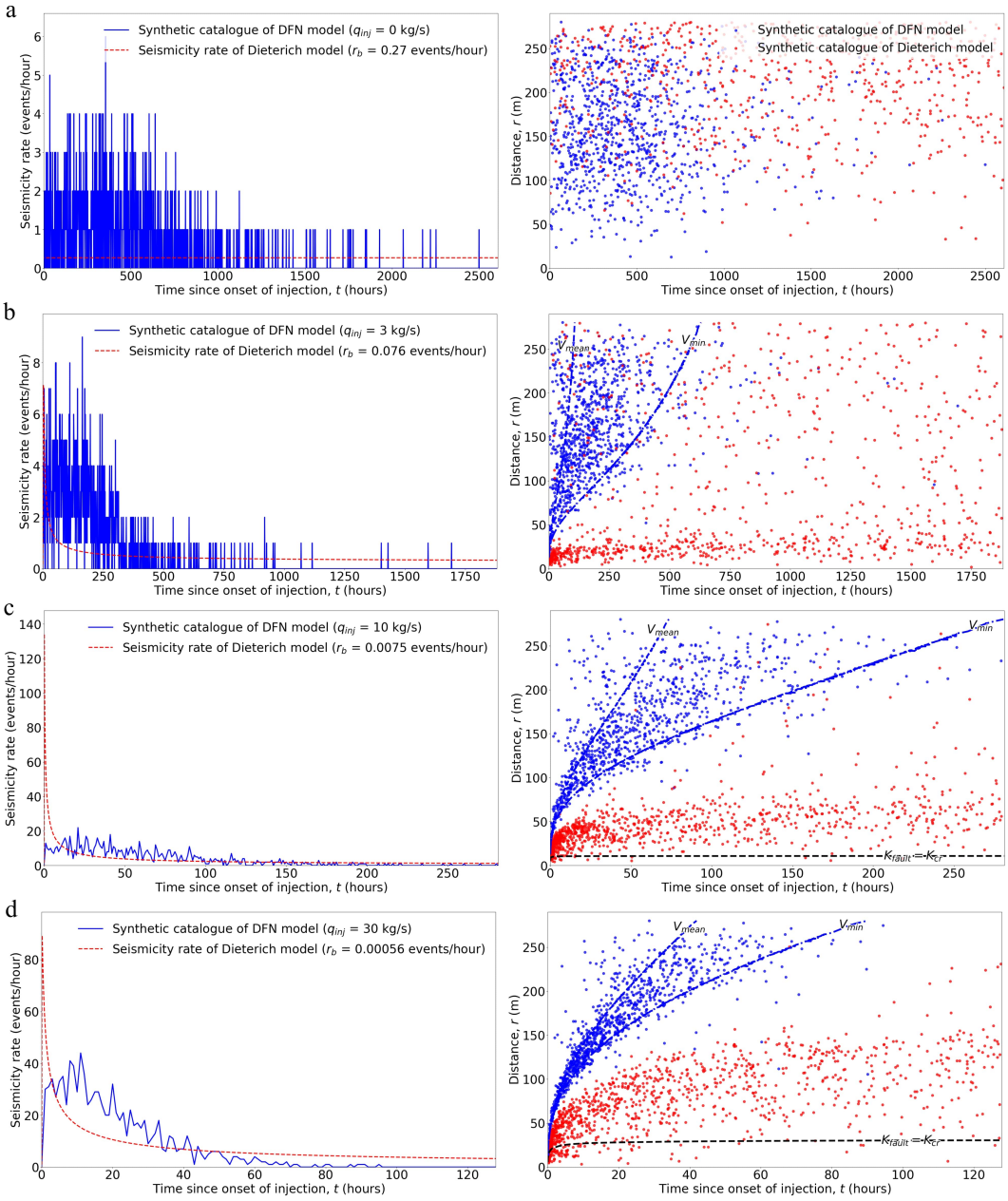

Figure 4.5: Dieterich Model Fits to DFN Catalogues with $r_{b,Dieterich}$ as a Free Parameter and $a_{Dieterich} = a_{DFN}$. The Dieterich model is matched to DFN catalogues at different injection rates by adjusting the background seismicity rate parameter, $r_{b,Dieterich}$ to match the total number of events. $r_{b,Dieterich}$ is lower than $r_{b,DFN}$ to compensate for the finite number of faults in the DFN model. $r_{b,Dieterich}$ is lower at higher injection rates where the Dieterich model predicts higher seismicity rates from accessing the infinite population of sources, while the total number of events in the DFN model is limited by the number of embedded fractures.

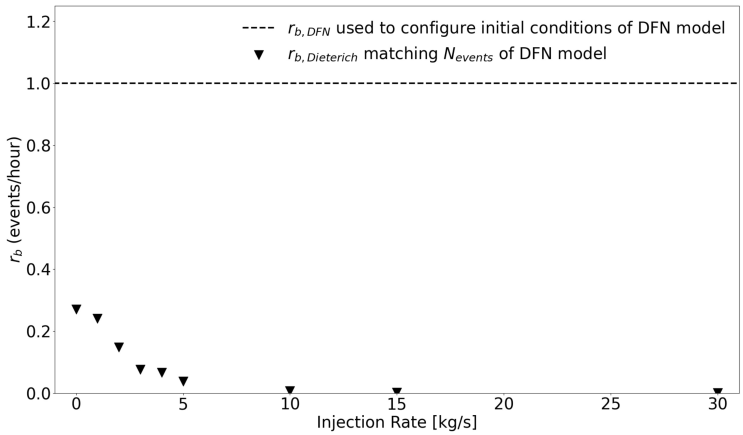

Figure 4.6: Sensitivity of $r_{b,Dieterich}$ to Injection Rate with $a_{Dieterich} = a_{DFN}$: $r_{b,Dieterich}$ of the best fit to the DFN catalgoues are plotted for all tested injection rates. $r_{b,Dieterich}$ is lower than the value of $r_{b,DFN}$ used to configure the initial conditions of the DFN model (dotted horizontal line) at all injection rates. $r_{b,Dieterich}$ decreases with increasing injection rate in order to match the total number of events in the DFN model which is limited by the number of embedded fractures.

continuous integration of the seismicity rate in space for the Dieterich model also results in a stronger peak of the seismicity rate in time at the onset of the injection followed by a more rapid decay. The comparatively muted peak of the DFN model is limited by the finite number of faults that experience the higher stressing rates closer to the injection source. The deviation of the finite fault network from the theoretical setting of continuously distributed nucleation sources is mitigated at later times, as the stressing rate decays to zero and the spatial gradient of the Dieterich seismicity rate decreases.

Figure 4.7 shows the comparisons between the two models when $a_{Dieterich}$ is no longer constrained to equal a_{DFN} but is inferred as a free parameter. With respect to a_{DFN}, $a_{Dieterich}$ decreases significantly for all injection rates in order to dampen the peak seismicity rate at the onset of the injection. Physically, lower values of a in rate-and-state friction represent lower initial resistance to sudden increases in the slip rate. The weakened resistance translates to lower times to instability in the Dieterich model such that seismicity is more easily observed at further distances experiencing lower stressing rates (Wenzel, 2017). This results in a seismicity rate distribution that varies less rapidly in space as the seismicity rate responding to slower stressing rates at further distances (containing larger volume fractions of the reservoir) are now higher than before. When integrated in space, the evolution of the seismicity rate in time is more gradual as in the DFN catalogue. Incidentally, the

greater radial distance of seismicity in the Dieterich model with lower values of a match better the spatial distribution of the DFN catalogue, although the fit in terms of the spatial location of events was not directly taken into account for the inversion. r_b is lowered further than when $a_{Dieterich} = a_{DFN}$ in order to match N_{events} as lower values of $a_{Dieterich}$ increases the total seismicity rate (Figure 4.8).

To match the faster rate of decay in the seismicity rate at higher injection rates, $a_{Dieterich}$ initially increases with the injection rate (Figure 4.8). At higher injection rates, the Dieterich models consist of discontinuities in the convexity of the seismicity rate history in time (e.g., Figure 4.7c&d). The visible bump near the onset of injection occurs due to the truncation of the singular pressure field. In order to avoid the singularity of the pressure profile at the origin, the Dieterich model is computed in space starting at the minimum radial distance of the faults in the DFN model. The effect of the truncation of the pressure field on the seismicity rate is amplified at lower values of a which increases the argument of the exponential in Equation 4.3. This causes a decrease in $a_{Dieterich}$ at higher injection rates. The DFN model is independent to truncation effects given that the fault closest to the origin avoids levels of pressure that are higher than the ambient normal stress.

4.6 Finite Size Effects Observed in Stimulation of GPK1 in Soultz-Sous-Forêts

We refer to the stimulation of the GPK1 injection well in Soultz-Sous-Forêts for evidence in real catalogues of physical effects we have highlighted thus far from considering reservoirs and faults of finite size. We focus in particular on the injection schedule lasting a period of about 400 hours between September 1 to September 18 of 1993. In the radial distribution of events of the relocated catalogue in Soultz-Sous-Forêts, a back-propagation front of the seismicity cloud during the injection period is visible (Figure 4.9) as in the DFN catalogues. The co-injection back-front was noted and studied in detail by De Barros et al. (2024) along with similar observations from a number of other injection sites and natural swarms. Particularly with respect to Soultz-Sous-Forêts, De Barros et al. (2024) noted an increase in the minimum magnitude close to the back-front as an indication that the back-front occurs due to the increase in nucleation size. The back-front of the DFN simulations could also occur due to the increase in nucleation size for initial distributions of time to instability such that the maximum time to instability of the system is large. With increasing maximum time to instability, the back-front predicted by the exhaustion of nucleation sources would converge more closely to the x-axis in the distance-time plot, and the nucleation length would become the

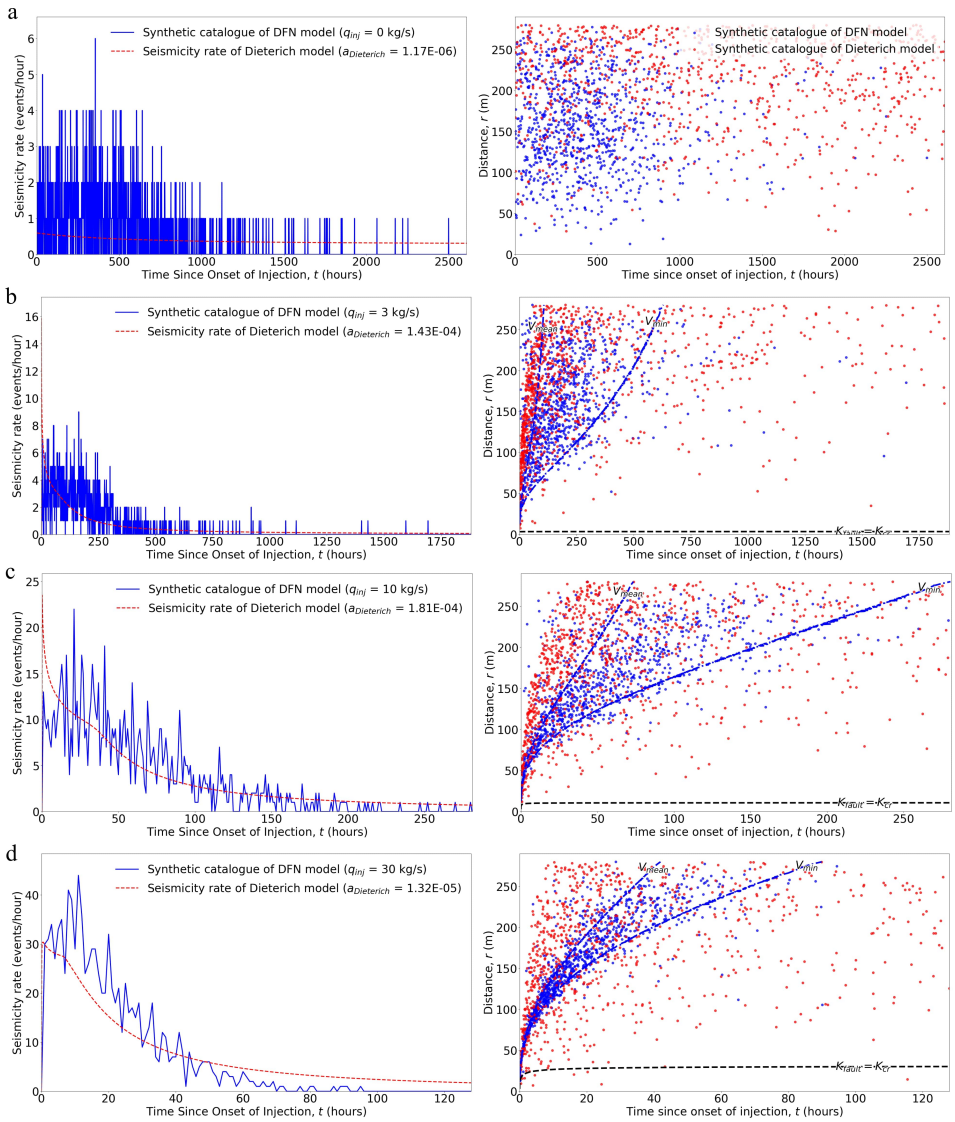

Figure 4.7: Dieterich Model Fits to DFN Catalogues with $r_{b,Dieterich}$ and $a_{Dieterich}$ as Free Parameters. The Dieterich model is matched to DFN catalogues at different injection rates by adjusting the background seismicity rate parameter, $r_{b,Dieterich}$ to match the total number of events, and adjusting $a_{Dieterich}$ to match the evolution of the seismicity rate with time. The Dieterich model tends to have higher peaks of the seismicity rate at the onset of injection due to accessing an infinite population of the nucleation sources, especially close to the injection source. To dampen the peak and match the DFN catalogue more closely, $a_{Dieterich}$ is lowered with respect to a_{DFN}. The peak is stronger at higher injection rates in the DFN catalogue, and $a_{Dieterich}$ increases slightly. Lower values of $a_{Dieterich}$ increase the seismicity rate at further distances and matches more closely the spatial distribution of events in the DFN catalogue.

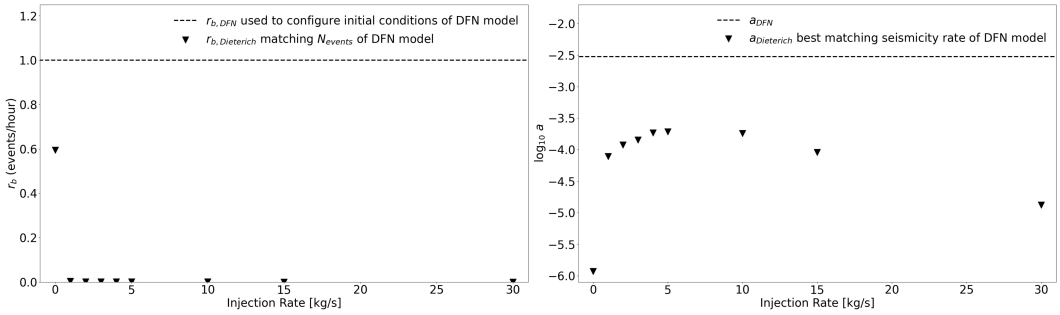

Figure 4.8: Sensitivity of Matching $r_{b,Dieterich}$ and $a_{Dieterich}$ to Injection Rate. $r_{b,Dieterich}$ and $a_{Dieterich}$ of the best fit to the DFN catalgoues are plotted for all tested injection rates. Both $r_{b,Dieterich}$ and $a_{Dieterich}$ are lower than $r_{b,DFN}$ and a_{DFN} at all injection rates. Compared to when $a_{Dieterich}$=a_{DFN} (Figure 6), $r_{b,Dieterich}$ is lowered even further as lower values of $a_{Dieterich}$ tends to increase the normalized seismicity rate. $a_{Dieterich}$ initially increases with the injection rate in order to match higher peaks of the seismicity rate evolution at the onset of injection, until around 5-10 kg/s where it begins to decrease due to effects of truncation of the singular pressure field. The systematic decrease in $a_{Dieterich}$ compared to a_{DFN} reveals that the underestimate of $a_{Dieterich}$ can be attributed to the exhaustion of a finite number of nucleation sources in real reservoirs.

limiting factor for the observed back-front. A qualitative difference between the two mechanisms would be that the minimum magnitude along the back-front for the case of source exhaustion should be more random as opposed to a systematic increase for the case of increasing nucleation size. As noted by De Barros et al. (2024), however, observational analysis of minimum magnitude is sensitive to noise, and those measured in Soultz were in fact below the magnitude of completeness. Here, we test the hypothesis that the co-injection back-front could occur due to the exhaustion of a finite fault network.

We match the temporal the recession of the seismicity cloud using Equation 4.9. A minimum slip rate of the initial distribution, V_{min} = 2.0e-15 m/s as V_{front} traces well the back front of the observed catalogue. Similarly, V_{mean} = 2.1e-12 m/s as V_{front} also follows the triggering front of the seismicity cloud. The fit to the triggering front does especially well in catching the transition from the $\sqrt{t}$ shape to a more linear curve that visibly occurs in the relocated catalogue at a period of about 150 hours. As discussed in Section 4.5, this transition may mark the point at which stress perturbations by the background tectonic loading and the initial time to instability of the nucleation sources become significant with respect to perturbations from the injection. The two values for V_{min} and V_{mean} would define the distribution of

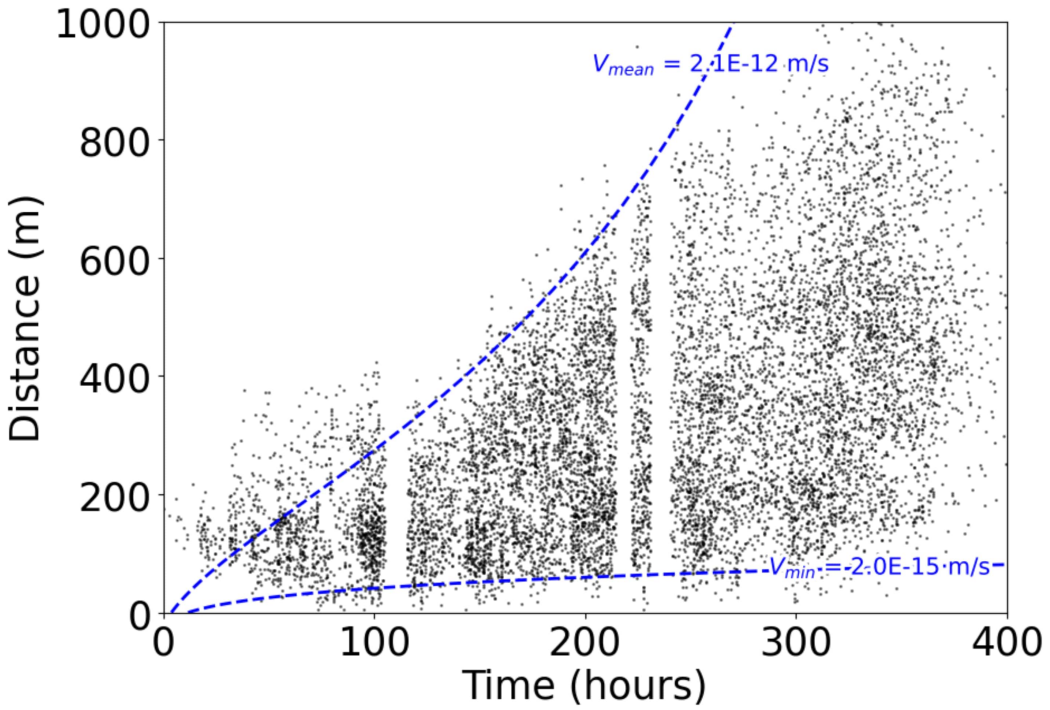

Figure 4.9: Matching of Triggering and Co-injection Back Fronts in the Relocated Catalogue of Soultz-Sous-Forêts: A transition in the shape of the triggering front from a $\sqrt{t}$ to linear curve and a co-injection back-propagation front are both observed in the relocated catalogue of the Soultz-Sous-Forêts stimulation. Both seismicity fronts are matched considering the time to instability (Equation 4.9 for the pressure history with an average and minimum initial slip rates of V_{mean} = 2.1e-12 m/s and V_{min} = 2.0e-15 m/s. The quality of the match shows that the spatial pattern of seismicity in Soultz can be explained by the exhaustion of nucleation sources in a finite fault network. The parameters of the model are summarized in Table 4.2.

initial slip rates for the fault network in Soultz-Sous-Forêts. For seismic sources that undergo stick-slip motion, the initial slip rates make sense that they would be significantly lower than the typical tectonic loading rate (~ 1e-9 m/s). The sources spend the most time during the aseismic loading period, or the 'stick' phase, and the slip rates should be orders of magnitude lower than the rate of loading.

Another interesting observation from the Soultz stimulation was by Cauchie, Lengliné, and Schmittbuhl (2020) observed that the source radii distribution both increased in the frequency of larger events and decreased in the frequency of smaller events during continuous injection (Figure 4.10a), possibly due to the initiation of new fractures. The increase in frequency of larger events with injection can also be explained by the notion that propagation of fluid-induced ruptures is limited by

the extent of fluid stimulation in space (Shapiro, Krüger, and Dinske, 2013). The decrease in frequency of smaller events may be due to the increase in frictional stability that drives smaller nucleation sources to be aseismic. For a finite setting, the stability criterion based on the spring stiffness translates to the nucleation size, h^*, or the minimum dimension of slip that a source must reach for it to grow unstable (Chen and Lapusta, 2009; Rubin and Ampuero, 2005),

$$h^* = \frac{\pi}{2} \frac{GbD_{RS}}{\bar{\sigma}(b-a)^2}. \tag{4.12}$$

A decrease in the effective normal stress due to injection would increase the nucleation size, possibly transitioning previously seismic faults to be aseismic depending on the size of the fault.

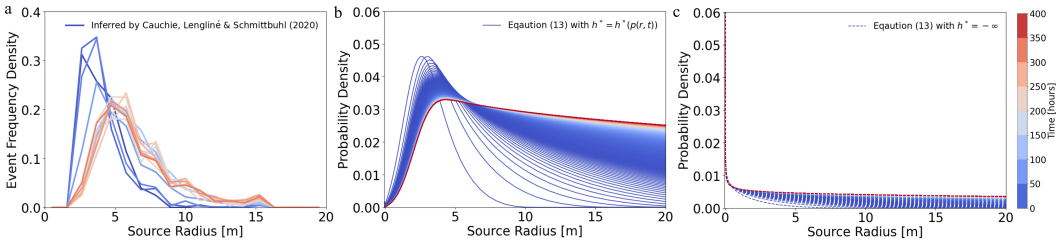

Figure 4.10: Evolution of Source Radii with Time in Soultz-Sous-Forêts and Representative Model of Rate of Event Magnitudes. (a) The event frequency density of source radii distribution due to the stimulation of the GPK1 injection well in Soultz-Sous-Forêts in 1993 is plotted at increasing time (catalogue developed by Cauchie, Lengliné, and Schmittbuhl (2020)). (b) The distribution is reproduced by a model of the rate of magnitudes (Equation 4.13 considering both the effect of stimulated volume on rupture propagation and the dependence of nucleation size on effective normal stress. The increase in nucleation size due to injection reproduces both the Gaussian shape of the distribution along with the decreasing frequency of smaller events with time. (c) Without consideration of the normal stress dependence of nucleation size, the events of the highest frequency have the smallest detectable size for all time. The parameters of the model are summarized in Table 4.2.

To test whether the injection-induced change in frictional stability can reproduce a qualitative match to the observation of Soultz-Sous-Forêts, we simulate a representative injection scenario and model the evolution of event magnitudes. Hydraulic properties are taken from the direct estimates from the GPK1 stimulation by Audigane, Royer, and Kaieda (2002). Initial normal stress conditions are linearly interpolated to the average injection depth of 2925m from that estimated for the GPK2 stimulation by Baisch et al. (2010). Initial shear stress is set to the product

of the Byerlee friction coefficient (0.6) and the initial normal stress, and the initial pore pressure is calculated as the hydrostatic pressure at the injection depth. A pressure source is defined at the origin of an infinite, homogeneous, isotropic, and elastic medium for which the injection pressure increases logarithmically as an approximation to the sequence of step-wise increase imposed at Soultz-Sous-Forêts. To account for the high extent of damage induced by the injection to the area surrounding the the well (Baria et al., 1999), the singular pressure field is offset by an effective well radius of 25m.

We compute the rate of individual magnitudes by an adaptation of the formalism introduced by Segall and Lu (2015). Restricting all ruptures to be contained within the stimulated region — a sphere of radius that grows as $\sqrt{4ct}$ —, the rate of events with magnitude, M_w, is a product of the rate of all events, R, the probability of the magnitude (assumed stationary as Gutenberg-Richter), $P_{GR}(M_w)$, and the probability that a circular rupture is fully contained in the stimulated region, $P_{in}(r_s(M_w))$ (derived in Appendix B of Segall and Lu, 2015). Here, we add the condition that the event only occurs if the rupture area is larger than the nucleation size. We account for the possible heterogeneity of the nucleation size from heterogeneity of rate-and-state parameters and stress conditions. Assuming the heterogeneity follows a Gaussian distribution, the rate of events with radius r_s follows

$$R(r_s,t) \equiv \int R_{Dieterich}(\boldsymbol{x},t) P_{GR}(r_s) P_{in}\left(\frac{r_s}{\sqrt{4ct}}\right) \Phi^{tr}(r_s - h^*(r,t))\, dV \qquad (4.13)$$

where Φ^{tr} is the cumulative density of the standard normal distribution, truncated at the lower end by $h^* > 0$. r_s relates to magnitudes by $\Delta\tau = \frac{7}{16}\frac{10^{1.5M_w+9.1}}{r_s^3}$ assuming a circular rupture area (Eshelby, 1957) with stress drop, $\Delta\tau$ = 3MPa. For rate-and-state parameters, we choose a and D_{RS} of 0.01 and 10μm, respectively, and $b - a$ proportional to the stress drop such that $\sigma(b-a)\ln\left(\frac{V_{dyn}}{V_{ini}}\right)$ = 3MPa, with V_{dyn} = 0.1 m/s and V_{ini} = 1e-9 m/s. Note that the value of $a_{Dieterich}$ used to compute the seismicity rate R is different from the more physical value of a used to calculate the nucleation size h^*. $a_{Dieterich}$ is chosen to be orders of magnitude lower than physically observed values of a from laboratory experiments to account for the infinite population effect (Section 5). The parameters of the simulation are summarized in Table 4.2.

The resulting evolution of the source radii distribution with time is shown in Figure 4.10b. As in Segall and Lu (2015), the rate of larger magnitudes increases with

time, as the limit for the maximum magnitude increases with injection duration. When accounting for the change in nucleation size, the rate of smaller magnitudes decrease as the nucleation size closer to the injection source (where there are more events) increases and events smaller than the nucleation size no longer occur. The rate-and-state parameters chosen for the simulation significantly decrease the rate of small events such that the peak of the initial distribution is around $M_w = 2.5$. The result is an evolution of a relatively Gaussian source radii distribution similar to that observed in Soultz-Sous-Forêts. The model significantly overpredicts the rate of larger events, which indicates that the $\sqrt{4ct}$ evolution of the stimulated sphere may overestimate the maximum size of the allowable rupture. Without accounting for aseismic nucleation sources, the peak of the distribution is the smallest detectable radius for all time.

4.7 Implications for Induced Seismicity Forecasting Through Physical Modeling

The differences documented here between the DFN and Dieterich models demonstrate that the assumptions of the Dieterich model pose strong biases when applied to reservoirs containing a finite number of faults. The reduction in $a_{Dieterich}$ that is needed to match a_{DFN} is consistent with the generally low values of $a\bar{\sigma}$ that is inferred from field observations. The DFN model suggests that the underestimation comes from the compensation for a more gradual decay of the seismicity rate in time (which in fact results from an exhaustion of a finite fault network), through a reduction of the the direct effect of rate-and-state friction. As a brief case study, we take the value of $a_{Dieterich}$ = 6e-5 inferred from the 2018 geothermal well stimulation of Otaniemi (Kim and Avouac, 2023). The ratio of a_{DFN} to $a_{Dieterich}$ for the highest injection rate of 30kg/s (Figure 7d) which produces maximum pore pressure similar to that measured in Otaniemi is 227, which multiplied to $a_{Dieterich}$ = 6e-5 of Otaniemi gives 0.014 — a typical value measured in laboratory experiments. Thus, the values of $a_{Dieterich}$ inferred from field data may be consistent with laboratory measurements if properly considering the bias of the infinite population effect.

Laboratory measurements of the direct effect and more generally, the consideration of rate-and-state effects in friction is still paramount even in the presence of the bias on $a_{Dieterich}$ from assuming an infinite fault network. To illustrate this point, we compare the response of two fault networks to a common injection scenario, where the networks share the same distribution of times to instability for the constant stressing rate, but with different values of a_{DFN} (0.003 and 0.013). Figure 4.11

shows the radial distributions and the seismicity rate history in time for the two catalogues. Even though the two fault networks would produce the same constant seismicity rate for a constant stressing rate, the two have noticeable differences for the evolution of pressure caused by the injection. Namely, seismicity of the network with the lower value of $a_{DFN} = 0.003$, which has a lower value of $a\sigma$, extends further in space. Additionally, the lower value of a which decreases t_a causes a more rapid decay in the seismicity rate during the injection period. Both results are consistent with what is predicted by the Dieterich model. The lower value of $a\sigma$ acts like a threshold stress in space that allows further propagation of the seismicity in space while the lower value of t_a corresponds directly to a faster relaxation time of the seismicity rate in response to a sudden change in stress. Thus, the effect of a finite fault network and finite nucleation from rate-and-state effects must be considered together in forecasts of induced seismicity.

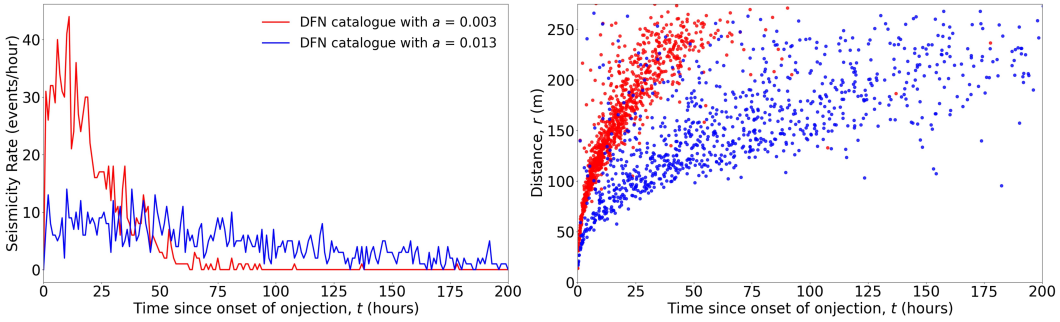

Figure 4.11: Effect of Finite Nucleation on Seismicity Rate in a Finite Fault Network: An injection triggers seismicity in two finite fault networks with the same distribution of times to instability under constant stressing but different values of a_{DFN} (0.003 and 0.013). The network with lower value of a_{DFN} = 0.003 produces both a seismicity pattern that extends further in space and a more rapid decay of seismicity rate in time. The two features are consistent with the dependence of seismicity on $a\sigma$ and t_a in the Dieterich model. A lower value of $a\sigma$ acts like a lower threshold value that allows further propagation of seismicity in space while a lower value of t_a corresponds directly to faster decay of seismicity rate for a sudden change in stress. Thus, the finite nucleation process in rate-and-state friction still has a significant impact on the seismicity rate of a finite fault network.

r_b of the Dieterich model lacks physical meaning in the finite setting. The orders of magnitude difference in the inferred values of r_b between the 2018 Otaniemi geothermal stimulation and the Basel Deep Heat Mining project (Kim and Avouac, 2023) may in fact be due to numerous factors not limited to differences in the fault density, the natural return period of the faults, and their initial conditions. The

dependence of r_b on the stressing rate indicates a possible difficulty in calibrating the Dieterich model to natural seismicity such as swarms (Sirorattanakul et al., 2022) and tidal loads (Ader et al., 2014), prior to applying the calibrated model to injection settings with higher stresses. Such features all highlight the importance of considering specific initial conditions among a finite network of faults when interpreting characteristics of induced seismicity through physical modeling.

The natural evolution of the fault network in the DFN models to steady conditions of constant seismicity rate driven by source to source interactions may be a useful mechanism to constrain initial conditions of a previously unmonitored reservoir. The convergence to steady seismicity rate as a result of interactive loading is supportive of the implicit statement of assumption 1 that such a steady seismicity rate exists. However, the steady seismicity rate is achieved differently in the DFN and Dieterich models. In the Dieterich model, steady seismicity rate is only possible for an indefinite period of time from having an infinite population of faults that continue to supply nucleation sources with infinitely low initial slip rates. In the DFN model, steady seismicity is reached by source interactions that even out the interevent duration to be roughly constant. Thus, the steady seismicity rate in the DFN model includes re-rupturing of the same nucleation source. This leads to a vastly different distribution of initial conditions that would be drawn from a single snapshot of a random instance in time from the two models. Since the life cycle of a single nucleation source is dominated in time by the aseismic and nucleation period, the overwhelming majority of the faults in the DFN model would be far from instability, thereby violating the 'no-healing' assumption of the Dieterich model. Figure 4.12 shows the final distribution of the long-term simulation of section 4.4 without the injection. Such a snapshot could in fact be used as a more realistic initial distribution for an injection setting. A systematic study of the long-term convergence of stress and slip rate conditions in more complex fault networks (e.g., with heterogeneity in fault size and frictional parameters) could allow better constraints of initial conditions that naturally arise from tectonic loading prior to injections.

4.8 Conclusions

In this chapter, we highlight the major assumptions of the Dieterich (1994) seismicity rate model and examine how they may bias interpretations of induced seismicity observed in real reservoirs by comparing it directly to a Discrete Fault Network (DFN) model. The comparisons reveal that parameters of the Dieterich model lack clear physical meaning in the finite analogue. The background seismicity

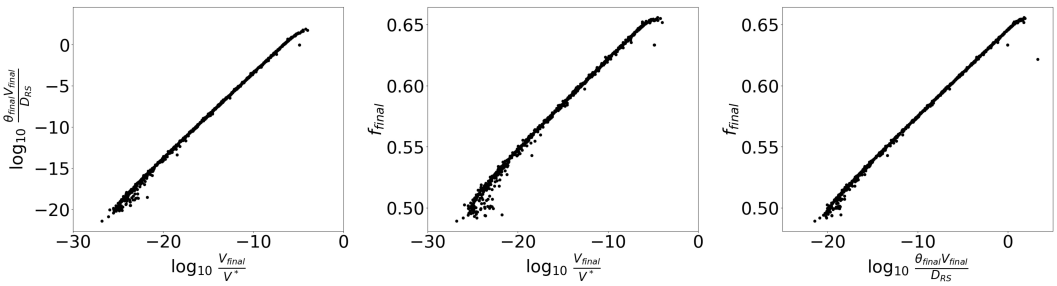

Figure 4.12: Steady-State Conditions of a Fault Network Under Constant Loading. The final distribution of the slip rate, $\frac{V_{final}}{V^*}$, the normalized state variable, $\frac{\theta_{final} V_{final}}{D_{RS}}$ and friction, f_{final}, of all faults at the end of a long-term simulation with constant loading are plotted in their phase planes. The plotted distribution produces a roughly constant seismicity rate with the majority of the faults being below-healing ($\frac{\theta_{final} V_{final}}{D_{RS}} < 1$). The numerical simulation provides a possible candidate for more accurate initial conditions of an unstimulated reservoir prior to injections.

rate parameter, r_b, shows a dependence on the stressing rate when inferred from catalogues of the DFN model due to the fact that r_b in the Dieterich model is based upon an infinite population of nucleation sources. Additionally, the direct effect parameter of rate-and-state friction, a, needs to decrease significantly in order to match the more gradual decay of the seismicity rate due to the exhaustion of nucleation sources. This decrease in a is consistent with the underestimates of $a\bar{\sigma}$ commonly encountered in matching the Dieterich model to real seismicity (Acosta et al., 2023; Bettinelli et al., 2008; Gross and Bürgmann, 1998; Gross and Kisslinger, 1997; Kim and Avouac, 2023; Toda et al., 1998, 2012). The comparisons to the DFN model confirm that the underestimates are due to the biases posed by the assumptions of the model rather than near-lithostatic levels of pore pressure. The authors do not discount the use of the Dieterich model entirely — its elegance and ease-of-use provide a valuable tool for simulating the response of a large population of faults — but emphasize that its parameters must be interpreted with care, especially in transferring a specific calibration to a new setting with different stressing rates or initial conditions (e.g., a new stimulation in a nearby well, a subsequent injection at the same location some time after the previous one, etc.).

The spatio-temporal pattern of seismicity in the finite setting, or specifically the triggering and back-propagation fronts are predicted excellently by the analytical estimate of the time to instability given an initial slip rate equal to the mean and the minimum of the initial distribution, respectively. Thus, the triggering front is not only dependent on fluid transport properties (Shapiro, Huenges, and Borm, 1997) or

its combination with nucleation characteristics (Kim and Avouac, 2023) but also the distribution of initial conditions of the fault network. The back-propagation front, in particular, occurs co-injection if the time to instability for the minimum slip rate is shorter than the injection duration. This is in contrast to the more common context in which the back front occurs immediately following shut-in due to the propagation of negative pressure rates. The Dieterich model does not predict a back front during injection as the maximum time to instability in an infinite population of sources is infinitely large. The relocated catalogue of the 1993 GPK1 stimulation in Soultz-Sous-Forêts shows such a back-front which can be fit qualitatively using the time to instability measure for V_{min} = 2.0e-15m/s. The co-injection back-propagation front may be the most salient characteristic of finite effects in an induced seismicity catalogue.

The change in frictional stability due to changes in the effective normal stress during injections is fully accounted for in the DFN model where the rate-and-state friction law is solved in its entirety without the no-healing assumption. The changes in the critical stiffness, κ_{cr} (for a single cell), or the nucleation size, h^* (for a fault discretized by multiple cells), allow previously seismic faults to become aseismic with a sufficient increase in pore pressure. Such faults tend to creep stably under loading, unlike in the Dieterich model where all nucleation sources that are initially unstable remain so regardless of changes to the local stress state. A simple model for the rate of magnitudes that accounts for the evolution of frictional stability reproduces the apparent increase in the source radius of induced events in Soultz-Sous-Forêts. The source radii distribution shifts at both the lower and upper ends of the distribution, from the elimination of smaller events that cannot reach the increased nucleation size, and the growth of the stimulated region that limits rupture propagation, respectively. The rate of larger events is overestimated by the model, possibly due to an overestimation of maximum magnitudes by the volume of stimulation, or due to a statistical manifestation of the low probability of larger events (Van der Elst et al., 2016).

An aspect of the assumptions of the Dieterich model not fully addressed here is the no-healing assumption. Both the prediction of the triggering and back-propagation fronts using Equation 4.9 still depend on the population of nucleation sources that are already accelerating towards failure to be the dominating initial condition of a fault network. In particular, the back front using Equation 4.9 may be overestimated (in the sense that it would be estimated to be further out in space at earlier times) without

accounting for faults below healing that would also be triggered by the injection. Such faults would have longer times to instability than predicted by Equation 4.3, and would drag the back front to be closer to the injection source. Thus, the fit to the co-injection back front in Soultz-Sous-Forêts may be an underestimation of the minimum slip rate. Additionally, the transition from a $\sqrt{t}$ to a linear evolution of the triggering front in Soultz-Sous-Forêts that is fit with Equation 4.9 has also been explained in terms of the propagation of aseismic slip although the rigorous analysis is limited to the case of a single fault (Sáez, 2023). In accounting for the full spectrum of possible initial states, long-term convergence of DFN simulations due to source interactions may serve as more accurate initial conditions for an injection setting. Source-to-source interactions in the DFN model lead to a self-organization of the fault network to steady-state conditions in terms of the seismicity rate under constant loading. The long-term condition of the fault network may be taken as the initial condition prior to injections as it represents a snapshot from the natural evolution of a fault network. The majority of the faults would be far from instability, making up initial conditions that are also below-healing ($\frac{V\theta}{D_{RS}} < 1$) or steady-state ($\dot{\theta} = 0$).

Both the DFN and Dieterich models use the aging law for the evolution of the state variable in rate-and-state friction, although recent studies have shown that the slip law may better match experiments (Bhattacharya, Rubin, and Beeler, 2017; Bhattacharya et al., 2022). The slip law is more nonlinear than the aging law such that an analytical treatment comparable to which was done by Dieterich (1994) may not be possible. Thus, the only way to test the slip law may be to use physical models such as the DFN model where the equations of motion are solved in their entirety. Similarly, recent experiments of gouge in the presence of fluids have revealed that rate-and-state parameters themselves may be depend on pore pressure (Bedford et al., 2021). Such physical complexities that may be important in the process of shear failure with fluids warrant a further look to determine the merit of their incorporation into constitutive relationships of future models.

Parameter	Variable	Value and Unit
Poroelastic Properties		
Shear modulus	μ	20 GPa
Drained Poisson's ratio	ν	0.25
Undrained Poisson's ratio	ν_u	0.3
Skempton's coefficient	B	0.75
Biot's coefficient	α	0.31
Transport Properties		
Permeability	k_{perm}	1.0e-15 m^2
Fluid viscosity	η	0.4 x 10^{-3} Pa· s
Reference fluid density	ρ_0	10^3 kg/m^3
Stress State		
Initial pore pressure	p_{ini}	0 MPa
Initial normal stress	σ_{ini}	100 MPa
Initial shear stress	τ_{ini}	60 MPa
Seismicity Rate Parameters		
Direct effect parameter	a	0.003
Evolution effect parameter	b	0.006
State evolution distance	D_{RS}	1 µm
Background stressing rate	$\dot{\tau}_r$	1.0 kPa/year

Table 4.1: Constant Parameters.

Parameter	Value and Unit
Permeability	6e-17 m^2/s
Storage coefficient	5e-9
Fluid viscosity	1.1 x 10^{-4} Pa· s
Reference fluid density	10^3 kg/m^3
Initial normal stress	48.1 MPa
Initial pore pressure	28.7 MPa
Initial shear stress	11.7 MPa
Direct effect parameter, a	0.010
Evolution effect parameter, b	0.018
State evolution distance, D_{RS}	5 µm
$a_{Dieterich}$	1e-5
Background stressing rate	1kPa/year

Table 4.2: Parameters for Simulation of Soultz-Sous-Forêts Stimulation.

Chapter 5

MODELING HIGH-FREQUENCY SEISMIC SIGNALS FROM DISTRIBUTED ACOUSTIC SENSING (DAS) AS ASPERITIES AND BARRIERS OF A HETEROGENEOUS FAULT

This chapter has been adapted from

Li, Jiaxuan et al. (2023). "The break of earthquake asperities imaged by distributed acoustic sensing." In: *Nature* 620.7975, pp. 800–806.

5.1 Introduction

Improvements in earthquake imaging - a challenging remote-sensing problem - have the potential to aid significantly towards a better understanding of earthquake rupture and fault physics. In particular, back-projection of far-field (teleseismic) waves using dense seismic arrays has enabled detailed examination of complex rupture processes during great earthquakes ($M_w > 7$) (Avouac et al., 2015; Ishii et al., 2005; Simons et al., 2011; Xu et al., 2009). Such studies have revealed that sources of high-frequency radiation during large megathrust earthquakes are often offset from the areas of high slip (Lay et al., 2012; Simons et al., 2011; Yao, Shearer, and Gerstoft, 2013; Yin and Denolle, 2021). Yet, the origin of high-frequency radiation during earthquakes is a topic of contentious debate in the seismological and geophysical community. Some argue that they originate from the breakage of smaller high-stress patches on the fault plane with higher fracture energy, possibly from heterogeneity of the stress state or material properties (Fan and Shearer, 2015; Koper et al., 2012; Meng, Inbal, and Ampuero, 2011). Others have proposed the possibility of elastic impact among a complex network of fault structure in the fault core and the damage zone (Tsai and Hirth, 2020; Tsai et al., 2021).

One of the challenges resides in the fact that high-frequency information is often lost in far-field recordings of smaller (and more frequent) earthquakes. Additionally, near-field imaging is challenging due to complex seismic waveforms. Recently, ultra-dense seismic arrays have enabled back-projection imaging of smaller features in moderately sized earthquakes ($M_w \sim 5, 6$) (Allmann and Shearer, 2007; Mesimeri, Zhang, and Pankow, 2021). Back-projection of the 2004 Parkfield, California with moment magnitude (M_w) 6.0 was able to identify the location of a high-frequency

radiator near an area of high slip gradient (Allmann and Shearer, 2007). Such observations are rare given the high cost and difficulty of installing ultra-dense seismic arrays. It remains relatively unknown how common such high-frequency radiators are in crustal earthquakes and whether and how they may affect the larger-scale rupture.

Distributed acousting sensing (DAS) is an increasingly promising technique in observational seismology where deformation of pre-existing fiber optic cables induced by seismic waves record high-frequency response across relatively long distances. DAS often leverages the existence of 'dark fiber' — underground telecommunication cables that are no longer in use — which solely requires the installation of a single interrogator at the end of the fiber network. The vast span of existing dark fiber networks in modern society often gives DAS superior azimuthal coverage at a fraction of the cost of conventional seismometer arrays. Recent highlights of DAS includes the identification of cap-rock above a magma chamber (Biondi et al., 2023) and improved detection of fluid-induced earthquakes from geothermal reservoirs (Li and Zhan, 2018).

A major caveat of DAS is coincidentally what also gives its biggest strength: the sheer amount of data. A typical DAS interrogator may record terabytes of data during a single day of recording (Dong et al., 2022). Such size of data poses challenges in storage but also in its interpretation. Computational models provide a possible bridge between the wealth of data and our understanding of the physical problem. In the field of earthquake physics, development in theory and its implementation in computational models have advanced, unimpeded by the practical difficulty in subsurface imaging. Efficient computational models enable us to answer the questions posed by better data, especially from high-volume sources such as DAS.

In this chapter, we model high-frequency recordings from an ultra-dense distributed acoustic sensing (DAS) array of a M_w 6.0 crustal earthquake (Lindsey and Martin, 2021; Zhan, 2020). A direct comparison of the models and observations suggests that the imaged subevents are due to the breaking of fault asperities and barriers – patches of lower and higher frictional resistance along a heterogeneous fault, respectively. The model also reveals how such asperities and barriers impact the larger-scale rupture pattern, providing an unprecedented level of detail in the imaging of a real fault rupture.

5.2 Identification of High-Frequency Radiators from The 2021 M_w 6.0 Antelope Valley Earthquake

The Antelope Valley M_w 6.0 crustal earthquake occurred on July 8th, 2021, at a depth of 7.5 km in the Antelope Valley of northern California, close to the California-Nevada border (Figure 5.1). It was the fourth earthquake of the past two decades that was greater than M_w 6 in the Walker Lane, an approximately 100-mile-wide fault zone between the Sierra Nevada Geomorphic Province and the Basin and Range Province. The focal mechanism and early aftershocks of the Antelope Valley event indicate a north-striking normal faulting plane dipping to the east (Fig. 5.1).

The earthquake was recorded by the 100-km-long Long Valley DAS array, which consists of two 50-km sections of telecom dark fiber to the north and south of the town of Old Mammoth (Figure 5.1). The 10,000 channels of the array are continuously sampled at 200Hz and distributed in 10-meter spacing between Mono Lake and Crowley Lake, mostly along the US-395 Highway. The DAS recording of the M_w 6.0 mainshock shows mostly unsaturated P and S wavefields (Fig. 5.2a). This rare dataset allowed, for the first time, the back-projection of high-frequency radiators during a moderate-sized earthquake using a DAS array (Fig. 5.2b). The details of the back-projection method specifically adapted for DAS data is beyond the scope of this thesis, and we refer the reader to Li et al. (2023) for more details. Conventional seismograms nearby — specifically, the timing of S-wave arrivals at five local strong-motion stations opearted by the USGS within an epicentral distance of 70 km (Fig. 5.1) — helped validate the DAS recordings. Long-period waveforms of the conventional seismograms also produced the moment-rate function - the time history of the rate of slip integrated over the rupture area. The moment-rate function has a duration of about 10 seconds which is relatively long, and is complex compared to other earthquakes of similar magnitude and depth (Vallée et al., 2011; Yin and Denolle, 2021).

The DAS imaging reveals four high-frequency subevents during the M_w 6.0 earthquake, hereafter referred to as subevents S0, S1, S2, and S3, according to their chronological order. The relatively weak first subevent, S0, has a similar origin time and location as the hypocenter of the M_w 6.0 mainshock as observed in the USGS catalog (Figure 5.3). Subevents S1, S2 and S3 occur approximately 0.6, 1.8, and 4.2 seconds after S0, respectively. The location and timing of the subevents identified by DAS can be validated independently by the recordings of S-wave arrivals by the conventional seismograms; the tangential components of the velocity seismograms,

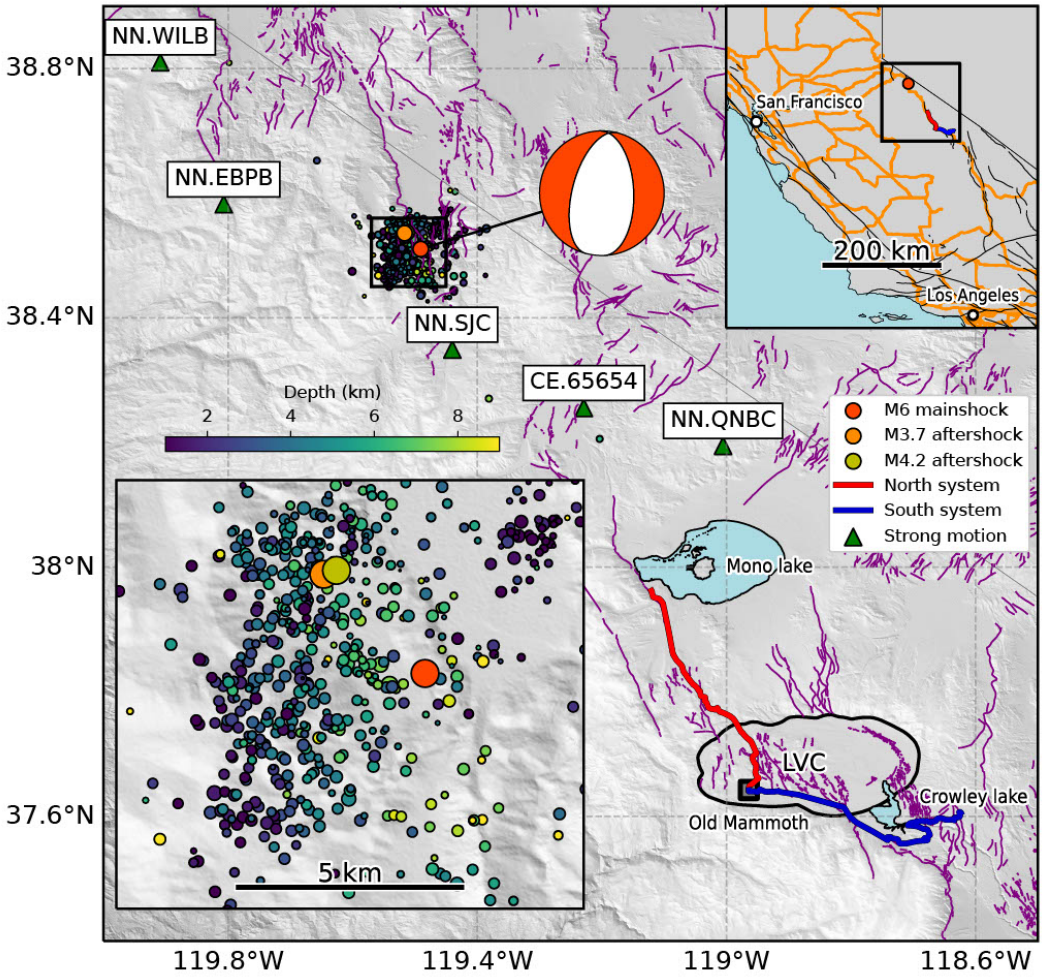

Figure 5.1: 100-km Fiber-Optic Cable as a Dense DAS array for Imaging a Crustal Earthquake. The 2021 Antelope Valley M_w 6.0 earthquake (red circle; focal mechanism shown by the red-and-white ball) occurred to the northwest of the DAS systems, within the central part of the Walker Lane fault zone hosting numerous faults (solid purple lines). The North DAS system (red line) starts from Old Mammoth and extends towards the northwest. The South system (blue line) extends to the east on the fringe of the Long Valley Caldera (LVC, indicated by the black closed curve). Five strong motion stations (green triangles) recorded unclipped data of the mainshock within a 70-kilometer epicentral distance. The 100-km fiber-optic cable used in this study represents a small portion of the currently proposed telecommunication fiber network (e.g., the 10,000-mile State of California Middle-Mile Broadband Initiative indicated by orange lines in the upper-right inset.)

which highlight high-frequency energy more than the displacement seismograms, show several strong pulses of S waves (Figure 5.3c). At each station, we find remarkable agreement between the arrival times of subevents S1-S3 predicted by the

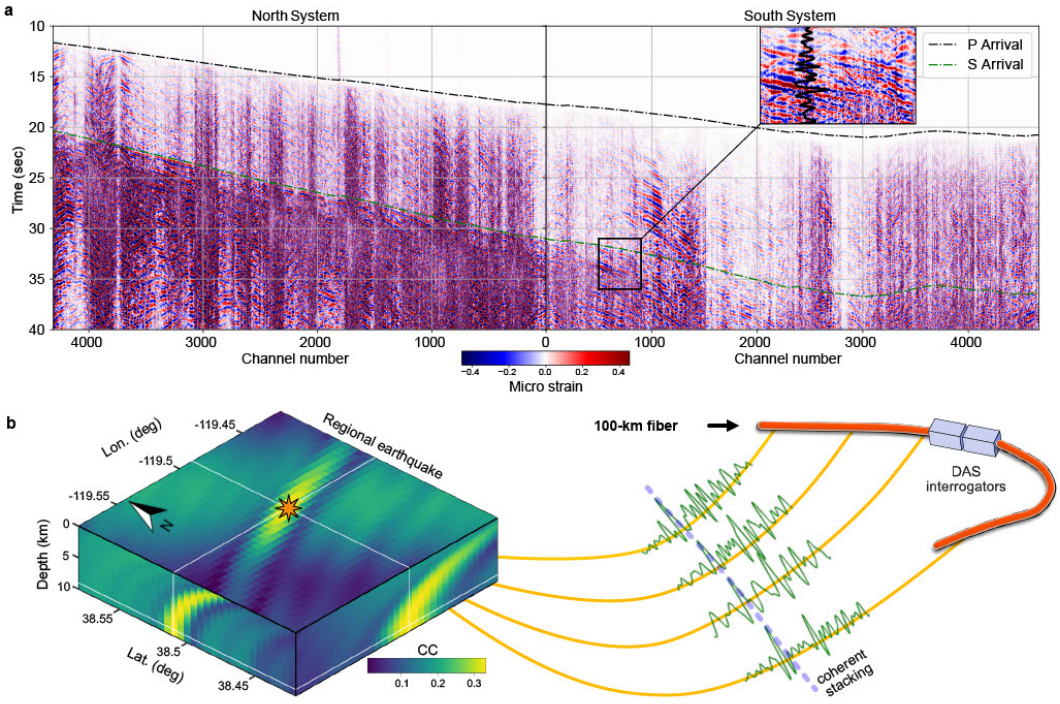

Figure 5.2: Seismic Recordings on Thousands of Closely Spaced Channels of the DAS Array Reveal Subevents in the M_w 6.0 Earthquake. (a) Seismic records (microstrain) of the M_w 6.0 event by DAS are plotted in shades of blue and red for negative and positive values, respectively. Channel number 0 is the location of the two DAS interrogators hosted at Old Mammoth. The predicted P and S arrival times (black and green lines) using a local 1D velocity model (Lee et al., 2014) match the onset of seismic energy consistently across all channels. The inset shows a zoomed-in view of the seismogram from a single channel, indicated by the black box. (b) The schematics of the 3D imaging technique using back-projection of both P and S correlograms are illustrated. Examples of S-phase correlograms averaged over 1000 channels are shown in green along the yellow ray paths. The back-projected correlograms stack coherently at the subevent location, resulting in a bright spot with high cross-correlation values (CC) in the 3D volume (yellow regions in the left block).

DAS back-projection and the timing of the tangential peak amplitudes (Figure 5.1 and Figure 5.3c). A simple scaling method along with strong-motion recordings of past earthquakes estimate individual magnitudes of M4.3, M4.6, M5.2, and M5.4, for subevents S0-S4, respectively (Li et al., 2023). The cumulative seismic moment of the subevents contributes to about 20% of the total moment of the M_w 6.0 earthquake.

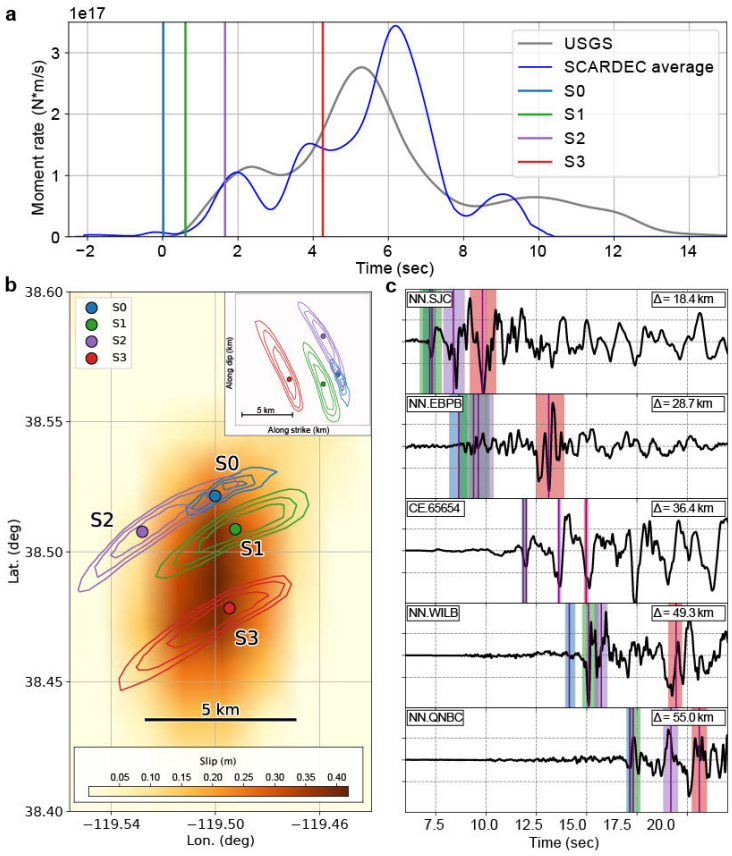

Figure 5.3: The Imaged Subevents in Relation to the Low-Frequency Finite-Fault Inversions and Recordings from Regional Seismic Stations. (a) The timing of the imaged subevents (colored vertical bars) with respect to the moment release history as captured by the USGS (grey curve) and SCARDEC methods (blue curve) indicates that the subevents occur within the first half of the earthquake. The last subevent appears to delay the release of moment release initially, before being followed by the highest peak in the moment release history. The relationship between the timing of the subevents and the shape of the low-frequency moment rate history provides valuable insights regarding the physical effect of the subevents on the overall rupture. (b) Locations of the subevents as inferred from back-projection with respect to the USGS finite-fault inversion of total slip (background colour) are indicated as the colored circles along with the contours of 70%, 80% and 90% of the peak correlation (colored contours). The inset displays the fault-plane view of the subevent locations. (c) The predicted arrival times of the S phase of the subevents (vertical lines) at five local strong-motion stations are indicated on top of the tangential components of the velocity seismograms (black curves), along with 70% of the peak correlations (shaded boxes). The clear match between the occurrence time of the subevents with peaks in the velocity seismograms support the accuracy of the DAS back-projection method.

5.3 Relationship Between the Subevents and the Overall Rupture

Several characteristics of the subevents offer clues to their physical origin. The subevents represent splashes of high-energy radiation as imaged by DAS, indicating abrupt local changes in the rupture process (Dunham, Favreau, and Carlson, 2003; Huang, Meng, and Ampuero, 2012; Madariaga, 1983). Such high-frequency radiation can be caused by several kinds of fault heterogeneity such as in frictional properties and fault geometry. Synthetic studies indicate that the exact origin of the high-frequency radiation is difficult to elucidate using back-projection results only (Li et al., 2022).

To gain further insight, we compare the high-frequency DAS back-projection with the low-frequency features of the moment rate history. First, the subevents occur when the overall moment release rate – which corresponds to the rate of slip integrated over the fault – is increasing, indicating that they promote the release of energy in the overall rupture. Second, the largest subevent S3 occurs after a marked decrease in the moment release rate. Third, subevent S3 is also preceded by a reduction in the earthquake rupture speed (Li et al., 2023): the rupture slows down to approximately 30% of the shear wave velocity before S3, despite propagating with the apparent speed of approximately 70-80% of the shear wave velocity between subevents S0 and S1 as well as between S0 and S2. Fourth, subevent S3 is followed by the second — and much larger — peak of the moment release. These observations suggest that the subevents occur as the breakage of stronger patches. The patches may act as an asperity or a barrier, defined by their tendencies to either promote or delay rupture propagation, respectively (Dunham, Favreau, and Carlson, 2003). The eventual failure of both types of patches result in a sudden release of energy and a general increase in the rupture speed. In particular, the fourth and largest subevent (S3) appears to delay rupture propagation initially, resulting in lower apparent rupture speed, before its failure leads to higher rupture speeds and larger slip. Such features make subevent S3 characteristic of a barrier.

The patches could originate from fault non-planarity, where compression of "bumps" lead to to locally higher fault-normal stress and hence higher frictional resistance. Patches of higher normal stress have been linked to supershear transitions (Dunham, Favreau, and Carlson, 2003), high-frequency radiation in subduction-zone earthquakes (Huang, Meng, and Ampuero, 2012), and foreshock-like seismicity in laboratory experiments (McLaskey and Kilgore, 2013) and numerical models (Schaal and Lapusta, 2019). Heterogeneity in fluid pressure due to hetereogeneous

fluid transport properties could also result in patches of high or low effective normal stress. Alternatively, stronger patches could comprise of different rock material with higher friction. In the following section, we test the hypothesis of frictional heterogeneity and the stress state using a computational model of a dynamic rupture.

5.4 A Dynamic Rupture Model of a Heterogeneous Fault with Asperities and Barriers

To illustrate how a fault with locally stronger patches can lead to rupture dynamics with subevents as captured by the DAS observations and the low-frequency properties of the overall event, we perform dynamic rupture simulations on a rate-and-state fault (Lapusta and Liu, 2009). Our simulations consider the slip on a 2-D fault embedded into a 3-D uniform, isotropic, and elastic medium. To conduct simulations of dynamic rupture, we utilize a spectral boundary integral method, which solves the evolution of slip rate and other variables along the fault by equating the evolving fault shear stress to its shear resistance (Geubelle and Rice, 1995). The evolution of shear stress on each discretized cell of the fault depends, in part, on slip elsewhere on the fault through wave-mediated dynamic stress transfers which, in part, depend on the bulk properties. We assign rock properties typical at seismogenic depths (Table 5.1).

The shear resistance along the fault follows the laboratory-derived Dieterich-Ruina rate-and-state friction law with the state evolution governed by the aging formulation Dieterich, 1979; Marone, 1998; Ruina, 1983:

$$\begin{aligned} \tau &= \bar{\sigma} f(V,\theta) = \sigma \left(f^* + a \log\left(\frac{V}{V^*}\right) + b \log\left(\frac{V^*\theta}{D_{RS}}\right)\right) \\ \dot{\theta}(V,\theta) &= 1 - \frac{V\theta}{D_{RS}} \end{aligned} \tag{5.1}$$

where τ is the shear resistance, $\bar{\sigma}$ is the effective normal stress, f^* is the reference steady-state friction coefficient at reference sliding rate V^*, D_{RS} is the characteristic slip distance, and a and b are the direct effect and evolution effect parameters, respectively. We use the version of the Equation 5.1 regularized for zero and negative slip rates (Noda and Lapusta, 2010). Dynamic slip can nucleate only if the region with velocity-weakening friction properties, $(a - b) < 0$, is larger than the nucleation size h^*_{RA}, which can be estimated as (Chen and Lapusta, 2009; Rubin and Ampuero, 2005):

$$h^*_{RA} = \frac{\pi}{2}\frac{GbD_{RS}}{(b-a)^2\sigma} \tag{5.2}$$

where G is the shear modulus. We choose our spatial discretization to resolve both this nucleation length scale as well as the rapid evolution of shear resistance and slip rate at the rupture front that occurs over the spatial length scale – the cohesive-like zone – which can be estimated as (Day et al., 2005; Lapusta et al., 2000; Palmer and Rice, 1973):

$$\Lambda_0 = C_1\frac{G}{W} \tag{5.3}$$

where $C_1 = \frac{9\pi}{32}$ is a constant and $W = \frac{b\sigma}{D_{RS}}$ is the weakening rate.

Our simulation methodology allows us to resolve earthquake sequences in their entirety, including spontaneous nucleation, dynamic rupture propagation, postseismic slip, and interseismic creep. However, here we use it to simulate a single instance of nucleation and dynamic rupture propagation on a fault segment with velocity-weakening steady-state properties of rate-and-state friction, with the initial conditions motivated by earthquake sequence simulations in models with similar fault properties. The initial conditions are then further tuned to produce the high-frequency features of the DAS back-projection and the low-frequency features of the final slip inversion and moment rate history.

Adjustable parameters in the model include the rate-and-state properties of the fault (f^*, a, b, D_{RS}), the initial conditions, and the size and properties of the high-stress patches. We tune these parameters simultaneously to fit the observed moment rate, duration of rupture, magnitude, and occurrence times of the individual subevents, assisted by known relationships between frictional properties and the resulting rupture dynamics from prior modeling (Barbot, Lapusta, and Avouac, 2012; Lapusta et al., 2000; Schaal and Lapusta, 2019). The relative locations of the high-stress patches, which are modeled as areas of higher effective normal stress (Figure 5.5), correspond exactly to the correlation peaks of the back-projection (Figure 5.3) with only minor differences for S3 within the range of high correlation to match its occurrence time.

The initial shear stress level is assigned with respect to τ_{dyn}, the dynamic shear resistance to which a given point on the fault converges as the rupture propagates through it, given by the steady-state shear resistance at a dynamic slip rate, V_{dyn}:

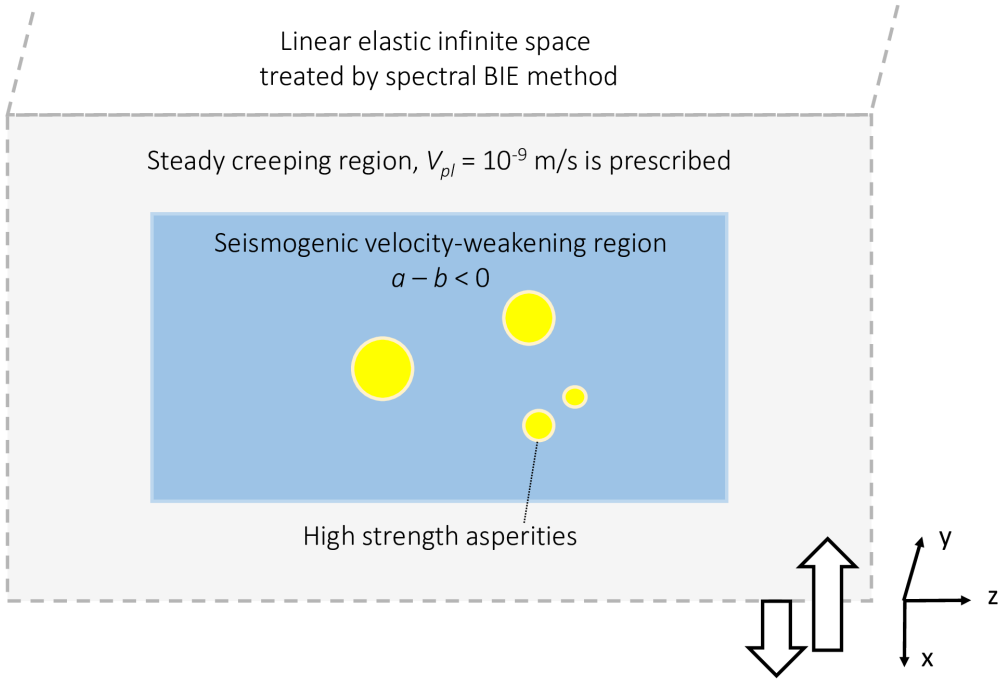

Figure 5.4: Schematic of the Dynamic Rupture Model. The spectral boundary-integral method simulates frictional slip between two infinite, homogeneous and elastic bodies in continuum and fully accounts for the effect of inertia. The computational domain consists of an outer region (colored in grey) with a prescribed rate of slip (at an approximate plate rate of 1e-9 m/s) to mimic tectonic loading on the seismogenic portion of the fault (colored in blue). The seismogenic portion consists of four circular patches (colored in yellow) with relatively high initial stress and frictional properties that match the observed behavior of the high-frequency radiators. The model provides an efficient method to rigorously test the hypothesis that the high-frequency radiation originates from patches of high stress on a heterogeneous fault.

$$\tau_{dyn} = \sigma \left(f^* + (a - b) \ln \frac{V_{dyn}}{V^*} \right). \tag{5.4}$$

To select the initial stresses, V_{dyn} is approximated to be 0.1 m/s. The sustained slip rate behind the rupture front may vary from 0.1m/s to several meters per second, but the exact value of V_{dyn} does not change τ_{dyn} much due to the weak dependence through the natural log (Equation 5.1). Initial stress levels sufficiently above τ_{dyn} present favorable conditions for rupture propagation, as they allow for positive stress drop. Initial stress levels below τ_{dyn} present unfavorable conditions for rupture propagation. Thus, shear stress level is prescribed to be above τ_{dyn} over the desired

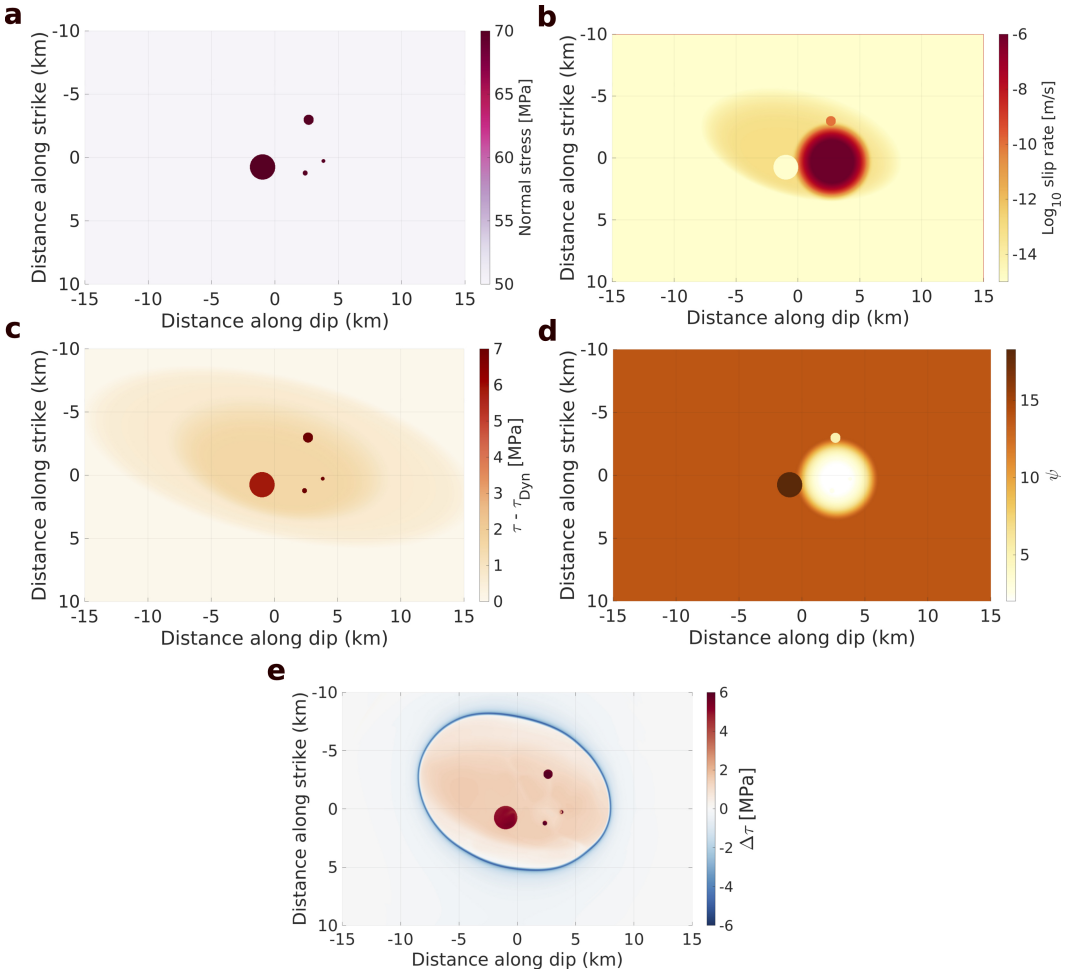

Figure 5.5: Distribution of Initial Conditions and Final Stress Drop Across the Fault. Contour plots show the distribution of (a) initial normal stress, (b), slip rate, (c) shear stress above the dynamic level, τ_{dyn}, (d) the normalized state variable, $\frac{V^*\theta}{D_{RS}}$, an (e) the distribution of the final stress drop after rupture arrest. The distribution of initial conditions are inspired by typical development of prestress profiles observed in long-term simulations. Patches of high normal stress have smaller nucleation size and are more inherently unstable than the surroundings, leading to lower slip rate and higher shear stress. When the rupture passes through the entire fault, the patches experience higher stress drop as they release the greater amount of stored energy The average stress drop across the fault is 1.4 MPa while the stress drop within the high-stress patches ranges from 5.0 to 6.1 MPa. The particular set of initial conditions and fault properties (which are non-unique) reproduce the timing of the subevents and the low-frequency moment rate history inferred from the Antelope Valley earthquake.

rupture region and to decrease towards its edges, with the boundary of the region coinciding with the region of slip as inferred from the USGS finite-fault inversion

(Figure 5.3). Based on long-term simulations, the initial stress level is chosen to be at maximum 1.5 MPa above the local τ_{dyn} near the nucleating region. The state variable is prescribed similarly to create a region of low θ near the nucleating region that increases gradually to a uniform value of 50 years. Given fault healing in the interseismic period with θ growing with the time, this serves as an appropriate initial condition for the region of the Antelope Valley earthquake which had not recorded an event at the scale of M_w 6.0 for at least such time. Once the shear stress and θ are prescribed, the slip rate is uniquely defined by Equation 5.1, resulting in a region of relatively low slip rate in the nucleation region (~1e-7 m/s) that decreases monotonically to a much lower rate corresponding to locked conditions at interseismic timescales (~1e-17 m/s, which is roughly less than a nanometer per year).

Initial conditions and frictional properties of the high-stress patches are configured in conjunction with the given properties of the background fault to match the observed data (Table 5.1). The level of initial shear stress above τ_{dyn} and the size of the high-stress patches are selected so that the event reproduces the estimated moment magnitude of each subevent. Since the static stress drop increases with larger initial stress, initial stress is in fact proportional to slip and the amount of moment released from breaking the high-stress patches. The patch sizes are chosen to be smaller than the local nucleation size given their higher normal stress, in order to mimic conditions that would promote the build-up of shear stress on the patches during interseismic loading without nucleating dynamic slip. The relative differences in the sizes of the patches are chosen to reflect the differences in the magnitudes of the subevents inferred from the scaling analysis (Li et al., 2023).

The initial conditions and frictional parameters of the high-stress patches are further tuned to illustrate how they can either impede or promote the rupture, in order to achieve the desired fit to the moment release rate in time. To understand how such properties could be selected systematically, it is useful to consider the friction-displacement history of a single point on the fault as a rupture passes through it. At the dynamic rupture front, the rate-and-state formulation yields an evolution of shear stress closely mimicking the linear slip-weakening law (Bizzarri and Cocco, 2003; Lapusta et al., 2000). Under these conditions, the initial friction, $\left(\frac{\tau}{\sigma}\right)_{ini}$, peak friction, $\left(\frac{\tau}{\sigma}\right)_{peak}$, and dynamic friction, $\left(\frac{\tau}{\sigma}\right)_{dyn}$ are given by:

$$\left(\frac{\tau}{\sigma}\right)_{ini} = f^* + a \ln\left(\frac{V_{ini}}{V^*}\right) + b \ln\left(\frac{\theta_{ini}}{\theta^*}\right)$$

$$\left(\frac{\tau}{\sigma}\right)_{peak} = f^* + a \ln\left(\frac{V_{dyn}}{V^*}\right) + b \ln\left(\frac{\theta_{ini}}{\theta^*}\right) \tag{5.5}$$

$$\left(\frac{\tau}{\sigma}\right)_{dyn} = f^* + a \ln\left(\frac{V_{dyn}}{V^*}\right) + b \ln\left(\frac{\theta_{dyn}}{\theta^*}\right)$$

where $\theta^* = \frac{D_{RS}}{V^*}$. The expression for the peak friction is an approximation that assumes that the peak friction is reached with negligible slip such that no evolution of the state variable has occurred; simulations show that this is a good assumption at the rupture tip. To break the high-stress patch, the incoming rupture has to dynamically supply the stress needed to make up the difference between the initial and peak friction, $\Delta\left(\frac{\tau}{\sigma}\right)_{df}$, given by:

$$\left(\frac{\tau}{\sigma}\right)_{dyn} - \left(\frac{\tau}{\sigma}\right)_{ini} \equiv \Delta\left(\frac{\tau}{\sigma}\right)_{df} = a \ln\left(\frac{V_{dyn}}{V_{ini}}\right). \tag{5.6}$$

This relation shows that either a lower initial slip rate, V_{ini}, or higher value of the rate-and-state parameter, a, can increase the distance to failure by increasing the amount of dynamic loading it requires to rupture. Making $\Delta\left(\frac{\tau}{\sigma}\right)_{df}$ large enough can temporarily stall the rupture, as dynamic slip surrounding the high-stress patch loads it to the needed peak stress. Increasing a also has the compounding effect of increasing the nucleation size of the patch, making it more inherently stable and unfavorable for dynamic rupture. Such an effect on the nucleation size could also be achieved by increasing D_{RS}, independent of changes to $\Delta\left(\frac{\tau}{\sigma}\right)_{df}$. An increase in D_{RS} would also reduce the weakening rate, W, post-peak, another unfavorable factor for dynamic rupture.

On the flip side, the tendency of the patch to further promote the rupture can be enhanced by increasing $\left(\frac{\tau}{\sigma}\right)_{ini}$. This would both decrease $\Delta\left(\frac{\tau}{\sigma}\right)_{df}$ and increase the dynamic and static stress drop, giving the rupture a bigger push. Increasing the weakening rate W, by increasing b and/or decreasing D_{RS} would make the rupture more dynamic as well as additionally decrease the nucleation size, making the patch more inherently unstable and favorable for dynamic rupture.

We refer to the best matching model as Model 1. It reproduces several key observations: the breaking of high stress patches radiate high-frequency slip perturbations with matching times of occurrence (Figures 5.6a, b); the rupture is delayed by subevent S3 causing an apparent slow-down in rupture speed and a drop in the moment rate function; the eventual breaking of S3 generates a significant acceleration of the rupture front, the momentum of which extends the original rupture further out and produces a larger second peak in the moment rate function (Figures 5.6b, g). The physical parameters of the model are summarized by Table 5.1 and 5.2).

Changing the characteristic behavior of patches between asperities and barriers illustrates their ability to control rupture propagation and seismic moment release. In Model 1, the patch corresponding to subevent S3 has higher a and lower V_{ini} than the surroundings, allowing it to initially impede the rupture (Figure 5.6g). This manifests in the apparent low rupture speed between S0 and S3. When the fourth patch ruptures, the moment released results in the second, larger peak of the moment-rate function (Figure 5.6b). If the patch is removed from the model (Model 2 in Figures 5.6c, d, h), the second peak is largely absent (Figures 5.6d). Alternatively, decreasing the value of a lowers the peak resistance of the patch in Model 3. The patch no longer impedes the rupture in Model 3, eliminating the observed delay in rupture speed and moment release (Figures 5.6e, f, ii). The moment rate history loses its two-peak shape, and consists of a largely monotonic increase followed by monotonic decay.

5.5 Conclusions

This first joint application of DAS and dynamic rupture modeling, coupled with traditional low-frequency seismic analysis, suggests a highly heterogeneous underlying fault with several prominent asperities and barriers that may control rupture dynamics. Such modulation of rupture behavior by patches of locally high stress may be ubiquitous since numerous other moderate-sized crustal earthquakes demonstrate similar or even longer duration and complex moment-release patterns in low-frequency observations. Only a handful has been resolved by local dense arrays (Allmann and Shearer, 2007). The DAS imaging produces a resolution similar to the dense Parkfield network of broad-band seismometers at a much lower cost. With the extensive existing/proposed network of onshore telecommunication fiber cables (e.g., the California Middle-Mile Initiative; Figure 5.1) (Ajo-Franklin et al., 2019; *State of California Middle-Mile Broadband Initiative* n.d.), DAS, aided by physics-based computational modeling, could provide a critical dataset for systematically

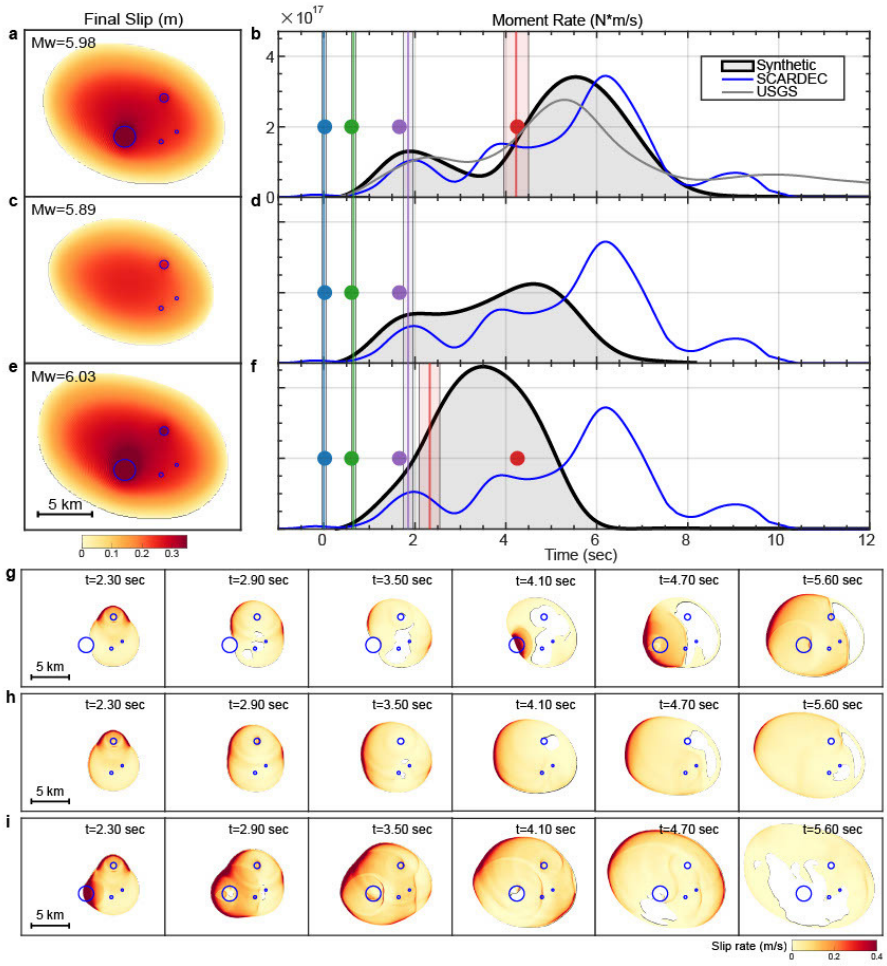

Figure 5.6: Subevents as Breakage of Stronger Fault Patches and Their Effect on Rupture Illustrated by Dynamic Rupture Modelling. a–f, Final slip (indicated by color gradient, a,c,e) and moment-rate evolution (black lines with grey shading, b,d,f) for three models: Model 1 with four patches that mimic the rupture process of the M_w 6.0 Antelope Valley event (a,b); Model 2 with the fourth patch removed (c,d); and Model 3 with a weaker fourth patch (e,f); the location of the patches are shown by blue circles (a,c,e). The simulated moment rate (grey-shaded black curves) for the preferred Model 1 (b) matches the main features of the SCARDEC (blue curve) and USGS finite-fault solutions (grey curve). The simulated times of the rupture breaking each high-stress patch (colored vertical lines, with colored boxes indicating the time range that the rupture front passes the patches) match the occurrence time of subevents from back-projection imaging (filled circles). g–i, Snapshots of slip rate on the fault illuminating the rupture process for Model 1 (g), Model 2 (h) and Model 3 (i). Eliminating or changing the fourth patch substantially affects total moment release and reveals the prominent role that the high-stress patches play in the propagation of the overall rupture.

investigating the rupture dynamics of moderate-sized and large crustal earthquakes. The continuation of the workflow demonstrated by this study could form a unique insight into the role of geometrical, stress, and material heterogeneities in earthquake ruptures.

It is important to note that the choices of the modeling parameters that match the observations are non-unique; the effects illustrated by the modeling and the observations can be achieved by other combinations of background fault and asperity/barrier parameters and initial conditions. A systematic exploration of how particular asperities and barriers manifest themselves in advanced seismological recordings would help interpret the physical origin of the heterogeneous patches more uniquely. Additionally, other physical mechanisms such as complex fault geometry provide alternative explanations. Future work consists of thorough examination of potential explanations by synthetic tests using dynamic simulations of physical mechanisms other than frictional heterogeneity such as the effect of damage zones and complex fault networks.

Parameter	Symbol	Value and Unit
Bulk Properties		
Shear wave speed	c_s	3.7 km/s
Shear modulus	G	38.2 GPa
Dilatational wave speed	c_p	6.4 km/s
Effective normal stress	$\bar{\sigma}$	50 MPa
Rate and State Parameters Outside of High-Stress Patches		
Reference slip velocity	V^*	1 μm/s
Reference friction coefficient	f^*	0.6
Direct effect parameter	a	0.003
Evolution effect parameter	b	0.00455
State evolution distance	D_{RS}	1.6 mm
Length Scales Outside of High-Stress Patches		
Quasi-static cohesive-zone	Λ_0	237 m
Nucleation size	h^*	3636 m
Cell size	Δ_z	25 m

Table 5.1: Constant Parameters.

Parameter	Patch ID				
	S0	S1	S2	S3	
				Model 1	Model 3
Effective normal stress (MPa)	70				
Patch radius (km)	0.15	0.2	0.4	1.0	
Direct effect parameter, a	0.003	0.003	0.003	0.0049	0.003
Evolution effect parameter, b	0.010				
Initial slip rate ($\log_{10}$ m/s)	-5.9	-5.9	-10	-20	
Nucleation size, h^* (m)	280	280	280	527	280
Quasi-static cohesive zone, Λ_0 (m)	77				

Table 5.2: Variable Parameters within High-Stress Patches.

Chapter 6

CONCLUSIONS AND FUTURE DIRECTIONS

In this thesis, we have used computational models to better understand frictional processes in the presence of fluids at a variety of scales. In the laboratory, we used spring-slider representations to infer the frictional properties of unstable gouge material. At the scale of a geothermal reservoir, we used a seismicity rate model for a population of spring-slider nucleation sources. Finally, we also used a dynamic rupture model to reproduce the rupture process as imaged by distributed acoustic sensing (DAS), a novel technology in earthquake imaging. This chapter summarizes the main findings of each study and delves into possible future directions of research.

6.1 Conclusions

The Bayesian probabilistic framework with MCMC sampling provides valuable insights into the frictional properties of unstable and realistic gouge material that is commonly found in the fault core. Synthetic inversions of stable velocity step experiments show that the method can accurately and precisely infer rate-and-state parameters with uncertainty range smaller than those achieved by local minimization of nonlinear least-squares residuals. An important observation with regards to the inversion method is that the sampling of rate-and-state parameters is better done logarithmically, due to the logarithmic dependence of friction on rate-and-state parameters such as D_{RS}. This is a significant improvement to the current state-of-the-art in the inversion for frictional parameters from stable velocity step experiments - the most common experiment for inference of rate-and-state parameters. The inversions of experimental data indicate that the presence of pressurized pore fluids stabilized the gouge during the stable phase, as the wet sample has higher a and D_{RS}.

Inversions of stick-slip data while assuming the material is close to critical stability allowed us to track the evolution of frictional parameters with slip since the stable velocity step. For the slip law, both experiments show minimal change in a along with an increase in b, decrease in D_{RS}, and decrease in μ^*. The constancy of a and decrease in D_{RS} are consistent with previously established interpretations related to the strength of the asperity contacts and the comminution of grains at the localized plane of shear, respectively. The reduction in D_{RS} could also represent a reduction

in the 'quality' of contact. Meanwhile, the aging law shows an increase in a, along with an increase in b and increase in D_{RS}. The changes to a and D_{RS} are less consistent with micro-physical interpretations of rate-and-state effects than when using the slip law. Furthermore, the best fitting model with the aging law has slip rates of the event phase that are significantly lower than those of the experiment. Overall, the slip law produces a closer fit to the experimental events while also demonstrating greater consistency in the evolution of rate-and-state parameters with respect to established interpretations of their micro-physical origin. A comparison between wet and dry experiments indicate that the presence of pressurized fluids led to an increase in the strength of the contacts, and a lesser decrease in the grain size with slip.

The best fitting spring-slider model with the slip law still shows significant discrepancies to the experiment in the evolution of creep during the strengthening phase and in the dependence of stick-slip dynamics on the loading rate. The spring-slider model has lower K_{max} and higher K_{min} and than the experiment, indicating the experiment both sticks more after an event and creeps more prior to an event. Additionally, the nucleation process is significantly more abrupt in the experiment. The spring-slider model also cannot reproduce the (lack of) dependence of stress drop on the loading rate that is observed in the experiment. A quasi-static finite-element model with the same rate-and-state properties suggests that the gouge in the sample likely slides in a spatially uniform manner. The same model also successfully reproduces the fit of the stable velocity step by the spring-slider model. Thus, the discrepancies between the spring-slider model and the experiment can likely be attributed to flaws in the rate-and-state formalism and the slip law rather than the idealization of a finite geometry to a single-degree-of-freedom system.

Physical models of the seismicity rate based on rate-and-state friction and stress changes due to pore-pressure diffusion successfully reproduce the seismicity observed during the EGS simulation of Otaniemi, Finland. While pore pressure measurements at the well indicate two possible diffusivities that fit either the build-up of pressure or its drawdown, the physical model suggests that the diffusivity of the medium is likely closer to the higher diffusivity fitting the build-up. We find that the effect of time-dependent nucleation is crucial in reconciling the higher diffusivity with the spatio-temporal distribution of triggered seismicity. Namely, the tendency of the parameter $a\sigma$ to act proportionally to a triggering threshold significantly affects the apparent diffusivity inferred from the triggering front in

Otaniemi. However, the effect of finite nucleation cannot be approximated well by introducing a stress threshold in the standard Coulomb friction model, at least in the context of rapid variations of injection rates common in EGS operations. The Omori law decay observed in Otaniemi is seen to depend strongly on fluid transport properties in the physical model. The physical model indicates that the Kaiser effect is present in Otaniemi, weakened by the successive variation of injection locations between different stages.

We show that a statistical model where the seismicity rate is predicted in time and space by convolution of a kernel function inspired by Omori law decay with the injection rate can provide a good match to the seismicity observed in Otaniemi. The existence of such linear convolution kernels is consistent with the identification of systematic decay patterns in the rate densities calculated by adaptation of the cascading algorithm of Marsan and Lengline (2008) to induced seismicity. The statistical model is extended to space by incorporation of a half-norm distribution component to the kernel mimicking the behavior of the physical model. We find that the validity of the method, which assumes a linear relationship between the injection history and the induced seismicity rate, depends strongly on the presence of the Kaiser effect. The convolution model would be applicable towards injection schedules that minimize the impact of the Kaiser effect by decreasing injection durations relative to the local diffusion time or by variation of injection locations in space.

We highlight the major assumptions of the Dieterich (1994) seismicity rate model and examine how they may bias interpretations of induced seismicity observed in real reservoirs by comparing it directly to a Discrete Fault Network (DFN) model. The comparisons reveal that parameters of the Dieterich model lack clear physical meaning in the finite analogue. The background seismicity rate parameter, r_b, shows a dependence on the stressing rate when inferred from catalogues of the DFN model due to the fact that r_b in the Dieterich model is based upon an infinite population of nucleation sources. Additionally, the direct effect parameter of rate-and-state friction, a, needs to decrease significantly in order to match the more gradual decay of the seismicity rate due to the exhaustion of nucleation sources. This decrease in a is consistent with the underestimates of $a\bar{\sigma}$ commonly encountered in matching the Dieterich model to real seismicity (Acosta et al., 2023; Bettinelli et al., 2008; Gross and Bürgmann, 1998; Gross and Kisslinger, 1997; Kim and Avouac, 2023; Toda et al., 1998, 2012). The comparisons to the DFN model confirm that the

underestimates are due to the biases posed by the assumptions of the model rather than near-lithostatic levels of pore pressure.

The spatio-temporal pattern of seismicity in the finite setting, or specifically the triggering and back-propagation fronts are predicted excellently by the analytical estimate of the time to instability given an initial slip rate equal to the mean and the minimum of the initial distribution, respectively. Thus, the triggering front is not only dependent on fluid transport properties (Shapiro, Huenges, and Borm, 1997) or its combination with nucleation characteristics (Kim and Avouac, 2023) but also the distribution of initial conditions of the fault network. The back-propagation front, in particular, occurs co-injection if the time to instability for the minimum slip rate is shorter than the injection duration. This is in contrast to the more common context in which the back front occurs immediately following shut-in due to the propagation of negative pressure rates. The Dieterich model does not predict a back front during injection as the maximum time to instability in an infinite population of sources is infinitely large. The relocated catalogue of the 1993 GPK1 stimulation in Soultz-Sous-Forêts shows such a back-front which can be fit qualitatively using the time to instability measure for V_{min} = 2.0e-15m/s. The co-injection back-propagation front may be the most salient characteristic of finite effects in an induced seismicity catalogue.

The change in frictional stability due to changes in the effective normal stress during injections is fully accounted for in the DFN model where the rate-and-state friction law is solved in its entirety without the no-healing assumption. The changes in the critical stiffness, κ_{cr} (for a single cell), or the nucleation size, h^* (for a fault discretized by multiple cells), allow previously seismic faults to become aseismic with a sufficient increase in pore pressure. Such faults tend to creep stably under loading, unlike in the Dieterich model where all nucleation sources that are initially unstable remain so regardless of changes to the local stress state. A simple model for the rate of magnitudes that accounts for the evolution of frictional stability reproduces the apparent increase in the source radius of induced events in Soultz-Sous-Forêts. The source radii distribution shifts at both the lower and upper ends of the distribution, from the elimination of smaller events that cannot reach the increased nucleation size, and the growth of the stimulated region that limits rupture propagation, respectively. The rate of larger events is overestimated by the model, possibly due to an overestimation of maximum magnitudes by the volume

of stimulation, or due to a statistical manifestation of the low probability of larger events (Van der Elst et al., 2016).

The modeling of the high-frequency DAS recordings of a M_w 6.0 earthquake suggests a highly heterogeneous underlying fault with several prominent asperities and barriers that may control rupture dynamics. The model demonstrates how the high-stress patches both inhibit and promote the overall rupture, while also contributing to a significant amount of the energy release themselves. The particular dependence of the quality of the high-stress patch — namely, whether they act as an asperity or a barrier — is expressed through a series of relationships between the initial, peak and dynamic stress at a single point on the fault governed by rate-and-state friction. In particular, the direct effect represented by a is directly proportional to the tendency for the point to delay the rupture by increasing the peak stress. On the other hand, an increase in b or decrease in D_{RS} tends to promote rupture propagation by increasing instability and the rate of weakening.

6.2 Future Directions

The work presented in this thesis suggest a number of future directions for further research. Direct application of the rate-and-state friction law and detailed examination of how well they match experiments and seismicity catalogues reveal possible areas of improvement to the state-of-the-art formulation of the constitutive relationship. The development of forecasting tools for induced seismicity questions whether they could be used to control seismicity and design optimization injection/extraction schedules. The successful application of the friction law to interpretation of DAS data encourages the use of big data and demands efficient methods to model such data. The following sections delve more deeply into theses ideas in greater detail.

Modeling Constitutive Laws of Shear Resistance for Gouge in Continuum from Experimental Stick-Slip with High Resolution of Slip History

The rate-and-state friction law as it is used today (Dieterich, 1979; Marone, 1998; Ruina, 1983) has been derived from experiments of stably sliding material that does not go under stick-slip motion spontaneously. The quality of the rate-and-state friction law to produce stick-slip is in fact an extrapolation of the experimentally validated region. Chapter 2 reveals in detail aspects of stick-slip motion that the friction law is not able to reproduce. Yet, unstable phase of frictional slip is possibly more relevant to civil safety as it is the regime of slip for the most devastating earthquakes. Various state evolution laws have been proposed to improve upon the

slip and aging laws (Kato and Tullis, 2001; Nagata, Nakatani, and Yoshida, 2012). Such laws still aim to reproduce the experimental observations from the stable regime of frictional slip. Significant improvements to the constitutive relationship could be made by efforts to better reproduce the unstable regime of slip.

The outstanding challenge to the modeling of unstable slip in experiments is that it is more difficult and non-unqiue than stable slip. Chapter 2.6 discusses in detail the non-uniqueness of the inversion for frictional parameters given the experimental observations of friction-displacement history. Thus, meaningful efforts to model unstable slip likely require further constraints from experimental observations. This could include high-resolution measurements of the slip history closer to the sliding sample. Notable examples include direct image correlation (DIC) at the surface of the sliding layer (Rubino, Rosakis, and Lapusta, 2017) and back-projection of acoustic emission sensors surrounding the sliding sample (Marty et al., 2019 and Figure 6.1). Such measurements provide detailed information about the rupture process at a finite scale. They also provide valuable scalar quantities such as the peak and minimum slip rate during and after the rupture.

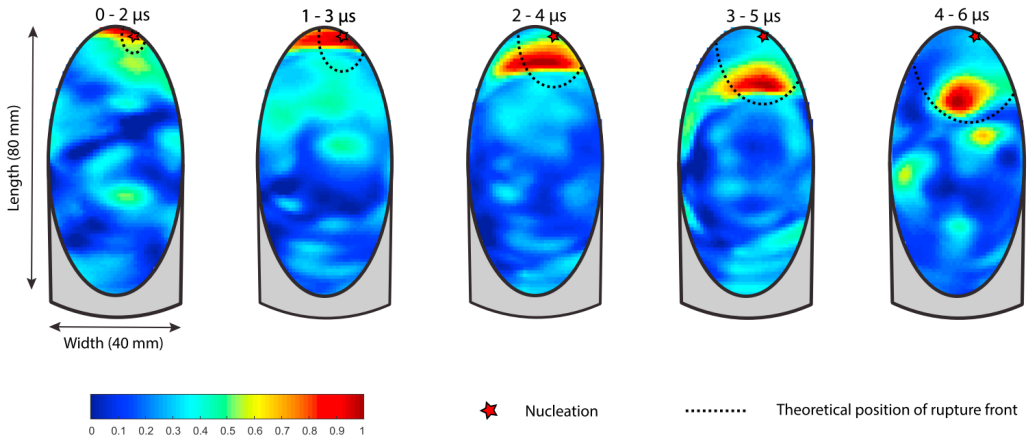

Figure 6.1: Back-Projection of Acoustic Emissions from Partial Rupture along Saw-Cut of Granite by Marty et al. (2019). The colors indicate the value of the coherency function from back-projection of acoustic emissions measured around the circumference of the sample. The coherency function tracks the evolution of rupture and reveals that the event consists of a nucleation region close to the edges, followed by dynamic slip through a portion of the frictional surface. The detailed documentation of the rupture process provides additional constraints on the friction law.

Another key aspect of the origin of rate-and-state friction that may not be appropriate for gouge material in unstable slip is that it was derived based on experiments of bare

surfaces. Bare surfaces can develop fine particles due to breakage of contact points after slip. However, such particles amount to negligible thickness, comparable to the height of the contact asperities. On the contrary, gouge may be better treated as a continuum material with varying levels localization and delocalization. Shear resistance is finite across the sliding portion of the gouge, which can vary in its thickness based on the strain rate. Additionally, detailed microstructure images during the initial loading stages of gouge material have documented the complex deformation structure that exists prior to the localization of shear that is parallel to the loading direction (Bedford and Faulkner, 2021 and Figure 6.2). The long-term evolution of friction observed in the experiments of Chapter 2 is a clear indication of how such processes significantly affect shear resistance within the gouge.

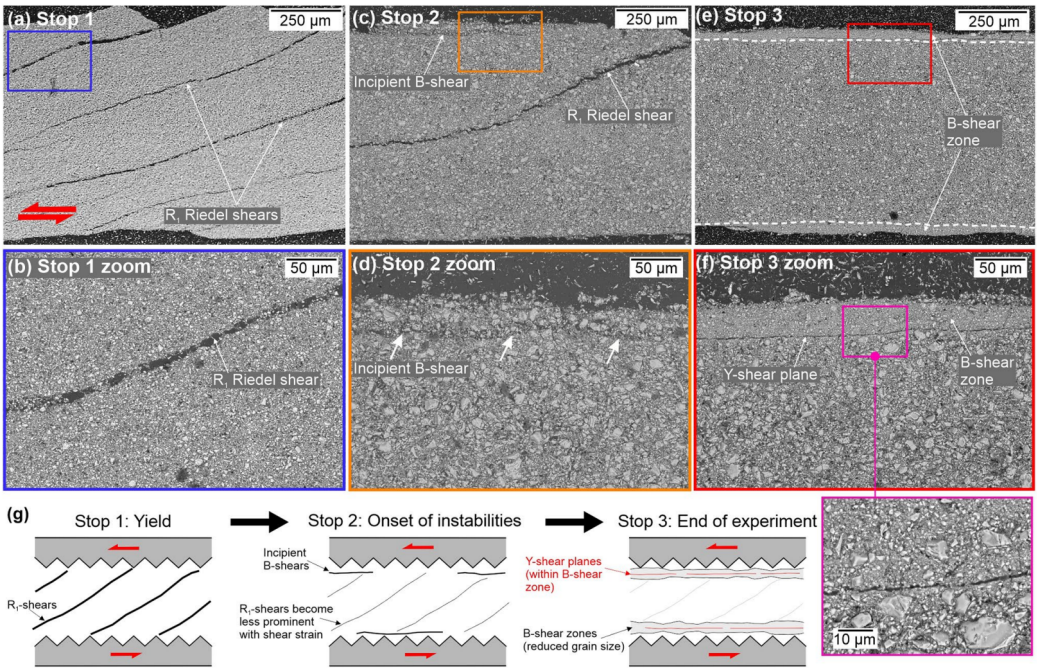

Figure 6.2: Backscatter Electron (BSE) Images of Complex Evolution of Deformation Structure in Gouge from Shear Loading by Bedford and Faulkner (2021). (a, b) After the sample has yielded, R1 Riedel shears crosscut the layer. (c, d) At the onset of stick-slip instabilities, R1 Riedel shears and incipient B-shears are observed. (e, f) At the end of the experiment after multiple stick-slip events, well-developed B-shears are observed at the top and bottom of the layer, with discrete Y-shear planes found within the main boundary shears (inset). (g) Schematic illustration of the microstructural evolution. The deformation history of the gouge is more complex and finite (in the direction perpendicular to loading) than that of a bare surface, and it is possible that continuum models may be better-suited to describe gouge.

A number of continuum models have been developed with the main goal of reproducing the complex deformation structure that leads to shear localization. Notable examples involve shear transformation zone (STZ) theory (Elbanna and Carlson, 2014) and cosserat continuum theory (Stathas and Stefanou, 2023). Earlier work points to how strain localization may be modelled in continuum based on plasticity (Rudnicki and Rice, 1975). Discrete element methods have also been used to model rate-and-state friction experiments (Ferdowsi and Rubin, 2020). These models are yet to be tested for the unstable regime of slip as observed in experiments. Future developments of continuum models should consider both the stable and unstable regime of frictional slip, aided by high-resolution experiments.

Control & Optimization of Induced Seismicity (Magnitudes)

Chapters 3 and 4 offer promising ways to forecast seismicity induced by fluid injections. In practicality, forecasting is not enough for industrial operations. An even more valuable framework could be to leverage accurate forecasts for control of induced seismicity and optimization of the underlying industrial process. In the scenario of geothermal well stimulation, the goal of the operation would be to achieve a certain level of pressure in a region around the injection source to cause permanent change of the rock permeability, while working under the constraint of triggering earthquakes of magnitudes smaller than a threshold value.

The discussion of the possibility to control induced seismicity highlights the importance of understanding the factors that affect induced earthquake magnitudes. Indeed, even an infinite number of induced earthquakes is tolerable, given that the magnitudes fall below a threshold value that represents the event with real potential of causing damage to civil safety. The argument that induced earthquakes follow statistical properties of natural earthquakes (Van der Elst et al., 2016) imply that controlling magnitudes is not possible; the probability of the threshold event is directly proportional to the number of earthquakes. Assumptions that the magnitude is bound in its upper limit by the volume of stimulation (Shapiro et al., 2011) provide more promise for a setting that can be controlled and optimized. However, such assumptions lack physical reasoning and already underestimate maximum magnitude events that have been observed (Van der Elst et al., 2016). Effects of pressure on frictional stability in gouge as revealed by Chapter 2 elucidate additional physical mechanisms that are currently unaccounted for in the friction law.

The development of control and optimization framework around induced seismicity has been demonstrated for the case of simple models, similar to those presented in Chapter 3 (Gutiérrez-Oribio and Stefanou, 2024; Stefanou, 2019). As Chapter 4 demonstrates, such models lack integral aspects of the physics that significantly affect the forecast. Additionally, they control the seismicity rate, rather than the total number of events (Figure 6.3). An accurate understanding of how injections are physically related to the magnitudes of the induced events is essential in developing a framework for control and optimization.

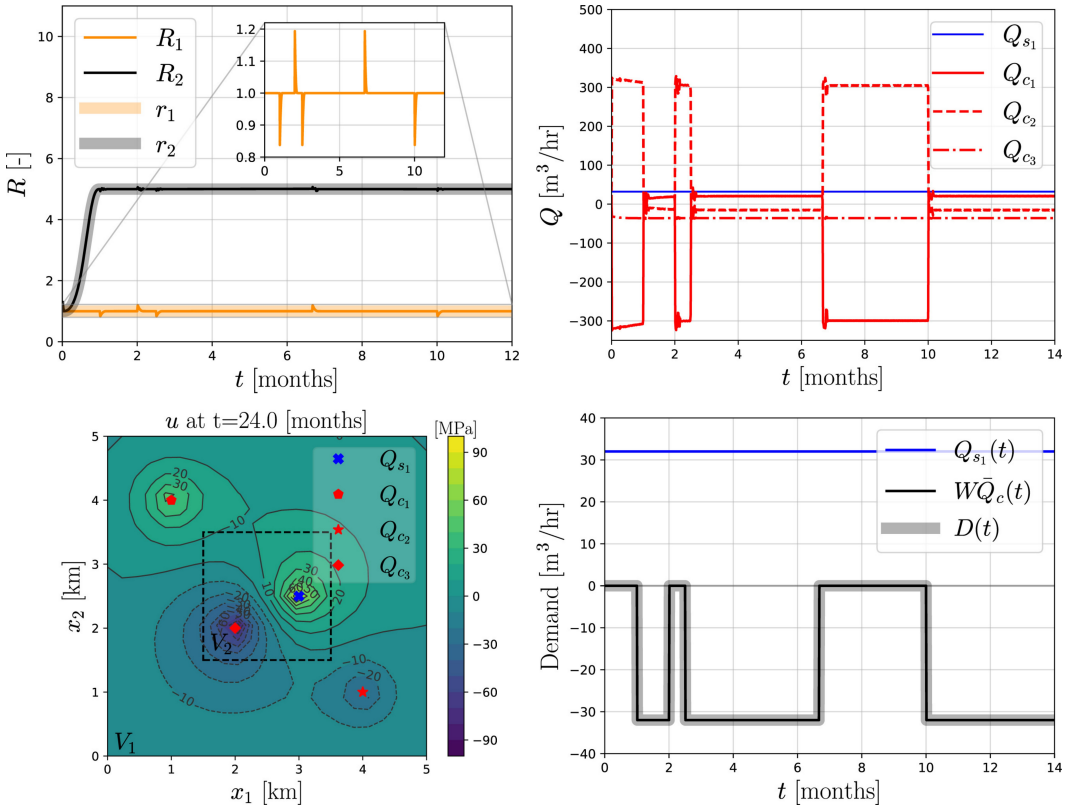

Figure 6.3: Control and Optimization of a 2D Reservoir by Gutiérrez-Oribio and Stefanou (2024). (Top left) Seismicity rate (solid black and orange curves) in regions, V_1 (the entire domain in bottom row) and V_2 (dotted domain in bottom row), follow the prescribed values (shaded lines). (Top right) Injection flux of the fixed well (blue) and injection fluxes of the control wells (red) follow the constraint of intermittent demand (black curve in bottom right panel). (Bottom left) . Fluid pressure distribution in the reservoir at the end of the simulation. The control strategy ensures the steady state of the pressure solution after approximately 24 months. Such framework allows the addition of more physics and harsher constraints on seismicity (such as on the total number of events rather than a fixed seismicity rate for indefinite time).

Surrogate Models of High-Fidelity Models for Dynamic Inversion

All models presented in this thesis employ assumptions that significantly reduce computational cost. In the case of the spring-slider model of Chapter 2, the finite system is reduced to a single-degree-of-freedom system. This assumption neglects the finite dimension of rupture propagation, the finite geometry of the experimental apparatus, and wave propagation across finite length scales. The seismicity rate model of Chapter 3 neglects source interactions and the full evolution of rate-and-state friction. The discrete fault network model of Chapter 4 assumes homogeneous and elastic bulk and neglects inertially driven wave propagation. Finally, the dynamic rupture model of Chapter 5 simulates a single fault that is perfectly planar, embedded in a homogeneous and infinite, elastic medium.

The assumptions give the significant advantage to the models that they are computationally efficient. This allows the Bayesian inversion with MCMC sampling of Chapters 2 and 3 and the manual tuning of parameters in Chapter 5. However, physical mechanisms that the models cannot consider (e.g., structural heterogeneity due to damage, non-linear deformation of the bulk and transport of fluids) are not negligible. Volume-based methods can simulate more complex sets of physics (Jia et al., 2023; Taufiqurrahman et al., 2023) (Figure 6.4). However, such models are computationally expensive, making inversion schemes unfeasible.

The advent of machine-learning in recent years has also entered the field of scientific computing in the form of surrogate modeling. Surrogate models form digital twins of high-fidelity models with drastically lower computational cost, often with the use of artificial neural networks (Cai et al., 2021). The development of accurate and efficient surrogate models for frictional processes could make formal inversions as presented in Chapters 2 and 5 with higher-fidelity models feasible. In the context of Chapter 2, this could allow an accurate representation of the finite apparatus geometry and the radiated energy within the finite bulk. In the context of Chapter 5, dynamic inversions could provide quantitative analysis of the level of non-uniqueness and uncertainty for the inversion.

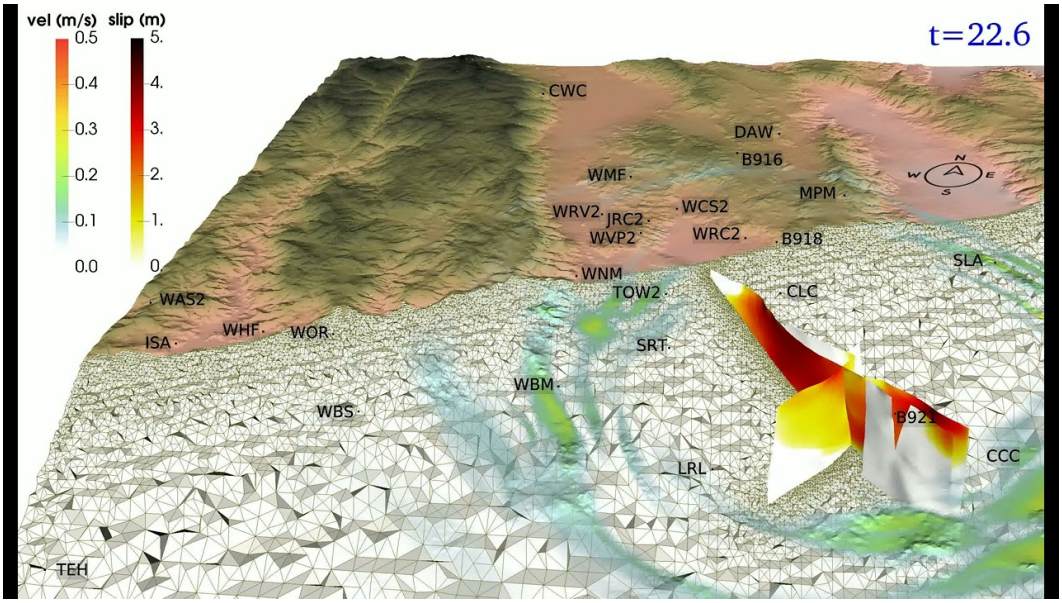

Figure 6.4: High-Fidelity Modeling of the 2019 Ridgecrest Earthquake Sequence by Taufiqurrahman et al. (2023). Slip along the Ridgecrest fault system is indicated in by the yellow-red colorbar while displacement rates in the bulk are represented by the white-green-yellow-red colorbar. The fully dynamic simulation with realistic topology requires great computational expense. Surrogate models provide a possible avenue towards the leverage of high-fidelity models in inversion schemes.

BIBLIOGRAPHY

Acosta, Mateo and Marie Violay (2020). "Mechanical and hydraulic transport properties of transverse-isotropic Gneiss deformed under deep reservoir stress and pressure conditions." In: *International Journal of Rock Mechanics and Mining Sciences* 130, p. 104235.

Acosta, Mateo et al. (2018). "Dynamic weakening during earthquakes controlled by fluid thermodynamics." In: *Nature Communications* 9.1, p. 3074.

Acosta, Mateo et al. (2023). "Earthquake nucleation characteristics revealed by seismicity response to seasonal stress variations induced by gas production at Groningen." In: *Geophysical Research Letters* 50.19, e2023GL105455.

Ader, Thomas et al. (2020). "Design and implementation of a traffic light system for deep geothermal well stimulation in Finland." In: *Journal of Seismology* 24, pp. 991–1014.

Ader, Thomas J. and Jean-Philippe Avouac (2013). "Detecting periodicities and declustering in earthquake catalogs using the Schuster spectrum, application to Himalayan seismicity." In: *Earth and Planetary Science Letters* 377, pp. 97–105.

Ader, Thomas J. et al. (2014). "Response of rate-and-state seismogenic faults to harmonic shear-stress perturbations." In: *Geophysical Journal International* 198.1, pp. 385–413.

Ajo-Franklin, Jonathan B et al. (2019). "Distributed acoustic sensing using dark fiber for near-surface characterization and broadband seismic event detection." In: *Scientific reports* 9.1, p. 1328.

Alghannam, Maryam and Ruben Juanes (2020). "Understanding rate effects in injection-induced earthquakes." In: *Nature Communications* 11.1, p. 3053.

Allmann, Bettina P. and Peter M. Shearer (2007). "A high-frequency secondary event during the 2004 Parkfield earthquake." In: *Science* 318.5854, pp. 1279–1283.

Almakari, Michelle et al. (2019). "Effect of the injection scenario on the rate and magnitude content of injection-induced seismicity: Case of a heterogeneous fault." In: *Journal of Geophysical Research: Solid Earth* 124.8, pp. 8426–8448.

Ampuero, Jean-Paul and Allan M. Rubin (2008). "Earthquake nucleation on rate and state faults–Aging and slip laws." In: *Journal of Geophysical Research: Solid Earth* 113.B1.

Audigane, Pascal, Jean-Jacques Royer, and Hideshi Kaieda (2002). "Permeability characterization of the Soultz and Ogachi large-scale reservoir using induced microseismicity." In: *Geophysics* 67.1, pp. 204–211.

Avouac, Jean-Philippe et al. (2015). “Lower edge of locked Main Himalayan Thrust unzipped by the 2015 Gorkha earthquake.” In: *Nature Geoscience* 8.9, pp. 708–711.

Avouac, Jean-Philippe et al. (2020). “A Convolution Model for Earthquake Forecasting Derived from Seismicity Recorded During the ST1 Geothermal Project on Otaniemi Campus, Finland.” In: *Proceedings World Geothermal Congress*, p. 1.

Bachmann, Corinne E. et al. (2011). “Statistical analysis of the induced Basel 2006 earthquake sequence: introducing a probability-based monitoring approach for Enhanced Geothermal Systems.” In: *Geophysical Journal International* 186.2, pp. 793–807.

Bachmann, Corinne E. et al. (2012). “Influence of pore-pressure on the event-size distribution of induced earthquakes.” In: *Geophysical Research Letters* 39.9.

Baisch, Stefan and Hans-Peter Harjes (2003). “A model for fluid-injection-induced seismicity at the KTB, Germany.” In: *Geophysical Journal International* 152.1, pp. 160–170.

Baisch, Stefan et al. (2006). “Induced seismicity during the stimulation of a geothermal HFR reservoir in the Cooper Basin, Australia.” In: *Bulletin of the Seismological Society of America* 96.6, pp. 2242–2256.

Baisch, Stefan et al. (2010). “A numerical model for fluid injection induced seismicity at Soultz-sous-Forêts.” In: *International Journal of Rock Mechanics and Mining Sciences* 47.3, pp. 405–413.

Barbot, Sylvain, Nadia Lapusta, and Jean-Philippe Avouac (2012). “Under the hood of the earthquake machine: Toward predictive modeling of the seismic cycle.” In: *Science* 336.6082, pp. 707–710.

Baria, Roy et al. (1999). “European HDR research programme at Soultz-sous-Forêts (France) 1987–1996.” In: *Geothermics* 28.4-5, pp. 655–669.

Bedford, John D. and Daniel R. Faulkner (2021). “The role of grain size and effective normal stress on localization and the frictional stability of simulated quartz gouge.” In: *Geophysical Research Letters* 48.7, e2020GL092023.

Bedford, John D., Daniel R. Faulkner, and Nadia Lapusta (2022). “Fault rock heterogeneity can produce fault weakness and reduce fault stability.” In: *Nature Communications* 13.1, p. 326.

Bedford, John D. et al. (2021). “The stabilizing effect of high pore-fluid pressure along subduction megathrust faults: Evidence from friction experiments on accretionary sediments from the Nankai Trough.” In: *Earth and Planetary Science Letters* 574, p. 117161.

Beeler, Nicholas M., Stephen H. Hickman, and Teng-Fong Wong (2001). “Earthquake stress drop and laboratory-inferred interseismic strength recovery.” In: *Journal of Geophysical Research: Solid Earth* 106.B12, pp. 30701–30713.

Beeler, Nicholas M. and David A. Lockner (2003). "Why earthquakes correlate weakly with the solid Earth tides: Effects of periodic stress on the rate and probability of earthquake occurrence." In: *Journal of Geophysical Research: Solid Earth* 108.B8.

Beeler, Nicholas M., Terry E. Tullis, and JD Weeks (1994). "The roles of time and displacement in the evolution effect in rock friction." In: *Geophyiscal Research Letters* 21.18, pp. 1987–1990.

Ben-Zion, Yehuda (2008). "Collective behavior of earthquakes and faults: Continuum-discrete transitions, progressive evolutionary changes, and different dynamic regimes." In: *Reviews of Geophysics* 46.4.

Bertani, Ruggero (2012). "Geothermal power generation in the world 2005–2010 update report." In: *geothermics* 41, pp. 1–29.

Bettinelli, Pierre et al. (2008). "Seasonal variations of seismicity and geodetic strain in the Himalaya induced by surface hydrology." In: *Earth and Planetary Science Letters* 266.3-4, pp. 332–344.

Bhattacharya, Pathikrit, Allan M Rubin, and Nicholas M Beeler (2017). "Does fault strengthening in laboratory rock friction experiments really depend primarily upon time and not slip?" In: *Journal of Geophysical Research: Solid Earth* 122.8, pp. 6389–6430.

Bhattacharya, Pathikrit et al. (2022). "The evolution of rock friction is more sensitive to slip than elapsed time, even at near-zero slip rates." In: *Proceedings of the National Academy of Sciences* 119.30, e2119462119.

Biondi, Ettore et al. (2023). "An upper-crust lid over the Long Valley magma chamber." In: *Science Advances* 9.42, eadi9878.

Bizzarri, Andrea and Massimo Cocco (2003). "Slip-weakening behavior during the propagation of dynamic ruptures obeying rate-and state-dependent friction laws." In: *Journal of Geophysical Research: Solid Earth* 108.B8.

Bommer, Julian J. et al. (2006). "Control of hazard due to seismicity induced by a hot fractured rock geothermal project." In: *Engineering geology* 83.4, pp. 287–306.

Bourne, Stephen J, Stephen J Oates, and Jan Van Elk (2018). "The exponential rise of induced seismicity with increasing stress levels in the Groningen gas field and its implications for controlling seismic risk." In: *Geophysical Journal International* 213.3, pp. 1693–1700.

Bourouis, Seid and Pascal Bernard (2007). "Evidence for coupled seismic and aseismic fault slip during water injection in the geothermal site of Soultz (France), and implications for seismogenic transients." In: *Geophysical Journal International* 169.2, pp. 723–732.

Brace, William F., JB Walsh, and WT Frangos (1968). "Permeability of granite under high pressure." In: *Journal of Geophysical research* 73.6, pp. 2225–2236.

Cai, Shengze et al. (2021). “Physics-informed neural networks (PINNs) for fluid mechanics: A review.” In: *Acta Mechanica Sinica* 37.12, pp. 1727–1738.

Calò, Marco et al. (2011). “Large-scale aseismic motion identified through 4-DP-wave tomography.” In: *Geophysical Journal International* 186.3, pp. 1295–1314.

Candela, Thibault et al. (2019). “Depletion-induced seismicity at the Groningen gas field: Coulomb rate-and-state models including differential compaction effect.” In: *Journal of Geophysical Research: Solid Earth* 124.7, pp. 7081–7104.

Cappa, Frédéric et al. (2006). “Hydromechanical modelling of pulse tests that measure fluid pressure and fracture normal displacement at the Coaraze Laboratory site, France.” In: *International Journal of Rock Mechanics and Mining Sciences* 43.7, pp. 1062–1082.

Cappa, Frédéric et al. (2019). “Stabilization of fault slip by fluid injection in the laboratory and in situ.” In: *Science advances* 5.3, eaau4065.

Cattania, Camilla and Paul Segall (2021). “Precursory slow slip and foreshocks on rough faults.” In: *Journal of Geophysical Research: Solid Earth* 126.4, e2020JB020430.

Cauchie, Léna, Olivier Lengliné, and Jean Schmittbuhl (2020). “Seismic asperity size evolution during fluid injection: case study of the 1993 Soultz-sous-Forêts injection.” In: *Geophysical Journal International* 221.2, pp. 968–980.

Chen, Ting and Nadia Lapusta (2009). “Scaling of small repeating earthquakes explained by interaction of seismic and aseismic slip in a rate and state fault model.” In: *Journal of Geophysical Research: Solid Earth* 114.B1.

Chester, Frederick M. and Judith S. Chester (1998). “Ultracataclasite structure and friction processes of the Punchbowl fault, San Andreas system, California.” In: *Tectonophysics* 295.1-2, pp. 199–221.

Chester, Frederick M. et al. (2004). “Structure of large-displacement, strike-slip fault zones in the brittle continental crust.” In: *Rheology and deformation of the lithosphere at continental margins*. Columbia University Press, pp. 223–260.

Chester, Judith S., Frederick M. Chester, and Andreas K. Kronenberg (2005). “Fracture surface energy of the Punchbowl fault, San Andreas system.” In: *Nature* 437.7055, pp. 133–136.

Chester, Judith S. and David L. Goldsby (2003). “Microscale characterization of natural and experimental slip surfaces relevant to earthquake mechanics.” In: *SCEC Annu. Prog. Rep*.

Cladouhos, Trenton T. et al. (2016). “Results from Newberry volcano EGS demonstration, 2010–2014.” In: *Geothermics* 63, pp. 44–61.

Corbi, Fabio et al. (2024). “Asperity size and neighboring segments can change the frictional response and fault slip behavior: Insights from laboratory experiments and numerical simulations.” In: *Journal of Geophysical Research: Solid Earth* 129.1, e2023JB026594.

Cornet, Francois H. and Yin Jianmin (1995). "Analysis of induced seismicity for stress field determination and pore pressure mapping." In: *Mechanics Problems in Geodynamics Part I*, pp. 677–700.

Day, Steven M. et al. (2005). "Comparison of finite difference and boundary integral solutions to three-dimensional spontaneous rupture." In: *Journal of Geophysical Research: Solid Earth* 110.B12.

De Barros, Louis et al. (2018). "Seismicity and fault aseismic deformation caused by fluid injection in decametric in-situ experiments." In: *Comptes Rendus Geoscience* 350.8, pp. 464–475.

De Barros, Louis et al. (2024). "Systematic observation of a seismic back-front during fluid injection in both natural and anthropogenic earthquake swarms." In: *Earth and Planetary Science Letters* 641, p. 118849.

Dempsey, David and Jeremy Riffault (2019). "Response of induced seismicity to injection rate reduction: Models of delay, decay, quiescence, recovery, and Oklahoma." In: *Water Resources Research* 55.1, pp. 656–681.

Dempsey, David and Jenny Suckale (2017). "Physics-based forecasting of induced seismicity at Groningen gas field, the Netherlands." In: *Geophysical Research Letters* 44.15, pp. 7773–7782.

Dempsey, David, Jenny Suckale, and Yihe Huang (2016). "Collective properties of injection-induced earthquake sequences: 2. Spatiotemporal evolution and magnitude frequency distributions." In: *Journal of Geophysical Research: Solid Earth* 121.5, pp. 3638–3665.

Di Toro, Giulio et al. (2011). "Fault lubrication during earthquakes." In: *Nature* 471.7339, pp. 494–498.

Dieterich, James (1994). "A constitutive law for rate of earthquake production and its application to earthquake clustering." In: *Journal of Geophysical Research: Solid Earth* 99.B2, pp. 2601–2618.

Dieterich, James H. (1979). "Modeling of rock friction: 1. Experimental results and constitutive equations." In: *Journal of Geophysical Research: Solid Earth* 84.B5, pp. 2161–2168.

– (1992). "Earthquake nucleation on faults with rate-and state-dependent strength." In: *Tectonophysics* 211.1-4, pp. 115–134.

Dong, Bin et al. (2022). "Real-time and post-hoc compression for data from Distributed Acoustic Sensing." In: *Computers & Geosciences* 166, p. 105181.

Dublanchet, Pierre (2018). "The dynamics of earthquake precursors controlled by effective friction." In: *Geophysical Journal International* 212.2, pp. 853–871.

Dublanchet, Pierre, Pascal Bernard, and Pascal Favreau (2013). "Interactions and triggering in a 3-D rate-and-state asperity model." In: *Journal of Geophysical Research: Solid Earth* 118.5, pp. 2225–2245.

Dublanchet, Pierre and Louis De Barros (2021). "Dual seismic migration velocities in seismic swarms." In: *Geophysical Research Letters* 48.1, e2020GL090025.

Dunham, Eric M., Pascal Favreau, and Jean M. Carlson (2003). "A supershear transition mechanism for cracks." In: *Science* 299.5612, pp. 1557–1559.

Elbanna, Ahmed E. and Jean M. Carlson (2014). "A two-scale model for sheared fault gouge: Competition between macroscopic disorder and local viscoplasticity." In: *Journal of Geophysical Research: Solid Earth* 119.6, pp. 4841–4859.

Ellsworth, William L. et al. (2019). "Triggering of the Pohang, Korea, earthquake (M w 5.5) by enhanced geothermal system stimulation." In: *Seismological Research Letters* 90.5, pp. 1844–1858.

Elmar, Elmar and Serge A. Shapiro (2002). "Microseismic monitoring of borehole fluid injections: Data modeling and inversion for hydraulic properties of rocks." In: *SEG International Exposition and Annual Meeting*. SEG, SEG–2002.

Eshelby, John Douglas (1957). "The determination of the elastic field of an ellipsoidal inclusion, and related problems." In: *Proceedings of the royal society of London. Series A. Mathematical and physical sciences* 241.1226, pp. 376–396.

Evans, Keith F. et al. (2005). "Microseismicity and permeability enhancement of hydrogeologic structures during massive fluid injections into granite at 3 km depth at the Soultz HDR site." In: *Geophysical Journal International* 160.1, pp. 388–412.

Fan, Wenyuan and Peter M. Shearer (2015). "Detailed rupture imaging of the 25 April 2015 Nepal earthquake using teleseismic P waves." In: *Geophysical Research Letters* 42.14, pp. 5744–5752.

Faulkner, Daniel R. and Phillip J. Armitage (2013). "The effect of tectonic environment on permeability development around faults and in the brittle crust." In: *Earth and Planetary Science Letters* 375, pp. 71–77.

Faulkner, Daniel R. et al. (2018). "Pore fluid pressure development in compacting fault gouge in theory, experiments, and nature." In: *Journal of Geophysical Research: Solid Earth* 123.1, pp. 226–241.

Ferdowsi, Behrooz and Allan M. Rubin (2020). "A granular physics-based view of fault friction experiments." In: *Journal of Geophysical Research: Solid Earth* 125.6, e2019JB019016.

Frye, Kevin M. and Chris Marone (2002). "Effect of humidity on granular friction at room temperature." In: *Journal of Geophysical Research: Solid Earth* 107.B11, ETG–11.

Gaucher, Emmanuel et al. (2015). "Induced seismicity in geothermal reservoirs: A review of forecasting approaches." In: *Renewable and Sustainable Energy Reviews* 52, pp. 1473–1490.

Gens, Antonio et al. (2011). “In situ behaviour of a stiff layered clay subject to thermal loading: observations and interpretation.” In: *Stiff Sedimentary Clays: Genesis and Engineering Behaviour: Géotechnique Symposium in Print 2007*. Thomas Telford Ltd, pp. 123–144.

Geubelle, Philippe H. and James R. Rice (1995). “A spectral method for three-dimensional elastodynamic fracture problems.” In: *Journal of the Mechanics and Physics of Solids* 43.11, pp. 1791–1824.

Giacomel, Piercarlo et al. (2024). “steadystate: A MATLAB-based routine for determining steady-state friction conditions in the framework of rate-and-state friction analysis.” In: *Geosphere* 20.3, pp. 965–980.

Goebel, Thomas HW and Emily E. Brodsky (2018). “The spatial footprint of injection wells in a global compilation of induced earthquake sequences.” In: *Science* 361.6405, pp. 899–904.

Goodfellow, Sebastian D. et al. (2015). “Hydraulic fracture energy budget: Insights from the laboratory.” In: *Geophysical Research Letters* 42.9, pp. 3179–3187.

Goodman, Jonathan and Jonathan Weare (2010). “Ensemble samplers with affine invariance.” In: *Communications in applied mathematics and computational science* 5.1, pp. 65–80.

Grigoli, Francesco et al. (2017). “Current challenges in monitoring, discrimination, and management of induced seismicity related to underground industrial activities: A European perspective.” In: *Reviews of Geophysics* 55.2, pp. 310–340.

Grigoli, Francesco et al. (2018). “The November 2017 M w 5.5 Pohang earthquake: A possible case of induced seismicity in South Korea.” In: *Science* 360.6392, pp. 1003–1006.

Gross, Susanna and Roland Bürgmann (1998). “Rate and state of background stress estimated from the aftershocks of the 1989 Loma Prieta, California, earthquake.” In: *Journal of Geophysical Research: Solid Earth* 103.B3, pp. 4915–4927.

Gross, Susanna and Carl Kisslinger (1997). “Estimating tectonic stress rate and state with Landers aftershocks.” In: *Journal of Geophysical Research: Solid Earth* 102.B4, pp. 7603–7612.

Gu, Ji-Cheng et al. (1984). “Slip motion and stability of a single degree of freedom elastic system with rate and state dependent friction.” In: *Journal of the Mechanics and Physics of Solids* 32.3, pp. 167–196.

Gu, Yaojun and Teng-fong Wong (1991). “Effects of loading velocity, stiffness, and inertia on the dynamics of a single degree of freedom spring-slider system.” In: *Journal of Geophysical Research: Solid Earth* 96.B13, pp. 21677–21691.

Guérin-Marthe, Simon et al. (2019). “Earthquake nucleation size: Evidence of loading rate dependence in laboratory faults.” In: *Journal of Geophysical Research: Solid Earth* 124.1, pp. 689–708.

Guglielmi, Yves et al. (2015). "Seismicity triggered by fluid injection–induced aseismic slip." In: *Science* 348.6240, pp. 1224–1226.

Gutenberg, Beno and Carl F Richter (1956). "Earthquake magnitude, intensity, energy, and acceleration: (Second paper)." In: *Bulletin of the seismological society of America* 46.2, pp. 105–145.

Gutiérrez-Oribio, Diego and Ioannis Stefanou (2024). "Insights of using control theory for minimizing induced seismicity in underground reservoirs." In: *Geomechanics for Energy and the Environment*, p. 100570.

Gwon, Gi-jeong and Yun-gyeong Song (Mar. 12, 2017). "Pohang Earthquake Shakes the Nation, CSAT Postponed for the First Time." In: *The Kyunghyang Shinmun*. URL: https://english.khan.co.kr/khan_art_view.html?artid=201711161713387&code=710100 (visited on 11/16/2017).

Häring, Markus O. et al. (2008). "Characterisation of the Basel 1 enhanced geothermal system." In: *Geothermics* 37.5, pp. 469–495.

He, Changrong, Teng-fong Wong, and Nick M Beeler (2003). "Scaling of stress drop with recurrence interval and loading velocity for laboratory-derived fault strength relations." In: *Journal of Geophysical Research: Solid Earth* 108.B1.

Healy, John H. et al. (1968). "The Denver earthquakes." In: *Science* 161.3848, pp. 1301–1310.

Heimisson, Elías R. (2019). "Constitutive law for earthquake production based on rate-and-state friction: Theory and application of interacting sources." In: *Journal of Geophysical Research: Solid Earth* 124.2, pp. 1802–1821.

Heimisson, Elias R. and Paul Segall (2018). "Constitutive law for earthquake production based on rate-and-state friction: Dieterich 1994 revisited." In: *Journal of Geophysical Research: Solid Earth* 123.5, pp. 4141–4156.

Heimisson, Elías R., Eric M. Dunham, and Martin Almquist (2019). "Poroelastic effects destabilize mildly rate-strengthening friction to generate stable slow slip pulses." In: *Journal of the Mechanics and Physics of Solids* 130, pp. 262–279.

Heimisson, Elías R. et al. (2022). "Coulomb threshold rate-and-state model for fault reactivation: application to induced seismicity at Groningen." In: *Geophysical Journal International* 228.3, pp. 2061–2072.

Hillers, Gregor et al. (2020). "The 2018 geothermal reservoir stimulation in Espoo/Helsinki, southern Finland: Seismic network anatomy and data features." In: *Seismological Research Letters* 91.2A, pp. 770–786.

Hirschberg, Stefan, Stefan Wiemer, and Peter Burgherr (2014). *Energy from the Earth: Deep Geothermal as a Resource for the Future?* Vol. 62. vdf Hochschulverlag AG.

Horne, Roland N. (1995). "Modern well test analysis." In: *Petroway Inc* 926, p. 987.

Huang, Yihe, Lingsen Meng, and Jean-Paul Ampuero (2012). "A dynamic model of the frequency-dependent rupture process of the 2011 Tohoku-Oki earthquake." In: *Earth, planets and space* 64, pp. 1061–1066.

Hulikal, Srivatsan, Nadia Lapusta, and Kaushik Bhattacharya (2018). "Static and sliding contact of rough surfaces: effect of asperity-scale properties and long-range elastic interactions." In: *Journal of the Mechanics and Physics of Solids* 116, pp. 217–238.

Ikari, Matt J. and Demian M. Saffer (2011). "Comparison of frictional strength and velocity dependence between fault zones in the Nankai accretionary complex." In: *Geochemistry, Geophysics, Geosystems* 12.4.

Ikari, Matt J., Demian M. Saffer, and Chris Marone (2009). "Frictional and hydrologic properties of clay-rich fault gouge." In: *Journal of Geophysical Research: Solid Earth* 114.B5.

Im, Kyungjae et al. (2017). "Geodetic imaging of thermal deformation in geothermal reservoirs-production, depletion and fault reactivation." In: *Journal of Volcanology and Geothermal Research* 338, pp. 79–91.

Im, Kyungjae et al. (2020). "Slip-rate-dependent friction as a universal mechanism for slow slip events." In: *Nature Geoscience* 13.10, pp. 705–710.

Ishii, Miaki et al. (2005). "Extent, duration and speed of the 2004 Sumatra–Andaman earthquake imaged by the Hi-Net array." In: *Nature* 435.7044, pp. 933–936.

Jia, Zhe et al. (2023). "The complex dynamics of the 2023 Kahramanmaraş, Turkey, M w 7.8-7.7 earthquake doublet." In: *Science* 381.6661, pp. 985–990.

Karimi, Mina and Kaushik Bhattacharya (2024). "Accelerated computational micromechanics for solute transport in porous media." In: *Computer Methods in Applied Mechanics and Engineering* 426, p. 116976.

Kato, Naoyuki and Terry E. Tullis (2001). "A composite rate-and state-dependent law for rock friction." In: *Geophysical research letters* 28.6, pp. 1103–1106.

Ke, Chun-Yu, Gregory C McLaskey, and David S Kammer (2022). "Earthquake breakdown energy scaling despite constant fracture energy." In: *Nature Communications* 13.1, p. 1005.

Kim, Kwang-Hee et al. (2018). "Assessing whether the 2017 M w 5.4 Pohang earthquake in South Korea was an induced event." In: *Science* 360.6392, pp. 1007–1009.

Kim, Taeho and Jean-Philippe Avouac (2023). "Stress-based and convolutional forecasting of injection-induced seismicity: application to the Otaniemi geothermal reservoir stimulation." In: *Journal of Geophysical Research: Solid Earth* 128.4, e2022JB024960.

Koper, Keith D. et al. (2012). "Imaging short-period seismic radiation from the 27 February 2010 Chile (Mw 8.8) earthquake by back-projection of P, PP, and PKIKP waves." In: *Journal of Geophysical Research: Solid Earth* 117.B2.

Kwiatek, Grzegorz et al. (2019). "Controlling fluid-induced seismicity during a 6.1-km-deep geothermal stimulation in Finland." In: *Science Advances* 5.5, eaav7224.

Lambert, Valère, Nadia Lapusta, and Stephen Perry (2021). "Propagation of large earthquakes as self-healing pulses or mild cracks." In: *Nature* 591.7849, pp. 252–258.

Langenbruch, Cornelius and Serge A. Shapiro (2010). "Decay rate of fluid-induced seismicity after termination of reservoir stimulations." In: *Geophysics* 75.6, MA53–MA62.

Lapusta, Nadia and Yi Liu (2009). "Three-dimensional boundary integral modeling of spontaneous earthquake sequences and aseismic slip." In: *Journal of Geophysical Research: Solid Earth* 114.B9.

Lapusta, Nadia et al. (2000). "Elastodynamic analysis for slow tectonic loading with spontaneous rupture episodes on faults with rate-and state-dependent friction." In: *Journal of Geophysical Research: Solid Earth* 105.B10, pp. 23765–23789.

Larochelle, Stacy et al. (2021). "Constraining fault friction and stability with fluid-injection field experiments." In: *Geophysical Research Letters* 48.10, e2020GL091188.

Lavrov, Alexander (2003). "The Kaiser effect in rocks: principles and stress estimation techniques." In: *International Journal of Rock Mechanics and Mining Sciences* 40.2, pp. 151–171.

Lay, Thorne et al. (2012). "Depth-varying rupture properties of subduction zone megathrust faults." In: *Journal of Geophysical Research: Solid Earth* 117.B4.

Lee, En-Jui et al. (2014). "Full-3-D tomography for crustal structure in southern California based on the scattering-integral and the adjoint-wavefield methods." In: *Journal of Geophysical Research: Solid Earth* 119.8, pp. 6421–6451.

Leeman, John R., Chris Marone, and Demian M Saffer (2018). "Frictional mechanics of slow earthquakes." In: *Journal of Geophysical Research: Solid Earth* 123.9, pp. 7931–7949.

Lei, Xinglin et al. (2008). "Earthquakes induced by water injection at 3 km depth within the Rongchang gas field, Chongqing, China." In: *Journal of Geophysical Research: Solid Earth* 113.B10.

Leonhardt, Maria et al. (2020). "Seismicity during and after stimulation of a 6.1 km deep enhanced geothermal system in Helsinki, Finland." In: *Solid Earth Discussions* 2020, pp. 1–29.

Li, Bo et al. (2022). "Rupture heterogeneity and directivity effects in back-projection analysis." In: *Journal of Geophysical Research: Solid Earth* 127.3, e2021JB022663.

Li, Jiaxuan et al. (2023). “The break of earthquake asperities imaged by distributed acoustic sensing.” In: *Nature* 620.7975, pp. 800–806.

Li, Qunyang et al. (2011). “Frictional ageing from interfacial bonding and the origins of rate and state friction.” In: *Nature* 480.7376, pp. 233–236.

Li, Zefeng and Zhongwen Zhan (2018). “Pushing the limit of earthquake detection with distributed acoustic sensing and template matching: A case study at the Brady geothermal field.” In: *Geophysical Journal International* 215.3, pp. 1583–1593.

Lindsey, Nathaniel J and Eileen R Martin (2021). “Fiber-optic seismology.” In: *Annual Review of Earth and Planetary Sciences* 49.1, pp. 309–336.

Linker, MF and James H. Dieterich (1992). “Effects of variable normal stress on rock friction: Observations and constitutive equations.” In: *Journal of Geophysical Research: Solid Earth* 97.B4, pp. 4923–4940.

Madariaga, Raul (1983). “High frequency radiation from dynamic earthquake fault models.” In: *Annales de Geophysique*. Vol. 1. 1, pp. 17–23.

Majer, Ernest L. et al. (2007). “Induced seismicity associated with enhanced geothermal systems.” In: *Geothermics* 36.3, pp. 185–222.

Marone, Chris (1998). “Laboratory-derived friction laws and their application to seismic faulting.” In: *Annual Review of Earth and Planetary Sciences* 26.1, pp. 643–696.

Marsan, David and Olivier Lengline (2008). “Extending earthquakes’ reach through cascading.” In: *Science* 319.5866, pp. 1076–1079.

Marty, Samson et al. (2019). “Origin of high-frequency radiation during laboratory earthquakes.” In: *Geophysical Research Letters* 46.7, pp. 3755–3763.

Massey Jr, Frank J. (1951). “The Kolmogorov-Smirnov test for goodness of fit.” In: *Journal of the American statistical Association* 46.253, pp. 68–78.

McClure, Mark W. and Roland N. Horne (2011). “Investigation of injection-induced seismicity using a coupled fluid flow and rate/state friction model.” In: *Geophysics* 76.6, WC181–WC198.

McGarr, Arthur (2014). “Maximum magnitude earthquakes induced by fluid injection.” In: *Journal of Geophysical Research: Solid Earth* 119.2, pp. 1008–1019.

McLaskey, Gregory C. (2019). “Earthquake initiation from laboratory observations and implications for foreshocks.” In: *Journal of Geophysical Research: Solid Earth* 124.12, pp. 12882–12904.

McLaskey, Gregory C. and Brian D. Kilgore (2013). “Foreshocks during the nucleation of stick-slip instability.” In: *Journal of Geophysical Research: Solid Earth* 118.6, pp. 2982–2997.

Melosh, H. Jay (1979). "Acoustic fluidization: A new geologic process?" In: *Journal of Geophysical Research: Solid Earth* 84.B13, pp. 7513–7520.

Mena, Banu, Stefan Wiemer, and Corinne Bachmann (2013). "Building robust models to forecast the induced seismicity related to geothermal reservoir enhancement." In: *Bulletin of the Seismological Society of America* 103.1, pp. 383–393.

Meng, Lingsen, Asaf Inbal, and Jean-Paul Ampuero (2011). "A window into the complexity of the dynamic rupture of the 2011 Mw 9 Tohoku-Oki earthquake." In: *Geophysical Research Letters* 38.7.

Mesimeri, Maria, Hao Zhang, and Kristine L Pankow (2021). "Backprojection imaging of the 2020 Mw 5.5 Magna, Utah, earthquake using a local dense strong-motion network." In: *Seismological Research Letters* 92.2A, pp. 640–646.

Miller, Stephen A. (2013). "The role of fluids in tectonic and earthquake processes." In: *Advances in geophysics* 54, pp. 1–46.

– (2020). "Aftershocks are fluid-driven and decay rates controlled by permeability dynamics." In: *Nature Communications* 11.1, p. 5787.

Mitchell, Tom M. and Daniel R. Faulkner (2009). "The nature and origin of off-fault damage surrounding strike-slip fault zones with a wide range of displacements: A field study from the Atacama fault system, northern Chile." In: *Journal of Structural Geology* 31.8, pp. 802–816.

Nagata, Kohei, M. Nakatani, and S Yoshida (2012). "A revised rate-and state-dependent friction law obtained by constraining constitutive and evolution laws separately with laboratory data." In: *Journal of Geophysical Research: Solid Earth* 117.B2.

Noda, Hiroyuki and Nadia Lapusta (2010). "Three-dimensional earthquake sequence simulations with evolving temperature and pore pressure due to shear heating: Effect of heterogeneous hydraulic diffusivity." In: *Journal of Geophysical Research: Solid Earth* 115.B12.

– (2013). "Stable creeping fault segments can become destructive as a result of dynamic weakening." In: *Nature* 493.7433, pp. 518–521.

Noël, Corentin et al. (2023). "The effect of shear displacement and wear on fault stability: Laboratory constraints." In: *Journal of Geophysical Research: Solid Earth* 128.4, e2022JB026191.

Noël, Corentin et al. (2024). "The effect of shear strain and shear localization on fault healing." In: *Geophysical Journal International* 236.3, pp. 1206–1215.

Norbeck, Jack H. and Justin L. Rubinstein (2018). "Hydromechanical earthquake nucleation model forecasts onset, peak, and falling rates of induced seismicity in Oklahoma and Kansas." In: *Geophysical Research Letters* 45.7, pp. 2963–2975.

Nur, Amos and John R. Booker (1972). "Aftershocks caused by pore fluid flow?" In: *Science* 175.4024, pp. 885–887.

Ogata, Yosihiko (1988). "Statistical models for earthquake occurrences and residual analysis for point processes." In: *Journal of the American Statistical association* 83.401, pp. 9–27.

Okada, Yoshimitsu (1985). "Surface deformation due to shear and tensile faults in a half-space." In: *Bulletin of the seismological society of America* 75.4, pp. 1135–1154.

Oliphant, Travis E. (2007). "Python for scientific computing." In: *Computing in science & engineering* 9.3, pp. 10–20.

Olsen, Kim B., Raul Madariaga, and Ralph J. Archuleta (1997). "Three-dimensional dynamic simulation of the 1992 Landers earthquake." In: *Science* 278.5339, pp. 834–838.

Palmer, Andrew Clennel and James Robert Rice (1973). "The growth of slip surfaces in the progressive failure of over-consolidated clay." In: *Proceedings of the Royal Society of London. A. Mathematical and Physical Sciences* 332.1591, pp. 527–548.

Perfettini, Hugo and Jean-Philippe Avouac (2004). "Postseismic relaxation driven by brittle creep: A possible mechanism to reconcile geodetic measurements and the decay rate of aftershocks, application to the Chi-Chi earthquake, Taiwan." In: *Journal of Geophysical Research: Solid Earth* 109.B2.

Rackauckas, Christopher and Qing Nie (2017). "Differentialequations. jl–a performant and feature-rich ecosystem for solving differential equations in julia." In: *Journal of open research software* 5.1, pp. 15–15.

Raleigh, CB, John H. Healy, and John D. Bredehoeft (1976). "An experiment in earthquake control at Rangely, Colorado." In: *Science* 191.4233, pp. 1230–1237.

Ranjith, Kunnath and James R Rice (1999). "Stability of quasi-static slip in a single degree of freedom elastic system with rate and state dependent friction." In: *Journal of the Mechanics and Physics of Solids* 47.6, pp. 1207–1218.

Rathbun, Andrew P. and Chris Marone (2013). "Symmetry and the critical slip distance in rate and state friction laws." In: *Journal of Geophysical Research: Solid Earth* 118.7, pp. 3728–3741.

Rice, James R. (2006). "Heating and weakening of faults during earthquake slip." In: *Journal of Geophysical Research: Solid Earth* 111.B5.

Rice, James R., Nadia Lapusta, and Kunnath Ranjith (2001). "Rate and state dependent friction and the stability of sliding between elastically deformable solids." In: *Journal of the Mechanics and Physics of Solids* 49.9, pp. 1865–1898.

Rice, James R. and Andy L. Ruina (1983). "Stability of steady frictional slipping." In.

Richter, Gudrun et al. (2020). "Stress-based, statistical modeling of the induced seismicity at the Groningen gas field, The Netherlands." In: *Environmental Earth Sciences* 79.11, p. 252.

Ross, Zachary E., Men-Andrin Meier, and Egill Hauksson (2018). "P wave arrival picking and first-motion polarity determination with deep learning." In: *Journal of Geophysical Research: Solid Earth* 123.6, pp. 5120–5129.

Ross, Zachary E. et al. (2018). "Generalized seismic phase detection with deep learning." In: *Bulletin of the Seismological Society of America* 108.5A, pp. 2894–2901.

Rubin, Allen M. and Jean-Paul Ampuero (2005). "Earthquake nucleation on (aging) rate and state faults." In: *Journal of Geophysical Research: Solid Earth* 110.B11.

Rubino, Vito, Ares J. Rosakis, and Nadia Lapusta (2017). "Understanding dynamic friction through spontaneously evolving laboratory earthquakes." In: *Nature communications* 8.1, p. 15991.

Rudnicki, John W. (1986). "Fluid mass sources and point forces in linear elastic diffusive solids." In: *Mechanics of materials* 5.4, pp. 383–393.

Rudnicki, John W. and James R. Rice (1975). "Conditions for the localization of deformation in pressure-sensitive dilatant materials." In: *Journal of the Mechanics and Physics of Solids* 23.6, pp. 371–394.

Ruina, Andy (1983). "Slip instability and state variable friction laws." In: *Journal of Geophysical Research: Solid Earth* 88.B12, pp. 10359–10370.

Rutqvist, Jonny and Curtis M Oldenburg (2008). "Analysis of injection-induced micro-earthquakes in a geothermal steam reservoir, the Geysers Geothermal Field, California." In: *ARMA US Rock Mechanics/Geomechanics Symposium*. ARMA, ARMA–08.

Sáez, Alexis (2023). "Three-dimensional fluid-driven frictional ruptures: theory and applications." PhD thesis. EPFL, Lausanne.

Sammis, Charles G. and Yehuda Ben-Zion (2008). "Mechanics of grain-size reduction in fault zones." In: *Journal of Geophysical Research: Solid Earth* 113.B2.

Schaal, Natalie and Nadia Lapusta (2019). "Microseismicity on patches of higher compression during larger-scale earthquake nucleation in a rate-and-state fault model." In: *Journal of Geophysical Research: Solid Earth* 124.2, pp. 1962–1990.

Schultz, Ryan et al. (2020). "Hydraulic fracturing-induced seismicity." In: *Reviews of Geophysics* 58.3, e2019RG000695.

Scotti, O and Francois H. Cornet (1994). "In situ evidence for fluid-induced aseismic slip events along fault zones." In: *International journal of rock mechanics and mining sciences & geomechanics abstracts*. Vol. 31. 4. Elsevier, pp. 347–358.

Scuderi, Marco M., Cristiano Collettini, and Chris Marone (2017). "Frictional stability and earthquake triggering during fluid pressure stimulation of an experimental fault." In: *Earth and Planetary Science Letters* 477, pp. 84–96.

Segall, Paul (1989). "Earthquakes triggered by fluid extraction." In: *Geology* 17.10, pp. 942–946.

Segall, Paul, Jean-Robert Grasso, and Antony Mossop (1994). "Poroelastic stressing and induced seismicity near the Lacq gas field, southwestern France." In: *Journal of Geophysical Research: Solid Earth* 99.B8, pp. 15423–15438.

Segall, Paul and S Lu (2015). "Injection-induced seismicity: Poroelastic and earthquake nucleation effects." In: *Journal of Geophysical Research: Solid Earth* 120.7, pp. 5082–5103.

Segall, Paul and James R. Rice (1995). "Dilatancy, compaction, and slip instability of a fluid-infiltrated fault." In: *Journal of Geophysical Research: Solid Earth* 100.B11, pp. 22155–22171.

Segall, Paul et al. (2006). "Earthquakes triggered by silent slip events on Kılauea volcano, Hawaii." In: *Nature* 442.7098, pp. 71–74.

Segall, Paul et al. (2010). "Dilatant strengthening as a mechanism for slow slip events." In: *Journal of Geophysical Research: Solid Earth* 115.B12.

Shapiro, Serge A., Oliver S. Krüger, and Carsten Dinske (2013). "Probability of inducing given-magnitude earthquakes by perturbing finite volumes of rocks." In: *Journal of Geophysical Research: Solid Earth* 118.7, pp. 3557–3575.

Shapiro, Serge A. et al. (2002). "Characterization of fluid transport properties of reservoirs using induced microseismicity." In: *Geophysics* 67.1, pp. 212–220.

Shapiro, Serge A. et al. (2006). "Fluid induced seismicity guided by a continental fault: Injection experiment of 2004/2005 at the German Deep Drilling Site (KTB)." In: *Geophyiscal Research Letters* 33.1.

Shapiro, Serge A. et al. (2011). "Magnitudes of induced earthquakes and geometric scales of fluid-stimulated rock volumes." In: *Geophysics* 76.6, WC55–WC63.

Shapiro, Sergei A., Ernst Huenges, and Günter Borm (1997). "Estimating the crust permeability from fluid-injection-induced seismic emission at the KTB site." In: *Geophysical Journal International* 131.2, F15–F18.

Shapiro, Sergei A. and Tobias M. Müller (1999). "Seismic signatures of permeability in heterogeneous porous media." In: *Geophysics* 64.1, pp. 99–103.

Simons, Mark et al. (2011). "The 2011 magnitude 9.0 Tohoku-Oki earthquake: Mosaicking the megathrust from seconds to centuries." In: *science* 332.6036, pp. 1421–1425.

Sirorattanakul, Krittanon et al. (2022). "The 2020 Westmorland, California earthquake swarm as aftershocks of a slow slip event sustained by fluid flow." In: *Journal of Geophysical Research: Solid Earth* 127.11, e2022JB024693.

Skarbek, Rob M. and Heather M. Savage (2019). "RSFit3000: A MATLAB GUI-based program for determining rate and state frictional parameters from experimental data." In: *Geosphere* 15.5, pp. 1665–1676.

Skempton, Alec W. (1984). "Effective stress in soils, concrete and rocks." In: *Selected papers on soil mechanics* 1032.3, pp. 4–16.

Smith, Jonathan D. et al. (2020). "Probabilistic earthquake locations of induced seismicity in the Groningen region, the Netherlands." In: *Geophysical Journal International* 222.1, pp. 507–516.

State of California Middle-Mile Broadband Initiative (n.d.). `https://middle-mile-broadband-initiative.cdt.ca.gov/`. Accessed: 2024-06-28.

Stathas, Alexandros and Ioannis Stefanou (2023). "Fault friction under thermal pressurization during large seismic-slip: Numerical analyses and extension of the model of frictional slip." In: *International Journal of Mechanical Sciences* 248, p. 108184.

Stefanou, Ioannis (2019). "Controlling anthropogenic and natural seismicity: Insights from active stabilization of the spring-slider model." In: *Journal of Geophysical Research: Solid Earth* 124.8, pp. 8786–8802.

Taufiqurrahman, Taufiq et al. (2023). "Dynamics, interactions and delays of the 2019 Ridgecrest rupture sequence." In: *Nature* 618.7964, pp. 308–315.

Tester, Jefferson W. et al. (2006). "The future of geothermal energy." In: *Massachusetts Institute of Technology* 358, pp. 1–3.

The Solar Power Duck Curve Explained (n.d.). `https://elements.visualcapitalist.com/the-solar-power-duck-curve-explained/`. Accessed: 2024-06-28.

Toda, Shinji, Ross S. Stein, and Takeshi Sagiya (2002). "Evidence from the AD 2000 Izu islands earthquake swarm that stressing rate governs seismicity." In: *Nature* 419.6902, pp. 58–61.

Toda, Shinji et al. (1998). "Stress transferred by the 1995 Mw= 6.9 Kobe, Japan, shock: Effect on aftershocks and future earthquake probabilities." In: *Journal of Geophysical Research: Solid Earth* 103.B10, pp. 24543–24565.

Toda, Shinji et al. (2012). "Aftershocks halted by static stress shadows." In: *Nature Geoscience* 5.6, pp. 410–413.

Tsai, Victor C. and Greg Hirth (2020). "Elastic impact consequences for high-frequency earthquake ground motion." In: *Geophysical Research Letters* 47.5, e2019GL086302.

Tsai, Victor C. et al. (2021). "Impact versus frictional earthquake models for high-frequency radiation in complex fault zones." In: *Journal of Geophysical Research: Solid Earth* 126.8, e2021JB022313.

Utsu, Tokuji (2002). "Statistical features of seismicity." In: *International Geophysics*. Vol. 81. Elsevier, pp. 719–732.

Vallée, Martin et al. (2011). "SCARDEC: a new technique for the rapid determination of seismic moment magnitude, focal mechanism and source time functions for large earthquakes using body-wave deconvolution." In: *Geophysical Journal International* 184.1, pp. 338–358.

Van der Elst, Nicholas J et al. (2016). "Induced earthquake magnitudes are as large as (statistically) expected." In: *Journal of Geophysical Research: Solid Earth* 121.6, pp. 4575–4590.

Vilarrasa, Victor and Jesus Carrera (2015). "Geologic carbon storage is unlikely to trigger large earthquakes and reactivate faults through which CO2 could leak." In: *Proceedings of the National Academy of Sciences* 112.19, pp. 5938–5943.

Wei, Shengji et al. (2015). "The 2012 Brawley swarm triggered by injection-induced aseismic slip." In: *Earth and Planetary Science Letters* 422, pp. 115–125.

Wenzel, Friedemann (2017). "Fluid-induced seismicity: Comparison of rate-and state-and critical pressure theory." In: *Geothermal Energy* 5, pp. 1–16.

White, Joshua A. and William Foxall (2016). "Assessing induced seismicity risk at CO2 storage projects: Recent progress and remaining challenges." In: *International Journal of Greenhouse Gas Control* 49, pp. 413–424.

Xu, Yan et al. (2009). "Rupture imaging of the Mw 7.9 12 May 2008 Wenchuan earthquake from back projection of teleseismic P waves." In: *Geochemistry, Geophysics, Geosystems* 10.4.

Yang, HongFeng et al. (2017). "Induced earthquakes in the development of unconventional energy resources." In: *Science China Earth Sciences* 60, pp. 1632–1644.

Yao, Huajian, Peter M Shearer, and Peter Gerstoft (2013). "Compressive sensing of frequency-dependent seismic radiation from subduction zone megathrust ruptures." In: *Proceedings of the National Academy of Sciences* 110.12, pp. 4512–4517.

Yin, Jiuxun and Marine A Denolle (2021). "The earth's surface controls the depth-dependent seismic radiation of megathrust earthquakes." In: *AGU Advances* 2.3, e2021AV000413.

Zaliapin, Ilya and Yehuda Ben-Zion (2013). "Earthquake clusters in southern California I: Identification and stability." In: *Journal of Geophysical Research: Solid Earth* 118.6, pp. 2847–2864.

Zang, Arno et al. (2014). "Analysis of induced seismicity in geothermal reservoirs–An overview." In: *Geothermics* 52, pp. 6–21.

Zbinden, Dominik et al. (2020). "Hydromechanical modeling of fault reactivation in the St. Gallen deep geothermal project (Switzerland): Poroelasticity or hydraulic connection?" In: *Geophysical Research Letters* 47.3, e2019GL085201.

Zhai, Guang and Manoochehr Shirzaei (2018). “Fluid injection and time-dependent seismic hazard in the Barnett Shale, Texas.” In: *Geophysical Research Letters* 45.10, pp. 4743–4753.

Zhan, Zhongwen (2020). “Distributed acoustic sensing turns fiber-optic cables into sensitive seismic antennas.” In: *Seismological Research Letters* 91.1, pp. 1–15.

Zimmerman, Robert W. (2018). *The Imperial College Lectures in Petroleum Engineering: Volume 5: Fluid Flow in Porous Media*. World Scientific.

Zoback, Mark D. and Steven M. Gorelick (2012). “Earthquake triggering and large-scale geologic storage of carbon dioxide.” In: *Proceedings of the National Academy of Sciences* 109.26, pp. 10164–10168.

Zöller, Gert, Matthias Holschneider, and Yehuda Ben-Zion (2005). “The role of heterogeneities as a tuning parameter of earthquake dynamics.” In: *Pure and Applied Geophysics* 162, pp. 1027–1049.

Appendix A

APPENDIX FOR CHAPTER 2

A.1 Estimate of Experimental Noise as a Gaussian Distribution

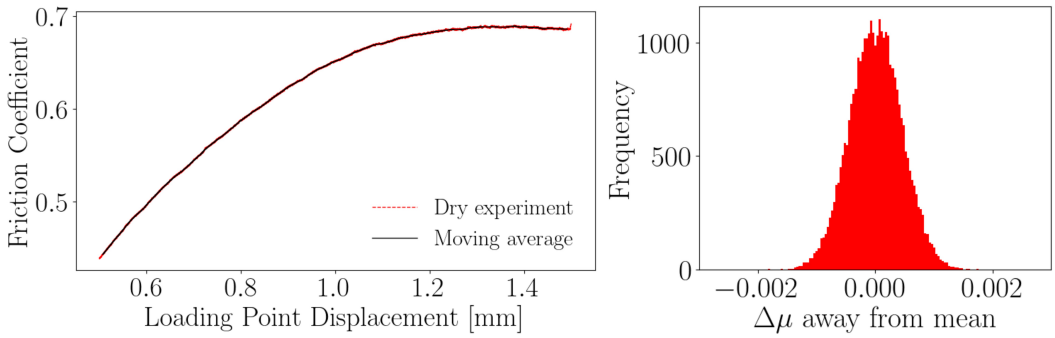

Figure A.1: Estimate of Experimental Noise as a Gaussian Distribution. (Left) A moving average of the friction measurement from the dry experiment is subtracted from the raw data in the first 1.5mm of loading point displacement. (Right) The difference between the raw data and the moving average is plotted as a histogram. The distribution closely resembles a Gaussian distribution. The standard deviation of 0.0004 is used as the standard deviation of Gaussian noise in the probabilistic model of Equation 2.8.

Appendix B

APPENDIX FOR CHAPTER 3

B.1 Demonstration of Marsan and Lengline (2008) Adaptation on Synthetic Catalogue

The adaptation of the Marsan and Lengline (2008) algorithm presented in Section 3.4 is demonstrated on a simple synthetic catalogue. We consider a stepwise injection scenario and a seismicity rate history that exhibits $1/t$ type of response to discretized injection cycles. Such a seismicity rate history can be computed as the convolution product of the injection rate history with a kernel that is the derivative of the Omori law decay function. Here, t_r is chosen to be 20 hours for an injection duration of 333.3 hours. The seismicity rate is computed for a total duration of 1000 hours. The resulting injection rate and seismicity rate are shown in Figure B.1.

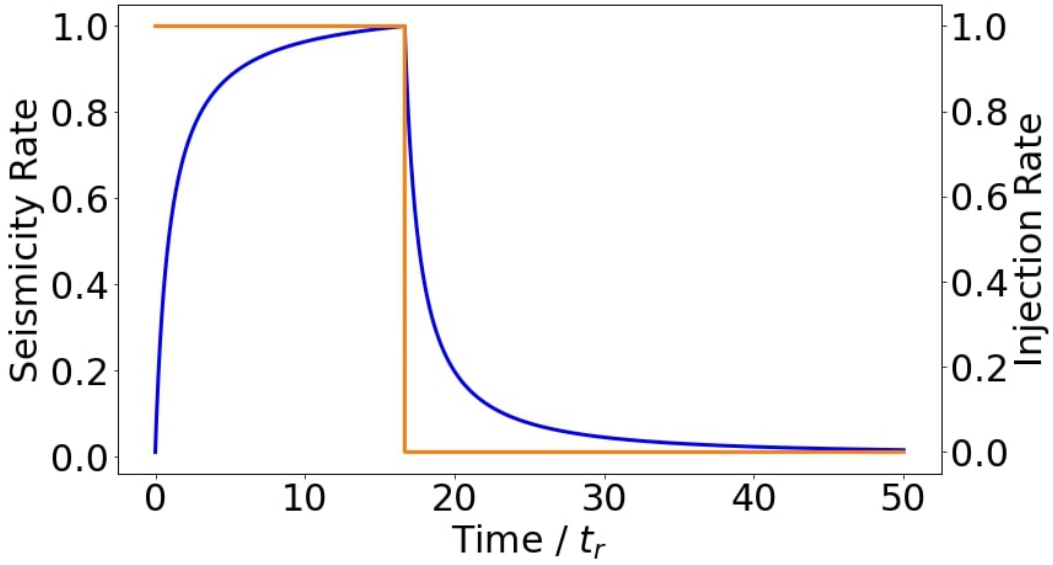

Figure B.1: Seismicity and injection rate for the demonstration of Marsan and Lengline (2008) adaptation. The seismicity rate is produced by convolution of the step-wise injection history with a kernel derived from the differentiation of the Omori law. The rates are normalized by their maximum values.

The Marsan and Lengline (2008) adaptation is performed on synthetic catalogues of the seismicity rate history and injection cycles that discretize the constant injection period. Figure B.2 shows the sensitivity of the bare rates to δt and the ratio of the

width of injection cycles, t_{Ic}. Both plots show that the algorithm identifies a $1/t$ type of decay in the bare rates as prescribed in the synthetic catalogue with minor sensitivity to δt and t_r/t_{Ic}.

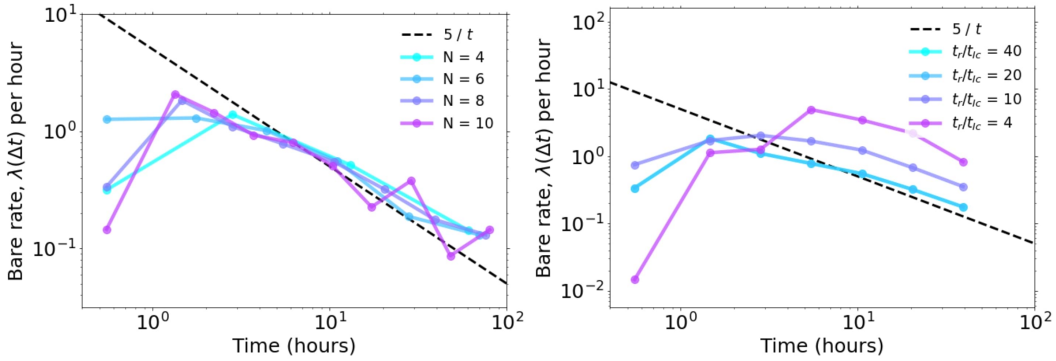

Figure B.2: Sensitivity of the bare rates to discretization of δt (left) and injection cycles by ratios of t_r to the duration of binned injection cycles, t_{Ic} (right). N represents the number of δt intervals used to discretize the interval of 1 to 100 hours in log space. Both plots show $1/t$ type of decay for all hyperparameters, with the exception of $t_r/t_{Ic} = 4$ for earlier times which represents cases of poor resolution of the injection history.

B.2 Horner Analysis of Spherical Well in Infinite Medium and MCMC Inversion of Fluid Transport Properties

The traditional Horner analysis for inference of diffusivity from well pressure measurements is adapted here for a spherical well in an infinite medium. Starting with the analytical solution of Equation 3.7, the $\operatorname{erfc}\left(\frac{1}{2}\xi\right)$ term is expanded in a Taylor series with truncation up to the first term

$$p(r,t) = \frac{q}{4\pi\rho_0 r}\frac{\eta}{k}\left(1 - \frac{r}{\sqrt{\pi c t}}\right) \tag{B.1}$$

This approximation is valid for large t and small r, i.e., at later times close to the injection well.

Pore pressure due to a boxcar injection scenario in which a step-wise injection with mass injection rate q is introduced at $t = 0$ and abruptly stops at $t = t_p$ can be found by superposition of two solutions

$$p(r,\Delta t) = \frac{1}{k}\frac{q\eta^{3/2}}{4\pi^{3/2}\rho_0}\sqrt{\frac{\alpha^2(\lambda_u + 2\mu)}{(\lambda_u - \lambda)(\lambda + 2\mu)}}\left(\frac{\sqrt{t_p + \Delta t} - \sqrt{\Delta t}}{\sqrt{\Delta t(t_p + \Delta t)}}\right), \tag{B.2}$$

where Δt is the time since the injection shut-ins at $t = t_p$. The fraction in the parentheses may be referred to as the modified Horner time which decreases with increasing Δt asymptotically to 0. If one plots the pore pressure during shut-in against the modified Horner time, k may be found in terms of the slope m as follows

$$k = \frac{\eta}{\pi}\left(\frac{q}{4\rho_0 m}\sqrt{\frac{\alpha^2(\lambda_u + 2\mu)}{(\lambda_u - \lambda)(\lambda + 2\mu)}}\right)^{2/3} \tag{B.3}$$

To match as best as possible the underlying assumptions of the Horner analysis which is based on an idealized scenario of a single boxcar injection starting from steady-state conditions, the injection pause beginning at about the 260-hour mark of Figure 3.2 is taken as it has the smallest number of cyclic injections since the last significant shut-in at around the 190-hour mark. t_p is taken to be the duration of the last injection cycle prior to shut-in. Plotting the well pressure measurement for a duration of 6.65 hours since shut-in against the modified Horner time results in Figure B.3.

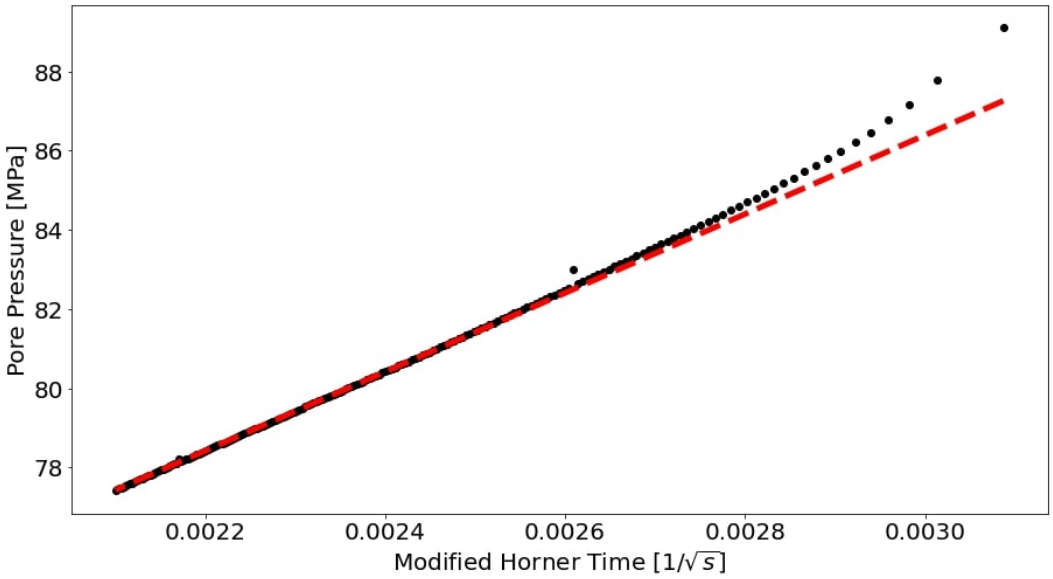

Figure B.3: Well pressure against modified Horner time during shut-in. Measurements of well pressure during a shut-in period is shown as a scatter plot against the modified Horner time in black. For later times during the shut-in period (earlier in terms of modified Horner time), the pressure evolution follows a linear relationship as predicted by Horner analysis. The red dashed line indicates the line of best fit through the linear portion of the curve, the slope of which results in a diffusivity of 0.018 m^2/s.

MCMC inversions are run to estimate the effective well radius w_r, and the ambient pore pressure p_0. The effective well radius is a measure of the damage surrounding the injection source that causes drops in the pressure. The effective well radius is added to the radius for computation of pore pressure. p_0 is simply added to the pore pressure variation due to injection. The final pressure profile is computed as follows

$$p(r,t) = \frac{q}{4\pi\rho_0(r+w_r)}\frac{\eta}{k_{true}}\,\mathrm{erfc}\left(\frac{1}{2}\xi\right) + p_0 \tag{B.4}$$

$$\xi = \frac{r+w_r}{\sqrt{c_{true}t}}$$

The MCMC algorithm aims to maximize the Gaussian log-likelihood between the measured and simulated pore pressure

$$\mathbb{P}(\theta) = -\frac{1}{2}\sum_{i=1}^{N}(p_i^0 - p(t=t_i, r=w_r, \theta))^2, \tag{B.5}$$

where p_i^0 is the observed well pressure at $t = t_i$, θ are model parameters and $i = \{1, 2, ..., N\}$ for N measurements. The sampler conducts 2000 iterations of 32 walkers with the chain length made to be longer than 50 times the auto-correlation length in order to ensure full exploration of the posterior distribution. The prior is assumed to be uniform for both variables between the ranges of $20 \sim 80$m and $40 \sim 60$ MPa. Interestingly, a global fit to the well pressure history with diffusivity also as a free parameter returns a value different from that inferred by Horner analysis. The prior on c is assumed to be uniform in the range of $0.01 \sim 0.1$ m^2/s.

B.3 Zaliapin and Ben-Zion (2013) Cluster Analysis.

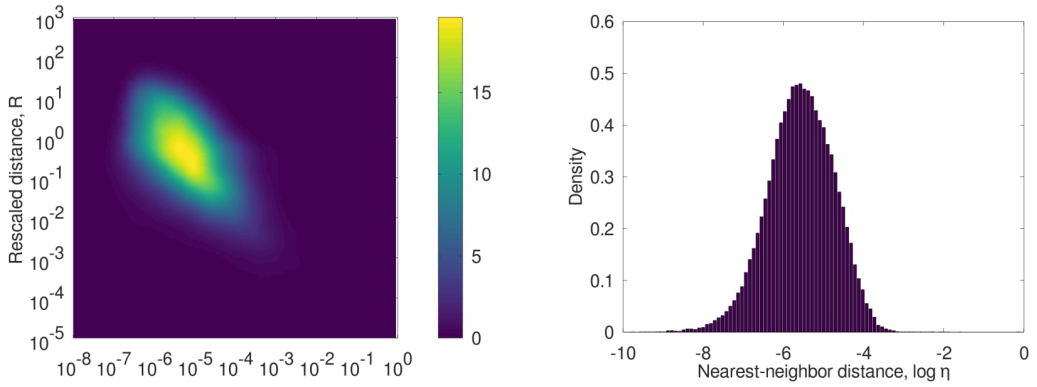

Figure B.4: Zaliapin and Ben-Zion (2013) cluster analysis. The contour plot (left) shows the distribution of the nearest-neighboring distance of all events in terms of their rescaled inter-occurrence time and distances. Following Zaliapin and Ben-Zion (2013), rescaled time, $T_{ij} = t_{ij}10^{-qbm_i}$ and rescaled distance, $R_{ij} = r_{ij}^{d_f}10^{-(1-q)bm_i}$ where t_{ij} and r_{ij} are the interevent times and distances, respectively, between events i and j, b is the b-value of the Gutenberg-Richter distribution, m_i is the magnitude of event i, d_f is the dimension of the earthquake hypocenter distribution, and q is a multiplicative factor. The histogram (right) plots the frequency distribution of the nearest-neighboring distances. Both plots exhibit strong uni-modal behavior, characteristic of absence of aftershock sequences.

B.4 Kaiser Effect in Heimisson and Segall (2018)

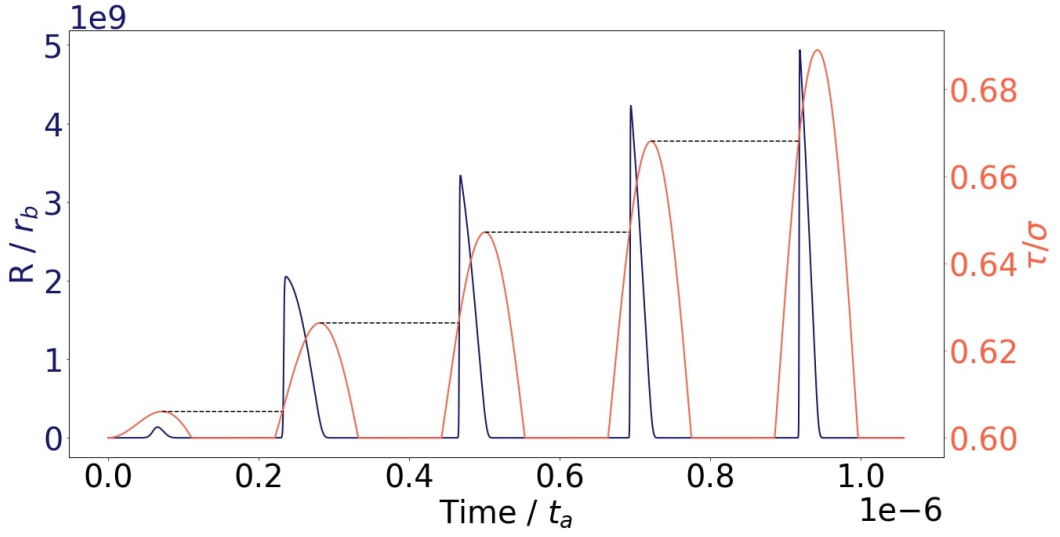

Figure B.5: Kaiser Effect in Heimisson and Segall (2018). Seismicity rate (purple) following the Heimisson & Segall (2018) formulation is plotted in response to a sinusoidal stress history (orange). The dotted lines track the previous maximum shear stress until it is superseded, during which the induced seismicity rate remains close to zero.

B.5 Sensitivity Analysis of γ_h on Physical Parameters and Estimating c_{hg} in Otaniemi

To identify an empirical relationship between γ_h and the non-dimensional parameters, we simulated boxcar injection scenarios using the rate-and-state model for a range of values of a an k. The injection rate, q, is varied for the characteristic pore pressure, $p_q = \frac{q\eta}{4\pi\rho_0 k w_r}$, to reach 0.1 of the ambient pore pressure, p_0, and $w_r = 31$m as from the MCMC inversion for c_{bu}. c and a are varied between $[0.01 \sim 0.1\ \mathrm{m^2/s}]$ and $[10^{-5} \sim 10^{-3}]$, respectively.

For estimating c_{hg} in Otaniemi, we infer from the cumulative relocated catalogue as opposed to binning discretized intervals to directly measure c_{hg} given the relatively small sample size. We note that integrating the spherical integrand of the half-norm distribution in time has an analytical form as follows

$$\int_0^{t_N} 4\pi r^2 \sqrt{\frac{2}{\pi c_{hg} t}} \exp\left(-\frac{r^2}{2c_{hg}t}\right) dt = \frac{4\sqrt{\pi} r^3}{c_{hg}} \Gamma\left(-0.5, \frac{r^2}{2c_{hg}t_N}\right) \tag{B.6}$$

where t_N is the occurrence time of the last event and Γ is the upper incomplete gamma function. Equation B.6 corresponds to the cumulative radial distribution of seismicity of a catalogue that follows the half-norm distribution in space with no decrease of the total seismicity rate in time. Fitting Equation B.6 to the distribution of the relocated catalogue is shown in Figure S6 with $c_{hg} = 0.011\ \mathrm{m^2/s}$. The fit also serves well for the spatio-temporal convolution model of Section 3.7 of the main text.

B.6 Standard Coulomb Model without Thresholds

To examine the effects of the nucleation process more closely, we compare the rate-and-state model with one that assumes instantaneous nucleation once the Coulomb criterion for failure is reached. In this case, the seismicity rate is directly proportional to the stressing rate. In relation to equation (15), the critical distribution assumes a constant value. The result from the Coulomb model with the Kaiser effect and resetting of the stress history with new injection stages is shown in Figure B.7. α_c is found to be 47250MPa/event/m^3. In time, decay during shut-ins resembles the Omori law although with slightly longer t_r. The seismicity rate also tends to be overestimated at the onset of injections. In space, the mean distance and triggering front are significantly overestimated. The threshold model presented in the main text

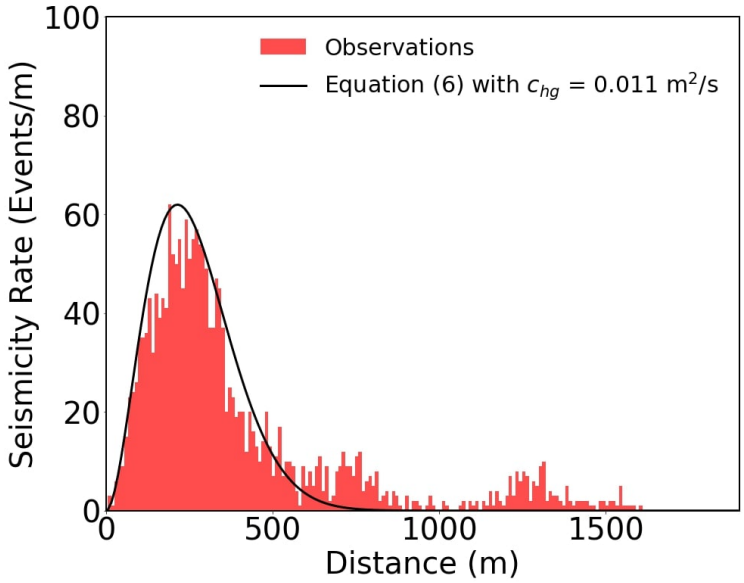

Figure B.6: Estimation of c_{hg} in Otaniemi. The cumulative radial distribution of the relocated catalogue (red) is compared to Equation B.6 with c_{hg} = 0.011 m^2/s (black). The estimated value of c_{hg} also gives a good fit to the observed catalogue when used to construct the spatio-temporal convolution kernel.

is seen to improve the temporal fit significantly but has relatively minimal impact on the spatial distribution of events.

B.7 Sensitivity Analysis of t_r on Physical Parameters

The dependence if t_r on both nucleation and stress relaxation can be demonstrated by an analysis of its sensitivity to parameters a, the rate-and-state friction parameter and k, the permeability. Single boxcar injection scenarios are tested under the rate-and-state model and t_r of the Omori law fit following shut-in is measured. k and a are varied between $[10^{-16} \sim 10^{-14}$ m$^2]$ and $[10^{-4} \sim 10^{-2}]$, respectively. The duration of the boxcar injections are chosen to be equal to the characteristic diffusion time, $t_c = \frac{L^2}{c}$, to ensure all simulations reach steady-state stress prior to shut-in. The injection rate, q, is also varied for the characteristic pore pressure at the boundary of the modelled domain, $p_q = \frac{q\eta}{4\pi\rho_0 kL}$, to reach 10^{-6} of the ambient pore pressure, p_0, so that near-lithostatic pore pressure is avoided. The size of the domain, L, is chosen to be 2000m as in previous models. All other parameters are identical to those listed in Table 3.1. Example simulations for two parameter sets that only differ in the value of a or k are showing in Figure B.8. One can see that there is significantly greater difference in t_r for a smaller change in the diffusivity than in a. Namely,

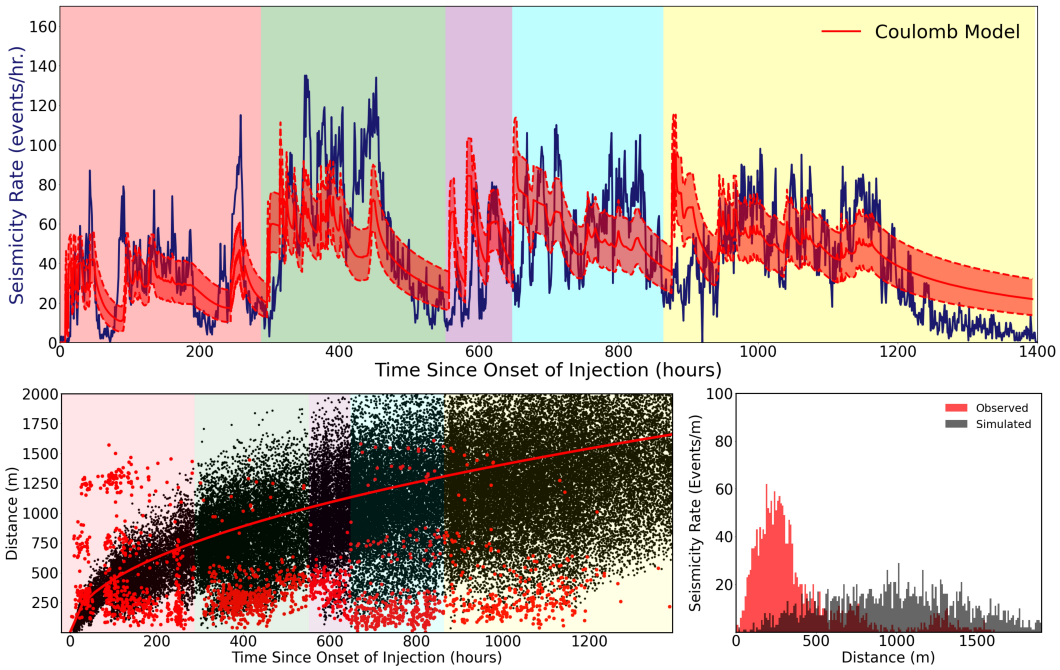

Figure B.7: Seismicity rate in time and space for standard Coulomb model without thresholds. $c_{true} = c_{bu} = 0.044$ m^2/s and $\alpha_c = 47250$MPa/event/m^3. In time, the KS-statistic returns 0.08, higher than the rate-and-state model (KS-statistic=0.025) with the same diffusivity. In space, the mean distance and triggering front are significantly overestimated, reaching further than the theoretical triggering front in red.

higher diffusivity leads to faster relaxation of pore pressure, faster relaxation of the seismicity rate, and lower t_r.

B.8 Validity Region of the Linear Convolution Method

The success of the linear convolution method in matching the observed seismicity rate in Otaniemi and the spatio-temporal variation of the seismicity predicted by the rate-and-state model is unexpected given the nonlinear mechanisms governing stress variations and earthquake triggering. Notably, the Kaiser effect predicts that the seismicity rate should lose its linearity to the forcing history with time, and nonlinear dependence on slip-rate of rate-and-state friction predicts a phase shift between seismic and stressing periodicities (Ader et al., 2014). The absence of a strong Kaiser effect is thus probably one factor that explains the success of the convolution model at fitting the observations from the Otaniemi EGS stimulations. If one interprets Coulomb friction as a limiting case of rate-and-state friction as a approaches zero (and nucleation becomes instantaneous), one may expect increasingly

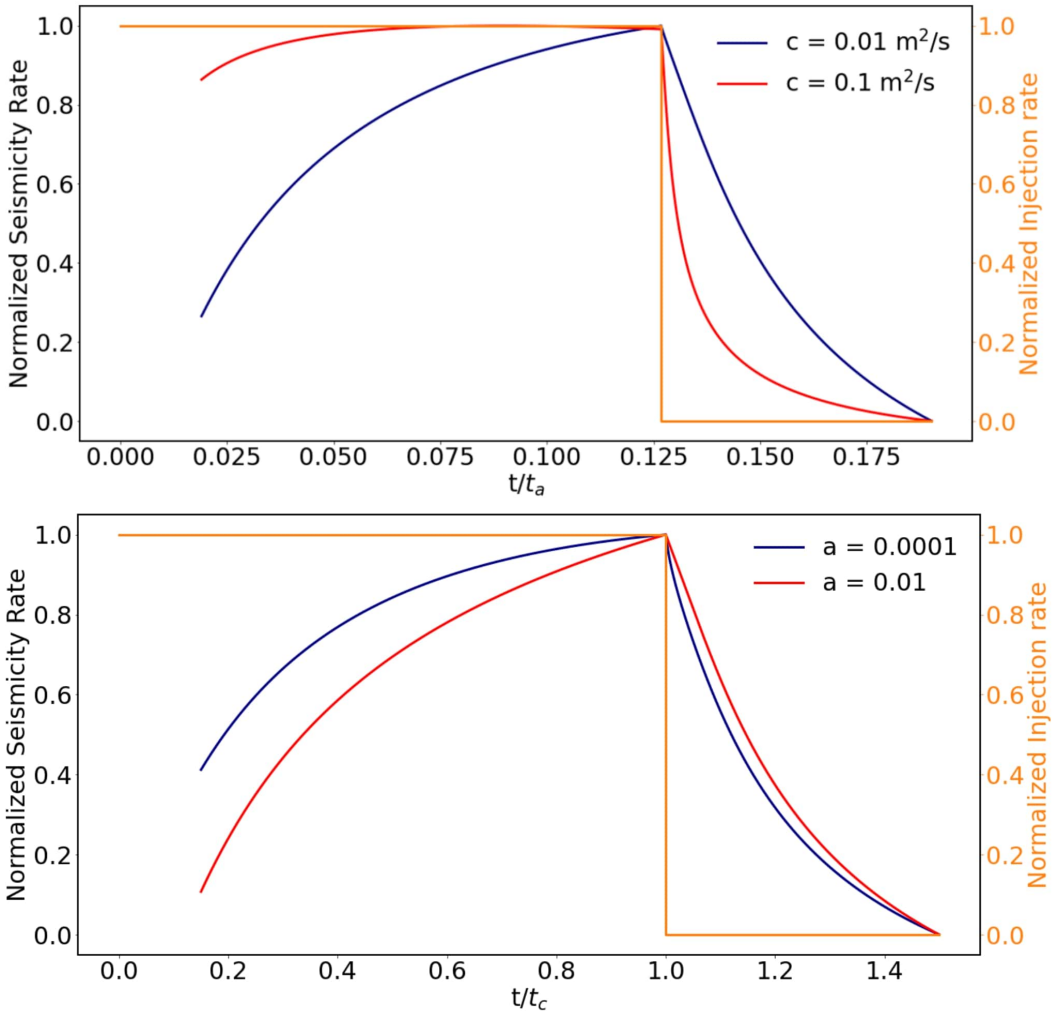

Figure B.8: Seismicity rates due to boxcar injections using the rate-and-state model. Top and bottom plots show two parameter sets that only differ by c and a, respectively. a and c are fixed at 0.0005 and 0.01 m^2/s for the top and bottom plots, respectively. t_r generally shows stronger dependence on fluid transport properties than on frictional parameter, a.

linear behavior to surface with decreasing values of a. It is thus hypothesized that the linear convolution model is valid if rate-dependence of friction and the Kaiser effect are relatively small.

To test this hypothesis, we assess the performance of the convolution model to approximate predictions from the rate-and-state model by varying systematically the importance of these effects. We simulate generic injection scenarios consisting of repeated boxcar injections under the rate-and-state model and measure the root mean squared error (MSE) of its approximation by the convolution model. The

number of boxcar injection cycles is chosen to be twenty as this is close to the average number of cycles within a single stage at Otaniemi. The seismicity rate is normalized to range from 0 to 1 for all scenarios. In this sensitivity analysis, the convolution kernel is not limited to the Omori-law with $p = 1$, which does not provide sufficiently accurate fits to all decay patterns across the tested parameter regimes; the decay pattern is often observed to be better matched with higher values of p depending on the physical parameters. In this regard, the linear convolution prediction is produced by taking the response of the model due to a constant injection scenario as the integral of a numerical convolution kernel. The duration of injections, t_I, is altered to be fractions of the characteristic diffusion time with the shut-ins held for equal time. The injection rate, q, is adjusted so that the characteristic pore pressure, $p_q = \frac{q\eta}{4\pi\rho_0 kL}$, is 10% of the ambient pore pressure, p_0, as is the case for the Otaniemi injection scenario given the average injection rate and the diffusivity from Horner analysis. L is chosen to be 2000m to match the parameters of previous models. Two non-dimensional variables are chosen as follows: the Kaiser effect is expected to be more significant for systems with higher diffusivity that allows locations further away to reach its maximum value in shorter time. The satisfaction of the maximum stress condition should also depend on the injection duration, where longer injections would subject regions in space to below their maximum stress for longer time. Thus, the ratio t_I/t_c is taken to be the representative parameter where a higher value would correspond to a stronger Kaiser effect. For delayed nucleation, we take $a\sigma/p_q$. Since p_q is constant across all simulations, the ratio measures the direct dependence on a. k, a, and t_I/t_c are varied between [$10^{-18} \sim 10^{-12}$ m^2], [0.0001 $\sim$ 0.02], and [$10^{-5} \sim 10^{-0.5}$], respectively, to reflect a wide range of diffusivity, frictional parameters, and injection scenarios. All other parameters are held constant as listed in Table 3.1.

The MSE is shown as a contour plot in Figure B.9. The contours exhibit a largely vertical structure, indicating stronger dependence on t_I/t_c than on $a\sigma/p_q$. MSE generally increases moving to the right, as expected by stronger Kaiser effect. Across most of the parameter regime, dependence on a is relatively minimal. The effect of the Kaiser effect seems to be amplified by stronger nucleation effects as MSE tends to increase moving upward. Given lower ratios of t_I/t_c, the convolution model does an excellent job, even with stronger nucleation effects.

We locate the possible region in the contour plot that may correspond to the Otaniemi scenario. We take the a relatively wide range of permeability and a surrounding the

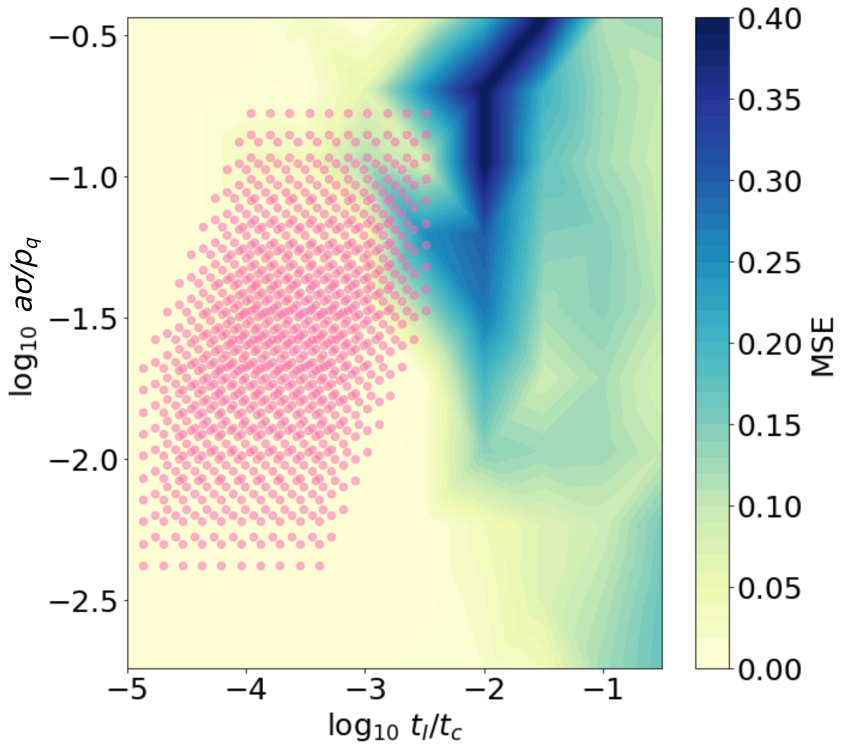

Figure B.9: Validity region of linear convolution model. The root mean squared error (MSE) of the linear convolution model to the rate-and-state model is shown as a contour plot. The contours have a mostly vertical structure, showing stronger dependence on the ratio t_I/t_c , or stress evolution from pore pressure diffusion. Higher values of the ratio correspond to stronger Kaiser effect which break linearity of the seismicity rate to injection cycles. Plotting a range of values that may correspond to the Otaniemi scenario in pink dots illustrates that Otaniemi may have had favourable conditions for linearity in the stress evolution process by avoiding strong impact from the Kaiser-effect. The parameter regime for Otaniemi is estimated by the range of permeability and rate-and-state parameter, a, inferred from this study, along with the average injection rate, injection duration and parameters of Table 3.1. Dependence on $a\sigma/p_q$ is relatively minimal showing that non-linearity of delayed nucleation may be sufficiently subsumed in the convolution model.

values inferred from Horner analysis and modelling, which is $[7 * 10^{-17} \sim 2 * 10^{-16}$ $m^2]$ and $[0.0001 \sim 0.0005]$, respectively. We also take an average injection rate of 600 L/min. and injection durations in the range of $[1 \sim 30$ hours] given the average duration of 13 hours at Otaniemi with a standard deviation of 15 hours. The resulting parameter regime is plotted by pink dots in Figure B.9, illustrating that the Otaniemi scenario may well have had favourable ratios of t_I/t_c for the convolution model by avoiding the Kaiser effect. The result is consistent with the evidence so far that the Kaiser effect may have been muted in Otaniemi. The result also implies

that the convolution model would not have been as successful given changes to the system that would increase t_I/t_c, e.g., by injecting for longer durations within a single stage.

B.9 Evolution of Injectivity in Otaniemi

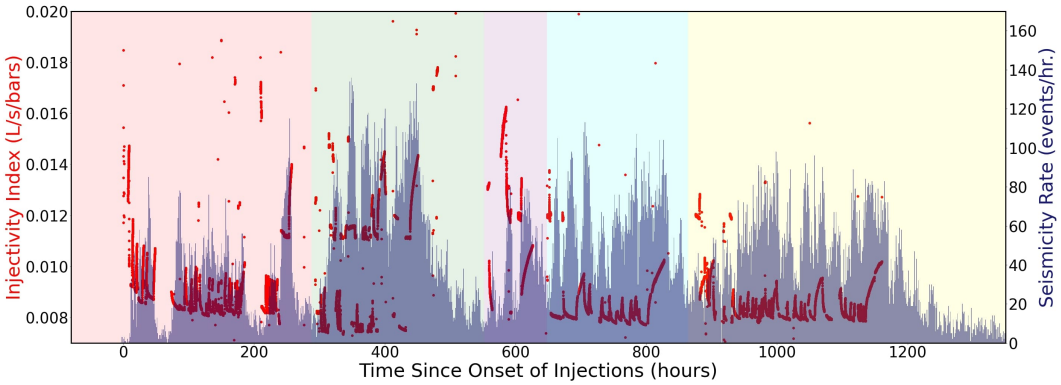

Figure B.10: Evolution of injectivity in Otaniemi. The injectivity index is plotted as a scatter plot in red over the observed catalogue of Leonhardt et al. (2020). Periods of high injectivity are often correlated with periods of high seismicity rate, likely due to increases in permeability from seismic activity.

Appendix C

APPENDIX FOR CHAPTER 4

C.1 Numerical Integration of Equation 4.5

We aim to solve for the normalized seismicity rate, $\hat{R} = \frac{R}{R_b}$:

$$\hat{R} = \frac{K(t)}{1 + \frac{1}{t_a}\int_0^t K(t')\,dt}$$

$$K(t) = \exp\left(\frac{\tau(t)}{a\bar{\sigma}(t)} - \frac{\tau_0}{a\bar{\sigma}_0}\right)$$

$$g \equiv \frac{\tau(t)}{a\bar{\sigma}(t)} - \frac{\tau_0}{a\bar{\sigma}_0}$$

where τ is the applied shear stress, p is pore pressure, $\bar{\sigma} = \sigma - p$ is the effective normal stress, $\dot{\tau}_r$ is the background stressing rate that produces background seismicity rate R_b, and a is the rate-and-state direct-effect parameter. The subscript o represents the initial value of the variable.

To avoid computing the exponential of the stress history which may cause overflow, we first solve for the log of the seismicity rate:

$$\hat{h} = \log\hat{R} = \log K(t) - \log\left(1 + \frac{1}{t_a}\int_0^t K(t')\,dt\right) \tag{C.1}$$

Next, we work in an incremental system where we store information about the integral up to time t_{n-1}:

$$\begin{aligned} d_n \equiv \log\left(1 + \frac{1}{t_a}\int_0^{t_n} K(t')\,dt\right) &= \log\left(1 + \frac{1}{t_a}\int_0^{t_{n-1}} K(t')\,dt + \frac{1}{t_a}\int_{t_{n-1}}^{t_n} K(t')\,dt\right) \\ &= \underbrace{\log\left(1 + \frac{1}{t_a}\int_0^{t_{n-1}} K(t')\,dt\right)}_{d_{n-1}} + \Delta d_n \end{aligned} \tag{C.2}$$

$$\Delta d_n = \log\left(1 + \frac{t_n - t_{n-1}}{t_a} \cdot (\exp(g_n - d_{n-1}) + \exp(g_{n-1} - d_{n-1}))\right) \tag{C.3}$$

Plugging equations C.3 and C.2 into Equation C.1 and taking the exponential returns the seismicity rate at time t.